Magnetism in topological materials

JIAN-RUI SOH

ST ANNE'S COLLEGE

UNIVERSITY OF OXFORD

A thesis submitted for the degree of

Doctor of Philosophy

Trinity term 2019

Abstract

Notions of topology are of considerable interest currently in physics, especially in the way topology influences the electronic properties of crystalline solids. This thesis concerns the experimental investigation of four different magnetic materials, which have been predicted to display a strong interplay between magnetism and the topology of the electronic band structure.

I demonstrate that $EuCd_2Sb_2$, below $T_N = 7.4\,K$, displays an A-type antiferromagnetic order on the Eu sub-lattice with a magnetic propagation vector of $\mathbf{k} = \left(0, 0, \frac{1}{2}\right)$. I also establish that the C_3 rotational symmetry along the crystal c axis (essential for the stabilisation of band crossings called Dirac nodes) is broken by the in-plane orientation of the Eu moments.

Following the initial discoveries of crystalline solids which can host topologically-protected band crossings called Weyl nodes, there is now a need for better material realisations, ideally comprising a single pair of nodes located at or very close to the Fermi level and in an energy window free from other overlapping bands. I propose that $EuCd_2As_2$, in a magnetic field of $B > 1.6\,T$ along the c axis, to be such a system. This material is of general interest as it represents the simplest possible Weyl semimetal, and is therefore a model system for fundamental investigations of Weyl physics.

I refute the proposition that semimetallic $YbMnBi_2$ hosts Weyl nodes induced by the time-reversal symmetry breaking mechanism. Furthermore, the full magnetic excitation spectrum of $YbMnBi_2$, which has been mapped for the first time, demonstrates that the magnetic order of the Mn sub-lattice is weakly coupled to the charge carriers in the Bi square net.

Finally, the complex magnetic order of the Mn sub-lattice in Mn_3Ge has been elucidated for the first time. This will shed light on the origin of the large anomalous Hall effect in Mn_3Ge, which is unusual for an antiferromagnet.

Acknowledgements

Firstly, it is a privilege to have been supervised by Andrew Boothroyd. I am deeply thankful for the trust that he has placed in me, for the insights that I have gleaned from him over the many discussions we have had and for fostering an intellectual environment where I have been able to contemplate the beauty of the universe expressed in the laws of physics.

I am also thankful to the following people who have helped me tremendously during the course of my research: Mike Glazer, Steve Blundell, Marein Rahn, Henrik Jacobsen, Chen Jiahao, Sun Jinzhao, Amalia Coldea, Roger Johnson, Radu Coldea, Paolo Radaelli, Kieran McCall and Mohamed Cheddi in Oxford; Christian Donnerer, James Vale and Cameron Dashwood in UCL; Fernando de Juan and Maia Vergniory in San Sebastian; Enrico Schierle and Eugen Weschke in Berlin; Sonia Francoual, Jennifer Sears and Pablo J. Bereciartua Perez in Hamburg; Alexandre Ivanov, Andrea Piovano and Navid Qureshi in Grenoble; Feng Zili and Shi Youguo in Beijing; Wang Hongyuan, Su Hao and Guo Yanfeng in Shanghai; Timur Kim, Alessandro Bombardi, Pascal Manuel, Dmitry Khalyavin and Fabio Orlandi in Harwell. I would also like to thank Dharmalingam Prabhakaran who introduced me to the beauty of crystals; Niels Shroeter who exemplified tenacity during our ARPES beamtimes; Matt Bristow and Pascal Weiß for teaching me the art of contacts making; Nat Davies and Matt Watson who have given me perhaps the best advice; Steve Simon and Des McMorrow for examining my thesis.

Through the many ups and downs of research, I am deeply indebted to my family who has always been there as my constant cheerleaders: Pa, Ma, Yong Sheng and Chang Li. I would also like to thank my church family who has been my constant support, providing a home away from home: Jon Chan, Lorraine Ow, Larissa See, Yashua Bhatti, Liz Wu, Antje Carrel and Alex Philips. A special mention goes to Rahul Ravindran, who drove me at 1 am to pick up crystals from the Clarendon before my experiment in Hamburg.

Finally, I would like to thank my wife Elenor Morgenroth for reminding me why I pursued science in the first place.

Contents

1 Introduction **12**

1.1 The Weyl equation . . . 12

1.2 Massless quasiparticle excitations in a crystal . . . 12

1.3 Topological protection . . . 13

1.4 Topological properties of Weyl fermions in a crystal . . . 16

1.4.1 TaAs structural family . . . 19

1.5 Control of massless fermions in crystals . . . 20

1.5.1 Spin-orbit coupling . . . 20

1.5.2 Strong correlations - Local vs itinerant magnetism . . . 26

1.5.3 Coupling between localised magnetism and electronic bands . 28

1.6 Examples of magnetic Weyl semimetals . . . 29

1.6.1 Rare-earth iridates . . . 30

1.6.2 112-pnictides . . . 32

1.6.3 $\mathrm{Mn_3X}$ . . . 34

1.6.4 111-compounds . . . 35

1.6.5 Other types of WSMs . . . 36

1.7 All not ideal . . . 37

1.7.1 Nodes close to E_F . . . 37

1.7.2 Number of Weyl nodes . . . 38

1.7.3 Irrelevant bands . . . 41

1.8 The ideal Weyl semimetal . . . 42

2 Experimental methods **45**

2.1 Diffraction and the reciprocal lattice . . . 45

2.2 Scattering cross-sections . . . 48

2.3 X-ray scattering . . . 49

2.3.1 Non-resonant elastic X-ray scattering . . . 49

2.3.2 Resonant elastic X-ray scattering (REXS) . . . 52

2.3.3 X-ray sources . . . 55

2.3.4 Examples . . . 57

2.4 Neutron scattering . . . 57

2.4.1 Coherent elastic nuclear scattering 57
2.4.2 Elastic magnetic scattering 59
2.4.3 Inelastic magnetic scattering 60
2.4.4 Examples 62
2.4.5 Neutron sources 62
2.5 Choice of radiation 63
2.6 Magnetotransport 65
2.7 SQUID measurements 66
2.8 Density functional theory 67

3 Magnetic and electronic structure of the layered rare-earth pnictide $\mathbf{EuCd_2Sb_2}$ 70

3.1 Introduction 70
3.2 Experimental and theoretical methods 72
3.3 Results and analysis 74
3.3.1 Magnetisation and magnetotransport 74
3.3.2 Resonant X-ray magnetic scattering 75
3.3.3 Magnetotransport 80
3.3.4 DFT + U Calculations 81
3.4 Conclusion 86

4 An ideal Weyl semimetal induced by magnetic exchange: $\mathbf{EuCd_2As_2}$ 88

4.1 Introduction 88
4.2 Methods and preliminary data 89
4.2.1 Single crystal X-ray diffraction 89
4.2.2 Magnetisation 91
4.2.3 Powder X-ray diffraction 92
4.2.4 Low-field magnetotransport 93
4.2.5 High-field magnetotransport 94
4.2.6 DFT Calculations 96
4.2.7 ARPES 98
4.3 Results 98
4.4 Conclusion 105

5 Magnetic structure and excitations of the topological semimetal $\mathbf{YbMnBi_2}$ 108

5.1 Introduction . . . 108

5.2 Experimental details . . . 111

5.3 Results and analysis . . . 113

5.3.1 Elastic neutron scattering . . . 115

5.3.2 Inelastic neutron scattering . . . 116

5.4 Discussion . . . 123

5.5 Conclusion . . . 126

6 Ground state magnetic structure of the $\mathbf{Mn_3Ge}$ 128

6.1 Introduction . . . 128

6.2 Experimental methods . . . 132

6.3 Results and analysis . . . 135

6.4 Discussion . . . 138

7 Conclusion 142

7.1 $EuCd_2Sb_2$ . . . 142

7.2 $EuCd_2As_2$ . . . 142

7.3 $YbMnBi_2$ . . . 143

7.4 Mn_3Ge . . . 144

8 Appendix 166

8.1 Derivations for $\frac{d\sigma}{d\Omega}$ . . . 166

Abbreviations

AFM	antiferromagnetic/antiferromagnet
AHE	anomalous Hall effect
ARPES	angle-resolved photoemission spectroscopy
BESSY	Berliner Elektronenspeicherring-Gesellschaft für Synchrotronstrahlung, Berlin
DESY	Deutsches Elektronen Synchrotron, Hamburg
DFT	density functional theory
DIAMOND	Diamond Light Source, Didcot
ESR	electron spin resonance
FM	ferromagnetic
GGA	generalised gradient approximation
HMFL	High Magnetic Field Laboratory, Nijmegen
ILL	Institut Laue Langevin, Grenoble
IS	spatial inversion symmetry
ISIS	ISIS neutron and muon source, Oxfordshire
MAC	Multi-analyser crystal
NHMFL	National High Magnetic Field Laboratory, Florida
PETRA III	Positron Elektron Tandem Ring Anlage (DESY)
PM	paramagnetic
PPMS	physical property measurement system
RKKY	Ruderman–Kittel–Kasuya–Yosida
REXS	resonant elastic X-ray scattering
SdH	Shubnikov–de Haas
SOC	spin-orbit coupling
SQUID	superconducting quantum interference device
TRS	time-reversal symmetry
WISH	long-wavelength neutron time-of-flight diffractometer (ISIS)
WSM	Weyl semimetal
XUV	extreme ultra-violet

Publications

- M. C. Rahn, J.-R. Soh, S. Francoual, L. S. I. Veiga, J. Strempfer, J. Mardegan, D. Y. Yan, Y. F. Guo, Y. G. Shi, and A. T. Boothroyd, *Coupling of magnetic order and charge transport in the candidate Dirac semimetal* $EuCd_2As_2$, Phys Rev. B **97**, 214422 (2018).

- J.-R. Soh, C. Donnerer, K. M. Hughes, E. Schierle, E. Weschke, D. Prabhakaran and A. T. Boothroyd, *Magnetic and electronic structure of the layered rare-earth pnictide* $EuCd_2Sb_2$, Phys. Rev. B **98**, 064419 (2018).

- Jian-Rui Soh, Henrik Jacobsen, Bachir Ouladdiaf, Alexandre Ivanov, Andrea Piovano, Tim Tejsner, Zili Feng, Hongyuan Wang, Hao Su, Yanfeng Guo, Youguo Shi, and Andrew T. Boothroyd, *Magnetic structure and excitations of the topological semimetal* $YbMnBi_2$, Phys. Rev. B **100**, 144431 (2019).

- J.-R. Soh, P. Manuel, N. M. B. Schröter, C. J. Yi, F. Orlandi, Y. G. Shi, D. Prabhakaran, and A. T. Boothroyd, *Magnetic and electronic structure of Dirac semimetal candidate* $EuMnSb_2$, Phys. Rev. B (accepted, 2019)

- J.-R. Soh, F. de Juan, M. G. Vergniory, N. B. M. Schröter, M. C. Rahn, D. Y. Yan, M. Bristow, P. Reiss, J. N. Blandy, Y. F. Guo, Y. G. Shi, T. K. Kim, A. McCollam, S. H. Simon, Y. Chen, A. I. Coldea and A. T. Boothroyd, *An ideal Weyl semimetal induced by magnetic exchange*, arXiv:1901.10022

Chapter 1

Introduction

This thesis concerns the properties of metals in which the electrons do not behave in a conventional way, specifically, electrons which have a linear dispersion at or near the chemical potential. These quasiparticle excitations can mimic the behaviour of relativistic Dirac or Weyl fermions and are robust against perturbations due to the protection afforded by topology. Materials that host massless charge carriers are interesting because of the enhanced charge transport properties which could be exploited in electronic devices.

In particular, I consider topological materials which display spontaneous magnetic order. If the magnetism in these crystals is intimately coupled to the electronic bands, altering the magnetic order – with, for example, an external magnetic field – might give us an experimental handle on these exotic quasiparticle excitations. Insights gleaned from the study of the coupling between the topology of the electronic band structure and magnetism can help realise a new class of spintronic devices based on magnetic topological semimetals.

In this introductory chapter, I outline some concepts that are pertinent to understanding how the topological features of the electronic bands of these magnetic semimetals can be created, identified and controlled.

1 Introduction

1.1 The Weyl equation

In 1929, Hermann Weyl predicted the existence of massless fermions [1]. He discovered this by considering the massless form of the Dirac equation [2], which describes massive relativistic fermions. Weyl arrived at the following equation,

$$\sigma^{\mu}\partial_{\mu}\psi = 0, \tag{1}$$

which is now known as the Weyl equation. Using the wave function $\psi = \chi e^{-i(\mathbf{k}\cdot\mathbf{r}-\omega t)}$ – here χ is a 2 component spinor – as a trial solution, one can arrive at an energy-momentum relation of these particles that is linear in $\mathbf{k}$, resembling that for the dispersion for light. Given that these eigenstates are massless, the handedness and the chirality of these spin $\frac{1}{2}$ particles are the same and the thermal distribution obeys Fermi–Dirac statistics.

However, it has been about 90 years since Weyl's prediction and this elusive massless fermion in free space has not yet been found [3]. The strongest candidate in recent times was the neutrinos, which was briefly (although erroneously [4]) touted to break the limit of the speed of light [5]. However, the presence of neutrino oscillations suggests that these neutrinos carry a mass [6], albeit a small one [7]. This nonetheless precludes these fermions from having a truly linear energy-momentum dispersion. Hence, as far as the particle physics community is concerned, the search continues for a massless fermion in free space.

1.2 Massless quasiparticle excitations in a crystal

On the other hand, Weyl's prediction can be realised in condensed matter, where the arrangement of the ions can be engineered in such a way that the Hamiltonian, which describes the behaviour of the electronic states in the vicinity of the Fermi energy, is identical to the Weyl equation [3, 8, 9, 10]. As such, the quasiparticle excitations that exist in such environment can masquerade as massless fermions. Here, the point from which the electronic bands disperse linearly in three dimensions is called a Weyl node and the quasiparticle excitation that this linearly dispersing band crossing gives rise to is called a Weyl fermion [9, 11, 12, 13].

As a starting point, the most obvious host of such particles will be crystalline materials [11, 14, 15, 16]. This is because the condensed matter physics community (i) has developed a good understanding of how to recreate the natural processes of the earth to produce high-quality crystals in the laboratory [17, 18], (ii) is able to use *ab initio* computational methods, expedited by the fact that these crystals have symmetries which speed up calculation, to study whether these system can give rise to linear dispersion in the electronic bands [3, 17, 19, 20] and (iii) can experimentally map the band dispersions of these electronic states with angle-resolved photoemission spectroscopy (ARPES) [3, 11, 21].

Despite these advantages, I list, non-exhaustively, some caveats that come along with using the crystalline lattice as a host. Firstly, although these fermions are massless, they will have speeds much lower than c, the speed of light in vacuum [9, 10, 22]. This arises because the gradient of the linear dispersion can be a lot less steep compared to that of light. Secondly, unlike fermions in free space, the dispersion of these particles cannot have an arbitrarily large wave vector $\mathbf{k}$, but are limited by the size of the Brillouin zone, which is of order of a reciprocal lattice vector $\mathbf{G}$ as a result of the translational symmetry of the crystal [22]. Thirdly, these quasiparticle excitations only exist within the crystal. They emerge from the system of conduction electrons and the periodic potential of the lattice [18, 23]. If these charge carriers are pulled out of the crystal, they will acquire the mass of a free electron.

1.3 Topological protection

Realising a linear dispersion in a crystal to create massless fermions is routinely possible [20, 24, 25, 26] and it gives rise to a whole host of desirable bulk crystalline properties: extremely high electron mobility, large magnetoresistance and stability to disorder [3, 10, 22]. However, if these crossing points are not robust but are destroyed when we perturb the crystal (e.g. with an applied field, strain, temperature etc.), then such materials are too unstable for electronic applications. One way to solve this problem is to take advantage of topology to afford protection to these nodes [3, 9, 10, 22].

The concept of topological protection is illustrated by the well-known Möbius strip, Fig. 1(a), which is formed by taking a strip of paper, applying a twist of

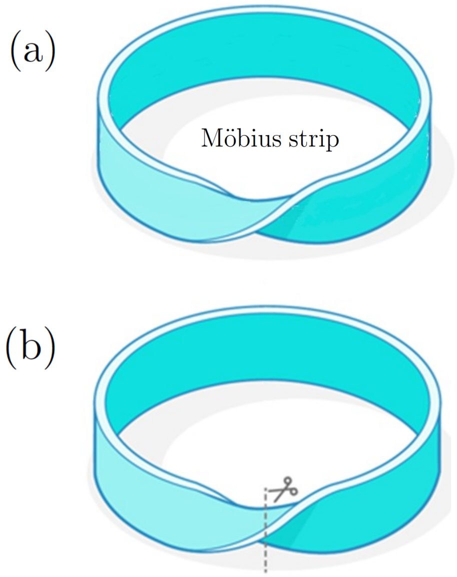

Figure 1: (adapted from [27]) (a) A Möbius strip can be formed by taking a strip of paper and applying a twist of 180° deg and connecting the ends. There is no way of continuously deforming the strip to give an ordinary loop unless something drastic is done [eg. cutting the strip (b), undoing the twist and connecting the ends of the paper].

180° deg then connecting the ends together. This is topologically distinct from an ordinary loop which is formed by connecting the ends of the strip of paper without the 180° deg twist; specifically, it is not possible to continuously deform a Möbius strip into an ordinary loop. Unless something drastic is done to the Möbius strip [e.g. cutting the strip, Fig. 1(b)], there is no way of unravelling the *twist* in the strip to change it from one state to the another. In the same way, in some crystals, the electronic bands are *twisted* in such a way that the crossing points are topologically protected [3, 9, 10]. For instance, in Weyl semimetals, Weyl nodes are examples of such crossing point [see Fig. 2(a)]. These nodes appear in pairs and will not be annihilated unless they meet in $\mathbf{k}$-space. From these nodes, the electronic bands disperse linearly in three dimensions and harbour massless Weyl fermions.

There is a strong set of criteria that distinguishes a topologically-protected Weyl node from a topologically trivial band crossing [9, 10, 11, 12]. Whilst the dispersion in both cases are identical and the differences subtle, the consequences are very different with the former being robust against the aforementioned perturbations

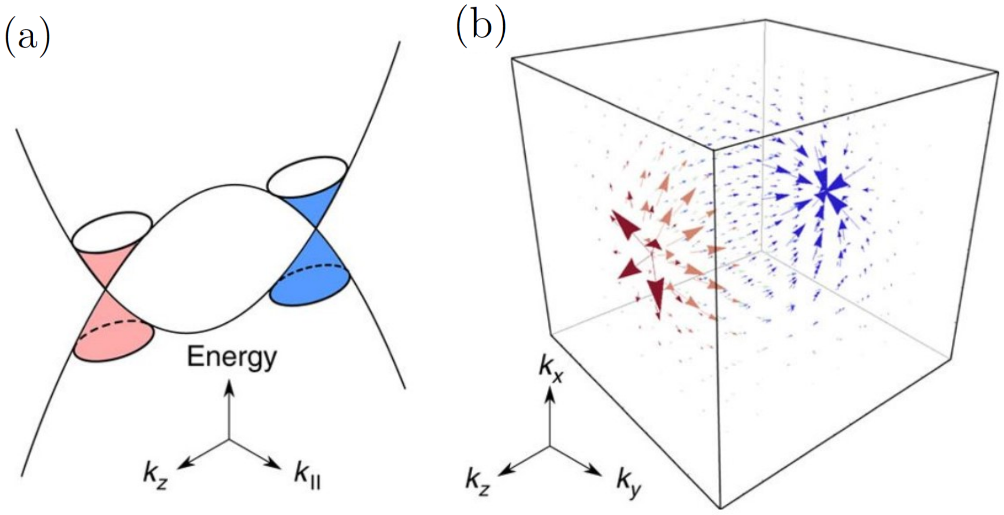

Figure 2: (adapted from [28]) In a typical semiconductor, the conduction and valence bands do not cross, giving rise to a small energy gap. In Weyl semimetals, Weyl nodes can arise from an inversion of the bands. (a) depicts parabolic valence and conduction bands intersecting at two points in **k**-space, which can arise from such a band inversion. Here, the energy dispersion of the electrons close to the nodes is linear with respect to momentum. (b) shows the vector plot of the Berry curvature in **k**-space, with the direction of the arrows showing that the flux of the Berry curvature from one monopole (red) to the other (blue). This flux is quantised and defines the non-trivial topological properties of the topological semimetal in question.

whilst the latter is not. If we take $u(\mathbf{k})$ as the Bloch wave function describing an electronic state with wave vector $\mathbf{k}$, we can consider the Berry connection, which is given by, $\boldsymbol{A}(\mathbf{k}) = -i\,\langle u(\mathbf{k})|\nabla_{\mathbf{k}}|u(\mathbf{k})\rangle$ [9, 11, 12]. Given that the vector $\boldsymbol{A}(\mathbf{k})$ is analogous to the vector potential in electro-magnetism, we can obtain the Berry curvature, $\boldsymbol{\Omega}(\mathbf{k}) = \nabla_{\mathbf{k}} \times \boldsymbol{A}(\mathbf{k})$. If the crossing point is indeed a Weyl node, then it acts as either a source or sink of Berry curvature in **k**-space [see Fig. 2(b)], with the total flux passing through a Gaussian surface which includes such a node, or more succinctly,

$$C = \frac{1}{2\pi}\int \boldsymbol{\Omega}(\mathbf{k}) \cdot d\boldsymbol{S}, \tag{2}$$

being +1 or −1 respectively [9, 10, 12].

On the other hand, if the net flux is 0, then the node is topologically trivial. Hence C, the Chern number, gives us a way to topologically classify nodes in the Brillouin zone. Examples of crystals that contain topologically-trivial nodes include Cd_3As_2 [29, 30, 31, 32] and Na_3Bi [33, 34] [see Fig. 3]. The nodes are protected by rotational symmetries rather than topology and are made up of doubly-degenerate conduction and valence bands meeting at four-fold degenerate Dirac points in **k**-space [11, 31, 35]. The points lie along the $\Gamma - A$ high symmetry line, which remains invariant under symmetry operations C_{4z} in Cd_3As_2 and C_{3z} in Na_3Bi, and are robust in so far as these rotational symmetries are not broken [31, 33]. For instance, in Cd_3As_2, the doubly-degenerate Cd $5s$ and As $4p$ bands, which cross to give rise to the Dirac points, are described by different irreducible representations under the C_{3z} symmetry transformation [31]. If the crystal is deformed, such that the rotational symmetry is broken, the bands can no longer be distinguished by C_{3z} and hybridise to give rise to a gap. This arises because these Dirac points can be considered as two copies of Weyl points which coincide in **k**-space and should be annihilated if not for the rotational symmetries of the host crystal [31, 33]. In Chapter 3, I explore the effects of broken rotational symmetries on Dirac nodes in $EuCd_2Sb_2$.

Compared to Dirac materials, such a hybridisation in Weyl semimetallic phases is precluded as the double degeneracy of the bands are lifted. As such, Weyl nodes are made up of singly-degenerate conduction and valence bands which touch at doubly-degenerate points [9, 10, 11]. The nodes come in pairs with opposite chirality and are separated in **k**-space. Under strain, applied field or other perturbations to the crystal, the nodes move around in **k**-space but will not annihilate, unless pairs of Weyl nodes with opposite chirality meet. This robustness stems from the non-trivial topological nature of the nodes.

1.4 Topological properties of Weyl fermions in a crystal

Weyl nodes have a definite chirality associated with the sign of the Chern number, and as a result the Weyl points have a definite helicity, i.e. the spin is locked to the direction of the momentum [3, 9, 11, 12]. As a result, back scattering processes that conserve spin, e.g. scattering from phonons, non-magnetic impurities, charge scattering from electrons, etc, can be reduced. The mass and the size of the Fermi

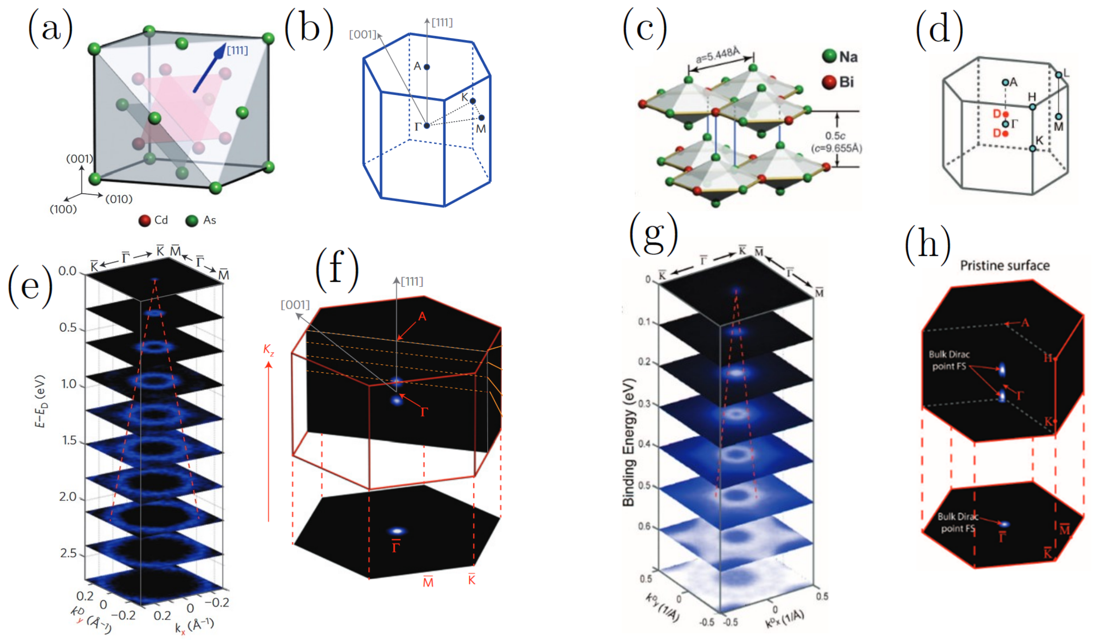

Figure 3: (adapted from [29, 34])(a) and (c) depict the crystal structure of Cd_3As_2 and Na_3Bi respectively. (b), (d), (f), (h) In both compounds, the pair Dirac nodes lie on the $\Gamma - A$ high symmetry line and are protected by the rotational symmetry along the [111] and [001] direction for Cd_3As_2 and Na_3Bi respectively. Each Dirac node comprises two copies of Weyl nodes that coincide in **k**-space. (e) and (g) depict the linearly dispersion of the bands in the vicinity of the Dirac points.

surface of these charge carriers can be estimated from the quantum oscillations observed in magnetotransport and other measurements [3, 11, 12].

Furthermore, since the Weyl points are separated in **k**-space, electrons can be *pumped* between nodes of opposite chirality [9, 10, 11]. This violation of the conservation of chiral charge, or chiral anomaly, increases the conductivity of Weyl materials with increasing applied field and can be achieved if the electric and magnetic field are applied in the same direction.

Moreover, in recent years, there has been a great deal of interest in measuring anomalous transport effects caused by Berry curvature in topological semimetals, especially the anomalous Hall effect (AHE). In a Weyl semimetal, the Berry curvature is associated with the separation Δk (in the $\hat{z}$ direction) of the Weyl nodes in **k**-space. For a single pair of nodes at $E_{\rm F}$, the anomalous Hall conductivity has the universal form [9, 10, 11],

$$\sigma_{xy}^{AHE} = \frac{e^2}{2\pi h}\Delta k. \tag{3}$$

This too, can be estimated from magnetotransport measurements.

Another distinct signature of the topological nature of the Weyl nodes in the crystal is the Fermi arcs [Fig. 4(c), (f)]. They connect the nodes that can be in any general **k**-space position in the Brillouin zone. Unlike the linearly dispersing electronic bands emanating from these nodes that appear in the bulk, these Fermi arcs manifest as surface states [3, 9, 11]. Detecting Fermi arc surface states with ARPES is the definitive way of demonstrating that a crystal hosts Weyl nodes (at least at the surface of the crystal) [3, 11, 12], [Fig. 4(e), (f)].

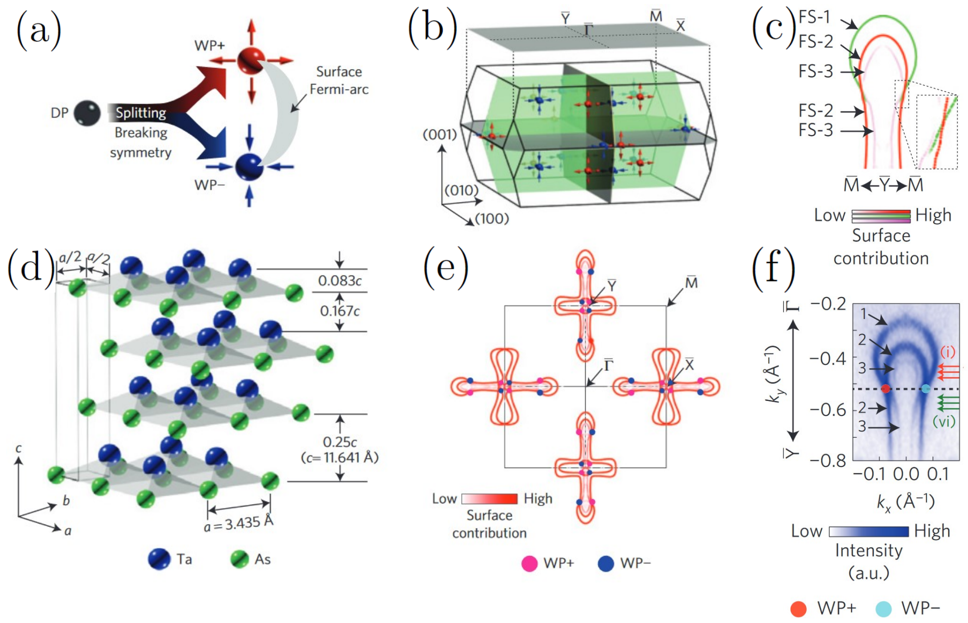

Figure 4: (adapted from [36]) (a) illustrates how the Dirac point splits into two Weyl nodes of opposite chirality due to inversion symmetry breaking. This is true for TaAs [see (d) for crystal structure] which lack an inversion centre. (b) shows the **k**-space distribution of the Weyl nodes that are in the vicinity of the chemical potential for TaAs. (e) is the projection of the nodes (viewing down the k_z direction) and the Fermi arcs connecting the nodes onto the $k_x - k_y$ plane. There is strong agreement between the (c) predicted and (f) measured Fermi arcs.

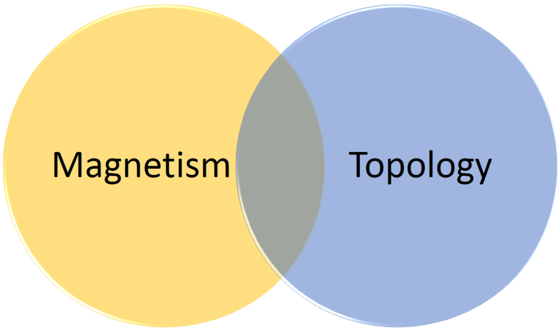

Figure 5: In this thesis, I investigate materials which display spontaneous magnetic order and non-trivial topological features in the electronic bands.

1.4.1 TaAs structural family

Weyl nodes can be found in crystals with either broken spatial inversion symmetry (IS), or broken time-reversal symmetry (TRS), or both [3, 9, 11, 12]. In these crystals, the electronic bands are singly-degenerate and the topologically protected Weyl points, if they exist, are not limited by the symmetries of host crystal and can be situated at any general position in **k**-space and energy [see Fig. 4(b)]. However, for the Weyl node to have an effect on the observable properties of the material, they have to be at or very close to the Fermi energy of the system [3, 9, 11, 12]. Here, I define Weyl semimetals (WSM) as crystals which contain Weyl nodes in the vicinity of the Fermi energy.

Examples of the first type (with broken inversion symmetry only) were found in 2015 with the first being TaAs [see Fig. 4]. This was confirmed by the observation of distinctive features of Weyl nodes: Fermi arcs connecting the points as revealed by ARPES [36, 37, 38], light masses of the charge carriers as indicated by the magnetotransport measurements [39], quantum transport induced by chiral anomaly [40], etc. Soon after, TaP, NbAs and NbP, which belong to the same non-centrosymmetric structural family as TaAs, were also found to host Weyl fermions [41, 42, 43].

1.5 Control of massless fermions in crystals

In Sections 1.1 and 1.2, I introduce the concept of Weyl fermions along with their properties and how they can be realised in crystals. Subsequently, in Sections 1.3 and 1.4, I consider how we can afford these massless fermions robust protection and summarised some of their attributes arising from the topological nature of the Weyl nodes. In Sections 1.5–1.6, I am going to discuss a class of WSMs where we can potentially exert stronger control of these topologically-protected massless charge carriers compared to those examples listed in 1.4.1.

This can be realised in crystalline materials with broken TRS, where magnetic order coexists with the topological electronic band structure [11, 12, 44]. If the Weyl nodes are strongly coupled to the magnetic sub-lattice of the host crystals, we can modulate the properties of these exotic quasiparticle excitations. Wielding control of massless charge carriers, which are robust against perturbations, can help realise a new generation of spintronic devices with low power consumption and resistance [11, 12, 44].

This is the class of materials that is investigated in my thesis, where the crystalline unit cell is decorated with magnetic ions such as Eu^{2+} and Mn^{2+}, which possess partially-filled $4f$ and $3d$ bands respectively, and heavy elements such as Sb, Bi, As and Ge, which support strong spin-orbit interaction. Such material systems provide for an avenue to explore the rich interplay between the physics of strong electron correlations, which produce magnetism, and large spin-orbit coupling (SOC), which gives rise to non-trivial topologies in the electronic band structure. Before considering examples of magnetic WSMs [1.6], I discuss in the subsequent sections the SOC phenomena which might cause the electronic bands to invert [1.5.1], strong electronic correlations which give rise to magnetism [1.5.2] and the possible exchange coupling between the two [1.5.3].

1.5.1 Spin-orbit coupling

In the search for topological materials, a particular route that has proved very successful in the identification of crystals with non-trivial band topology is in the exploration of materials that possess heavy constituent atoms (eg. As, Sb, Bi, Se, Te). This *modus operandi* is in fact common across the three different topological material classes: topological insulators, Dirac and Weyl semimetals. Here, the underlying principle is that these heavy atoms can give rise to a large SOC strength, which roughly scales as Z^4 (where Z is the atomic number), and alter the topology of the electronic band structure. This subsection aims to address how the spin-orbit coupling phenomena (i) produces topological features in the electronic band structure, and (ii) informs some of the material considerations when deciding which elements are used in the host crystal. This can also shed light on certain trends of the electronic band evolution across a family of isostructural compounds and guide the search for better topological materials. While there will inevitably be some overlap with the earlier discussions on the topological nature of the bands, I will focus, in particular, on how the SOC aspect bears out in the band topology of the various classes of topological materials.

Topological insulators The isostructural A_2B_3 (A=Sb, Bi; B=Se, Te) family of compounds crystallises with a trigonal unit cell which can be described by the $R\bar{3}m$ (No. 166) space group. The five atoms in the rhombohedral primitive unit cell are situated at Wyckoff positions 6*c* (Sb, Se-1) and 3*a* (Se-2). Here Se-1 and Se-2 refer to Se atoms at two symmetry inequivalent Wyckoff sites [see Fig. 6(a)]. DFT *ab initio* band structure calculations suggest that all four A_2B_3 compounds are insulating in the bulk [45] [see Figs. 6(b)–(e)].

Sb_2Se_3 in particular, as shown in Fig. 6(b), is a narrow-gap semiconductor ($E_G \sim$1 eV [46]), with hole and electron bands formed by Sb 5p and Se-1 4p states respectively [45]. At the Γ point, these bands display p_z orbital character with normal ordering with respect to energy. In other words, if the constituent atoms of the crystal are separated to give isolated elements, we find that these electronic bands can be smoothly deformed to give the energy levels of Sb and Se atoms. Since the electronic structure of the crystalline bands and the energy level of isolated Sb and Se atoms belongs to the same topological class, we classify Sb_2Se_3 as a trivial insulator.

On the other hand, in Bi_2Se_3, Bi_2Te_3 and Sb_2Te_3, the ordering of the valence and conduction bands with respect to energy at the Γ point is inverted compared to the atomic case. For instance in Bi_2Se_3, the energy of the Bi 6p states at the Γ point lies below that of the Se-1 4p states, as shown in Fig. 7(a), which is switched compared to the energy levels of isolated Bi and Se atoms. Hence, we might intuitively expect that such a *twisting* of the valence and conduction bands, giving rise to a band inversion, would lead to band crossings at discrete points or along nodal lines in **k**-space near the Fermi energy. However, the DFT calculations demonstrate that Bi_2Se_3, Bi_2Te_3 and Sb_2Te_3 are all insulating in the bulk [45]. This arises because in all three compounds, the bands which cross are doubly-degenerate and are described by the same irreducible representation with respect to the C_{3v} double group along the k_z axis [35]. As such, these electronic states hybridise and give rise to an energy gap in the electronic dispersion at the Fermi energy. Due to this band gap in the Bi_2Se_3 crystal, there is no way to smoothly deform the inverted Bi $6p$ and Se-1 $4p$ bands to give us the atomic case without having the bands to cross. Hence we say that the bands in Bi_2Se_3, Sb_2Te_3 and Bi_2Te_3 are topologically non-trivial and belong to a different topological class compared to that of Sb_2Se_3.

In other words, the trivial topology of the electronic bands of narrow-gap semiconductors, like Sb_2Se_3, can be altered by inverting the order of the valence and conduction bands. Notably, this band inversion can be induced in many ways other than the SOC mechanism described thus far: magnetic exchange, lattice strain,

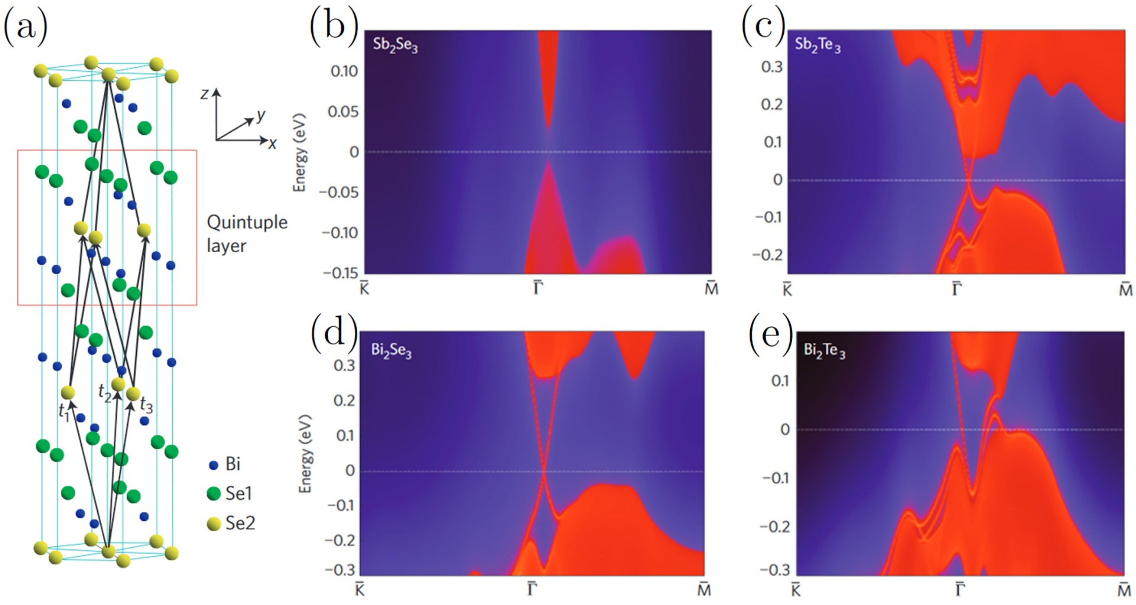

Figure 6: (adapted from [45]) (a) The crystal structure of Bi_2Se_3. (b)–(e) depict the energy and momentum dependence of the local density of states for Sb_2Se_3, Sb_2Te_3, Bi_2Se_3 and Bi_2Te_3 respectively.

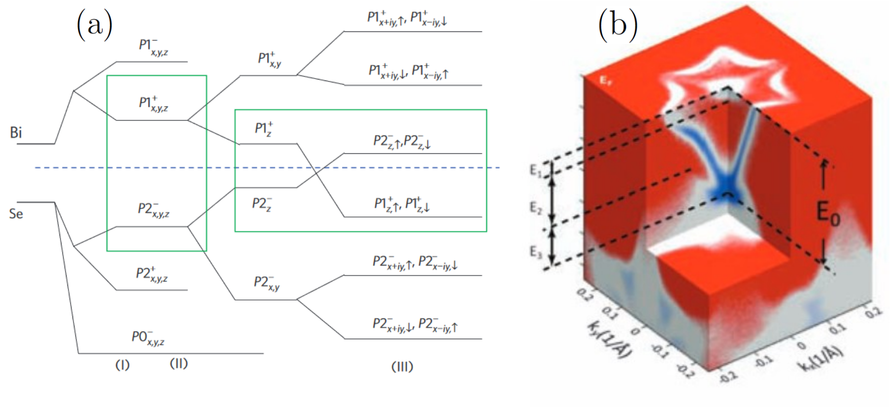

Figure 7: (adapted from [45, 47]) (a) In the context of the Bi_2Se_3 crystal, the ordering of the Bi and Se p_z atomic orbitals with respect to energy is inverted at the Γ point. Here, the three stages, (I)–(III), demonstrate the effects of chemical bonding, crystal-field splitting and SOC respectively on the energy levels of the orbitals. (b) The experimental energy dispersion of the surface states in Bi_2Te_3, measured with ARPES, reveals a Dirac cone.

crystalline symmetries and the Kondo effect [48, 49, 50, 51]. Nonetheless, the SOC mechanism, accounts for the band inversion in most of the experimentally confirmed topological materials. It is, therefore, instructive to consider how this brings to bear in the A_2B_3 family of compounds. For instance, comparing Sb_2Se_3 and Sb_2Te_3, we find that the strength of SOC is larger in the latter compound, given that Te is heavier compared to Se, giving rise to band inversion and a non-trivial band topology. The same is true if we consider Sb_2Se_3 and Bi_2Se_3. Note, however, that the inverted band structure – while necessary – is not sufficient for the existence of a non-trivial electronic band topology [19]. To properly ascertain the nature of the bands, we need to calculate the Chern number.

Although Bi_2Se_3, Bi_2Te_3 and Sb_2Te_3 are all predicted to be insulating in the bulk [45], these materials have conducting states on the crystal surfaces that are protected by topology [47, 52, 53] [see Fig. 6(c)–(e)]. This arises because the inverted bands cannot be smoothly deformed to give the atomic case unless the electronic bands cross, resulting in electronic states on the surface of the crystals. The 2D energy momentum dispersion of these surface states in the topological insulators are reminiscent of the Dirac cones in graphene [47] [see Fig. 7(b)]. Moreover, given that the electronic bands emanating from these topologically protected crossing points on the surface are linearly dispersing, the massless quasiparticle excitations that they host have reduced back scattering due to spin-momentum locking [45].

Dirac semimetals This discovery of topological two-dimensional Dirac cones also sparked off the search for crystals which host bands that disperse linearly in three dimensions, where electronic states are not just on the surface of the crystal but also in the bulk [11, 31, 35]. The approach undertaken in the study by Wang *et al.* (Ref. [31]) was to consider how the hybridisation of the doubly-degenerate bands, which cross due to the band inversion, could be prevented.

Within the A_2B_3 (A=Zn, Cd; B= P, As) family of narrow-gapped semiconductors, $\mathrm{Cd_3As_2}$ has received particular interest as the Cd $5s$ and As $4p$ bands, which are inverted at the Γ point, belong to different irreducible representations of the C_{4v} double group along the $\Gamma - Z$ high symmetry direction [31]. Hence, unlike the case in $\mathrm{Bi_2Te_3}$, $\mathrm{Bi_2Se_3}$ and $\mathrm{Sb_2Te_3}$ where the bands which cross hybridise completely, in $\mathrm{Cd_3As_2}$ the bands are gapped at all but two points in $\mathbf{k}$-space at $(0, 0, \pm k_0)$ near the Fermi energy, as shown in Figs. 3(b) and (f). Here, doubly-degnerate electronic bands disperse linearly in three dimensions from these four-fold degenerate Dirac points. Again, the inverted band structure at the Γ point is driven by the large SOC arising from the heavy Cd and As atoms. This is contrasted with $\mathrm{Zn_3As_2}$, $\mathrm{Zn_3P_2}$ and $\mathrm{Cd_3P_2}$, which possess lighter elements and have normal band ordering near E_F due to the weaker SOC.

The same is also true for the $A_3\mathrm{Bi}$ (A= K, Na, Rb) family of compounds, where a band inversion at the Γ point is present [33]. The inverted bands in $\mathrm{Na_3Bi}$ are described by different irreducible representations with respect to the C_{3v} double group along the $\Gamma - A$ high symmetry line. As such these bands, which have Na $2s$ and Bi $6p$ orbital character, are gapped out at all but two Dirac points from which the electronic bands disperses linearly in three dimensions, as shown in Figs. 3(d), (g) and (h).

Unfortunately, both of these Dirac semimetals are not suitable for device applications: the constituent elements of $\mathrm{Cd_3As_2}$ are very toxic; $\mathrm{Na_3Bi}$ is very unstable in air. As such, an extensive search for other compounds with such Dirac nodes in the electronic band structure was soon underway. These studies considered compounds that would not only have an inverted band structure, due to the presence of heavy elements, but also band crossings which can be described by different irreducible representations. Specifically, the compounds have to possess the C_3, C_4 or C_6 symmetries so that the double group along these rotational axes will have at least two distinct irreducible representations describing the electronic states. This is not the case for the C_2 symmetry which has only one irreducible representation along the axis of two-fold rotation. Examples of such compounds include the XYBi (X = Ba, Sr; Y = Cu, Ag and Au) family [35].

Weyl semimetals In Section 1.3, I pointed out that these Dirac crossing points, which have a Chern number of zero, are not protected by topology and considered other ways in which the hybridisation of band crossings can be prevented. That is, rather than exploiting certain rotational symmetries of the crystal, the band hybridisation can be avoided by the lifting of the double degeneracy in the bands via TRS or inversion symmetry breaking to create three-dimensional linearly dispersing bands that are robust against perturbations.

In a recent theoretical study of the topological phase transition between TIs and normal insulators [49, 55], Murakami *et al.* considered all the space groups that lack an inversion centre (138 in total) and studied how the electronic band topology changes with the strength of SOC, which is described succinctly by a tuning parameter m, and the extent of inversion symmetry breaking. If the crystal has an inversion centre, the study found that the normal and topological gapped phases are demarcated by a sharp Dirac semimetal phase at a given m value. On the other hand, if inversion symmetry is broken, the topological phase diagram shows that a broad WSM phase can be stabilised over a range of m values [Fig. 8(a)]. Again the SOC phenomenon is important in the creation of Weyl nodes in the Brillouin zone.

Furthermore, the strength of SOC determines the extent of band inversion and hence the distance between the Weyl nodes in the Brillouin zone. For instance, in the TaAs family of compounds, [54] Liu *et al.* found the separation between the Weyl nodes increases in the following order: NbP, TaP and TaAs [Fig. 8(b) and (c)]. This roughly scales as the atomic number of the constituent atoms and hence the strength of SOC. The study also found that the Weyl nodes coincide in $\mathbf{k}$-space if

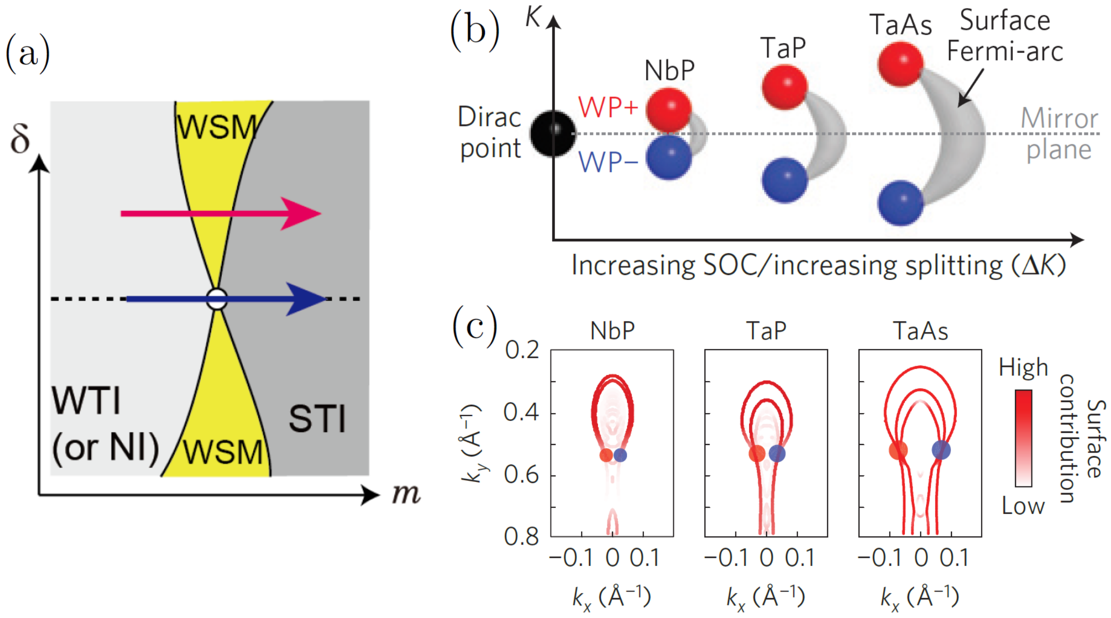

Figure 8: (adapted from [49, 54]) (a) shows the topological phase diagram where δ is the extent of inversion symmetry breaking and m is the strength of SOC. (b) and (c) demonstrate that the distance between the Weyl nodes depends on the strength of SOC.

there is no SOC giving rise to Dirac nodes. Furthermore, on the other extreme, if the SOC strength is too strong, it might cause the Weyl points to annihilate with each other or be pushed beyond the Brillouin zone. This is the case in the Mn_3X ($X=$ Ge, Sn) family of compounds where Mn_3Sn has fewer Weyl nodes compared to Mn_3Ge, as shown in Fig. 9, due to the stronger SOC arising from the heavier Sn atom [56].

1.5.2 Strong correlations - Local vs itinerant magnetism

Magnetism in condensed matter can arise from ions that have incompletely-filled shells. For instance, rare-earth magnetism is produced by the incompletely-filled $4f$ shells in ions such as Nd^{3+} and Eu^{2+}. Similarly, magnetism in transition metal ions such as Mn^{2+} originates from incompletely-filled $3d$ shells. Yet, the nature of the magnetism and the interaction between these magnetic ions strongly depend on the spatial distribution of the electronic wavefunctions. For instance, the $3d$ electrons are usually highly delocalised while the $4f$ electrons are highly localised. This bears out in the size of the moment of the magnetic ions, the nature of the interaction

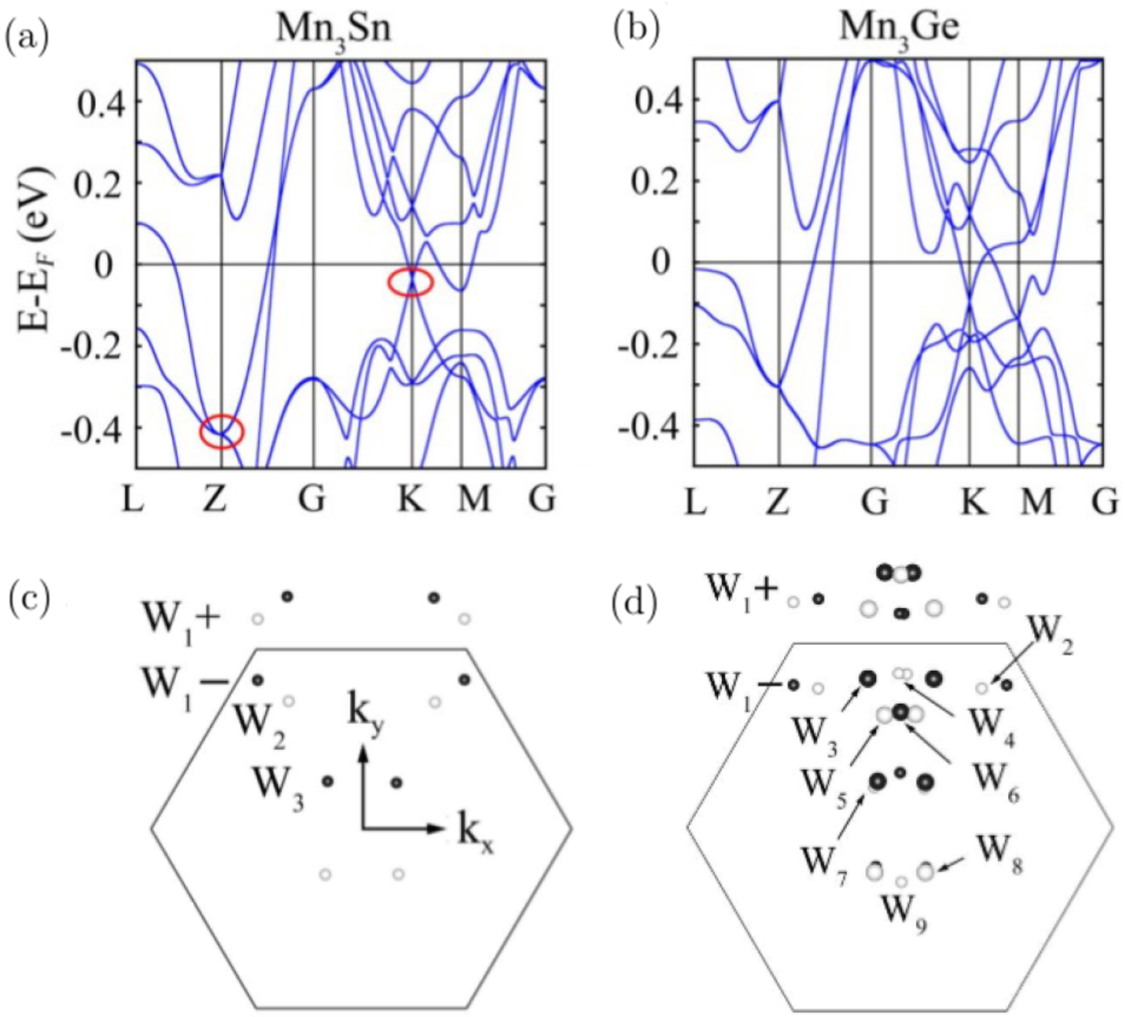

Figure 9: (adapted from [56]) Panels (a) and (b) show the electronic band dispersion along high symmetry lines of the hexagonal Brillouin zone of Mn_3Sn and Mn_3Ge respectively. The projection of the position in momentum space of the Weyl nodes in Mn_3Sn and Mn_3Ge on to the $k_x - k_y$ plane (which is bounded by the hexagonal zone boundary) are shown in panels (c) and (d) respectively.

between the magnetic species and the contribution to electron conduction in the crystal. The following two paragraphs discuss the local and itinerant models used to describe magnetic phenomena in $4f$ and $3d$ electrons respectively.

The local magnetic moment description provides a satisfactory description in lanthanides with partially-filled $4f$ orbitals. Here the localised $4f$ orbitals overlap weakly, which leads to narrow $4f$ bands and drives the bands into a Mott insulating state to minimise the strong on-site electron-electron Coulomb interactions. Hence the $4f$ electrons do not participate in electron conduction in the bulk crystal. Furthermore, the size of the moment depends on how the electrons in the unfilled $4f$ arrange themselves. In Eu^{2+} ($4f^7$) for example, the most energetically favourable arrangement of the 7 electrons produces the large moment of a pure spin state of S $= 7/2$ with $\mu_{eff} = 7.94\mu_B$ and $\mu_{sat} = 7.0\mu_B$. This optimal arrangement of the electrons, summarised by Hund's rules, minimises the coulomb interactions between the $4f$ electrons. In terms of exchange, the localised magnetism in the rare-earths is usually characterised by low ordering temperatures mediated by metallic valence bands due to the negligible overlap between the $4f$ ions. This is also known as the Ruderman–Kittel–Kasuya–Yosida (RKKY) interaction.

On the other hand, the magnetism which arises from delocalised $3d$ electrons (for example Fe, Mn, Co) is often better described in an itinerant electron framework. Magnetism is produced by exchange splitting in the spin up and spin down $3d$ bands so as to reduce the Coulomb interaction between the electronic states. These $3d$ electrons may also contribute to the electron conduction. It follows that the T_{N} is typically around room temperature due to the strong interactions between the itinerant $3d$ electrons. Furthermore, due to the delocalised nature of the $3d$ electrons, there is orbital quenching of the angular momentum of the $3d$ orbitals. This tends to result in a smaller moment in $3d$ magnetism compared to that in $4f$ magnetism.

1.5.3 Coupling between localised magnetism and electronic bands

In this subsection, I discuss a possible mechanism that might drive the coupling between the electronic bands and magnetism in systems where non-trivial band topology co-exists with spontaneous magnetic order. As I have discussed earlier, in some compounds, the linear band crossings are stabilised by additional rotational symmetries along crystalline axes of high symmetry. These features are protected from gapping out if the bands which cross can be distinguished as different irreducible representations of the rotational symmetries along these axes. For magnetic crystals, the symmetry of the spontaneous magnetic order also needs to preserve these rotational symmetries for these band crossings to survive hybridisation. Otherwise, if the rotational symmetries are broken then gaps will form where the bands cross. Furthermore, if an external field can influence the magnetic order in such a

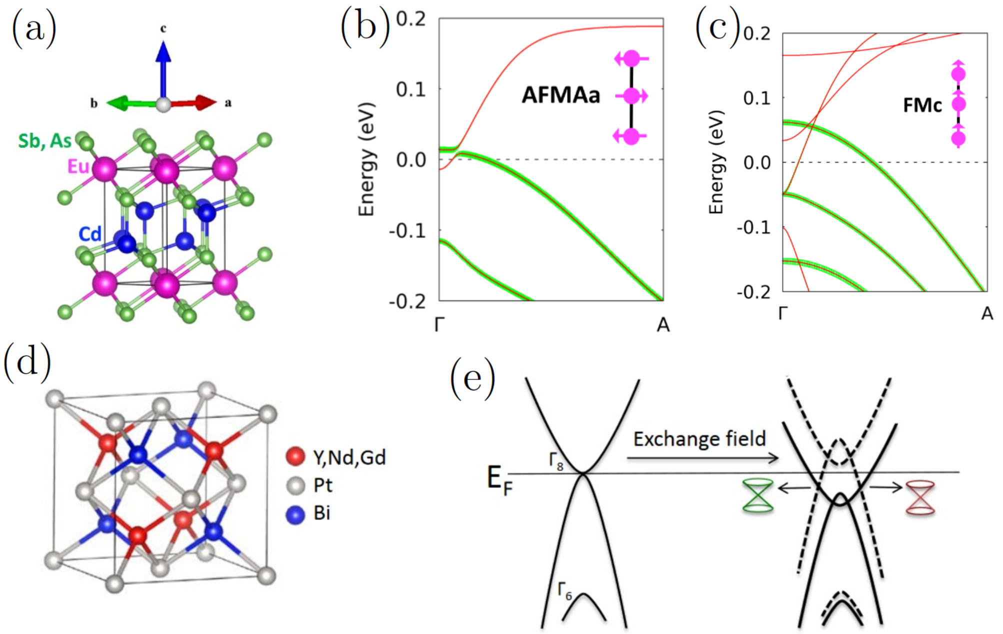

Figure 10: (adapted from [58, 59, 60]) Panels (a) and (d) show the crystal structure of $EuCd_2Pn_2$ (Pn= Sb, As) and RePtBi (Re = Y, Nd, Gd) respectively. Panels (b), (c) and (e) show how the Weyl nodes are induced when an external field is applied along the [001] and [111] directions for $EuCd_2Sb_2$ and GdPtBi respectively.

way that these rotational symmetries are broken for a system in which the symmetries are otherwise preserved, we essentially have an experimental handle with which to control the existence of the gaps. The reverse is also true, where band gaps can be closed when the symmetry is preserved by means of an external field. Some examples of the latter type, shown in Fig. 10, include GdPtBi [57, 58] and $EuCd_2Pn_2$ (Pn = Sb, As) [59, 60].

1.6 Examples of magnetic Weyl semimetals

As I have described earlier, Weyl semimetals can occur in two types of crystals, one having broken spatial inversion symmetry, and the other having broken time-reversal symmetry (TRS)[9]. In the following few sections, I list some examples of candidate crystals of the latter type, that is magnetic WSMs, and the corresponding experimental evidence [11].

1.6.1 Rare-earth iridates

The rare-earth pyrochlore iridate family, $Re_2\mathrm{Ir}_2\mathrm{O}_7$ (Re = rare-earth ion), was the first system that was proposed to host Weyl nodes through broken TRS [61]. The topologically-protected crossing points arise out of the competition between the large spin-orbit coupling and the strong electronic correlations in the Ir $5d$ bands, which also give rise to magnetism. The cubic crystal structure (space group $Fd3m$, No. 227) contains two interpenetrating pyrochlore sub-lattices [Ir and rare-earth; see Fig. 11(a)] [62, 63]. It was predicted that the crystal could host Weyl fermions if the Ir spin structure display an all-in-all-out (AIAO) magnetic configuration. However, since Ir has a small magnetic moment size and is also neutron absorbing ($\sigma^{\mathrm{Ir}}_{abs} = 425$ barns), it was initially difficult to determine the nature of the magnetic order by neutron powder diffraction [64, 65]. Moreover, it is not feasible to map the spin-wave spectrum of the pyrochlore iridates, which is needed to differentiate between different irreducible representations describing the Ir spin structure, by the conventional method of inelastic neutron scattering due to the small size of the single crystals. These hurdles were eventually overcome by means of the resonant magnetic X-ray scattering technique, which confirmed the AIAO magnetic order and measured the spin-wave dispersion in $\mathrm{Sm}_2\mathrm{Ir}_2\mathrm{O}_7$ [66].

One member of the rare-earth iridate family, namely $\mathrm{Nd}_2\mathrm{Ir}_2\mathrm{O}_7$, displays strongly anisotropic magnetotransport, with the in-plane resistivity changing by $\sim$3 orders of magnitude for fields applied in different directions of the crystal axes [67, 69][see Figs. 11(b) and (c)]. Such a huge anisotropy can only arise from modifications of the electronic bandstructure resulting from changes in the spin structure. This suggests a strong exchange coupling between the Ir $5d$ bands, which are responsible for charge transport, and the Nd $4f$ states, which give rise to the large magnetic moments that are more susceptible to the applied magnetic field [64, 69, 70, 71]. If $\mathrm{Nd}_2\mathrm{Ir}_2\mathrm{O}_7$ does indeed host massless Weyl fermions, this strong coupling gives us a handle to modulate the properties of these exotic charge carriers. I contributed to a resonant elastic X-ray scattering (REXS) study of the ground state structure of both magnetic sub-lattices in $\mathrm{Nd}_2\mathrm{Ir}_2\mathrm{O}_7$, and how the corresponding spin configurations change in an applied field. This work is not presented in this thesis as we are awaiting additional beam time to complete the study.

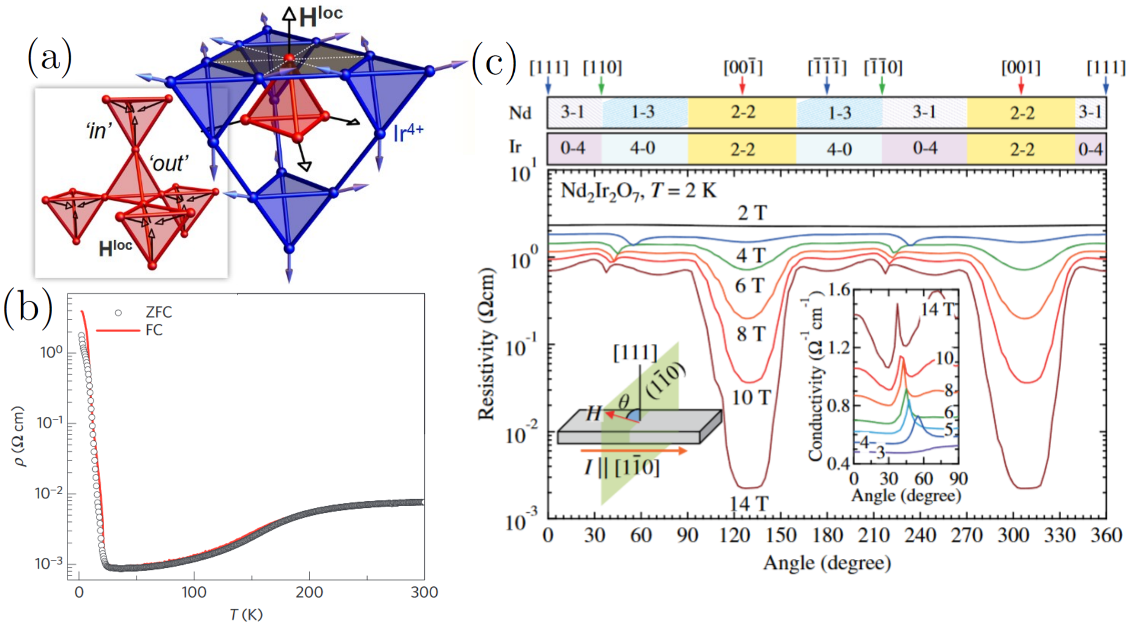

Figure 11: (adapted from [64, 67, 68]) (a) Crystal structure of the $Re_2Ir_2O_7$ family of compounds. Here, the red and blue spheres correspond to the rare-earth and Ir sub-lattices respectively. The AIAO order on the Ir sub-lattice induces a local exchange field on the rare-earth ion site ($\boldsymbol{H}_{loc}$). The metal-to-insulator transition of $Nd_2Ir_2O_7$, as shown in the in-plane resistivity measurements (b), is suppressed when the field is applied along the [001] direction (c).

A recent AHE study of the another member of the 227-iridate family, $Pr_2Ir_2O_7$, also suggested the existence of Weyl points in the crystal [68]. However, there is no straightforward way of interpreting the data as many pairs of Weyl points contribute to charge transport. Moreover, as the $5d$ electrons are strongly correlated, it is difficult to properly describe the electronic bands of the rare-earth iridate compounds with *ab initio* DFT methods, which are best suited for weakly interacting wavefunction states [61, 71]. Corrections to these methods like DFT+U and DMFT also do not fully account for the correlations in these electronic states [61, 62, 71]. Furthermore, it has not been possible to validate the *ab initio* predictions with ARPES as the experimental dispersion is smeared out due to the strong electron correlations, and as the crystals are difficult to cleave [72].

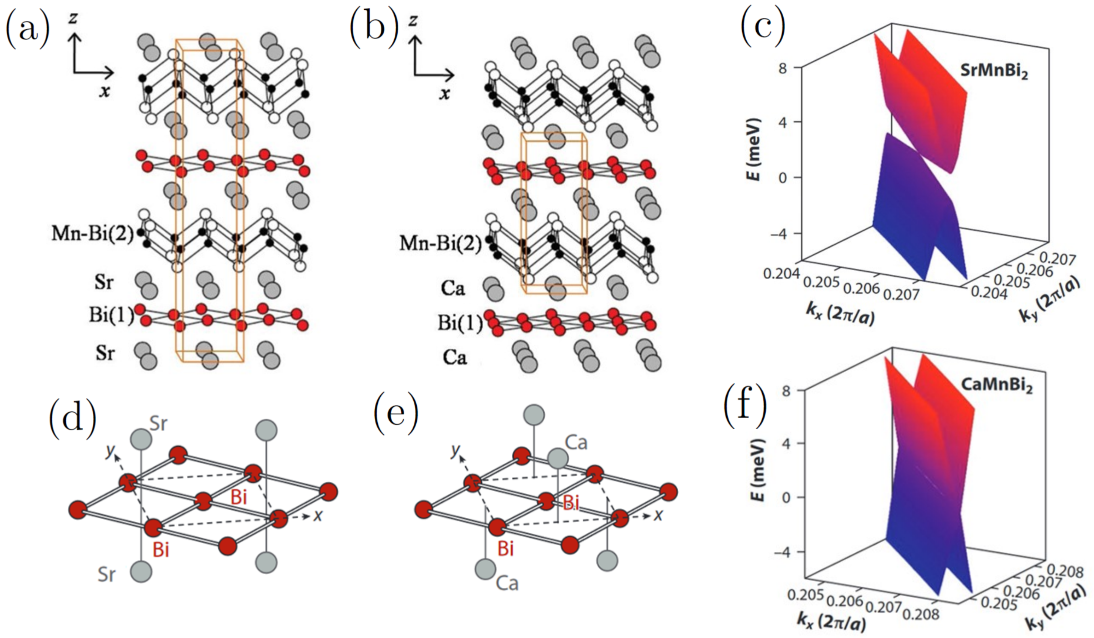

Figure 12: (adapted from [73]) (a) and (b) shows the crystal structure of $SrMnBi_2$ and $CaMnBi_2$, respectively, of the AMnX_2 structural family. (d) and (e) exemplifies the in-plane bismuth layers that are responsible for the charge transport in both of the 112-pnictides. The linearly dispersing electronic bands in the $k_x - k_y$ plane of (c) $SrMnBi_2$ and (f) $CaMnBi_2$ are highly anisotropic.

1.6.2 112-pnictides

The AMnX_2 (A= Ca, Sr, Ba, Eu, Yb; X= Bi, Sb) structural family [see Figs. 12(a) and (b)], which displays AFM order on the Mn sub-lattice near room temperature, is also predicted to host topological fermions [73, 74, 75, 76, 77, 78, 79, 80, 81, 82, 83]. These charge carriers are contained in the 2D in-plane pnictide layer of the orthorhombic or tetragonal crystal structure [see Figs. 12(d) and (e)]. Below the Néel temperature, if the Mn moments are fully ordered along the c axis, then the electronic bands are doubly-degenerate with an avoided Dirac node of Bi $4p_{x,y}$ or Sb $5p_{x,y}$ bands due to SOC. This gap is created due to the lack of additional crystalline rotational symmetries required to prevent the hybridisation of the bands. Within this 112-pnictide family, $SrMnSb_2$ was suggested to host Weyl fermions [84]. The orthorhombic unit cell, which can be described by the $Pnma$ space group (No. 62), contains a zig-zag Sb layer which hosts the predicted topological charge carriers. It was predicted that if the Mn magnetic order was canted away from the fully collinear structure, the net ferromagnetic in-plane component will lift the double degeneracy in the bands to create Weyl fermions. Although evidence for a canted Mn spin structure has been demonstrated from single crystal neutron diffraction measurements [84], ARPES and SdH data of the compound indicate trivial band topology [85]. This suggest that coupling between the Mn sub-lattice to the pnictide layer is too weak to create Weyl fermions.

Another candidate Weyl semimetal in the 112-pnictide family, where the predicted nodes are created by the same mechanism, is $\mathrm{YbMnBi_2}$ [74]. The tetragonal unit cell, which can be described by the $P4/nmm$ space group (No. 129), contains a 2D square net of Bi atoms that hosts the purported topological fermions [74, 78, 79]. This prediction was supported by the SdH oscillations in the magnetotransport data which pointed to a light mass of the charge carriers, consistent with $\mathrm{YbMnBi_2}$ having Weyl nodes near E_F [78]. The ARPES measurements of $\mathrm{YbMnBi_2}$, which show some evidence of Fermi arcs emanating from the supposed Weyl nodes, are however not definitive as the claimed arcs are unfortunately difficult to distinguish from hole bands which are adjacent to them [74]. Moreover, neutron diffraction studies which will be sensitive to the predicted canting of 10° in the Mn spins has not yet been reported [79]. I present, in Chapter 5, single crystal magnetic neutron diffraction of $\mathrm{YbMnBi_2}$ to ascertain whether the Mn sub-lattice does indeed display the predicted canted structure. Moreover, if the canted structure produces Weyl fermions, it might alter the cross-plane exchange coupling between the Mn moments. This could lead to, for instance, an enhancement of the bandwidth of the magnon spectrum. This is also presented in Chapter 5.

In $\mathrm{EuMn}X_2$, the pnictide layer is sandwiched by two interpenetrating magnetic sub-lattices (Eu and Mn) [81, 82, 83, 86]. Such a structure may lead to an enhancement of the coupling between the topological quasiparticle excitations and magnetism, compared to that in compounds with a non-magnetic atom on the A site. Compared to all of the compounds in the $A\mathrm{Mn}X_2$ family explored thus far, $\mathrm{EuMn}X_2$ demonstrates a significantly stronger coupling between the topological charge carriers and magnetism as evidenced by magnetotransport measurements. This highlights the significance of having a magnetic ion on the A site to enhance the coupling, as has been suggested by Klemenz *et al.* Moreover, magnetotransport in $\mathrm{EuMn}X_2$,

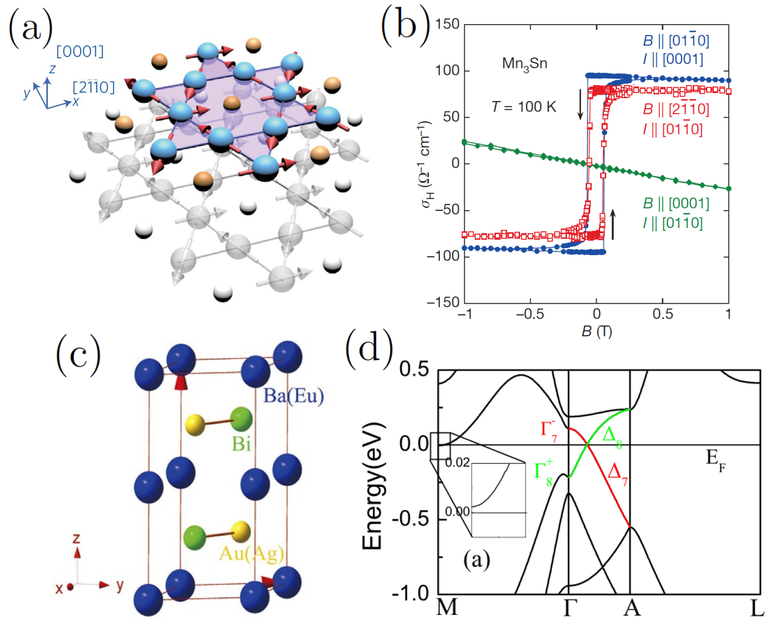

Figure 13: (adapted from [88, 89, 90]) The unit cell of (a) Mn_3X (X=Ge, Sn) and (c) XYBi (X=Ba, Eu; Y=Au, Ag, Cu) can both be described by the $P6_3/mmc$ space group. Mn_3Sn displays large anomalous Hall effect that can be switched with a small applied field. (d) In BaAuBi, the electronic bands which cross along the $\Gamma - A$ high symmetry line transforms as different irreducible representations, with respect to the C_{3z} rotation, and hence do not hybridise to give rise to an energy gap.

which is strongly anisotropic, could arise from some f–p exchange between the Eu $4f$ bands, which give rise to magnetism, and the Bi $4p$ or Sb $5p$ electronic states, which dominate charge transport in the pnictide layer. More specifically, it is the exchange between the half-filled $4f$ states and the charge carriers since $\mathrm{YbMn}X_2$ does not demonstrate such a behaviour [74, 87]. Such a coupling in $\mathrm{EuMn}X_2$ leads to changes in the electron bandstructure due to changes in the magnetic structure of the Eu sub-lattice. I contributed to a recent study of the ground state magnetic configuration and the electronic bandstructure of EuMnSb_2, which support this. Results of this study will be reported separately.

1.6.3 Mn_3X

Another candidate material class is the hexagonal AFM Mn_3X (X= Ge, Sn, Ga). The Mn sub-lattice can be described by a stacked kagome lattice along the c axis, which gives rise to a frustrated magnetic order [Fig. 13(a)]. Recent experiments demonstrated that Mn_3Ge and Mn_3Sn display large anomalous Hall effect at room temperature, as shown in Fig. 13(b), which is unusual for antiferromagnets. This was attributed to the compounds having Weyl points in the Brillouin zone, which is supported by *ab initio* bandstructure calculations. Moreover, these studies also suggest that the Weyl nodes can be moved in **k**-space by altering the spin structure with an external applied field. However, the true ground state magnetic structure is still not yet known. This is addressed in Chapter 6.

1.6.4 111-compounds

The experimental validation of the theoretical prediction by Wang *et al.* that additional rotational symmetries, like C_3 and C_4 in Na_3Bi and Cd_3As_2 respectively [31, 33], along high symmetry lines can prevent the hybridisation of the electronic band crossings and produce symmetry protected Dirac nodes has sparked off similar theoretical predictions for other materials. These studies have focused on crystals which possess these rotational symmetries to identify if the associated electronic bands which cross along these high symmetry lines (along the axis of rotation) can be described by different irreducible representations.

One class of material that has been identified is the 111-family of hexagonal ZrBeSi-type compounds, which crystallises in the $P6_3/mmc$ space group [35, 90]. These hexagonal compounds possess the C_3 rotational symmetry along the crystal c axis, which is necessary to prevent the hybridisation of the bands along the $\Gamma - A$ high symmetry line. Examples include XYBi (X = Ba, Sr; Y = Cu, Ag and Au). Here, electronic bands that dominate charge transport comes from the bismuth states, which produces the strong spin-orbit interaction that drives the band inversion along $\Gamma - A$ [see Figs. 13(c) and (d)].

To create Weyl nodes in these centrosymmetric crystals, Du *et al.* [90] considered magnetic variants such as EuYBi and $Ba_{0.5}Eu_{0.5}Y$Bi, in the hope that the magnetic order of Eu^{2+} might lift the double degeneracy in the electronic bands to create Weyl nodes via the TRS-breaking mechanism. The creation of a WSM state in the XYBi family of compounds is certainly promising given that EuCuAs [91], which is isostructural to EuYBi, displays intimate coupling between the magnetic order on the Eu^{2+} sub-lattice and charge transport. The strong exchange between the two will facilitate the creation of Weyl nodes via TRS breaking. Despite this, the magnetic structure of the EuYBi family of compounds has not yet been studied, due in part to the fact that these compounds contain the strongly neutron absorbing europium. In collaboration with Jinzhao Sun, I have identified the ground state magnetic structure of EuCuAs and how the magnetic configuration changes in an applied field with REXS (I16, Diamond) and powder neutron diffraction (WISH, ISIS). This work is ongoing and is not presented in this thesis.

1.6.5 Other types of WSMs

Another route to create Weyl nodes in crystals via TRS breaking, other than the ones that have been discussed thus far (namely in Re_2Ir$_2$O$_7$ [1.6.1], 112-pnictides [1.6.2], Mn$_3$X [1.6.3] and the 111-compounds [1.6.4] where the Weyl nodes are spontaneously induced [Fig. 14(b)]) is to apply an external magnetic field. In this case, the Weyl nodes are magnetically induced by the applied field and the dominant mechanism driving the creation of the Weyl nodes depend on whether the crystal is non-magnetic or magnetic.

If the crystal is non-magnetic, the double degeneracy is lifted by the Zeeman effect. Here, the applied field essentially separates the Weyl nodes that would otherwise coincide in **k**-space in the absence of a field to give rise to Dirac nodes. Examples of such crystals include ZrTe$_5$ [92], Na$_3$Bi [93], Cd$_3$As$_2$ [28, 94, 95] and YbPtBi [96][Fig. 14(a)]. Given that the distance between the nodes is proportional to the strength of the applied field [94], high field strengths are required to achieve a non-negligible separation of the Weyl nodes in **k**-space sufficient for experimental studies.

On the other hand, if the crystal is magnetic, the band splitting is driven mainly by the exchange interaction between the magnetic moments and the topological states. Here, the magnetic field serves to alter the configuration of the magnetic structure, which in turn modifies the electronic bands via exchange coupling. In these systems, the Zeeman effect, although present, is not the dominant interaction that creates the Weyl nodes, unless the magnetic moments are fully polarised by the applied field and the bands fully exchange split. Examples of such crystals include the magnetic half-Heuslers RePtBi [Re = Gd, Nd; Fig. 14(a)] [57, 58, 97, 98] and

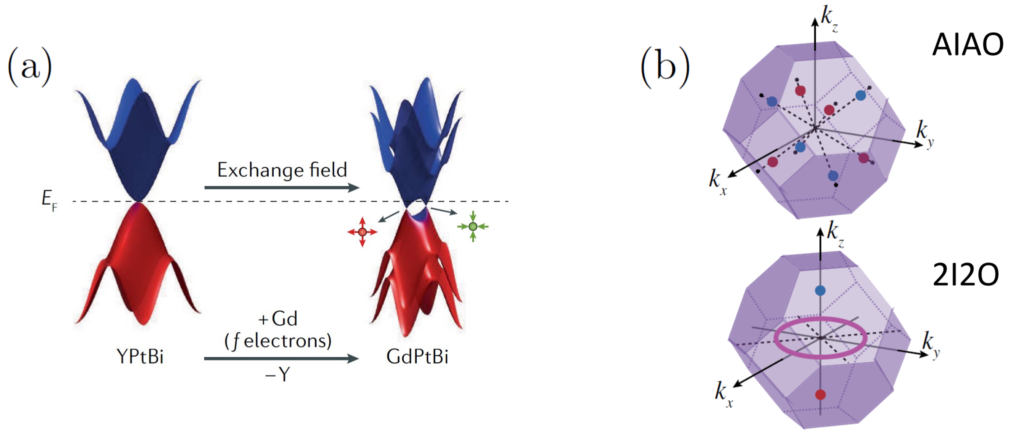

Figure 14: (adapted from [69, 99]) (a) Weyl nodes can be induced by exchange interaction between the electronic bands and the $4f$ magnetic moments. (b) In the rare-earth pyrochlore iridates, the all-in-all-out (AIAO) order gives rise to Weyl nodes in the Brillouin zone. This becomes a line node when the moments are driven into the two-in-two-out (2I2O) configuration in an applied field.

the 122-pnictides $\mathrm{EuCd_2}Pn_2$ [$Pn = \mathrm{Sb, As}$; Figs. 10(b) and (c)] [59, 60]. Compared to non-magnetic crystals, larger band splitting can potentially be realised in these materials, giving rise to a larger separation of the Weyl nodes in **k**-space.

In both cases, the detection of Fermi arc surface states with ARPES, which is the definitive test for the presence of Weyl nodes, can be excluded as ARPES cannot be performed in an applied field. Instead, alternative tests commonly used to verify the existence of Weyl nodes for this class of WSMs is from the anomalous Hall effect [57, 58, 98] and the Chiral anomaly [57, 60, 95, 97], which can be probed in magnetotransport studies.

1.7 All not ideal

1.7.1 Nodes close to E_F

The compounds discussed thus far, along with some other candidate WSM materials that have been suggested, are tabulated in Table 1. Although these crystals have

Weyl nodes that are generally distributed in energy, only the nodes that are in the vicinity of E_{F} will have an observable effect on the material. For instance, in the isostructural compounds TaAs [15, 100], TaP [43], NbAs [42] and NbP [41], the observed Fermi arcs only emanate from and connect the nodes that are near the Fermi energy, even though there are many other nodes distributed above and below E_{F}. Hence, the ideal case is if the nodes are exactly at the Fermi energy, where the the topological features of the nodes will dominate in the bulk properties. Under the heading $|E - E_{\mathrm{F}}|$ in Table 1, I list the smallest energy difference between the Fermi energy and all of the Weyl nodes in the Brillouin zone. The case where $|E - E_{\mathrm{F}}| = 0$ applies for $Pr_2Ir_2O_7$ [61, 68, 71, 101], LaAlGe [102, 103], the chalcopyrites ($CuTlSe_2$, $AgTlSe_2$, $AuTlSe_2$, $ZnPbAs_2$) [104], HgTe [105] and $Zr_{0.725}Nb_{0.275}Co_2Sn$ [44]. For the other compounds where the nodes are not exactly at E_{F}, there is a possibility of shifting the energy of the nodes with chemically suitable dopants. This is indeed the case for the magnetic Heusler $Zr_{1-x}Nb_xCo_2Sn$ [44] where the Weyl nodes in the parent phase ($x = 0$) is not at the Fermi energy, but can be tuned to be at the E_{F} by alloying with the dopant Nb ($x = 0.275$). The $|E - E_{\mathrm{F}}|$ column, however, does not reflect the distance between all nodes and the E_{F}. In LaAlGe, for instance, only 8 nodes lie at the E_{F} whereas the other 16 are not.

1.7.2 Number of Weyl nodes

As I discussed earlier, these compounds can be categorised into two main classes based on the mechanism that induces the Weyl nodes: non-centrosymmetric crystals (with broken IS only) and magnetic crystals (with broken TRS).

The total number of nodes in crystals of the first type comes in multiples of four. This arises because a Weyl node at $\mathbf{k}_0$, under TRS, is converted into another Weyl node at $-\mathbf{k}_0$ with the same chirality and given that the net Berry flux in the Brillouin zone has to be 0, there will be another pair of nodes with opposite chirality.

The listed crystals in Table 1 are arranged in descending order of the number of Weyl nodes near E_{F}. On the top of the list of this class is the TaAs structural family along with the half-Heusler LaAlGe [102, 103], which has 6 sets of four nodes near E_{F}. Further down the list of crystals in this class include the molybdenum-doped tungsten di-telluride ($Mo_xW_{1-x}Te_2$) [106], the chalcopyrites ($CuTlSe_2$, $AgTlSe_2$,

$AuTlSe_2$, $ZnPbAs_2$) [104] and the binary mercury telluride (HgTe) under strain [105], with 2 sets of four nodes near E_F. Having many sets of these nodes, however, makes it harder to disentangle effects from the different nodes and perform fundamental tests of the Weyl physics. Hence there has been a considerable effort to search for non-centrosymmetric crystals with less nodes near E_F. This search culminated with the prediction that the transition metal di-tellurides, $MoTe_2$ [107, 108] and WTe_2 [109], can realise the minimum four nodes near E_F.

On the other hand, for magnetic crystals, if a Weyl node is present at momentum $\mathbf{k}_0$, another node with the opposite chirality must be present at $-\mathbf{k}_0$. As a result, the total number of nodes in crystals with broken TRS comes in multiples of two. Hence, WSMs of this class can potentially realise a single pair of Weyl nodes near E_F, half the minimum number of nodes in non-centrosymmetric crystals. Despite this prospect, identifying compounds with this minimum number of Weyl nodes has been challenging. Also listed in Table 1 are compounds with broken TRS arranged according to the number of Weyl nodes near E_F. In some of these magnetic crystals, the nodes are created by spontaneous magnetic order whereas in others, the nodes are induced by magnetic exchange when the magnetic moments are fully polarised along certain applied field directions. On the top of the list is the hexagonal Mn_3Ge [56] which possess 17 pairs of Weyl nodes created by the spontaneous collinear magnetic order of the Mn sub-lattice. As described earlier, the position of these nodes in this antiferromagnet can, purportedly, be manipulated with an applied field. Next on the list are the 227-pyrochlore iridates (e.g. $Pr_2Ir_2O_7$ [61, 68, 71, 101]) which host 12 pairs of Weyl nodes if the Ir sub-lattice does indeed display the AIAO spin structure below the Néel temperature. This is followed by compounds with 6 pairs of nodes in the Brillouin zone which include the Shandite $Co_3Sn_2S_2$ [110], where the nodes are induced by the spontaneous ferromagnetic order of the cobalt moments, and the hexagonal AFM Mn_3Sn, where the nodes are predicted to be responsible for the large AHE at room temperature [56]. Like Mn_3Ge, $EuCd_2Sb_2$ has an odd number of pairs of Weyl nodes, which is not allowed for crystals which have broken IS only. The 5 pairs of nodes in this hexagonal rare-earth 122-pnictide antiferromagnet are induced by magnetic exchange when the Eu moments are fully polarised along the crystal c axis by an external field [60]. Examples of magnetic crystals with 4

Table 1: A non-exhaustive list of Weyl semimetal candidates. This list also indicates whether there are other bands that cross the E_{F}, which might shroud the contributions from the Weyl nodes. The four *mechanisms* for producing Weyl nodes are breaking time reversal symmetry (TRS), breaking inversion symmetry (IS), breaking TRS by magnetic exchange (e-TRS) and breaking IS in a crystal under strain (s-IS).

Compound	Pairs of Weyl Nodes	Irre. Bands	$\lvert E - E_{\mathrm{F}}\rvert$ (meV)	*Mechanism*	Reference
Mn_3Ge	17	Yes	8	TRS	[56]
$Pr_2Ir_2O_7$	12	Yes	0	TRS	[61, 68, 71, 101]
LaAlGe	12	Yes	0	IS	[102, 103]
TaAs	12	Yes	2	IS	[15, 100]
TaP	12	Yes	24	IS	[43]
NbAs	12	Yes	38	IS	[42]
NbP	12	Yes	26	IS	[41]
Mn_3Sn	6	Yes	86	TRS	[56]
$Co_3Sn_2S_2$	6	Yes	60	TRS	[110]
$EuCd_2Sb_2$	5	Yes	50	e-TRS	[60]
$YbMnBi_2$	4	Yes	40	TRS	[74]
$SrMnSb_2$	4	Yes	700	TRS	[84, 85]
GdPtBi	4	Yes	>0	e-TRS	[57, 58, 97, 98]
$Mo_xW_{1-x}Te_2$	4	Yes	80	IS	[106]
$CuTlSe_2$	4	No	0	IS	[104]
$AgTlTe_2$	4	No	0	IS	[104]
$AuTlTe_2$	4	No	0	IS	[104]
$ZnPbAs_2$	4	No	0	IS	[104]
HgTe	4	No	0	s-IS	[105]
$MoTe_2$	2	Yes	6	IS	[107, 108]
WTe_2	2	Yes	52	IS	[109]
$Zr_{0.725}Nb_{0.275}Co_2Sn$	1	Yes	0	TRS	[44]
$EuCd_2As_2$	1	No	0	e-TRS	[59, 111]

pairs of nodes include the 112-pnitides ($YbMnBi_2$ [74] and $SrMnSb_2$ [84, 85]), where the nodes are induced spontaneously by an in-plane component of the Mn magnetic order, and the half-Heusler GdPtBi [57, 58, 97, 98], where the nodes are created by magnetic exchange when the Gd moments are fully polarised.

As there are many pairs of Weyl points in all of these aforementioned WSM candidates, it is difficult to distinguish the contributions from the different nodes to the bulk measurements (e.g. AHE, magnetotransport, etc.) and link the observables of these materials to specific nodes. Hence, an ideal WSM crystal will contain a single pair of Weyl nodes, which is the minimum number that conserves the net Berry flux. Such a material will belong to the second class (with broken TRS) and will be a suitable platform to perform fundamental tests of Weyl physics.

1.7.3 Irrelevant bands

Another difficulty with identifying suitable WSMs is the existence of extraneous, topologically-trivial, bands which cross the Fermi surface. The quasiparticles in these bands will inevitably contribute to properties of the material and make it harder to isolate effects due to the Weyl fermions. This has indeed been proposed to be the case for the magnetic Heuslser family $X\mathrm{Co}_2Z$ (X =V, Zr, Nb, Ti, Hf; Z=Si, Ge, Sn) [44]. Here a single pair of Weyl nodes is predicted to lie along the [110] direction, driven by the ferromagnetic order of the magnetic cobalt sub-lattice in the same direction. However, *ab initio* calculations predict that there are other bands which cross the Fermi energy in this family of cubic crystals. The presence of other bands will potentially shroud the effects of topological nodes on the bulk material properties. This arises because the electron eigenstates with trivial topology will have a significantly higher density of states compared to that for Weyl nodes, which have a vanishing density of states as the chemical potential approaches the crossing points.

The ideal test bed for the physics of Weyl fermions will, hence, be in crystals with Weyl nodes that are in an energy window free from other irrelevant non-topological bands. This is case for the chalcopyrites ($CuTlSe_2$, $AgTlSe_2$, $AuTlSe_2$, $ZnPbAs_2$) [104] and the binary mercury telluride (HgTe) under strain [105], all of which, however, have 4 Weyl nodes at E_F.

1.8 The ideal Weyl semimetal

None of the WSM candidates suggested thus far fulfill all three requirements of (i) hosting a single pair of Weyl fermions (ii) in the vicinity of the Fermi energy and (iii) in an energy window free from other bands. To perform fundamental tests of Weyl physics, there is an imperative need to find better material realisations of a WSM which satisfy all three requirements [3, 9, 11, 12]. The search for an ideal WSM is the topic of Chapter 4.

CHAPTER 2

Experimental Methods

A physicist, in my view, observes the natural workings of the (seemingly ordered) universe around us, assigns numbers to quantify (where possible) the phenomenon under investigation, and then writes down a model to describe it.

The definition of a physical variable in a model should, therefore, not be ambiguous. It is upon that firm description of the physical quantity that we can then proceed to design careful experiments and make precise measurements to ascertain if the model provides a good description of the phenomena or not. On that note, it is also an art, in my view, to make a case for why a particular size of the error bar is chosen as it may exclude one model from another.

However, caution must be taken, especially if a model provides for an extremely good description of the phenomena in question, to distinguish between a description and a prescription. While nature might seem to *follow* the model, it should not be assumed that natural phenomena *obeys* these *laws*. In my view, we have to be cautious not to ascribe a quality to an observation that is a feature of a model. Nonetheless, a good model can serve to predict other phenomena and offer us deep insights into the mysterious inner workings of our universe.

In the area of magnetic topological crystalline materials, there has been a wealth of *ab initio* studies predicting the existence of massless charge carriers in the crystals. However, when I embarked on my thesis, there were not many experimental studies devoted to making well-qualified statements, based on the measured quantities, about the existence of these quasiparticle excitations in these crystals. For instance, in many of these studies, the magnetic structure was not solved.

What I have tried to achieve in my thesis is to perform experiments to address some of these open questions rigorously. In this chapter, I outline some of the experimental techniques that I employed to investigate these magnetic topological materials.

2 Experimental methods

2.1 Diffraction and the reciprocal lattice

The aim of this section is to relate the physical crystal that has been described thus far with experimentally measurable physical quantities obtained from neutron and X-ray studies. While it is more natural and intuitive to describe[1] crystals in terms of the lattice positions, $\mathbf{R}_n = n_1\mathbf{a}_1 + n_2\mathbf{a}_2 + n_3\mathbf{a}_3$ (where $n_1, n_2, n_3 \in \mathbb{Z}$ and $\mathbf{a}_1$, $\mathbf{a}_2$, $\mathbf{a}_3$ are primitive lattice vectors of the direct lattice), the abstract description of the crystal in reciprocal space[2] offers a better comparison with experimental results from scattering studies. This succinct and elegant way of describing the crystal in terms of the Fourier components is given by, $\mathbf{G} = h\mathbf{b}_1 + k\mathbf{b}_2 + l\mathbf{b}_3$ where $\mathbf{b}_1, \mathbf{b}_2, \mathbf{b}_3$ are the primitive lattice vectors of the reciprocal lattice such that $\mathbf{a}_i \cdot \mathbf{b}_j = \delta_{ij}$ and h, k, l are integers.

This abstract description arises naturally from how radiation interferes constructively after scattering from the periodic arrangement of ions in the crystal. Within this formalism, there is a term that is proportional to $\exp(i\mathbf{q} \cdot \mathbf{R}_n)$, where $\mathbf{q}$ is the scattering vector [see Fig. 15(a)]. This term, when summed over the lattice array, adds constructively when the exponents in each term are in phase, that is, when $\mathbf{q} \cdot \mathbf{R}_n = 2\pi$, giving rise to coherent scattering when $\mathbf{q} = \mathbf{G}$ since $\mathbf{G} \cdot \mathbf{R}_n = 2\pi$.

In single crystal diffraction studies, we can measure the fraction of the incident radiation scattered into the (θ, ϕ) direction, which I define here as $d\sigma/d\Omega$, the differential cross-section. When the diffraction condition of $\mathbf{q} = \mathbf{G}$ is met, then the scattered intensity at the given (θ, ϕ) will be very large relative to the background (see Sections 2.3.1 and 2.4.1). The resulting spatial distribution of the intensity of the scattered radiation will correspond directly with the 3D lattice points mapped out by these reciprocal lattice vectors. From this, we can extract the lattice param-

---

[1] It is worth distinguishing a physical crystal from a lattice, which is a mathematical concept. The former is a regular arrangement of atoms while the latter is an infinite set of points that display spatial translation symmetry, $T : \mathbf{r} = \mathbf{r} + \mathbf{R}_n$, which in 3D space have only 14 different types (and in my view is a rather neat result shown by Bravais). Strictly speaking, the term *crystalline lattice* does not make sense. However, I think the way around this impasse is to use the term *describe*, where what I mean is that we can use the idea of a lattice to describe a physical crystal.

[2] The Fourier transformation of the lattice points from real to reciprocal space.

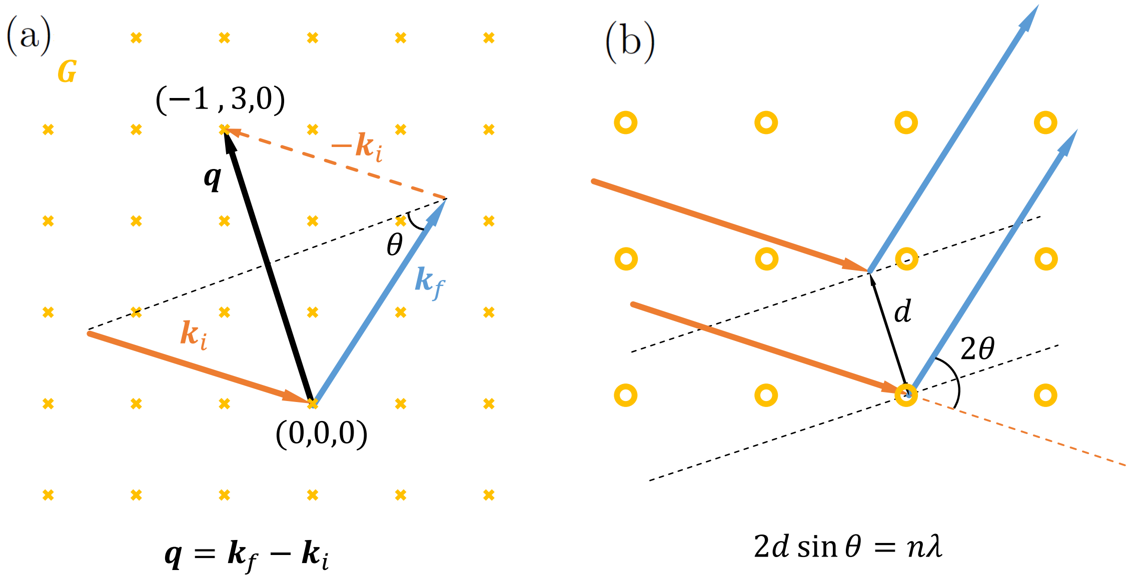

Figure 15: (a) depicts elastic scattering, where $|\mathbf{k}_f|$=$|\mathbf{k}_i|$, in the $(h\,k\,0)$ plane of reciprocal (or momentum) space. Here I define the scattering vector as $\mathbf{q} = \mathbf{k}_f - \mathbf{k}_i$, where $\mathbf{k}_i$ and $\mathbf{k}_f$ are incoming and scattered beam wavevectors respectively. When $\mathbf{q}$ matches the reciprocal lattice vector $\mathbf{G}$ (orange crosses), we get coherent scattering. (b) illustrates elastic scattering in real space where the beam is scattered by a scattering angle of 2θ. Alternatively, the scattering event can be visualised as the reflection of the incoming beam by uniformly spaced layers, with interlayer spacing d.

eters to find out the distances between atoms, the space group of the crystal, the arrangement of the atoms within the unit cell and the single crystal quality among many other things.

The magnetic structure of crystals that display antiferromagnetic ordering in the magnetic ions can also be elucidated by radiation. In these crystals, the magnetic moments cancel out and do not produce a net magnetisation in bulk measurements. Hence it is difficult to identify the arrangement of the magnetic ions solely from magnetometry measurements. The magnetic order in these single crystals can provide significant contributions to $d\sigma/d\Omega$. In terms of the spatial distribution of this magnetic scattering intensity, this can manifest at reciprocal lattice positions which are rational fractions or irrational fractions of $\mathbf{G}$, depending on whether the magnetic arrangement is commensurate or incommensurate with the host crystal structure.

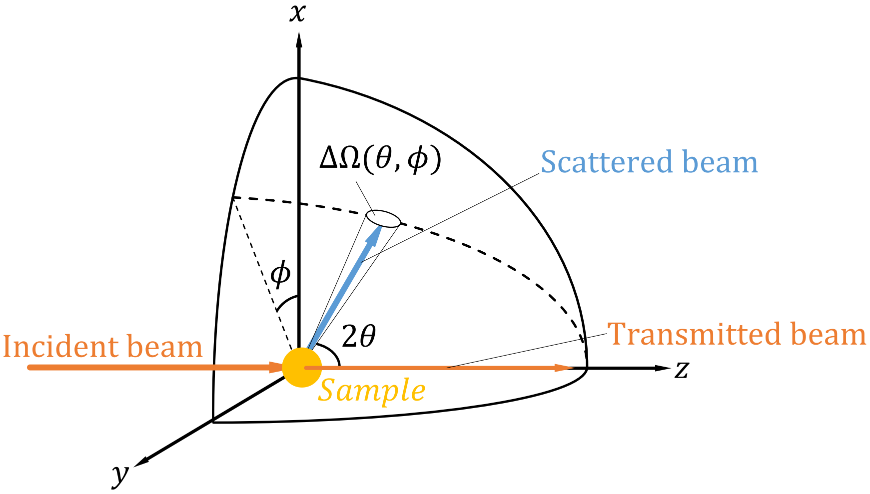

Figure 16: The scattering geometry in both spherical polar and Cartesian coordinates. Here, 2θ is the scattering angle as defined earlier. If $\phi = \pm 90°$, then the experiment is said to be done in the horizontal scattering geometry within the y–z plane.

From this, the magnetic structure, the size of magnetic moment and the critical exponent β, which describes the magnetic order parameter near the transition temperature, can be determined. The magnetic scattering also allows us to estimate the correlation length of the magnetic order and is sensitive to the presence of magnetic domains among many things.

The behaviour of electrons that *live* in a periodic coulomb potential and the excitations of an ordered magnetic periodic lattice can also be succinctly described in reciprocal space as the energy dispersion of electronic wavefunction states and magnon modes, respectively. For the electronic band structure, which can be mapped with angle-resolved photoemission spectroscopy (ARPES) and calculated with density functional theory (DFT), the wave vector $\mathbf{k}$ for a given energy eigenstate defines a plane-wave envelope, $e^{i\mathbf{k}\cdot\mathbf{r}}$, specifying the spatial modulation of the electron wavefunction along $\mathbf{r}$. On the other hand, for the magnon modes, this plane wave defines the relative phase of spin precession of the magnetic ions at position $\mathbf{r}_m$. Furthermore, the $E - \mathbf{k}$ spectrum of these quasiparticles and collective excitations are periodic across Brillouin zones and possess some point group symmetry elements of the crystalline (or magnetic) space group. Hence, it is natural to present these energy dispersions along high symmetry lines in **k** space that connect high symmetry points in the Brillouin zone [see section 2.8]. These dispersions provide an estimate of the propagation speed of the collective excitations, the effective mass of the quasiparticles near E_F, how the topology of the bands are related to the magnetic and crystalline symmetry, exchange constants, etc.

2.2 Scattering cross-sections

In this section, I want to define the differential cross-section $d\sigma/d\Omega$ properly. It is defined in such a way that it is independent of the incoming radiation flux Φ_0 and the actual experimental set-up. As such, we know that these physical quantities are the fundamental properties arising from the crystal. It also makes comparing data sets from different experimental set-ups easier as well. The total cross section is defined as [112],

$$\sigma = \frac{\text{(total number of neutrons/photons scattered per second in all directions)}}{\text{the flux of the incident radiation, } \Phi_0}.$$

This quantity can be understood as such: if a sample is irradiated with flux Φ_0, σ gives a measure of how much of the incident radiation is scattered, regardless of direction. Intuitively, it gives a sense of how much *space* there is between the scatterers in a sample, which depends on the mechanism that gives rise to scattering. In other words, this probability of radiation scattering from crystalline materials depends on the total cross-sectional area the scattering atom *presents* to the radiation. For instance, in neutron scattering, the cross-sectional area presented by the atoms is very small as the strong interaction is very short ranged [113]. On the other hand, X-rays, which interact electromagnetically with the electron cloud of these scatterers, tend to have a higher total cross-section [114]. Here the scattering area that the atoms present is significantly larger compared to that for neutrons.[3]

In these scattering experiments, we can measure the neutrons or X-rays that are scattered into certain angular directions with a detector, which, in turn, subtends

---

[3] Yet, if we also consider the stronger interaction in neutron scattering (strong force) compared to X-ray scattering (electromagnetic force), both processes have very similar scattering lengths on the order of of $\sim r_0$

a solid angle, $\Delta\Omega(\theta,\phi)$. This can gives us an estimate[4] of the probability that the incident radiation with wavevector $\mathbf{k}_i$ will be scattered into the solid angle element $d\Omega(\theta,\phi)$, which is centred on the scattered wavevector $\mathbf{k}_f$. This is defined by the differential cross-section [112],

$$\frac{d\sigma}{d\Omega} \simeq \frac{(\text{total number of neutrons/photons detected per second in solid angle } \Delta\Omega(\theta,\phi))}{\Phi_0\,\Delta\Omega\,\eta},$$

where η is the detector efficiency. Here, the scattered radiation may not necessarily be isotropic, but could have a strong angular dependence. Similar to σ, this quantity is material-specific and should not depend on experimental conditions such as the size of detector or the incident flux as these are normalised out.

Finally, I define the double differential cross-section, $\frac{d^2\sigma}{d\Omega dE_f}$, which gives the number of neutrons scattered per second into the solid angle $d\Omega(\theta,\phi)$ in the direction (θ,ϕ) with final energy between E_f and $E_f + dE_f$. This can be measured with an analyser crystal[5] which selects the energy of the scattered neutron/X-ray within the uncertainty of ΔE_f.

2.3 X-ray scattering

2.3.1 Non-resonant elastic X-ray scattering

Before we consider X-ray scattering in the context of a crystalline solid, we first treat elastic scattering from a fixed atom with N electrons.[6] Here the X-ray photon interacts electromagnetically with the electron cloud that can be described by a continuous electron density function and is given by [114],

$$\rho(\mathbf{r}) = N \int d\mathbf{r}_2 d\mathbf{r}_3 ... d\mathbf{r}_N |\Psi(\mathbf{r},\mathbf{r}_2,...,\mathbf{r}_N)|^2. \tag{4}$$

The amplitude of scattering at $\mathbf{r}$ due to this continuous scatterer is proportional to volume element $d\mathbf{r}$ at $\mathbf{r}$, namely $\rho(\mathbf{r})d\mathbf{r}$. In the second quantisation formalism of radiation, this elastic scattering process involves annihilating a photon (with wave

---

[4] I use the word estimate because, the quantity $\frac{d\sigma}{d\Omega}$ is a differential. We usually choose the detector slits to be small enough so that we do not pick up effects due to the variation of $\frac{d\sigma}{d\Omega}$ across the detector area but not at the cost of expediency of the experiment or the neutron/X-ray counts on the detector.

[5] This admittedly is also scattering and has a corresponding $\frac{d\sigma}{d\Omega}$.

[6] This is treated more comprehensively by Altarelli and Sivia in Refs. [114, 112].

vector $\mathbf{k}$ and incident polarisation $\boldsymbol{\epsilon}$) and creating a photon (with wave vector $\mathbf{k}'$ and scattered polarisation $\boldsymbol{\epsilon}'$), yet leaving the system unchanged. In other words, this elastic process does not impart (or absorb) any energy such that initial and final state of the system, namely $\Psi(\mathbf{r}_1, \mathbf{r}_2, ..., \mathbf{r}_N)$, are in same state. The amplitude of scattering a photon with incident wave $\mathbf{k}$ to a photon with scattered wave vector $\mathbf{k}'$ is proportional to $\int\, d\mathbf{r}\, \Psi^*(\mathbf{r})\, \boldsymbol{\epsilon}\, a(\mathbf{k}) \exp(i\mathbf{k}\cdot\mathbf{r}) \cdot \boldsymbol{\epsilon}'^*\, a^\dagger(\mathbf{k}') \exp(i\mathbf{k}'\cdot\mathbf{r})\Psi(\mathbf{r})$, where $a^\dagger(\mathbf{k})$ and $a(\mathbf{k})$ are the creation and annihilation operators respectively [114]. Hence, the elastic X-ray scattering cross section from a single fixed atom is given by [114],

$$\frac{d\sigma}{d\Omega} = r_0^2 |f(\mathbf{q})|^2 (\boldsymbol{\epsilon}'^* \cdot \boldsymbol{\epsilon})^2. \tag{5}$$

Here, $f(\mathbf{q}) = \int d\mathbf{r} \exp(i\mathbf{q}\cdot\mathbf{r})\, \rho(\mathbf{r})$, or the Fourier transform of the electron density, is defined as the atomic form factor and r_0 is the classical electron radius. In this description, the polarisation dependence in the transition rate originates from the way perturbation from light on the momentum of the electron, $\hat{\mathbf{p}}$, enters the Hamiltonian describing the light-matter interaction. Classically, this can be understood as the incident photon polarising the electron cloud with the incident polarisation $\boldsymbol{\epsilon}$ such that probability of scattering a photon with polarisation $\boldsymbol{\epsilon}'$ is dependent on the relative polarisation of the incoming and outgoing photon [114, 115, 116]. Moreover, given that X-rays are scattered by electrons, the intensity of scattering varies with the atomic form factor $f(\mathbf{q})$, which scales with the atomic number of the scatterer Z_A, and decreases monotonically with $|\mathbf{q}|$.

For X-ray scattering from a periodic array of atoms, described by m basis atoms in the unit cell at positions $\mathbf{r}_m$ with respect to each lattice points $\mathbf{R}_n$, we have [114],

$$\frac{d\sigma}{d\Omega} = r_0^2 \left| \sum_n \exp(i\mathbf{q}\cdot\mathbf{R}_n) \sum_m f_m(\mathbf{q}) \exp(i\mathbf{q}\cdot\mathbf{r}_m) \right|^2 (\boldsymbol{\epsilon}'^* \cdot \boldsymbol{\epsilon})^2. \tag{6}$$

Here, $f_m(\mathbf{q})$ is the form factor of the atom at site m and $\rho(\mathbf{r}) = \sum_{m,n} \rho_m(\mathbf{r} - \mathbf{R}_n - \mathbf{r}_m)$ is the periodic electron density cloud [112, 114, 115, 116, 117].

In the case where the incident X-rays are unpolarised – as is the case in the Laue camera and 6-circle κ laboratory diffractometer (Supernova) used in this work – the radiation is averaged over all polarisations such that the term $(\boldsymbol{\epsilon} \cdot \boldsymbol{\epsilon}'^*)^2 = (1 + \cos^2\theta)/2$. As such we recover the expression for Thomson scattering of light. However, at synchrotron sources, the incoming light is polarised in the plane of

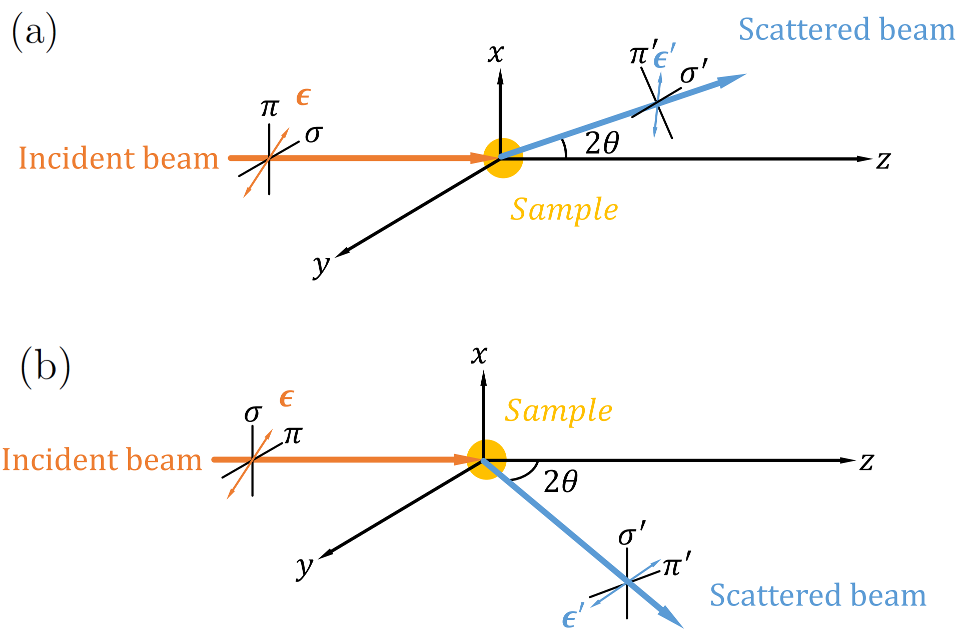

Figure 17: The (a) vertical and (b) horizontal scattering geometry and the corresponding definitions of the incident and scattered light polarisations.

the undulator (which could be π or σ depending whether the experiment is in the horizontal or vertical scattering geometry [see Fig. 17]).

Equation (6), in my view, is a beautiful equation connecting the spatial distribution of the scattered X-rays with information about the underlying crystal structure. It allows us to pry into the inner workings of a crystal to identify which atoms are in the crystal, how they arrange themselves, whether they interact, etc. For instance, the form factor, $f_m(\mathbf{q})$, which looks unassuming, can contain rich information about the identity of the atoms in the basis which might decorate each lattice point. Furthermore, the phase factor $(i\mathbf{q}\cdot\mathbf{r}_m)$, which can give rise to extinctions in the scattered intensity that are otherwise allowed by the lattice, can shed light on how the atoms arrange themselves within the basis.[7] In equation (6) it is, as if, in irradiating the crystal with the incident X-rays, each atom in the lattice acts a point source of X-rays (weighted by the form factor) to give rise to the X-ray diffraction pattern we observe. Furthermore, other rich subtleties can be captured in the equation. A pointed example is how the atomic form factor may differ for the same element on inequivalent symmetry sites due to the different chemical environment where they reside. This might give rise to peaks that are otherwise forbidden if we had assumed

---

[7] Notwithstanding the phase problem where the phase information is lost when we measure $\frac{d\sigma}{d\Omega}$.

that the form factor is isotropic and identical for all atoms of the same element.

2.3.2 Resonant elastic X-ray scattering (REXS)

As some of the crystals which I have studied in my thesis contain atoms which are strongly neutron absorbing (e.g. $\mathrm{EuCd_2As_2}$, $\mathrm{EuCd_2Sb_2}$), studying the magnetic order of these topological materials with powder neutron diffraction is not feasible. Furthermore, crystals of these materials currently available tend to be relatively small ($\lesssim$ 1mm), which compounded with the fact that magnetic neutron scattering has a small scattering cross-section, makes studying the evolution of these spin structures in an applied magnetic field less expedient. An alternative method is to use X-rays tuned to the resonant energy (which is close to absorption energy) of the magnetic ion in question. This not only leads to a strong enhancement in the scattering amplitude but also to a strong dependence on the polarisation of the incoming and scattered X-rays. The theoretical framework for this phenomena is covered in more detail in Refs. [114, 117, 118].

In my thesis, resonant X-ray magnetic scattering was used to study the magnetic order of $\mathrm{EuCd_2Sb_2}$ and how it evolves in an applied field. The derivations for the expressions that describe the scattering cross-section in the soft X-ray resonant scattering in $\mathrm{EuCd_2Sb_2}$ are based on the work by Hill and McMorrow [118], and are described in more detail in the Appendix [see Chapter 8]. Nonetheless, there are some salient points that I would like to address here, namely, how the magnetic propagation vector $\boldsymbol{\tau}$ and the spin orientation can be identified.

For the $\mathrm{EuCd_2Sb_2}$ sample in particular, a new set of peaks appeared as the sample was cooled below the magnetic ordering temperature [see Fig. 18]. In general, magnetic scattering can appear as additional intensity on top of existing Bragg peaks or as purely magnetic peaks at reflections that are not allowed by the lattice or basis. The expression describing the additional intensity arising from the scattering of $\mathrm{EuCd_2Sb_2}$ with incident X-rays tuned to the resonant edge of europium is given by,[8]

$$\left.\frac{d\sigma}{d\Omega}\right|_{E1}^{\mathrm{REXS}} \simeq 1/4F^{(2)2}\delta(\mathbf{q}-\mathbf{G})$$
$$+\,1/4\cos^2\theta F^{(1)2}\delta(\mathbf{q}-\mathbf{G}\pm\boldsymbol{\tau})$$
$$+\,1/16\left(\sin^2\theta+1\right)F^{(2)2}\delta(\mathbf{q}-\mathbf{G}\pm 2\boldsymbol{\tau}).$$

This is adapted from the general expression for REXS that is shown in Refs. [114, 118]. Here, $F^{(1)}$ and $F^{(2)}$ are strongly energy-dependent dimensionless co-efficients which describe the resonant strengths for the dipole transitions [114, 115, 118] and 2θ is the scattering angle. By indexing the additional peaks with a suitable $\boldsymbol{\tau}$ (or $\boldsymbol{\tau}$s) one can identify the magnetic propagation vector (or vectors) of the magnetic sub-lattice. In general, these peaks may or may not be commensurate with the host crystal structure. Fortunately for $\mathrm{EuCd_2Sb_2}$, the magnetic peaks can simply be indexed by the hexagonal unit cell with a magnetic propagation vector of $\boldsymbol{\tau} = (0,0,\frac{1}{2})$. This means that the magnetic contribution does not have to contend with the strong Bragg peaks, where the magnetic intensity will manifest, perhaps, as a small additional contribution on top of the strong structural peak. In those cases, it might be expedient to study magnetic peaks at forbidden Bragg reflections. By studying the intensity of say the $\mathbf{q}=(0,0,\frac{1}{2})$ peak, we can estimate the magnetic ordering temperature, the order parameter β and the size of the correlation length ξ (from the inverse width of the peaks).

Furthermore, the scattering amplitude for REXS also displays a strong dependence on the orientation of the magnetic moment, which can be identified by studying the scattered X-ray intensity of certain peaks. The origin of this strong sensitivity of the scattered intensity to the light polarisations and the direction of the magnetic moments is treated with more detail in Refs. [114, 117, 118]. Nonetheless it is instructive to consider the general expression for REXS which is given by [114],

$$\frac{d\sigma}{d\Omega} = \left|\left\langle a \left| \sum_n e^{i\mathbf{q}\cdot\mathbf{r}_n}\left[\left(\hat{\boldsymbol{\epsilon}}'\cdot\hat{\boldsymbol{\epsilon}}\right)F^{(0)} - i\left(\hat{\boldsymbol{\epsilon}}'\times\hat{\boldsymbol{\epsilon}}\right)\cdot\hat{\mathbf{z}}_n F^{(1)} + (\hat{\boldsymbol{\epsilon}}'\cdot\hat{\mathbf{z}}_n)(\hat{\boldsymbol{\epsilon}}\cdot\hat{\mathbf{z}}_n)F^{(2)}\right]\right| a \right\rangle\right|^2. \tag{7}$$

---

[8] Here I considered the scattering from the σ-σ' and σ-π' channels and an in-plane magnetic order of the europium spins. Also, I use $\simeq$ instead of $=$ as the contributions from the $F^{(0)}$ term is ignored.

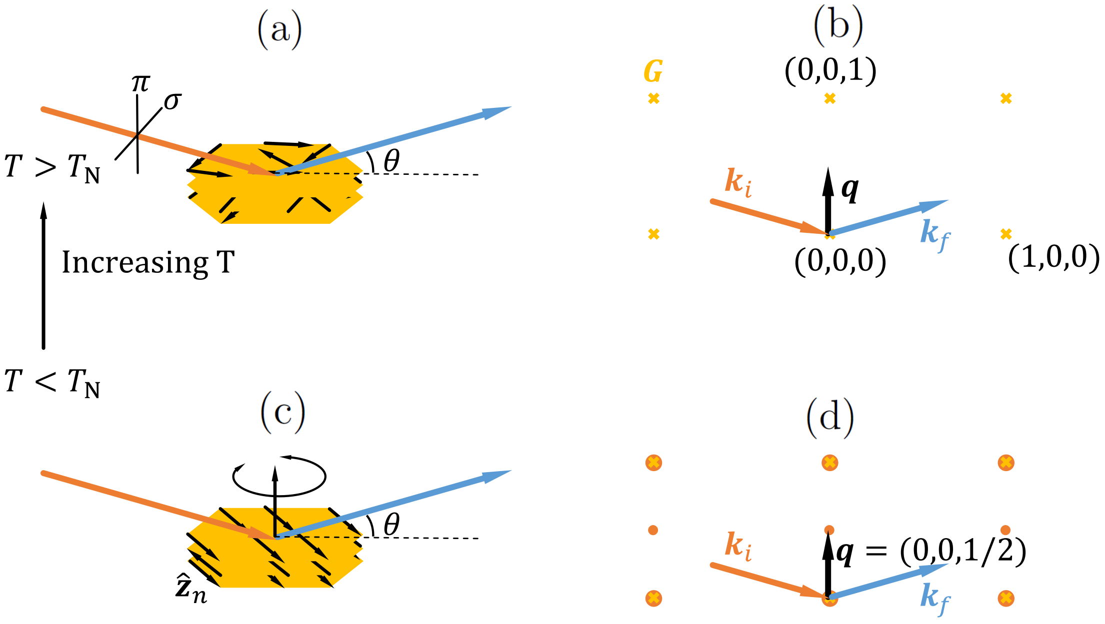

Figure 18: Illustration of REXS of $\mathrm{EuCd_2Sb_2}$ in the real and reciprocal space – in the $(h\,0\,l)$ plane – at temperatures above and below T_N. The (a) crystal displays magnetic order (c) as it is cooled below T_N. This manifests as (d) additional intensities in reciprocal space (b).

The first term (with the $F^{(0)}$ coefficient which was omitted earlier) refers to the charge Bragg peaks while the last two terms refer to the magnetic dipolar interactions as described earlier. $\mathbf{r}_n$ refers to the lattice sites of the magnetic species, $\hat{\mathbf{z}}_n$ is the magnetic moment at site n, $|a\rangle$ and $\langle a|$ are the initial and final states of the crystal respectively and $\hat{\boldsymbol{\epsilon}}$ and $\hat{\boldsymbol{\epsilon}}'$ refer to the polarisation of the incident and scattered X-ray [see Fig. 18]. (7) explicitly shows how the scattered intensity depends on the orientation of the spins ($\hat{\mathbf{z}}_n$), and incoming and outgoing X-ray polarisations, $\hat{\boldsymbol{\epsilon}}$ and $\hat{\boldsymbol{\epsilon}}'$ respectively. Reflections arising from the second term in the expression, which is linear in $\hat{\mathbf{z}}_n$, can be particularly helpful when identifying the spin orientation. The can done by studying the intensity of the $\mathbf{q} = (0,0,\frac{1}{2})$ peak with different permutations of incoming and outgoing X-ray polarisations [119] or different angular positions of the crystal about the scattering vector $\mathbf{q}$, as was done for the $\mathrm{EuCd_2Sb_2}$ study [see Fig. 18(c)].

2.3.3 X-ray sources

In the exploration of magnetic topological materials in my thesis, I used X-rays from two main sources: synchrotron X-rays to study the magnetic structure of $EuCd_2Sb_2$ and lab X-rays to study the orientation and the crystalline quality of the samples.

X-rays from the lab-based sources are produced when accelerated electrons are made to collide with a metal target (e.g. copper, molybdenum) [114]. The energy spectrum of the X-rays, which depends on the type of anode material and the accelerating voltage used, can generally be described by a continuous curve, arising from the *bremsstrahlung* effect, superposed with sharp spikes, which come from the characteristic transitions of the given target metal [114]. If, for example, the copper target is used, the dominant signal that is detected arises from the K_α transition ($\lambda^{\mathrm{Cu}}_{K_\alpha}$=1.5406 Å) as it has the highest intensity. As part of my study of the magnetic crystals, I used the 6-circle κ diffractometer (Agilent, Supernova) to check the quality, structure and orientation of the samples [see Fig. 19(a)]. I mount the crystal on the end of a sample mount with oil (if the sample is small) or GE varnish (if the sample is larger). Next, I used the CrysAlisPro software (version 38.41) to perform an automatic scan of the full sphere in reciprocal space,

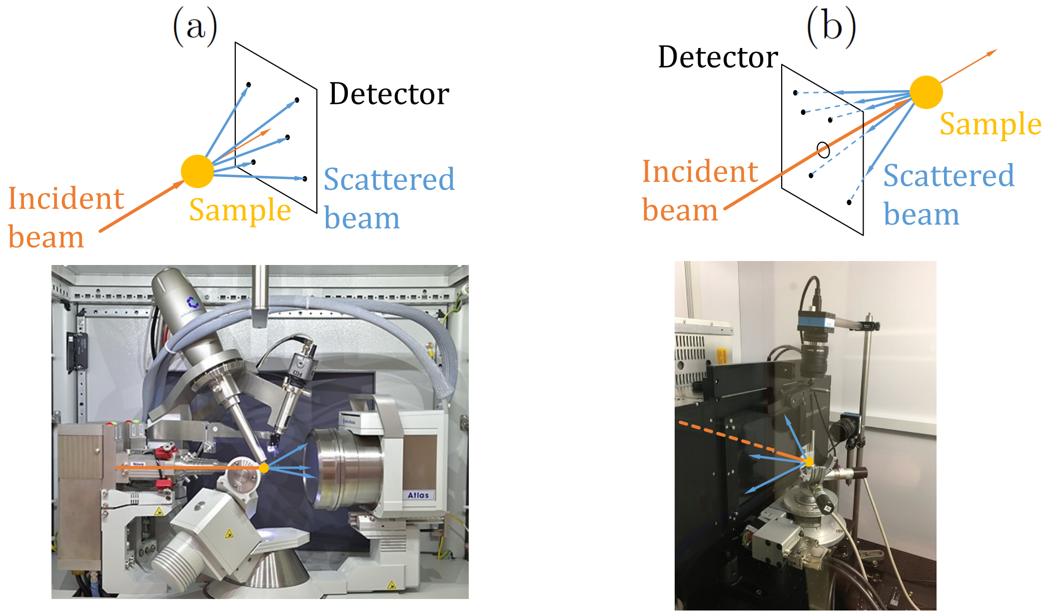

Figure 19: The (a) 6-circle and (b) Laue diffractometers used in my thesis are operating in the transmission and reflection experimental geometry respectively.

where the sample is rotated through 4π steradians. The program also provides for an automatic analysis of the detected peaks, where the crystal structure, cell parameters, orientation with respect to the sample mount (UB matrix) and quality (powder lines, twinning, stacking faults) can be identified. As lab X-rays typically penetrate a few microns into a sample, care has to taken when interpreting the X-ray diffraction data as the surface X-ray diffraction pattern may not be a good indication of the underlying bulk crystalline quality.

If the crystals that require aligning are too large to be used on the Supernova XRD, I use the Laue diffractometer instead. Here, X-ray scattering is performed in the back-reflection geometry [see Fig. 19(b)]. The Laue technique is useful for aligning crystals for X-ray/neutron/ARPES beamtime experiments and magneto-transport/magetometry measurements.

On the other hand, the X-rays used for REXS experiments are produced by synchrotron sources. In my work I used PETRA III (DESY, 6.0 GeV), Diamond Light Source (Oxfordshire, 3 GeV) and BESSY II (Helmholtz-Zentrum Berlin, 1.7 GeV). In Diamond, the electrons are accelerated in three particle accelerators, starting off with a linear accelerator, followed by a booster synchrotron and eventually in a large storage ring.[9] These electrons are steered around the polygon-shaped ring by bending magnets, and in doing so, produce very intense light that propagates tangentially to the electron path. Here, the term synchrotron is derived from synchronised increase in the magnetic field strength of the bending magnets as the kinetic energy of electrons is increased [114, 117]. The synchrotron light arrives in pulses as the electrons that are accelerated around the synchrotron come in packets (or bunches).

A special alternating array of magnets called insertion devices (e.g. undulators) can be placed in the straight sections of the electron paths to produce light of higher intensity. This is how the X-rays are produced at the beamlines that I have used for the X-ray studies: UE46-PGM01 (BESSY II), P09 (PETRA III) and I16 (Diamond). These undulators not only produce X-rays with high flux but also with a large range of wavelengths, which is useful for tuning the light to match the resonant frequency

---

[9] This information is taken from https://www.diamond.ac.uk/Public/How-Diamond-Works.html

in the L_3 or M_5 edges of some magnetic ions that I have studied in my thesis.

2.3.4 Examples

I have been involved in several REXS studies. At P09 (DESY, Germany), the magnetic order of $EuCd_2As_2$ (Eu L_3), $EuMnSb_2$ (Eu L_3; Mn K) and $Nd_2Ir_2O_7$ (Nd L_3; Ir L_3) was studied with hard X-rays. Similarly, the magnetism of $EuCd_2Sb_2$ and $EuCd_2As_2$ was explored with soft X-rays at the Eu M_5 edge at UE46-PGM01 (BESSY II, Germany). I have also been involved in the study of the magnetic structure of EuCuAs at I16 (Diamond, UK). Only the study of the magnetic structure of $EuCd_2Sb_2$ is reported in this thesis.

2.4 Neutron scattering

Neutrons can also be used as a probe to study the magnetism of single crystals. Given that neutrons do not carry an electric charge, they mainly scatter with the nuclei in solids (via the strong force) or unpaired electrons (via the magnetic dipole-dipole interaction). In the following three sub-sections, I explore these two phenomena in turn, relating them to the experiments and discussing what we can learn about the magnetic structure and dynamics of these topological materials.

2.4.1 Coherent elastic nuclear scattering

I will first consider the strong (nuclear) interaction between neutrons and a single nucleus before generalising the discussion to treat elastic neutron scattering in the context of a crystalline solid. Although the nature of this interaction mediated by gluons is very strong, it is very short ranged (~ 1 fm). This short-ranged interaction potential can be described by [112, 113, 120],

$$\hat{V}(\mathbf{r}) = b\delta(\mathbf{r}),$$

such that, in the Born approximation, the amplitude of scattering a neutron with initial momentum $\mathbf{k}$ elastically into a state with momentum $\mathbf{k}'$ is proportional to $\int d\mathbf{r}\exp(i\mathbf{k}\cdot\mathbf{r})\hat{V}(\mathbf{r})\exp(i\mathbf{k}'\cdot\mathbf{r})$. Hence, the scattering cross-section for a single nucleus is given by [112, 113, 120],

$$\frac{d\sigma}{d\Omega} = |b|^2. \tag{8}$$

In other words, the single fixed nucleus provides a potential $\hat{V}(\mathbf{r})$ to mediate the transition of the neutron wavefunction from $\psi_{\mathbf{k}} \propto \exp(i\mathbf{k}\cdot\mathbf{r})$ to $\psi_{\mathbf{k}'} \propto \exp(i\mathbf{k}'\cdot\mathbf{r})$ [120]. Here we take the nuclear form factor b (which can be a complex number and is more commonly known as the nuclear scattering length) to be approximately constant, independent of the neutron wavelength (for non-absorbing elements) and scattering vector $\mathbf{q}$. The approximation of the nuclear scattering potential to a delta-function works extremely well for the neutron energies employed in experiments to study condensed matter. If the nuclear form factor b is complex, it adds a negative exponent to the scattering cross-section which describes neutron absorption. This is relevant for intermetallic compounds $\mathrm{EuCd_2As_2}$ and $\mathrm{EuCd_2Sb_2}$ studied in this thesis that contain highly neutron-absorbing elements europium and cadmium. For these materials, synchrotron radiation is a better technique for studying magnetic structure [see Section 2.5].

For neutron scattering from an array of ions (described by an m ion unit cell basis which decorates lattice positions $\mathbf{R}_n$), the potential can be described by $\hat{V}(\mathbf{r}) = \sum_{m,n} b_m \delta(\mathbf{r}-\mathbf{R}_n-\mathbf{r}_m)$ [112, 113, 120] such that the scattering cross-section is given by,

$$\frac{d\sigma}{d\Omega} = \left| \sum_n \exp(i\mathbf{q}\cdot\mathbf{R}_n) \sum_m b_m \exp(i\mathbf{q}\cdot\mathbf{r}_m) \right|^2 . \tag{9}$$

Here the scattering length, b_m, is element (and in fact isotope) specific and varies haphazardly across the periodic table. Given that only neutrons that get very close to the nuclei can scatter, the bulk of the neutrons do not interact with the crystal and, as far as the samples used in this thesis are concerned (dimensions $< 5 \times 5 \times 5$ mm^3), they typically penetrate the whole crystal.[10] Furthermore, note that in this discussion, I take the incoming neutron beam to be unpolarised where the spin 1/2 is taken to be spherically averaged. Depending on the objective of the experiment, it might be advantageous to polarise the incoming neutron beam (or in some cases essential) and to analyse the polarisation state of the outgoing beam. This can be achieved by the choice of monochromator crystal and the analyser set-up, which is discussed further in Chapter 6.

---

[10] Even though a small fraction of the radiation will scatter, the scattering cross-section is comparable to that for X-ray scattering due to the stronger interaction.

2.4.2 Elastic magnetic scattering

I will now turn to consider the electro-magnetic interaction between neutrons and a single magnetic ion before treating the general case of elastic scattering of neutrons with the magnetic ions in the context of a host crystal. Even though the electro-magnetic interaction between neutrons (due to their spin) and the magnetic ion (due to its unpaired electrons), mediated by virtual photons, is considerably weaker compared to the strong interaction, it is more long ranged. As a result, both mechanisms (strong and electromagnetic interaction) can lead to a comparable number of neutron scattering events.

The interaction potential between a neutron and a magnetic ion can be described by $\hat{V}(\mathbf{r}) = -\mu_0 \boldsymbol{\mu}_\mathrm{n} \cdot \mathbf{M}(\mathbf{r})$, where $\boldsymbol{\mu}_\mathrm{n}$ is the magnetic moment of a neutron, μ_0 is the permeability of free space and $\mathbf{M}(\mathbf{r})$ represents the magnetisation emanating from the magnetic ion. Hence, the elastic scattering cross-section for a single magnetic ion is given by [112, 120, 121],

$$\frac{d\sigma}{d\Omega} = \left(\frac{\gamma r_0}{2\mu_\mathrm{B}}\right)^2 |\mathbf{M}_\perp(\mathbf{q})|^2 , \tag{10}$$

where γ is the gyromagnetic ratio, $r_0 = \mu_0 e^2/(4\pi m_e)$ is the classical radius of an electron and μ_B is the Bohr magneton. Here, $\mathbf{M}_\perp(\mathbf{q})$ is the component of $\mathbf{M}(\mathbf{q})$ that is perpendicular to the scattering vector $\mathbf{q}$, which can be defined by [112, 120, 121],

$$\mathbf{M}_\perp(\mathbf{q}) = \mathbf{M}(\mathbf{q}) - (\mathbf{M}(\mathbf{q}) \cdot \hat{\mathbf{q}})\hat{\mathbf{q}},$$

where $\mathbf{M(q)}$ refers to the Fourier transform of the spatial distribution of magnetic field, $\mathbf{M(r)}$ [see Fig. 20(b)]. While it seems peculiar that only the component of the magnetic moment which is perpendicular to the scattering vector $\mathbf{q}$ will be contributing to the magnetic scattering, it is actually very helpful in identifying the orientation of the magnetic moments. The expression for $\mathbf{M}(\mathbf{q})$, which can be quite complicated in general, can be substantially simplified for the magnetic scattering with the unpaired $3d$ electrons of Mn^{2+} ions, which was considered for my thesis. If we assume the orbital angular momentum to be quenched, we can write the magnetisation as,

$$\mathbf{M}(\mathbf{q}) = -g\mu_\mathrm{B} f(\mathbf{q})\mathbf{S},$$

where g is the Landé g-factor (=2 for fully quenched orbital angular momentum) and $\mathbf{S}$ is the spin quantum number. Here, the magnetic form factor $f(\mathbf{q})$, which is the Fourier transform of an electric spin distribution in space, decreases monotonically with $|\mathbf{q}|$. Hence, depending on the crystal lattice spacing, it may be advantageous to study magnetic reflections with small $|\mathbf{q}|$.

I will now turn to consider magnetic scattering in the context of a crystalline solid, where the magnetic ions display long-range magnetic order. Here the sum is taken over the magnetic ions such that,

$$\mathbf{M}(\mathbf{q}) = -\mu_{\mathrm{B}} \sum_{j} g_j \mathbf{S}_j f_j(\mathbf{q}) \exp(i\mathbf{q} \cdot \mathbf{r}_j), \tag{11}$$

where $f_j(\mathbf{q})$ is the magnetic form factor, $\mathbf{S}_j$ is the spin quantum number and $\mathbf{r}_j$ is the position of the j^{th} magnetic ion. Here, the magnetic moments vector $\mathbf{S}_j$ at site j does not have to be collinear with respect to the other magnetic moments or even be of the same magnetic subspecies. Furthermore, in this formalism, it is actually more expedient to describe these *magnetic* reflections in reference to the host crystallographic unit cell. This is especially helpful if we have to account for the possibility of a magnetic superstructure that might transcend the underlying atomic crystal structure. For instance, we can describe a magnetic structure that is incommensurate with the host crystal structure with magnetic propagation wave vectors, $\boldsymbol{\tau}$, with respect to the reciprocal lattice $\mathbf{G}$. Analogous to coherent elastic scattering, the diffraction condition is met when the scattering vector $\mathbf{q} = \mathbf{G} \pm \boldsymbol{\tau}$ and magnetic reflections can show up if $|\mathbf{M}_{\perp}(\mathbf{q})| \neq 0$ [see Figs. 20 for an example.].

2.4.3 Inelastic magnetic scattering

In my thesis, I studied the cooperative excitations of the ordered Mn^{2+} magnetic moments about the average orientations along the c axis. The excitation energy (E) of these magnons can be mapped using inelastic neutron scattering as a function of wavevector $\mathbf{q}$. The expression for the partial differential cross-section for magnetic inelastic scattering of $\mathrm{CaMnBi_2}$, which is isostructural to $\mathrm{YbMnBi_2}$, has been worked out by Rahn *et al.* [122]. Adapting the expression to the case for $\mathrm{YbMnBi_2}$, I arrived at the partial differential cross-section,

$$\frac{d^2\sigma}{d\Omega dE_f} = \frac{k_f}{k_i} \left(\frac{\gamma r_0}{2}\right)^2 g^2 f^2(\mathbf{q}) S(\mathbf{q}, E), \tag{12}$$

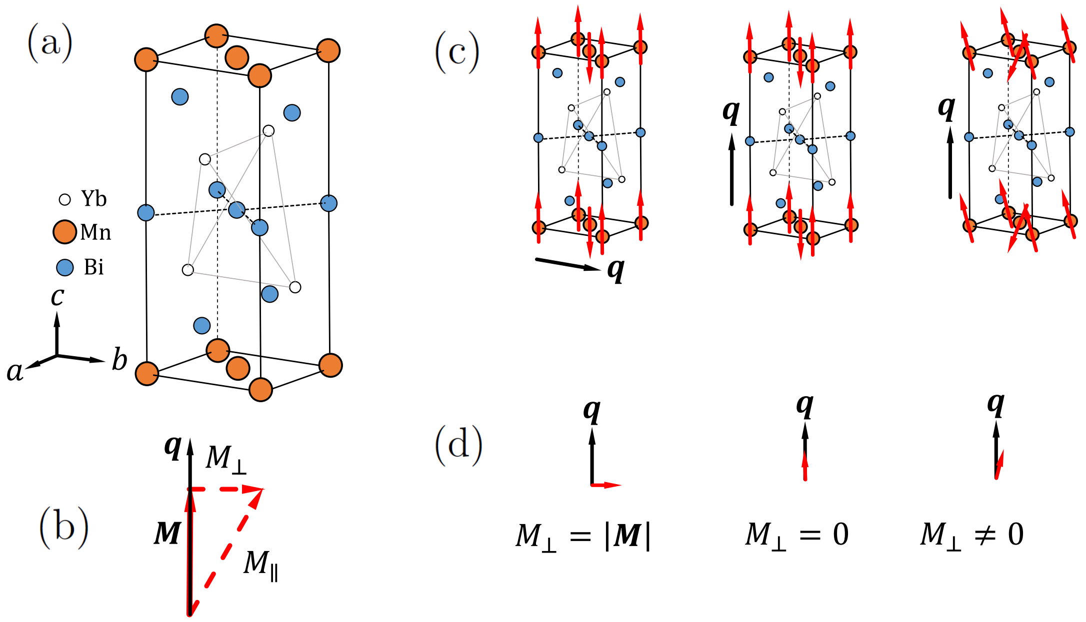

Figure 20: (a) The tetragonal unit cell of $\mathrm{YbMnBi_2}$. (b) Magnetic neutron scattering is only sensitive to the component of the magnetisation that is perpendicular to the scattering vector $\mathbf{q}$. (d) shows the magnetic components that is perpendicular to the scattering vector $\mathbf{q}$ for various scattering configurations and magnetic structures shown in (c).

where k_i and k_f are magnitudes of the incoming and outgoing wavevectors. Similar to elastic magnetic neutron scattering, the scattered intensity is only sensitive to components of the magnetic fluctuation that are perpendicular to the scattering vector $\mathbf{q}$. For $\mathrm{YbMnBi_2}$, $\mathbf{q}||c$ is not a problem, because if the spins are aligned along c then the spin deviations are perpendicular to c. Furthermore, the scattered neutron intensity also decreases monotonically with $|\mathbf{q}|$ due to the magnetic form factor $f(\mathbf{q})$. As such, the experiment geometry on the triple-axis spectrometer IN8 (ILL) has to be optimised to study spin-waves with $\mathbf{q}$ that is close to the Γ point to maximise the signal-to-noise ratio. For $\mathrm{YbMnBi_2}$, $S(\mathbf{q},\omega)$ is in turn given by [122],

$$S(\mathbf{q},\omega) = NS\frac{A(\mathbf{q}) - B(\mathbf{q})}{E(\mathbf{q})}\left[n(\omega)+1\right]\delta(\hbar\omega - E), \tag{13}$$

where N is the number of magnetic ions per sub-lattice, S is the spin quantum number and $E(\mathbf{q})$ is the magnon dispersion relation. Here the thermal population of magnons with respect to energy can be described by the Bose-Einstein statistics or $n(\omega) = \left(e^{(\beta E)} - 1\right)^{-1}$. The terms $A(\mathbf{q})$ and $B(\mathbf{q})$ are functions of the different

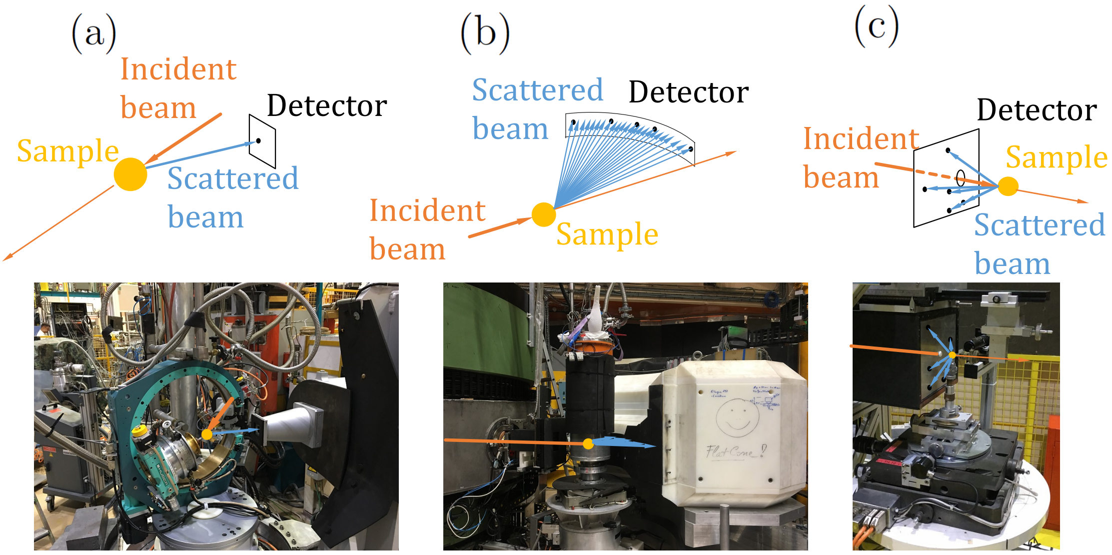

Figure 21: (a)–(c) The various scattering geometries of the D10, IN8 and OrientExpress beamlines at the ILL.

magnetic exchange couplings between the magnetic moments and is discussed in further detail in Ref. [122].

2.4.4 Examples

In this thesis, I studied the magnetic structure and dynamics of single crystalline $YbMnBi_2$ at the following beamlines: WISH (ISIS), D10 (ILL), IN8 (ILL) and OrientExpress (ILL) [see Fig. 21 for illustrations of the last three.]. I also used polarised neutrons to study the non-collinear magnetic structure of Mn_3Ge single crystals at the D3 beamline at the ILL.

Furthermore, I have studied three europium-based compounds with neutrons on the WISH diffractometer ($EuMnSb_2$, $EuCd_2As_2$ and EuCuAs). The high flux at WISH meant that the magnetic signal was still discernible despite the strong neutron absorption of the rare-earth ions. These studies are not reported here.

2.4.5 Neutron sources

At ISIS, the neutrons are produced by bombarding a tungsten target with a high-energy proton beam. The beam is produced by initially accelerating H^- ions in a linear accelerator followed by a synchrotron. This gives rise to pulses (50 Hz) of

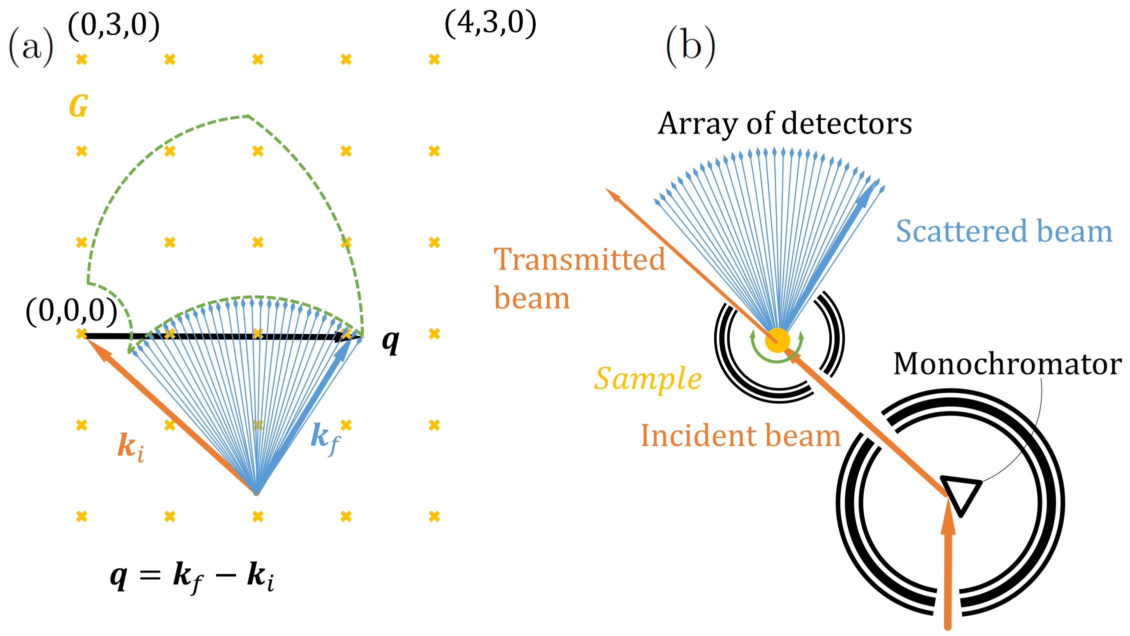

Figure 22: Illustration of the inelastic neutron scattering of $\mathrm{YbMnBi_2}$ in (a) reciprocal and (b) real space. In this experiment, the scattered neutrons are detected by an array of 31 detectors. This translates to an arc in **k**-space. A rotation of the sample in real space – shown by the green arrow in (b) – corresponds to the arc sweeping out an area in reciprocal space bounded by the green dashed line in (a).

spalled neutrons that are eventually slowed down in a series of moderators (water, methane and liquid hydrogen) and are subsequently guided to the various beam lines.

Neutrons at the ILL reactor source, on the other hand, are produced via the controlled fission of uranium-235. The energy distribution of the continuous neutron flux produced from this source can be described by the Maxwell-Boltzmann statistics at $T = 300\,\mathrm{K}$ with a peak intensity of neutrons with $E = 25$ meV.

2.5 Choice of radiation

In this subsection, I discuss the different considerations when deciding which type of radiation is used to study the magnetic order and excitations in single crystalline samples. This is strongly linked to the nature of the interaction between the radiation and the sample [see Sections 2.3.2, 2.4.1,2.4.2 and 2.4.3], the properties (mass, surface, etc.) of the single crystals under investigation, and the phenomena to be probed.

The chemical vapour transport method used in this work usually produce small crystals ($\sim 1 \times 1 \times 1$ mm^3). Due to the small neutron scattering amplitude, such samples are not feasible for neutron scattering. Nonetheless, this crystal growth method yields high-quality single crystals with natural shiny facets. Given that the electromagnetic interaction is relatively strong (X-rays can typically only penetrate a few hundreds of nm), the near-pristine surface of these crystals mean that these samples are very suited for synchrotron X-ray diffraction studies. This is not always possible for flux-grown crystals that may have substantial amount of flux on the crystal surface.

Furthermore, other than the mass (and size) limitation, crystals containing strongly neutron absorbing elements (e.g. Ir, Eu, Cd) severely reduce the intensity of scattered neutrons. For such compounds, X-rays would be a more suitable probe. Moreover, the resonant X-ray scattering technique provides for ion specificity, where the scattered signal is dominated by the contributions from ions whose absorption edge energy matches the incident X-ray energy. This is helpful if there is more than one type of magnetic species in the crystal. Whereas for magnetic neutron scattering, distinguishing between the contribution from different magnetic species, especially if the magnetic sub-lattices have the same magnetic propagation vector and spin orientation, is less straight forward.

Magnetic resonant X-ray scattering does, however, pose some limitations. By virtue of fixing the incident X-ray energy to match that of the resonant energy of the element under investigation (and hence $\mathbf{k}_i$), the technique does restrict the accessible $(h\,k\,l)$ reflections for long wavelengths.[11] In terms of inelastic scattering, neutrons tend to prove more useful for mapping magnon dispersion because a finite change in X-ray momentum leads to a very tiny change in X-ray energy (typically 1 part in 10^6), which is very difficult to resolve experimentally. While the measurement of magnons using X-rays is currently possible with resonant inelastic X-ray scattering, it is however limited by the energy resolution of the currently available instruments [114].

---

[11] This is not an issue for short wavelengths as the full reciprocal space is accessible

2.6 Magnetotransport

In this work, I define the 3×3 resistivity matrix $\underline{\rho}$ as $\mathbf{E} = \underline{\rho}\mathbf{j}$ where $\mathbf{E}$ and $\mathbf{j}$ are the electric field and current vectors respectively. Estimates of the resistivity matrix elements ρ_{ij} [where $i, j = (x, y, z)$] for my single crystalline samples were obtained by performing magnetotransport measurements on a PPMS (Physical Property Measurement System, Quantum Design) in a Hall configuration with the standard five-contact method. Gold wires (15 μm, AU519209, Advent Research) were bonded to the crystalline samples with conductive silver glue (4929N, DuPont). This gives rise to a typical contact resistance of $\sim 2\ \Omega$. Samples were mounted on a standard PPMS (Quantum Design) puck with GE varnish (VGE-7031, LakeShore cryotronics) and insulated from the ground with a piece of quartz. Hall measurements were performed in $\mathbf{B}$ fields of up to 16 T applied along the $\hat{z}$ axis and temperatures down to 1.8 K in a pressure of $\sim 10^{-9}$ Torr [see Fig. 23(a)].

The in-plane resistivity, ρ_{xx}, is obtained by $\rho_{xx} = V_x A / I_x l$ where V_x is the potential drop across the in-plane contact leads, I_x is the current magnitude, A is the cross-sectional area of the sample (with surface normal to the direction of I_x) and l the distance between the contacts [see Fig. 23(a)]. The Hall resistivity ρ_{xy} is given by $\rho_{xy} = V_y t / I_x$ where t is the thickness of the sample in the z direction and V_y is the potential drop across the Hall wire contacts. As the position of the contacts will slightly deviate from the ideal Hall bar configuration, the measured in-plane potential drop and Hall voltage, namely V_x' and V_y', will carry contributions from the Hall and in-plane resistivity components respectively. Given that the *true* V_x and V_y will be symmetric and anti-symmetric about $B = 0$ respectively, both V_x' and V_y' can be symmetrised to give V_x and V_y. To remove the Hall contribution in the measured in-plane voltage, V_x' is symmetrised via $V_x = 1/2 \times [V_x'(B) + V_x'(-B)]$. Similarly, to remove the contribution from the in-plane potential drop across the Hall leads, V_y' is symmetrised via $V_y = 1/2 \times [V_y'(B) - V_y'(-B)]$.

The resistivity matrix $\underline{\rho}$ can be inverted to give the conductivity tensor

$$\begin{bmatrix} \sigma_{xx} & \sigma_{xy} & \sigma_{xz} \\ \sigma_{yx} & \sigma_{yy} & \sigma_{yz} \\ \sigma_{zx} & \sigma_{zy} & \sigma_{zz} \end{bmatrix},$$

where $\sigma_{xx} = \rho_{xx}/(\rho_{xx}^2 + \rho_{xy}^2)$ and $\sigma_{xy} = -\rho_{xy}/(\rho_{xx}^2 + \rho_{xy}^2)$.

2.7 SQUID measurements

A superconducting quantum interference device (SQUID) magnetometer (Magnetic Properties Measurement System, Quantum Design) was used to perform the two principal magnetic measurements: magnetisation as a function of temperature and field. Measurements as a function of field were performed up to $\mu_0 H = \pm 7\,\mathrm{T}$. The field is generated by superconducting wires that are wound as a solenoid around the cylindrical sample environment. Temperature-dependent measurements (in a non-zero fixed field) can be performed in the temperature range of $T = 1.8\,\mathrm{K}$ to $370\,\mathrm{K}$, which is achieved by a combination of a liquid helium and liquid nitrogen jacket.

The magnetometry studies in my thesis are limited to single-crystalline samples. These are placed in the middle of a 20 cm long plastic straw and secured with Kapton tape [see Fig. 23(b)]. To reduce background effects from the Kapton tape, the tape extends along the entire length of the straw. The straw is attached to the rigid sample rod which is connected to an actuator that translates the sample, vertically, through superconducting detection coils which are connected to the SQUID. The

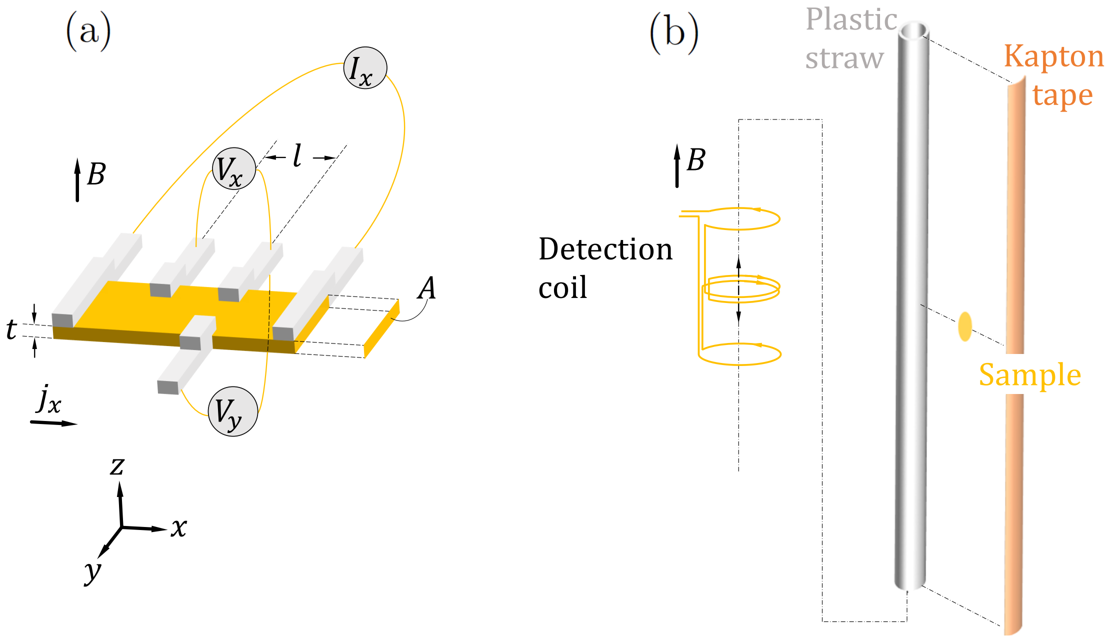

Figure 23: The sample geometry for (a) magnetotransport and (b) magnetometry measurements.

motion of the sample through the coils induces a current in the detection coil due to the changing magnetic flux. This gives us an estimate of the dipole field emanating from the sample and hence how susceptible the magnetic moments in the sample are to the applied field with an accuracy on the order of 10^{-8} emu.

2.8 Density functional theory

The electronic band structure calculations were based on the implementation of density functional theory (DFT) provided by the plane wave basis Quantum Espresso suite [123]. The calculations were performed in three steps.

- First, I run a self-consistent calculation. This is based on the experimental cell parameters and Wyckoff positions of the atoms in the unit cell. The **k**-point sampling mesh used for the calculations is based on a Monkhorst-Pack grid.[12] Furthermore, depending on which crystal is studied, I can also specify the magnetic structure and perform calculations that account for the large spin-orbit coupling in heavy atoms.

- Next, I define a path in reciprocal space (which does not necessarily have to be along a high symmetry line) and repeat the calculations along the said trajectory in **k**-space. This allows me to study how the electron bands disperse, the degeneracy of the electronic states and the effect of spin-orbit coupling strength on the band structure. For instance, I can track the influence of the pnictide atom on the electronic band structure of the isostructural family $\mathrm{EuCd_2}Pn_2$ (Pn = As, Sb, P).

- Finally, I perform band character analysis to study the nature of the electronic bands near the Fermi energy. This is important especially when dealing with magnetic topological materials. While DFT is well-suited to describe bands that have weak electron-electron interactions, it does not treat strong electron correlations well. Hence, in studying the topology of the electronic bands, I

---

[12] While having a finer the mesh does seem like an attractive proposition, it gives rise to a greater number of sampling points and hence an appreciably longer time for the calculation to achieve convergence. Hence, **k**-point mesh is chosen based on how substantial the self-consistent energy changes after the number of sampling points are increased.

know the calculations can be trusted if the electronic bands near the Fermi energy have *s* and *p* orbital character as these states are well described by DFT.

As part of my thesis, I present the electronic band structure of $EuCd_2Sb_2$ in detail. Other topological materials which I have studied but are not presented here include: $YbMnBi_2$, $EuMnSb_2$, $EuCd_2As_2$, $YbCd_2As_2$, $EuZn_2As_2$, Mn_3Ge, Mn_3Sn, Na_3Bi, K_3Bi, EuS, $RhTe_2$, $OsTe_2$, OsO_2, IrO_2, RhO_2, CaAgP, CaAgAs, CaAgZn, CaCuAs, EuCuAs, CaCuSb, CaCdGe, CaCdSn and CaAgZn.

CHAPTER 3

Magnetic and electronic structure of the layered rare-earth pnictide $EuCd_2Sb_2$

In this chapter, I present the magnetic structure of $EuCd_2Sb_2$, which was studied with synchrotron X-rays for the first time, and the implications in terms of electronic transport, band structure and magnetisation.

Resonant elastic X-ray scattering (REXS) at the Eu M_5 edge reveals an AFM structure in layered $EuCd_2Sb_2$ at temperatures below $T_{\mathrm{N}} = 7.4\,\mathrm{K}$ with a magnetic propagation vector of $(0, 0, 1/2)$ and spins in the basal plane. Magnetotransport and REXS measurements with an in-plane magnetic field show that features in the magnetoresistance are correlated with changes in the magnetic structure induced by the field. *Ab initio* electronic structure calculations predict that the observed spin structure gives rise to a gapped Dirac point close to the Fermi level with a gap of $\Delta E \sim 0.01\,\mathrm{eV}$. The results of this study indicate that the Eu spins are coupled to conduction electron states near the Dirac point.

3 Magnetic and electronic structure of the layered rare-earth pnictide $EuCd_2Sb_2$

3.1 Introduction

Condensed matter systems which combine non-trivial electron band topology and magnetic order provide an arena in which to investigate the interplay between the physics of strong electron correlations and large SOC [11, 71, 124, 125, 126]. The intrinsic symmetries in these crystal structures afford protection to exotic quasiparticle excitations which possess a whole host of desirable properties such as extremely high mobility and large magnetoresistance [29, 31].

Systems in which topological charge carriers are coupled to magnetism have strong potential for spintronic device applications, where the current can be modulated by altering the spin structure with an externally applied field. The coexistence of the two phenomena can be realised in europium-based antimonides, EuX_2Sb_2 (X=Cu, Pd, Zn, Cd) [127, 128, 129, 130, 131]. These 122-pnictides possess $4f$ electrons which give rise to strong electron correlations, and heavy Sb which produces large SOC.

Within the family of EuX_2Sb_2, $EuCd_2Sb_2$ has recently garnered interest due to the discovery of a large thermoelectric figure of merit ZT of 0.60 at 617 K [133]. This led to systematic investigations of various substitutions in $Yb_xEu_{1-x}Cd_2Sb_2$ [134], $CaCd_2Sb_2$ [134], $Eu(Zn_{1-x}Cd_x)_2Sb_2$ [135] and $Eu(Cd_{1-x}Mn_x)_2Sb_2$ [136]. The large ZT in $EuCd_2Sb_2$ was attributed to the heavy masses of Cd and Sb, which give rise to the low thermal conductivity, and to the presence of conducting Eu $4f$ states, which leads to a large enhancement in the density of states near E_F compared to $CaCd_2Sb_2$ [133]. The latter feature, however, is contradicted by an electron-spin resonance (ESR) study of $EuCd_2Sb_2$, which suggested a localised moment picture for the Eu spins [137]. Highly localised $4f$ orbitals usually host strong electron-electron correlations which were not included in the electronic structure calculations in Ref. [133]. Furthermore, the physics of large SOC in the Cd and Sb bands was not explored.

Consistent with strong electronic correlations, $EuCd_2Sb_2$ displays AFM order of the Eu spins below $T_\mathrm{N} \simeq 7.4\,\mathrm{K}$, as evidenced by magnetic susceptibility [131, 133, 137, 138], Mössbauer spectroscopy [131], ESR [137] and heat capacity measurements [133]. Moreover, electronic transport measurements show an anomaly in the conductivity at T_{N}, suggesting that the spin structure is coupled to the charge carriers [133]. Up to now, however, there are no reports on the ground state magnetic structure in $\mathrm{EuCd_2Sb_2}$, which would shed light on the nature and consequences of this coupling.

In the light of this, I set out in this study (i) to determine the magnetic structure by single-crystal soft X-ray resonant magnetic scattering, and (ii) to investigate the nature of electrical conduction through *ab initio* electronic structure calculations including correlations. X-rays, rather than neutrons, were used for the diffraction study because of the very strong neutron absorption of both Eu and Cd. I find that in zero field the Eu spins order in an A-type AFM structure with the spins lying in the *ab* plane, and predict that this AFM structure gives rise to a gapped Dirac point along the $\Gamma - A$ high symmetry line in the Brillouin zone. I also find that field-induced changes in the magnetic order are correlated with features in the magnetoresistance.

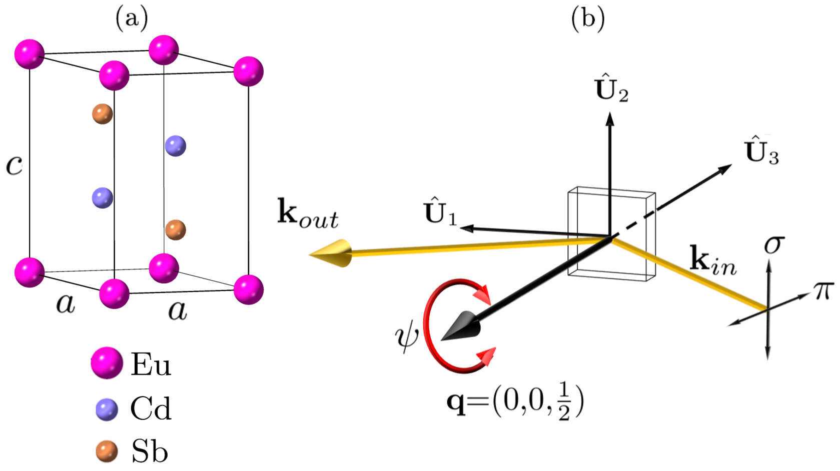

Figure 24: (a) A unit cell of $\mathrm{EuCd_2Sb_2}$. (b) The experimental set-up for the REXS experiment, with $\hat{\mathbf{U}}_1$, $\hat{\mathbf{U}}_2$ and $\hat{\mathbf{U}}_3$ defined as in Refs. [118, 132]. The crystal was mounted with the c axis parallel to the scattering vector $\mathbf{q}$. In the high magnetic field chamber, the field was applied along the direction of $\hat{\mathbf{U}}_1$ ($H \perp c$). The magnetotransport and magnetisation measurements reported in this study were also performed with $H \perp c$.

3.2 Experimental and theoretical methods

$EuCd_2Sb_2$ single crystals were prepared by a chemical vapour transport method by Dharmalingam Prabhakaran.[13] All handling was carried out in an argon glove box. Stoichiometric amounts of high purity Eu (99.9%), Cd (99.99%) and Sb (99.999%) elements were mixed and loaded in an alumina crucible, which was then sealed in an evacuated quartz tube. The tube was slowly heated to 1275 K, kept for 24 h and quenched to room temperature. The quartz tube was opened, and the powder reground and reloaded in the crucible with iodine as the transport agent. The crucible was sealed in the quartz tube, which was heated to 1325 K and kept for a week before being cooled slowly to room temperature. Small single crystals were separated from the crucible and used for my measurements. The crystal structure and crystallographic quality of the crystals was studied on a Rigaku SuperNova single-crystal diffractometer operated with a Cu K_α source.

The REXS measurements were performed on the UE46-PGM1 beamline [139] at the BESSY II storage ring with Christian Donnerer[14] and Enrico Schierle,[15] the beamline scientist. A plane grating monochromator was used to tune the X-ray energy to match that of the Eu M_5 edge (1.1284 keV). The dipole transition at the M_5 edge ($3d$ to $4f$) directly probes the magnetic $4f$ states, which leads to a strong enhancement of the magnetic scattering.

The REXS experiment was performed in the horizontal scattering geometry in the two-circle XUV diffractometer [Fig. 24(b)]. The sample was cooled below T_N by a liquid helium flow cryostat in conjunction with an aluminium shield to reduce beam heating. The cryostat achieved a base temperature of 4.5 K, but due to beam heating I estimate the sample temperature to be about 5 K. As in a typical magnetic X-ray scattering experiment, the magnetic structure is determined by studying the azimuthal dependence of the scattered intensity with σ and π incident photons [119, 140, 141, 142]. The intensity of the scattered beam was estimated with a AXUV100

---

[13] Department of Physics, University of Oxford, Clarendon Laboratory, Parks Road, Oxford OX1 3PU, United Kingdom.

[14] London Centre for Nanotechnology, University College London, London WC1H 0AH, United Kingdom.

[15] Helmholtz-Zentrum Berlin fur Materialien und Energie, Albert-Einstein-Straße 15, D-12489 Berlin, Germany.

avalanche photodiode with no polarisation analysis. Therefore, when σ-polarisation was used, both the $\sigma \rightarrow \sigma'$ and $\sigma \rightarrow \pi'$ channels contributed to the scattered intensity. Likewise, $\pi \rightarrow \sigma'$ and $\pi \rightarrow \pi'$ channels contributed to the scattered intensity when π-polarisation was used. To study the evolution of the magnetic structure in an external magnetic field, diffraction measurements were performed in the high field chamber with fields of up to 2 T applied in the direction of $\hat{\mathbf{U}}_1$ [Fig. 24(b)].

A SQUID magnetometer (Quantum Design) was used to perform magnetisation measurements as a function of temperature and field applied perpendicular to the c axis ($H \perp c$). Data for $H \parallel c$ have been reported previously [137]. Measurements as a function of field were performed for $H \leq 3$ T at fixed temperatures T between 1.8 and 8 K, while temperature-dependent measurements were performed for $T = 1.8$ to 50 K at fixed fields up to 1 T. Field- and temperature-dependent electronic transport measurements were performed for $H \leq 5$ T and 2 K $\leq T \leq$ 100 K on a Physical Property Measurement System (Quantum Design). Gold wires were bonded to the single crystal with silver paste in a four probe configuration.

To further explore the effects of magnetic order on electronic transport in $EuCd_2Sb_2$, I carried out *ab initio* electronic structure calculations using the implementation of density functional theory (DFT) provided by the plane wave basis Quantum Espresso suite [123]. A Monkhorst-Pack mesh [143] of $8 \times 8 \times 6$ was used for $\mathbf{k}$-point sampling. Relativistic pseudopotentials were used to account for the strong spin-orbit interaction in cadmium and antimony [144]. The generalised gradient approximation (GGA) functional was used to describe the exchange correlation [145]. A spin-polarised calculation was also implemented to account for the possible spin splitting in the electronic bands due to the magnetic europium ions [146]. To model the strong electron correlations in the highly-localised europium $4f$ orbitals, a correction to the exchange-correlation functional was implemented [147, 148, 149, 150, 151]. This additional functional has an associated parameter U, which resembles the U in the Hubbard model. In this work $U = 3.1$ eV was used, the justification for which will be given later (see Section 3.3.4). The unit cell was doubled along the c axis to accommodate the $(0, 0, 1/2)$ AFM propagation vector found in the REXS study.

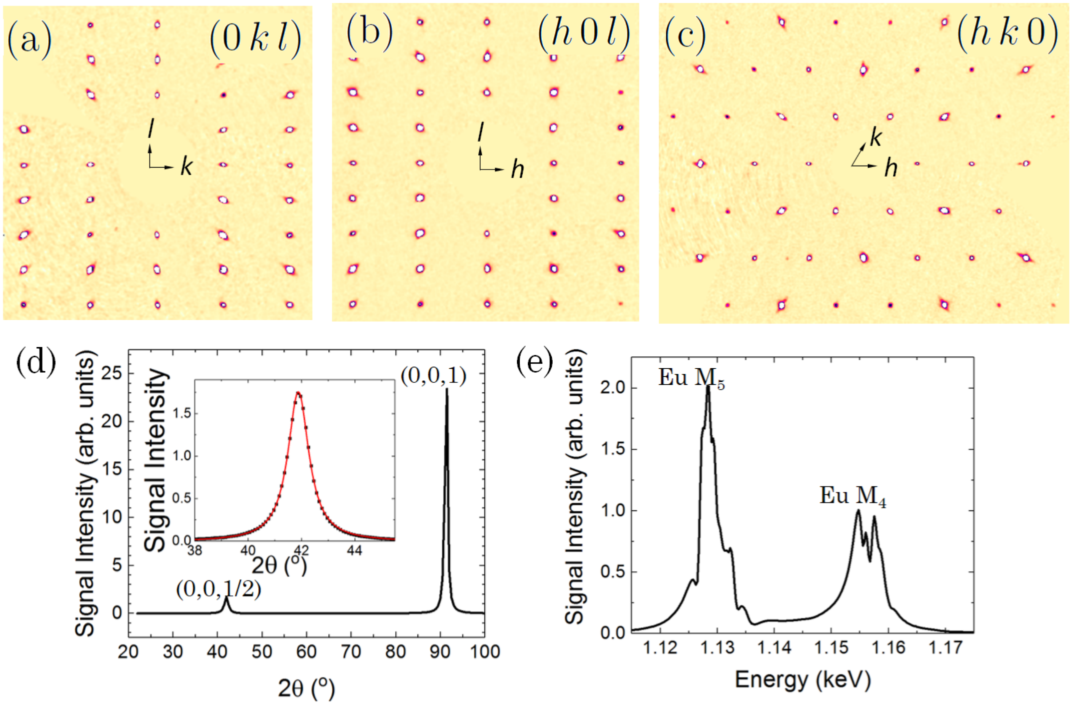

Figure 25: (a)-(c), Reciprocal space maps of the $(0\,k\,l)$, $(h\,0\,l)$ and $(h\,k\,0)$ planes respectively show high crystalline quality in the flux-grown crystal. (d) The long $\theta - 2\theta$ $(0\,0\,L)$ scan through the $(0\,0\,\frac{1}{2})$ and $(0\,0\,1)$ peaks obtained from REXS of $EuCd_2Sb_2$. The insert which plots the rocking scan of the magnetic peak in more detail demonstrates the high crystalline quality. (e) The fixed-$\mathbf{q}$ energy scan of $EuCd_2Sb_2$ measured below the Néel Temperature.

3.3 Results and analysis

Laboratory single crystal X-ray diffraction revealed the high crystalline quality of the flux-grown crystals [see Fig. 25], and confirmed the $P\bar{3}m1$ space group with room temperature cell parameters $a = 4.7030(9)$ Å, $c = 7.7267(18)$ Å, and Wyckoff positions 1a $(0, 0, 0)$, 2d $(1/3, 2/3, 0.6322(3))$ and 2d $(1/3, 2/3, 0.2473(5))$ for the Eu, Cd and Sb atoms, respectively, in close agreement with the earlier studies [131, 133, 134, 138] [see Table 6]. These structural parameters were used in the subsequent DFT calculations.

3.3.1 Magnetisation and magnetotransport

The temperature dependent susceptibility, $\chi(T)$, for various fields is shown in Fig. 26(a). Upon cooling, the susceptibility first increases then peaks sharply at $T_N \simeq 7.4\,\mathrm{K}$, signalling that AFM order has set in. The low field data are well described by the Curie–Weiss law, $\chi(T) = C/(T - \theta_p)$, $C = \mu_0\mu_{\mathrm{eff}}^2/3k_{\mathrm{B}}$, with $\mu_{\mathrm{eff}} = 8.07(5)\,\mu_{\mathrm{B}}$ and $\theta_{\mathrm{p}} = -3.8(2)\,\mathrm{K}$ [see Fig. 26(c)].

Figure 26(b) displays the isothermal magnetisation curves at various temperatures. At $T = 1.8$ K ($T \ll T_{\mathrm{N}}$) the magnetisation increases linearly with field before saturating at $M_{\mathrm{sat}} \simeq 6.95\,\mu_{\mathrm{B}}\,\mathrm{f.u.}^{-1}$ for fields above $\mu_0 H_{\mathrm{c}} \simeq 2\,\mathrm{T}$. As there is one Eu ion per formula unit, the values of M_{sat} and $\mu_{\mathrm{eff}}^2 = g_J^2 J(J+1)\mu_{\mathrm{B}}^2$ are fully consistent with divalent Eu^{2+} ($4f^7$, $S = 7/2$, $g_J = 2$). The deviations from linearity that demarcate the AFM phase vanish above the Néel temperature. Taken together with the susceptibility, transport and REXS measurements (see later), I propose the $\mu_0 H$–T phase diagram given in Fig. 27. The values of T_{N}, θ_{p} and μ_{eff} found here are consistent with those from earlier investigations, see Table 6.

3.3.2 Resonant X-ray magnetic scattering

When the sample was cooled below T_{N}, a reflection with scattering vector $\mathbf{q} = (0, 0, 1/2)$ was observed [Fig. 26(d)]. The intensity of the peak was strongly enhanced when the photon energy was tuned to the Eu M_5 edge [See Fig. 25(e)]. These observations are consistent with magnetic Bragg scattering from an AFM structure in which the Eu spins are ferromagnetically aligned in the *ab* plane and antiferromagnetically stacked along the *c* axis, i.e. an A-type AFM. There are two irreducible representations (irreps) of the space group that are compatible with the

Table 2: Magnetic and structural parameters of $\mathrm{EuCd_2Sb_2}$ found in this work and previous investigations. $*$ and † denote single crystalline and polycrystalline samples respectively.

T_{N} [K]	θ_{p} [K]	μ_{eff}	a [Å]	c [Å]	Reference
7.4(1)	−3.8(2)	8.07(5)	4.7030(9)	7.7267(18)	this work*
7.4	−4.6(5)	8.11(1)	4.699(2)	7.725(2)	[131]*,†
7.22	−3.14(7)	7.83(4)	4.6991(1)	7.7256(2)	[133], [134]†
7.8	−3.3	7.37	4.698(1)	7.723(1)	[138]*
7.4	−3	7.83	-	-	[137] †

observed propagation vector of $(0, 0, 1/2)$: Γ_3 and Γ_5. The magnetic structures described by these irreps differ only in the direction of the Eu spins, which point either parallel (Γ_3) or perpendicular (Γ_5) to the c axis, as shown later in Figs. 32(a) and (d). To establish which of the two irreps describes the symmetry in the AFM phase of EuCd$_2$Sb$_2$ I performed an azimuthal (ψ) scan and recorded the scattered intensity with both σ and π incident polarisations. During the scan the sample temperature was $T \simeq 5\,$K.

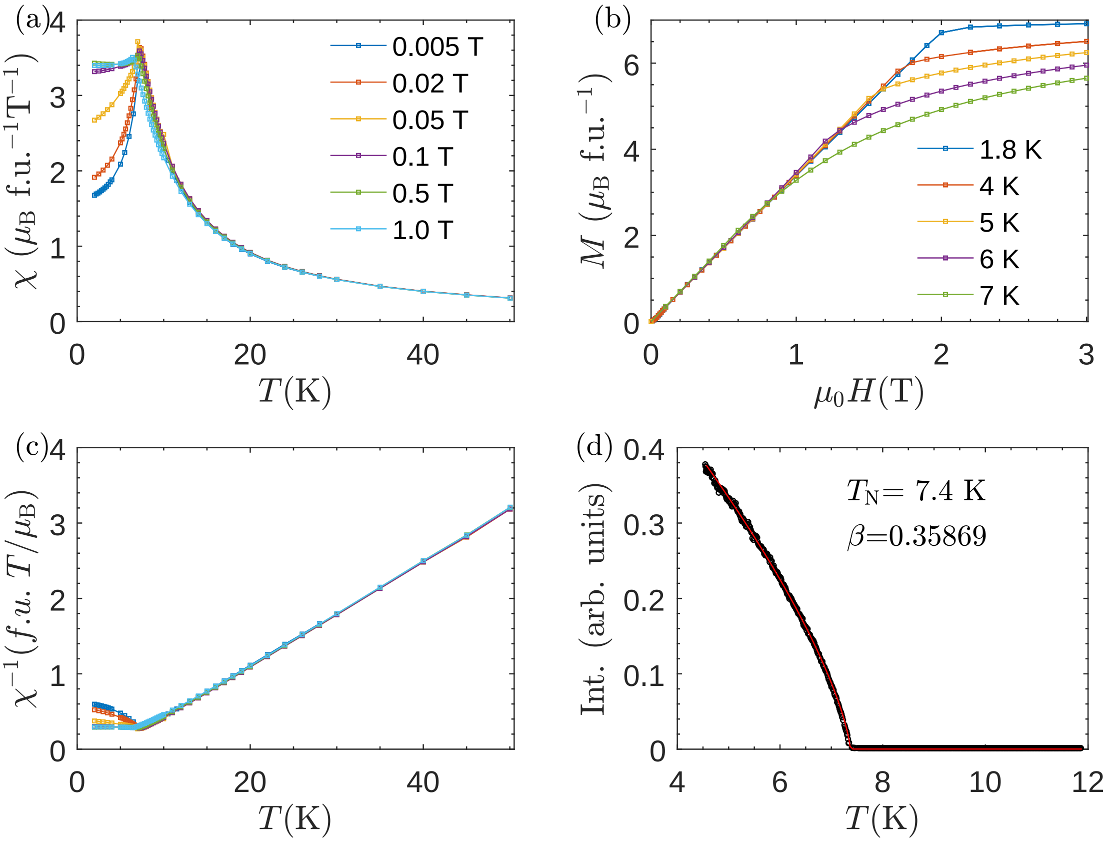

Figure 26: (a) Temperature dependence of the susceptibility χ measured at various field strengths with $H \perp c$. (b) Isothermal magnetisation with $H \perp c$ at various temperatures. (c) Plot of inverse magnetic susceptibility in EuCd$_2$Sb$_2$ at various in-plane field strengths. This is fitted to obtain an estimate of the μ_{eff} which is given by, $\chi^{-1} = C/(T - T_c) = (\mu_{eff}^2 \mu_0 n)/(3k_B(T - T_c))$. (d) The temperature dependence of the intensity of the $(0, 0, 1/2)$ reflection for a sample. The magnetic reflection comes from a doubling of the EuCd$_2$Sb$_2$ unit cell along the c axis. The temperature dependence of the peak intensity fits very well to a power law with critical exponent $\beta = 0.3671$, the value for the 3D Heisenberg universality class.

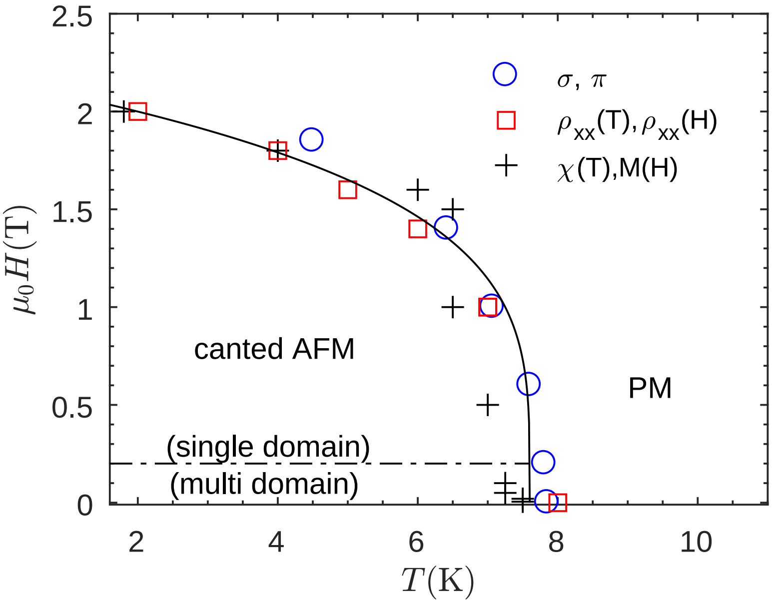

Figure 27: The $\mu_0 H$-T phase diagram ($H \perp c$) obtained from the anomalies in the soft X-ray, magnetotransport and magnetic susceptibility data. The line demarcates the paramagnetic (PM) from the canted AFM phase. The spin scattering in the charge carriers is supressed when $\mathrm{EuCd_2Sb_2}$ develops spontaneous magnetic order or when the spin structure is in the fully polarised state. A small field of 0.2 T is sufficient to re-orientate the multi-domain AFM to a single-domain AFM phase with spins canted towards the applied field.

The calculated angular variation of the X-ray scattering amplitude for the Γ_3 and Γ_5 structures is given in Table 3. Results for the four linear incident and scattered polarisation channels are listed, but as the polarisation of the scattered photons was not analysed in my experiment the intensities in the σ' and π' channels for a given incident polarisation need to be summed. If the spin structure has Γ_3 symmetry, the scattered intensity averaged over both final polarisation states is the same for both polarisation states of the incident photons. Furthermore, in the scattering geometry, the c axis, and hence the spins, lies along the scattering vector $\mathbf{q}$, such that a rotation of the sample about $\mathbf{q}$ in an azimuthal scan will produce no variation in the scattering amplitude.

On the other hand, if the spin structure displays Γ_5 symmetry, the scattered intensity with π incident polarisation should be larger than that with σ polarisation. This arises from the additional contribution from the $\pi \rightarrow \pi'$ scattering channel [see

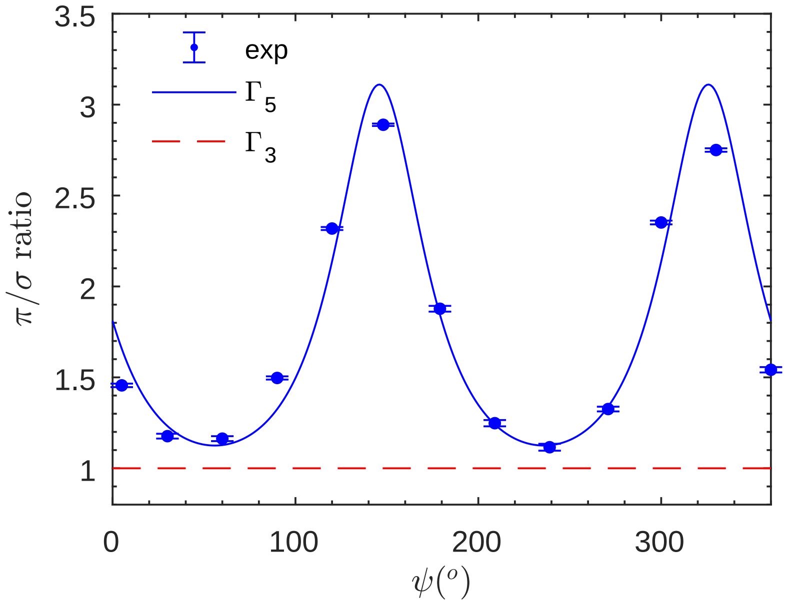

Figure 28: Variation in the intensity ratio for π and σ incident polarisations in an azimuthal scan at the $(0, 0, 1/2)$ magnetic Bragg peak. The data were recorded at $T \simeq 5\,\text{K}$. The full line shows a fit to the three domain model with Eu spins lying in the plane (Γ_5 structure). If the Eu spins point along the c axis (Γ_3 structure), the π/σ intensity ratio should be unity and show no angular dependence (broken line).

Table 3]. Furthermore, because the Eu spins lie in the plane in this irrep, a rotation of the sample about the scattering vector $\mathbf{q}$ will produce a ψ dependence in the intensity of the scattered beam.

Table 3: Calculated scattering amplitudes for the Γ_3 or Γ_5 magnetic structures of EuCd$_2$Sb$_2$ (Refs. [115, 118]). z_1, z_2 and z_3 are the projections of the magnetic moment onto the $\hat{\mathbf{U}}_1$, $\hat{\mathbf{U}}_2$ and $\hat{\mathbf{U}}_3$ basis vectors as defined in Fig. 24 and Ref. [118]. Here 2θ is the scattering angle.

Scattering Channel	Scattering Amplitude	
	Γ_3	Γ_5
$\sigma \to \sigma'$	0	0
$\sigma \to \pi'$	$z_3 \sin\theta$	$z_1 \cos\theta$
$\pi \to \sigma'$	0	$-z_1 \cos\theta$
$\pi \to \pi'$	$z_3 \sin\theta$	$-z_2 \sin 2\theta$

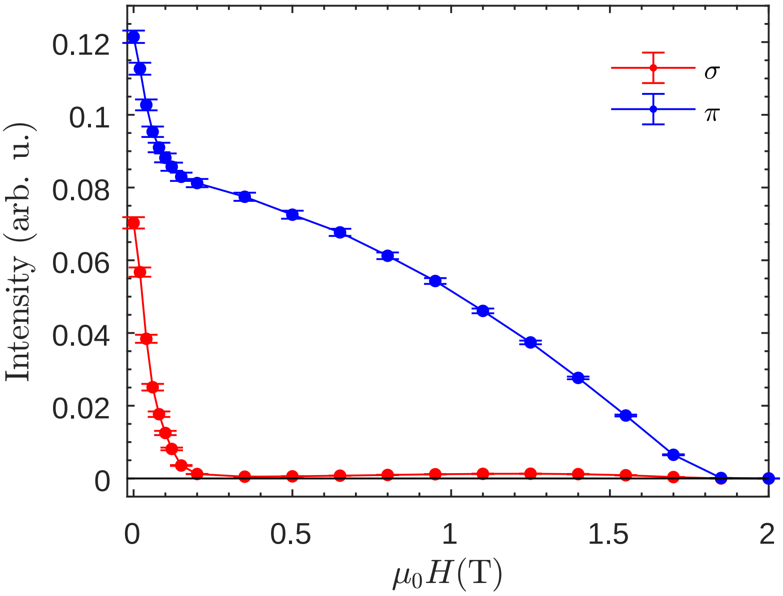

Figure 29: The field dependence ($H \perp c$) of the $(0, 0, 1/2)$ magnetic reflection measured with σ and π incident polarisations. The data were recorded at temperature $T \simeq 5\,\mathrm{K}$ and azimuthal angle $\psi = 0$.

In Fig. 28 I plot the ratio of the scattered intensity with π incident polarisation to that with σ incident polarisation, as a function of ψ. The data show that for all ψ angles the π/σ ratio is greater than 1, consistent with the Γ_5 irrep. Moreover, there is a strong angular dependence of the π/σ ratio which can be described by a three-domain model for the Γ_5 structure, with the in-plane orientation of Eu spins in each domain rotated by $\pm\,120°$ around the c axis relative to the other two domains. The three-domain model was recently found to describe the magnetic order in $\mathrm{EuCd_2As_2}$, which has the same Γ_5 magnetic structure as found here [152]. The domain populations that give the best fit to the data are 18.4%, 73.5% and 8.1%, respectively. This preferential population of one domain could potentially arise from the fact that the angular dependent measurements were performed after the field dependent measurements below T_N.

When a magnetic field is applied in the $\hat{\mathbf{U}}_1$ direction [see Fig. 24(b)], the scattered intensity in the $(0, 0, 1/2)$ reflection initially decreases strongly with field for both incident polarisations, as shown in Fig. 29. At $\mu_0 H \simeq 0.2\,\mathrm{T}$ the intensity measured with σ polarisation has dropped to zero, and intensity with π polarisation has decreased by about one-third relative to zero field. At higher fields, the π intensity

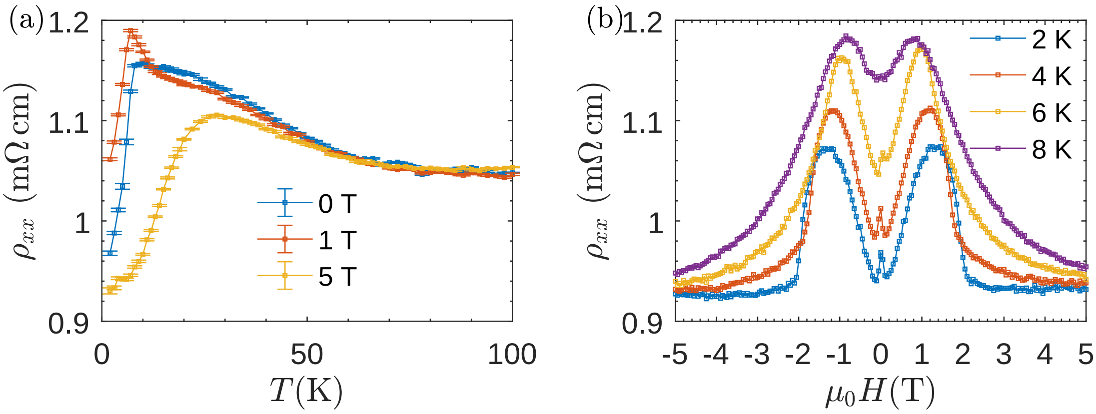

Figure 30: (a) Temperature dependence of the in-plane resistivity ρ_{xx} at three different field strengths ($H \perp c$). (b) Isothermal $\rho_{xx}(H)$ at several temperatures.

continues to decrease, eventually vanishing when $\mu_0 H \simeq 1.8\,\mathrm{T}$, a field close to the critical field H_c at which the magnetisation saturates [see Fig. 26(b)].

The field-dependent behaviour can be understood as follows. Application of small in-plane fields causes the spins in each 120° domain to rotate away from the field while remaining in the plane and antiferromagnetically coupled along the c axis. By the time $\mu_0 H \simeq 0.2\,\mathrm{T}$, the spin component z_1 along the field direction has become zero, so the intensity with σ incident polarisation vanishes and the intensity with π incident polarisation is reduced because only the $\pi \rightarrow \pi'$ channel contributes (Table 3). Fields above 0.2 T induce a FM component along the field direction which saturates at $\mu_0 H \simeq 1.8\,\mathrm{T}$. This canted spin structure can be regarded as a combination of FM order of the z_1 spin components and AFM order of the z_2 spin components. As a result, FM Bragg peaks appear and increase in intensity with increasing field at the expense of the AFM peaks. The effect on the $(0, 0, 1/2)$ peak is to decrease the intensity in the π channel to zero without any change to the intensity in the σ channel, which remains zero.

3.3.3 Magnetotransport

Figure 30(a) plots the in-plane resistivity ρ_{xx} as a function of temperature for three different fields. In zero field there is a sharp drop in ρ_{xx} below T_N, most likely caused by a suppression of spin scattering due to AFM order. At $\mu_0 H = 1\,\mathrm{T}$, ρ_{xx} is slightly peaked around T_N, and the reduction below T_N is less than in zero field. Finally, at

$\mu_0 H = 5\,\mathrm{T}$ the regime of reduced ρ_{xx} extends up to about 25 K.

To help understand the magnetoresistance behaviour I also measured ρ_{xx} as a function of in-plane field at several temperatures. The data are plotted in Fig. 30(b). At $T = 2\,\mathrm{K}$, three distinct features can be identified in $\rho_{xx}(H)$: (i) In the low field regime ($|\mu_0 H| \lesssim 0.2$ T), associated with the rotation of the spins away from the applied field, there is a small drop in ρ_{xx} which could be due to a reduction in spin scattering as the multiple 120° spin domains form into a single domain. (ii) In the intermediate regime (0.2 T $\lesssim |\mu_0 H| \lesssim$ 2 T), there is a peak in ρ_{xx} which ends at the saturation field. The fractional change in $\rho_{xx}(H)$ reaches about 15% at the maximum. This increase in charge carrier scattering is associated with the canted spin structure, as discussed above. (iii) In the high field regime ($|\mu_0 H| > 2\,\mathrm{T}$), the spins are fully polarised and the anomalous resistive phase is fully suppressed. At higher temperatures, the initial low-field drop in ρ_{xx} becomes smaller and vanishes for $T > T_{\mathrm{N}}$, and the region of negative magnetoresistance extends to higher fields consistent with the increase in the saturation field with temperature.

3.3.4 DFT + U Calculations

In this section I discuss the results of *ab initio* electronic structure calculations performed to understand the nature of the electron conduction in the AFM phase of $\mathrm{EuCd_2Sb_2}$. The calculated electron band structure along high symmetry lines in the Brillouin zone, plotted in Fig. 31(a), reveals a low density of electronic states near the Fermi energy, E_{F}. This is consistent with the semimetallic nature of the compound as suggested by transport measurements [133, 137], but contradicts a study of the thermoelectric properties of $\mathrm{EuCd_2Sb_2}$ by Zhang *et al.* [133]. In that study, a large density of states near E_{F} was predicted and was attributed to the flat $4f$ electron bands from the europium species residing at the Fermi energy. In fact, the position of these $4f$ bands depends strongly on the value of the Hubbard U parameter. A choice of $U = 0\,\mathrm{eV}$ will cause the $4f$ bands to lie at E_{F}, as found in Ref. [133]. In my calculations I chose a value of $U = 3.1$ eV. This choice was guided by a recent ARPES measurement performed on a similar material $\mathrm{EuCd_2As_2}$ which places the $4f$ electrons $\sim 2\,\mathrm{eV}$ below the Fermi level [153]. Based on this evidence it is unlikely that the magnetic $4f$ bands contribute significantly to electrical conduction.

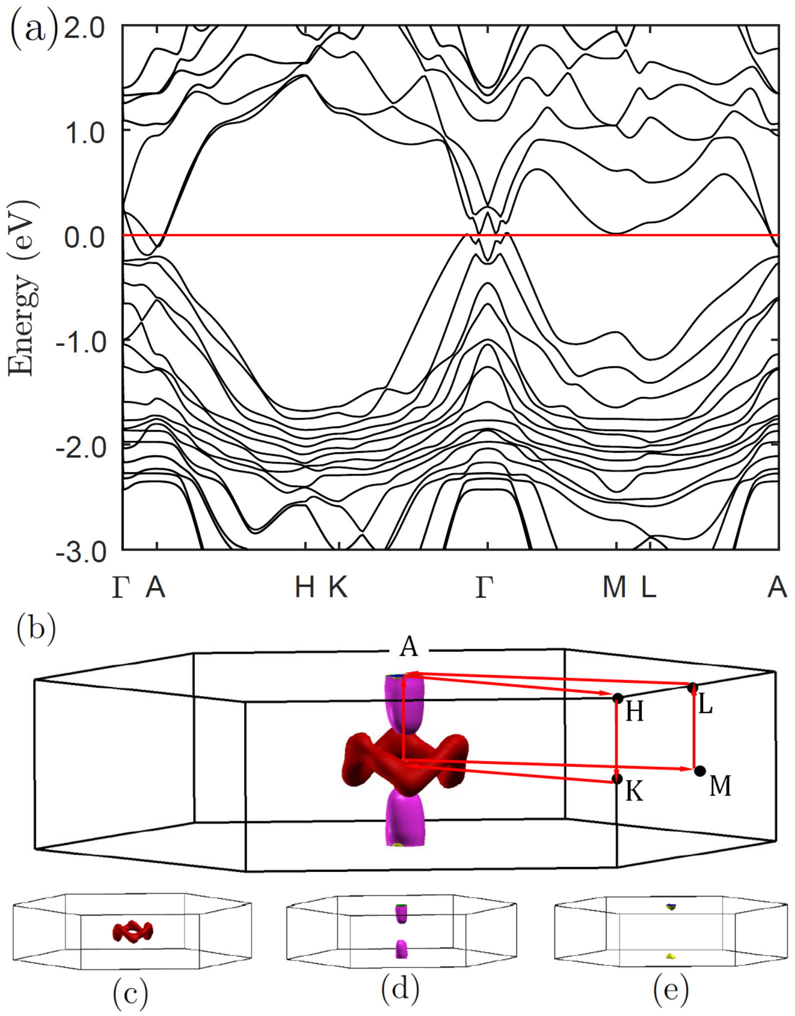

Figure 31: (a) Band structure of $EuCd_2Sb_2$ along the high symmetry lines of the hexagonal Brillouin zone, with the path shown in (b). The Fermi surface of $EuCd_2Sb_2$ in the first Brillouin zone (b) is made up of one hole pocket (c) and two electron pockets (d) and (e). The Fermi pockets have a mixture of Sb $5p$ $J_z = \frac{1}{2}$, Sb $5p$ $J_z = \frac{3}{2}$ and Cd $5s$ $J_z = \frac{1}{2}$ band character. All of these surfaces are two-fold degenerate.

The Fermi surface comprises one electron pocket and two hole pockets, both with mixed Cd $5s$ and Sb $5p$ orbital character [Fig. 31 (b)–(e)]. As mentioned above, the Eu $4f$ states which are responsible for producing the local magnetic moments reside ~ 2 eV below E_{F} [Fig. 32(g)]. This means that the charge carriers in the conducting Cd-Sb double corrugated layer are weakly correlated, and DFT is well suited to calculate the band dispersion in the vicinity of E_{F}.

$EuCd_2Sb_2$ has several ingredients which could lead to non-trivial band topology.

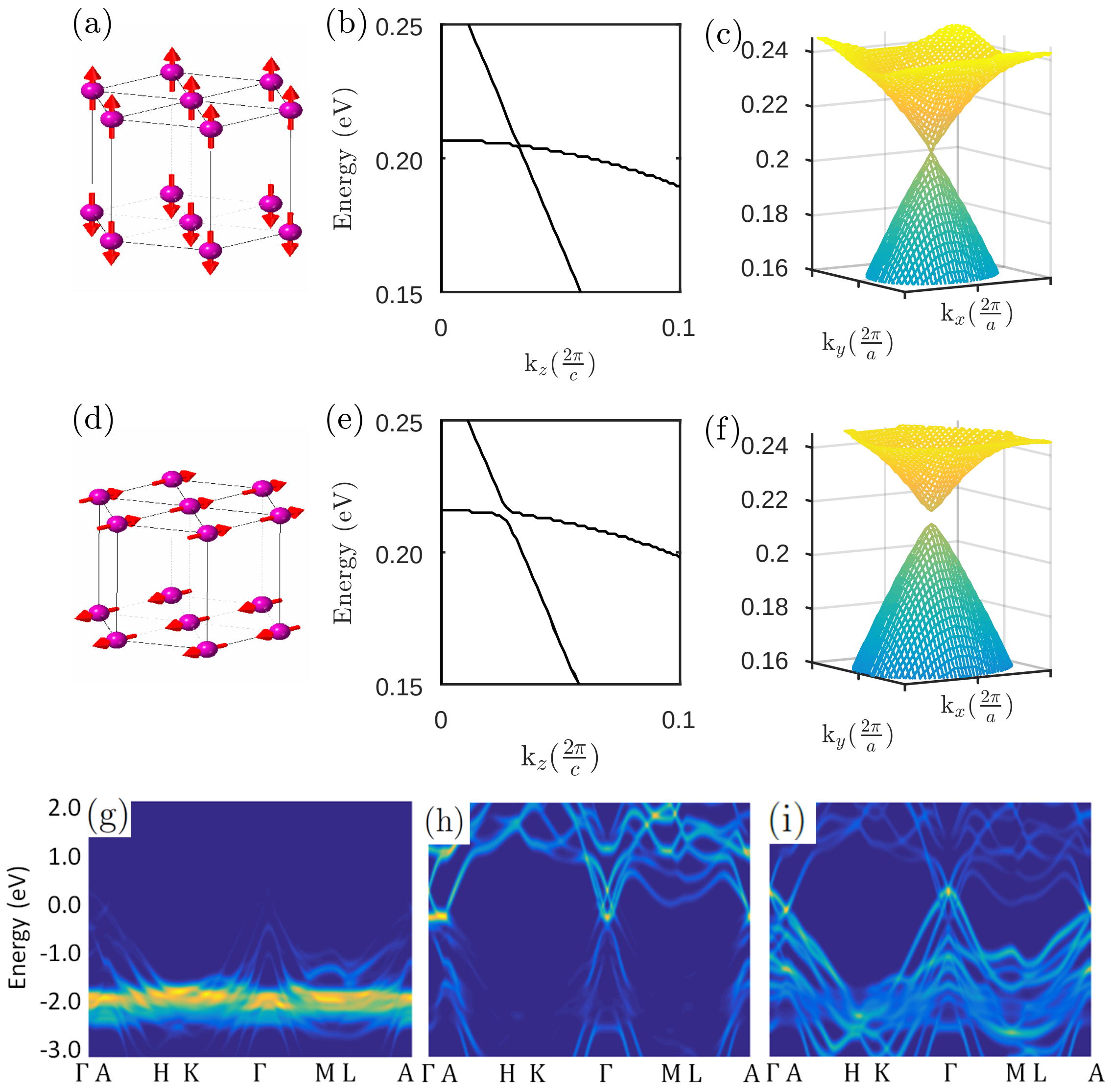

Figure 32: (a)–(f) Magnetic structure, detail of bands along the $\Gamma - A$ high symmetry line, and electronic dispersion in the $k_x - k_y$ plane close to the Dirac point. (a)–(c) Γ_3 magnetic structure. The Γ_3 irrep of the Eu spin structure would preserve the C_3 symmetry along $\Gamma - A$ and afford protection to the Dirac point at $k_z = 0.0324$. (d)–(f) Γ_5 magnetic structure as found here for $EuCd_2Sb_2$. The Γ_5 irrep, on the other hand, breaks this C_3 symmetry and opens up a gap along $\Gamma - A$ and in the $k_x - k_y$ plane. The colour scale is indicative of the weight of the (g) Eu $^2F_{7/2}$, (h) Sb $^2S_{1/2}$ and (i) Sb $^2P_{3/2}$ orbitals. The results of the orbital analysis of the elements in $EuCd_2Sb_2$ suggest that the europium magnetic $4f$ bands do not contribute to the conduction.

First, the heavy masses of Cd and Sb could lead to band inversion due to the large SOC. Second, the three-fold (C_3) symmetry along the Γ–A line in reciprocal space [wave vectors $(0, 0, k_z)$] might protect some accidental band crossings [36]. Third, in the AFM ordered phase, both non-symmorphic time-reversal symmetry and inversion symmetry of the crystal are preserved [154], resulting in a two-fold

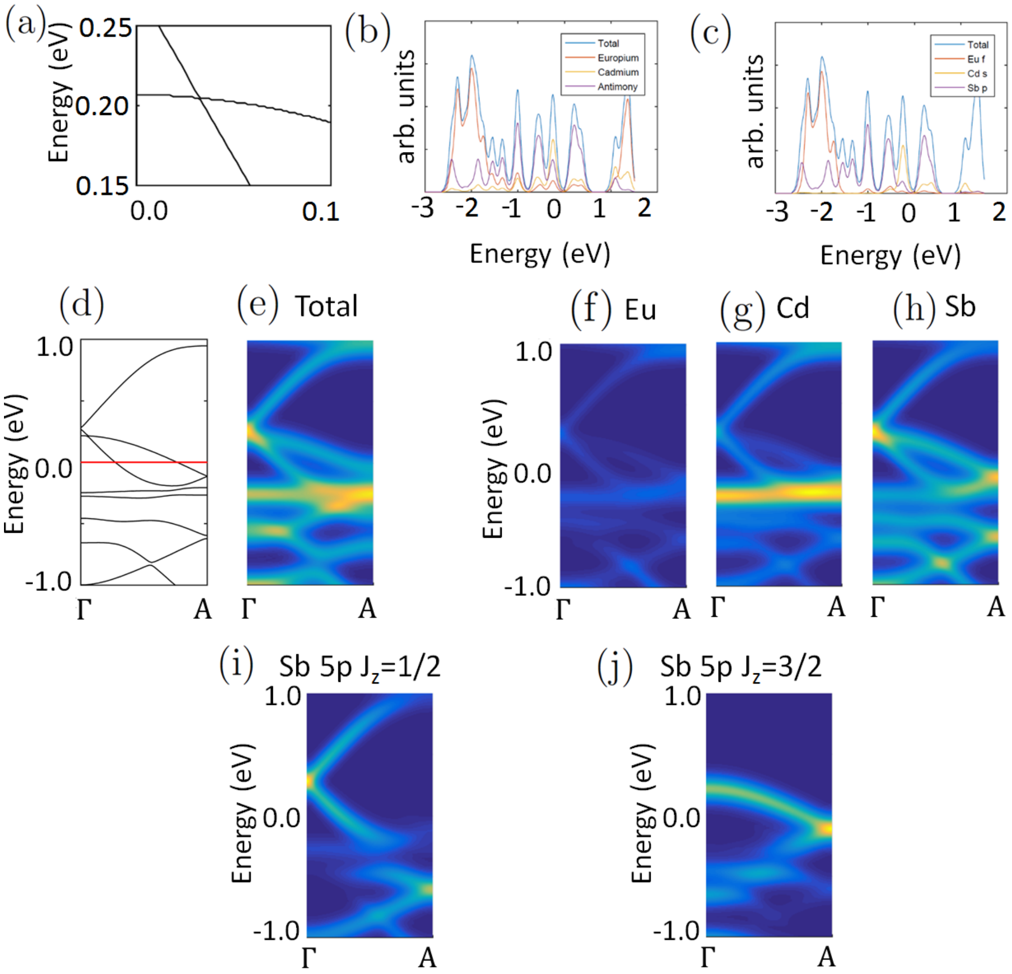

Figure 33: To demonstrate the nature of the (a) band crossing along the $\Gamma - A$ discussed in the text, I plot the density of states and the corresponding contributions from the three constituent elements in (b) from europium, cadmium and antimony. It shows that the main contribution comes from antimony. This is also shown in the band character plot along the $\Gamma - A$ line from the (e) total, (f) europium, (g) cadmium and (h) antimony where the main contribution comes from antimony. (d) shows the band structure spaghetti plot. Furthermore, the main contribution to the bands in (a) are from p orbitals in antimony as shown in the partial density of states plot in (c). (i) and (j) show that the crossing in (a) is between $J_z = \frac{1}{2}$ and $J_z = \frac{3}{2}$.

degeneracy in the electronic bands.

I have identified a gapped band crossing with $\Delta E \sim 0.01$ eV at $k_z = 0.0266\,\mathrm{r.l.u.}$ along the $\Gamma - A$ high symmetry line, $0.215\,\mathrm{eV}$ above E_F [Figs. 32(e) and (f)]. The energy gap arises because for $T < T_\mathrm{N}$ the C_3 symmetry along the $\Gamma - A$ line is broken by the in-plane orientation of the spins in the Γ_5 AFM structure. If, instead, the spins were to point along the c axis, as would occur in the Γ_3 magnetic structure, the linear band crossing would be protected, see Figs. 32(b) and (c). In terms of band structure, the bands which cross derive from the $^2\mathrm{P}_{3/2}$ orbitals of the Sb $5p$ bands with $J_z = \frac{1}{2}$ and $\frac{3}{2}$ (see Fig. 33). In a c axis field J_z remains a good quantum number and so the states which cross belong to different irreducible representations of the C_3 point group. In this case, doubly-degenerate valence and conduction Sb $5p$ bands meet at a four-fold degenerate point in $\mathbf{k}$-space from which the bands disperse linearly, i.e. a Dirac point, as depicted in Figs. 32(b) and 32(c). In $\mathrm{EuCd_2Sb_2}$, on the other hand, we have in-plane spin alignment, so the $J_z = 1/2$ and $3/2$ bands hybridise, forming a gap at the Dirac point.

Given the evidence found here for a coupling between Eu spins and electronic conduction it is possible that the magnetically-induced energy gap at the Dirac point could influence the transport properties of $\mathrm{EuCd_2Sb_2}$. However, there is no evidence that the gapped band crossing in $\mathrm{EuCd_2Sb_2}$ is exactly at E_F, and there are several other bands in the vicinity of E_F which could contribute to the electronic transport (see Fig. 33). Nonetheless, my analysis shows that the symmetry in the spin structure affects features in the band structure of $\mathrm{EuCd_2Sb_2}$, and emphasises the importance of elucidating the orientation of the Eu spins. It also opens up the possibility of realising a magnetic Dirac material in the 122-pnictides via spin structure which preserves the C_3 symmetry. A possible strategy is to find another member of the family which has spins pointing along the c axis. Indeed a similar situation is found in rare-earth half-Heuslers where the nature of the band topology is strongly linked to the spin-orientation: $\mathrm{Eu_{0.5}Ba_{0.5}AgBi}$ is predicted to host Weyl fermions protected by the C_3 symmetry along the $\Gamma - A$ line where the Eu spins point along the c axis; these Weyl points annihilate in the case of EuAgBi where the spins lie in the basal plane [90].

Finally, it is also interesting to compare the physical properties of $\mathrm{EuCd_2Sb_2}$ with those of $EuCd_2As_2$ [152, 154, 155] and $EuZn_2Sb_2$ [129, 156, 157], which are isostructural and also exhibit Eu antiferromagnetic order with similar magnetic ordering temperatures: 9.5 K in $EuCd_2As_2$ and 13.3 K in $EuZn_2Sb_2$. Of these, $EuCd_2As_2$ is a semimetal and $EuZn_2Sb_2$ is a semiconductor with a band gap of around 0.5 eV. A comparison of the band structures reveals a progression in the extent of inversion in the conduction and valence bands. The band inversion is greatest in $EuCd_2Sb_2$, with several bands crossing at E_{F} as shown here, whereas in $EuZn_2Sb_2$ there is no band crossing. In $EuCd_2As_2$ the bands touch at a Dirac point in $\mathbf{k}$-space, which becomes gapped for $T < T_{\mathrm{N}}$ for the same reason as described here for $EuCd_2Sb_2$. These band crossing features can be understood from the relative sizes of the spin-orbit coupling in the double-corrugated conducting layers, which increases in the order $EuZn_2Sb_2$ to $EuCd_2As_2$ to $EuCd_2Sb_2$. This suggests that a desired level of band crossing can be achieved in the europium-based 122-pnictide by control of the chemical composition.

3.4 Conclusion

I have determined that the magnetic propagation vector in $EuCd_2Sb_2$ is $(0, 0, 1/2)$, and shown unambiguously that the moments lie in the (001) plane. I have also established how the magnetic structure is changed by an in-plane magnetic field, and find that features observed in the magnetoresistance correlate closely with field-induced changes in the magnetic structure. My results show that a coupling exists between localised Eu spins and electron transport in $EuCd_2Sb_2$. Based on DFT calculations I predict that for $T < T_{\mathrm{N}}$ there exists a gapped Dirac point close to the Fermi level, and although it remains to be seen to what extent this feature may influence the charge transport in $EuCd_2Sb_2$, my findings suggest that non-trivial band topologies could be induced by magnetic order in the wider family of Eu-based hexagonal 122-pnictides.

CHAPTER 4

An ideal Weyl semimetal induced by magnetic exchange: $EuCd_2As_2$

In this chapter, I present theoretical and experimental evidence that $EuCd_2As_2$, in magnetic fields greater than 1.6 T applied along the c axis, is a Weyl semimetal with a single pair of Weyl nodes. *Ab initio* electronic structure calculations, verified at zero field by angle-resolved photoemission spectra, predict Weyl nodes with wavevectors $\mathbf{q} = (0, 0, \pm 0.03) \times 2\pi/c$ at the Fermi level when the Eu spins are fully aligned along the c axis. Shubnikov–de Haas oscillations measured in fields parallel to c reveal a cyclotron effective mass of $m_\mathrm{c}^* = 0.08\, m_\mathrm{e}$ and a Fermi surface of extremal area $A_\mathrm{ext} = 0.24\,\mathrm{nm}^{-2}$, corresponding to 0.1% of the area of the Brillouin zone. The small values of m_c^* and A_ext are consistent with quasiparticles near a Weyl node. The identification of $EuCd_2As_2$ as a model Weyl semimetal opens the door to fundamental tests of Weyl physics.

---

4 An ideal Weyl semimetal induced by magnetic exchange: $EuCd_2As_2$

4.1 Introduction

Weyl semimetals (WSMs) exhibit exceptional quantum electronic transport due to the presence of topologically-protected band crossings called Weyl nodes [10, 11]. The nodes come in pairs with opposite chirality, but their number and location in momentum space is otherwise material specific.

Weyl nodes are distinct from other topological features of electron band structures in several respects, including (i) the bulk bands that cross at a Weyl node are non-degenerate, (ii) the associated Weyl fermions have a definite chirality, and (iii) the Weyl nodes are protected against perturbations that do not couple the nodes [10, 11, 61]. Moreover, the individual nodes within a pair act as a source and a sink of Berry curvature, a topological property of the electronic wavefunctions which relates directly to several anomalous transport phenomena [11, 158].

Weyl semimetal phases in crystals require either broken spatial inversion symmetry, or broken time-reversal symmetry (TRS), or both. There are a number of experimental realisations of the first type (with broken inversion symmetry only), especially in the TaAs structural family [36, 37, 38, 42, 159], but magnetic WSMs (with broken TRS) are still rare. The few known candidates are complicated by multiple pairs of Weyl nodes and/or by extra (non-topological) Fermi surface pockets which shroud the Weyl nodes [61, 89, 98, 110, 155, 160]. Magnetic WSMs are important for fundamental studies of Weyl fermions because it is possible for such systems to have only a single pair of Weyl nodes which, due to inversion symmetry, are guaranteed to be at the same energy and so have a vanishing density of states. By contrast, WSMs formed by breaking inversion symmetry (but with TRS) have a minimum of four nodes which are in general separated in energy.

Following the initial discoveries [36, 37, 38] there is now a need for better material realisations of WSMs, ideally comprising a single pair of Weyl nodes located at or very close to the Fermi level and in an energy window free from other overlapping bands. Here I propose the layered intermetallic $EuCd_2As_2$ [152, 155] to be such a system. I show that Weyl nodes in $EuCd_2As_2$ are magnetically-induced via exchange

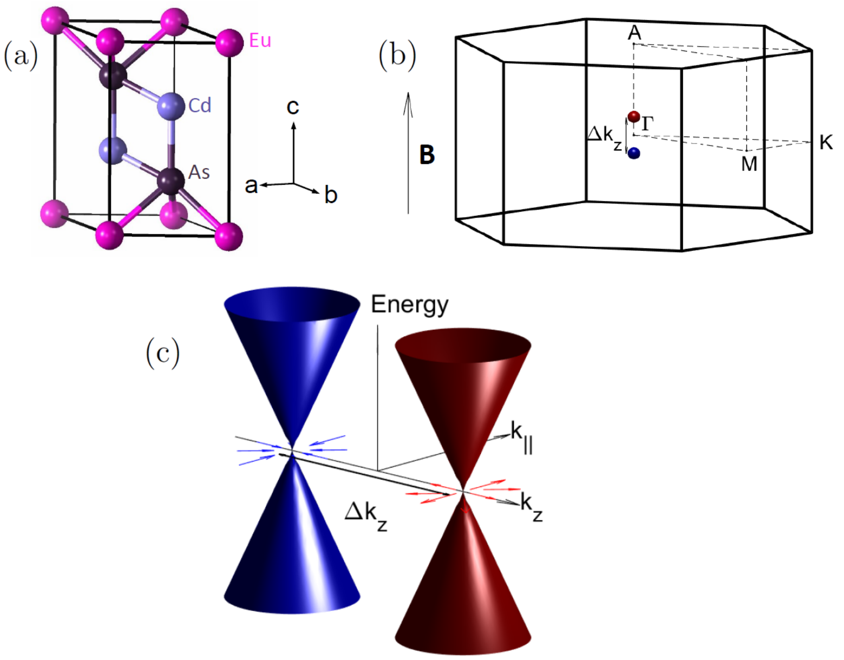

Figure 34: Crystal structure of $EuCd_2As_2$ and location of Weyl nodes in the Brillouin zone. (a) The trigonal unit cell for the space group $P\bar{3}m1$ (No. 164). The Weyl fermions predominantly occupy orbitals in the double-corrugated Cd_2As_2 layers, which are sandwiched between the Eu layers [152]. (b) The Weyl nodes lie along the A–Γ–A high symmetry line and are separated by Δk_z (not shown to scale). (c) In the fully polarised state, singly-degenerate conduction and valence bands meet at a pair of Weyl nodes from which the bands disperse linearly. The nodes act as a source and sink of Berry curvature and have distinct chirality which depends on the direction of the field applied along the c axis.

coupling, emerging when the Eu spins are aligned by a small external magnetic field applied along the c axis.

4.2 Methods and preliminary data

4.2.1 Single crystal X-ray diffraction

The bulk single crystals of $EuCd_2As_2$, which has a trigonal crystal structure [Fig. 34(a)] containing alternating layers of Eu^{2+} and $[Cd_2As_2]^{2-}$ [138], were grown by the NaCl/KCl flux method described in Ref. [131] by D. Y. Yan and Y. G. Shi.[16] The

---

[16] Beijing National Laboratory for Condensed Matter Physics, Institute of Physics, Chinese Academy of Sciences, Beijing 100190, China.

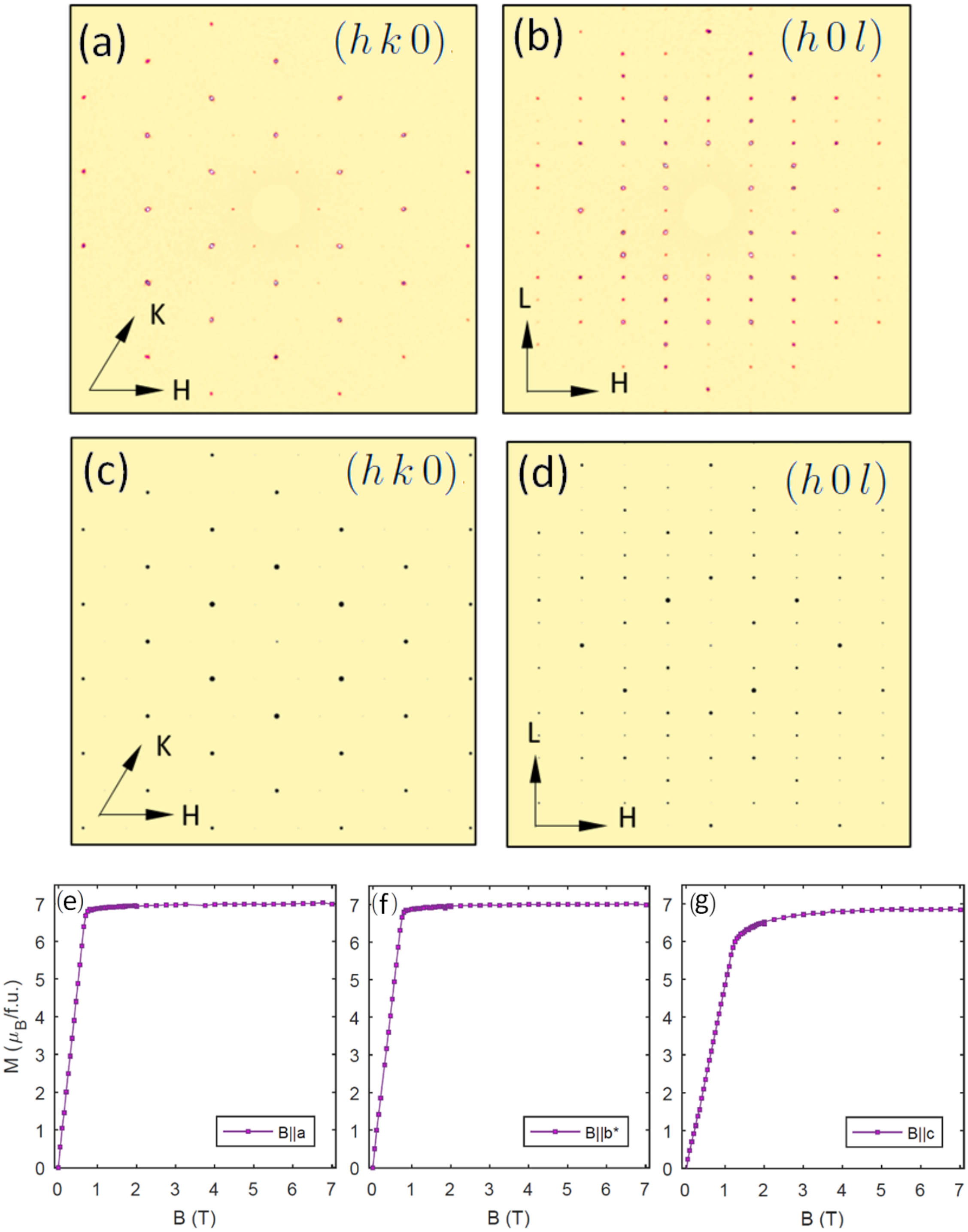

Figure 35: (a)-(d) X-ray diffraction intensity maps in different reciprocal space planes for single crystalline $EuCd_2As_2$. (e)-(g) The magnetisation data for single crystalline $EuCd_2As_2$ at T=2 K.

crystal structure and crystallographic quality of the flux-grown $EuCd_2As_2$ single crystals were checked by me on a 6-circle X-ray (Mo, K_α) diffractometer (Oxford Diffraction). Figs. 35 (a) and (b) present the scattered intensities in the $(h\,k\,0)$ and

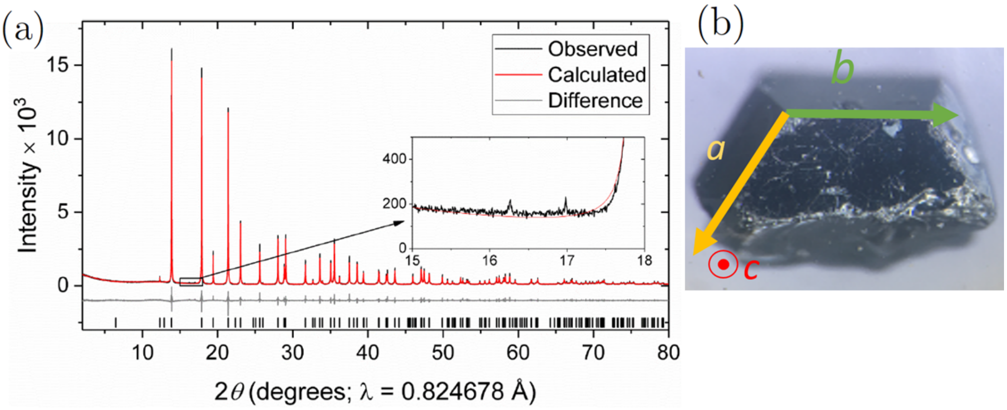

Figure 36: (a) Synchrotron X-ray powder diffraction pattern for $EuCd_2As_2$. Rietveld plot of the $EuCd_2As_2$ sample with inset to show the two largest peaks not indexed by the $EuCd_2As_2$ phase. The X-ray powder diffraction data were collected at room temperature with the MAC detector on the I11 beamline. (b) Image of a flux-grown crystal of dimensions ($2.62 \times 1.92 \times 1.25$ mm^3) with the corresponding crystal axes.

$(h\,0\,l)$ planes, respectively. Figs. 35 (c) and (d) are the corresponding calculated reciprocal space maps. The intensity distribution and the pattern of experimental Bragg peaks in panels (a), (b) agree well with those in the calculated maps in panels (c), (d). Of the 956 detected Bragg reflections, 98.7% fit with the $P\bar{3}m1$ space group (No. 164), in agreement with previous studies [131, 138, 152, 155]. The flux-grown crystals have natural facets that reflect the underlying hexagonal symmetry, as shown in Fig. 36(b). The direction of the corresponding crystal axes, a, b and c, was identified using a laboratory 6-circle X-ray diffractometer (Oxford Diffraction). The axes in Fig. 36(b) correspond to that in the crystal structure in Fig. 34(a).

4.2.2 Magnetisation

Magnetisation measurements of single crystalline $EuCd_2As_2$, which displays A-type AFM order with in-plane Eu moments, were performed on a SQUID magnetometer (Quantum Design) at 2 K in fields up to 7 T. The curves in Figs. 35 (e), (f) and (g) correspond to measurements in field directions $B||a$, $B||b^*$ and $B||c$ respectively. In all field directions, the saturated moment is M_{sat} 7 μ_B/f.u., which is consistent with the expected moment for fully divalent Eu^{2+} ($4f^7$, S = 7/2, L = 0). For $B||a$ and b^*, the Eu moments fully saturate at $B \sim 0.8$ T, whereas for B_c, the coercive field

Table 4: Structural parameters obtained from Rietveld refinement against powder X-ray diffraction data collected at room temperature using the MAC detector on the I11 beamline. The lattice parameters are $a = 4.44204(2)$Å; $c = 7.33071(5)$ Å; unit cell volume = 125.269(1) Å^3; space group = $P\bar{3}m1$; $\chi^2 = 1.767$. * Not refined.

Site	x	y	z	Occupancy	U_{11} [Å^2]	U_{22} [Å^2]	U_{33} [Å^2]
Eu	0	0	0	1*	0.0147(8)	U_{11}	0.0093(7)
Cd	1/3	2/3	0.6332(1)	1*	0.0163(8)	U_{11}	0.0093(7)
As	1/3	2/3	0.2474(2)	1*	0.0116(8)	U_{11}	0.0109(8)

is ~ 1.6 T. These results agree with the magnetometry measurements reported in Refs [131, 138, 152].

4.2.3 Powder X-ray diffraction

For detailed structural analysis I cleaved and ground a small $EuCd_2As_2$ crystal with an approximate 1:1 volume ratio of grounded glass (in order to minimise absorption and preferred orientation effects). This powder was then loaded into a 0.5 mm diameter borosilicate capillary. The capillary was measured using synchrotron powder X-ray diffraction using the MAC detector on the I11 beamline at the Diamond Light Source, Didcot UK by Jack Blandy.[17] The wavelength of the X-ray radiation was 0.824678 Å. The powder X-ray diffraction data was analysed by Rietveld refinement using TOPAS academic, version [161] by Blandy. The Rietveld plot of the powder diffraction data is shown in Fig. 36(a). The sample was found to be ~99% pure hexagonal $EuCd_2As_2$. Two or three very small peaks are not indexed by the $EuCd_2As_2$ model. These peaks most likely arise from a small Eu_xO_y or Eu_xAs_y impurity (there are a few possible polymorphs). There is no trace of any Cd_3As_2 impurity phase. When allowed to vary, each of the atomic site occupancies converged to 100% within the error. Therefore, in the final fit the occupancies were fixed at 100%. The refined structural parameters, listed in Table 4, are consistent with literature data [131].

---

[17] Department of Chemistry, University of Oxford, Inorganic Chemistry Laboratory, Oxford, OX1 3QR, UK.

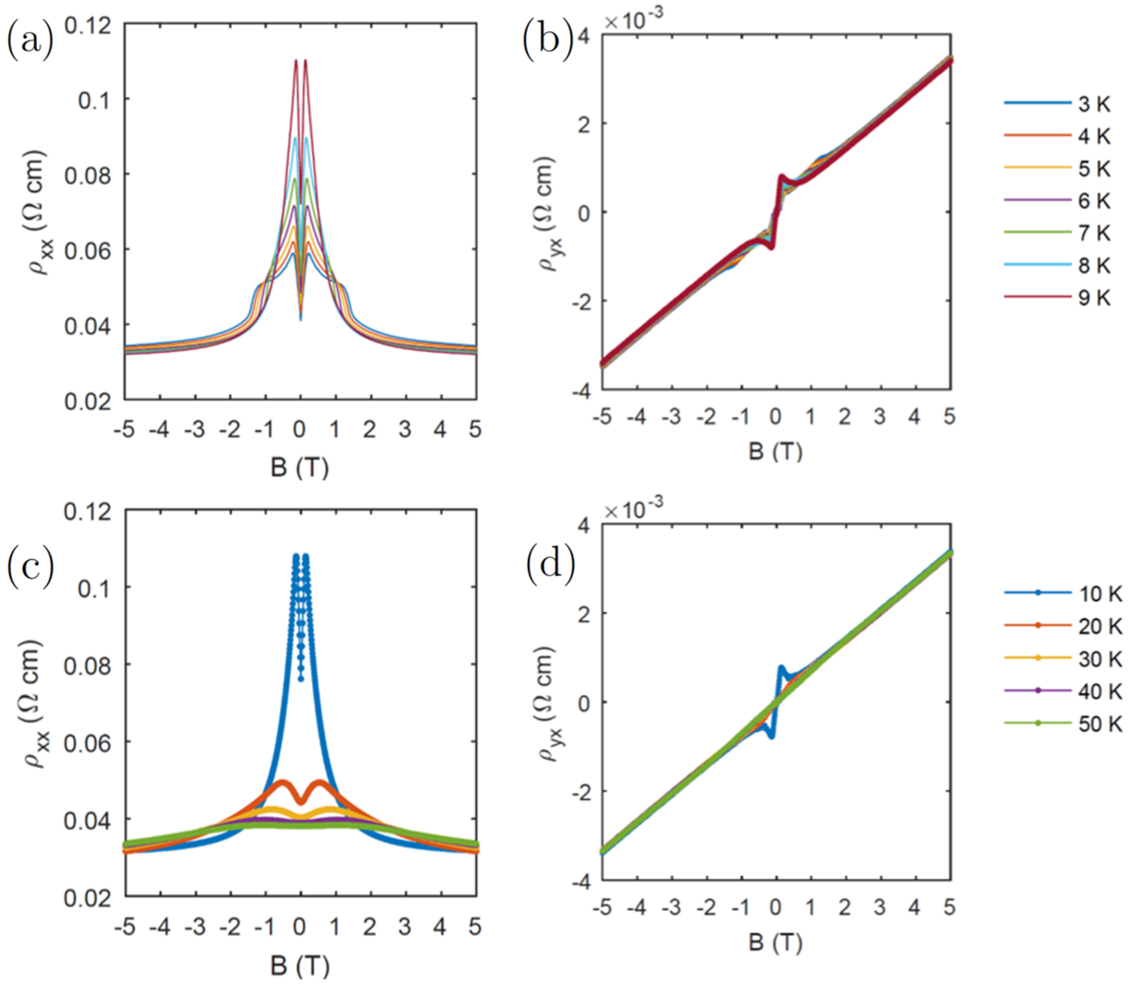

Figure 37: Longitudinal and Hall resistivity of $EuCd_2As_2$ at various temperatures with $B||c$. (a), (c) The longitudinal resistivity at various temperatures below and above T_N respectively. (b), (d) Similarly for the Hall resistivity.

4.2.4 Low-field magnetotransport

Low field ($\mu_0 H < 16$ T) magnetotransport measurements were performed by a five-probe method on a 14 T PPMS (Quantum Design) with $B||c$. The crystal was shaped into a Hall bar with dimensions of $0.91 \times 0.33 \times 0.056$ mm^3. Figs. 37 (a)–(d) show the symmetrised in-plane longitudinal and Hall resistivities, ρ_{xx} and ρ_{yx}, at various temperatures above and below T_N. Below T_N, the longitudinal resistivity peaks in an applied field of ~ 0.2 T and decreases at higher field strengths, as shown in Fig. 37(a). The resistivity peak increases with temperature up to T_N and is then suppressed at higher temperatures as shown in Fig. 37(c). This is in agreement with earlier magnetotransport studies of $EuCd_2As_2$ [152]. Above T_N, the Hall resistivity increases linearly with applied field as shown in Fig. 37(d). As the sample is cooled

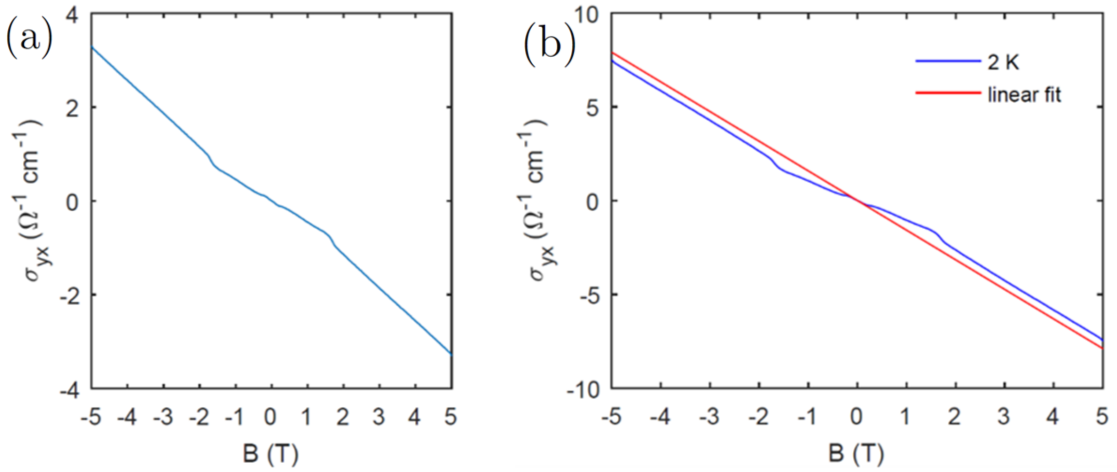

Figure 38: (a) The in-plane Hall conductivity of EuCd$_2$As$_2$ with $B||c$ is obtained by inverting the resistivity matrix. (b) An anomalous component to the Hall conductivity above the linear background (in red) is saturated above the coercive field ($B > B_c$). The anomalous component of the Hall conductivity is obtained by subtracting $\sigma_{yx}(B)$, with the linear background and shown in Fig. 44(a).

below T_{N}, an anomalous feature (-2 T$< B <$ 2 T) above the linear background develops as shown in Fig. 37(b). This deviation from the linear background is most pronounced at ± 0.2 T.

The in-plane conductivity, $\sigma_{yx}(B)$, obtained by inverting the resistivity matrix is given by, $\sigma_{yx} = -\frac{-\rho_{yx}}{\rho_{xx}^2+\rho_{yy}^2}$, and is shown in Fig. 38(a). In the measured field range with $B > B_c$, $\rho_{xx}(B)$ is approximately constant [Fig. 37(a) and (b)] and $\rho_{yx} << \rho_{xx}$. Therefore the normal part of σ_{yx} is approximately linear in B. Given this, a linear background was subtracted from $\sigma_{yx}(B)$ to give $\sigma_{yx}^{AHE}(B)$ in Fig. 44(a).

4.2.5 High-field magnetotransport

High-field magnetotransport measurements were performed at the HFML in Nijmegen (up to 37 T) and at the NHMFL in Tallahassee (up to 45 T) using an ac four-probe technique by Matt Bristow and Pascal A. Reiß[18] respectively. Fig. 39(a) shows the in-plane resistivity measured on one such crystal with dimensions of $0.5 \times 0.2 \times 0.085$ mm^3, at HFML at 1.4 K and in fields up to 37 T with $B||c$. The resistivity displays approximately 3 periods of Shubnikov—de Haas (SdH) quantum oscillations. To remove the magnetoresistance background and extract the

---

[18] Department of Physics, University of Oxford, Clarendon Laboratory, Oxford, OX1 3PU, UK.

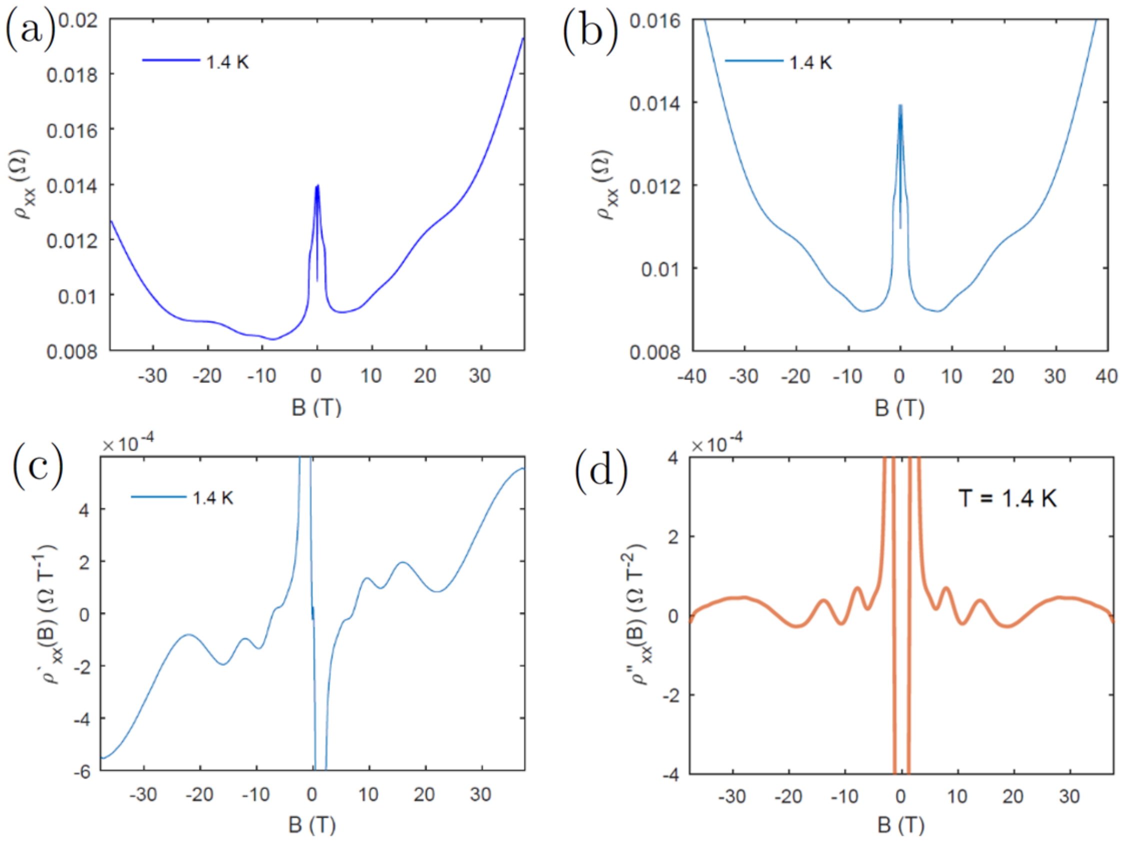

Figure 39: (a)–(d) Shubnikov–de Haas oscillations in magnetotransport data measured up to 37 T. (a) In-plane resistivity, $\rho_{xx}(B)$, as function of magnetic field at 1.4 K with $B||c$. (b) Symmetrised data. By plotting the (c) first and (d) second derivatives with respect to B, namely $\rho'_{xx}(B)$ and $\rho''_{xx}(B)$, I am clearly able to observe the peaks and valleys of the quantum oscillations.

information about the oscillatory spectrum, I (i) symmetrised the data as shown in Fig. 39(b), (ii) took the first and second derivatives of the symmetrised data as shown in Figs. 39(c)-(d), (iii) found the peaks and valleys of these oscillations, and (iv) calculated the gradient of the slope of the Landau fan plot as shown in Fig. 43(f). Note, however, that if integers are assigned to the maxima rather than the minima in ρ_{xx}, as prescribed in Ref. [162], then the value of F, the frequency of the SdH oscillation, would be unchanged but the the intercept related to the phase of the oscillation will change. In addition, the first Landau level would be at 20 T not 30 T.

Fig. 40(a) shows the raw in-plane resistivity data obtained from the 45 T Bitter magnet at the NHMFL at 1.7 K and 2.8 K with $B||c$. I augment the high-field

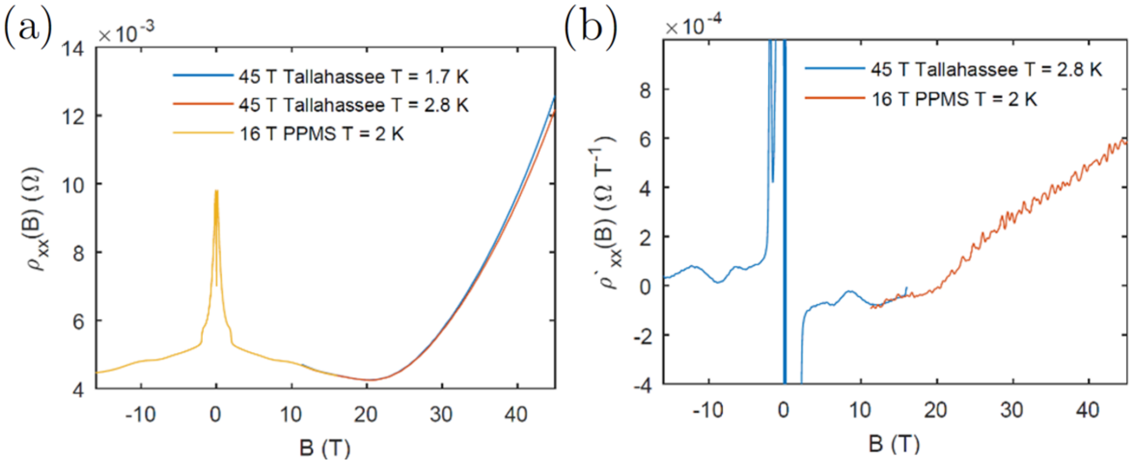

Figure 40: Magnetotransport data measured up to 45 T. (a) In-plane resistivity, $\rho_{xx}(B)$, as a function of magnetic field with $B||c$ measured at T = 1.7 K and T = 2.8 K for 11 T $< B <$ 45 T and T = 2 K for -16 T $< B <$ 16 T. (b) The first derivative of $\rho_{xx}(B)$ with respect to B.

(11 T $< B <$ 45 T) data with low-field (-13 T $< B <$ 13 T) measurements performed on a 14 T PPMS (Quantum Design). In the same way, I plot the first derivative of $\rho_{xx}(B)$, in Fig. 40(b).

Prior to these high-field experiments, the resistivity of the as-grown single crystal samples were measured on the 16 T by me. SdH oscillations in the resistivity of these flux-grown $EuCd_2As_2$ crystals was observed across numerous samples. The frequency of these oscillations are listed in Table 5. As there is only 1 period of oscillation for measurements below 16 T, there is a larger uncertainty in the estimate of the oscillation frequency obtained in the data up to 16 T compared to that which is obtained in the data up to 37 T. Nonetheless, the estimated frequencies from the different instruments are consistent within the experimental errors.

4.2.6 DFT Calculations

Initial density functional theory (DFT) calculations of the electronic structure of $EuCd_2As_2$ were performed on the Quantum Espresso suite. Apart from the different atoms, lattice parameters and pseudopotentials, the methods employed for $EuCd_2As_2$ is identical to that for $EuCd_2Sb_2$ which is described in Chapter 3. Sub-

Table 5: Frequency of SdH oscillations measured on different $EuCd_2As_2$ crystals from the same batch.

Sample	Frequency [T]	Remarks
DF2	25(3)	Nijmegen measured to 37 T
DF2	23(7)	16 T PPMS
CD13	23(2)	16 T PPMS
BQ1	23(5)	16 T PPMS
CL1	21(5)	16 T PPMS
CQ1	22(4)	16 T PPMS
CQ5	20(7)	16 T PPMS
CQ7	19(5)	16 T PPMS

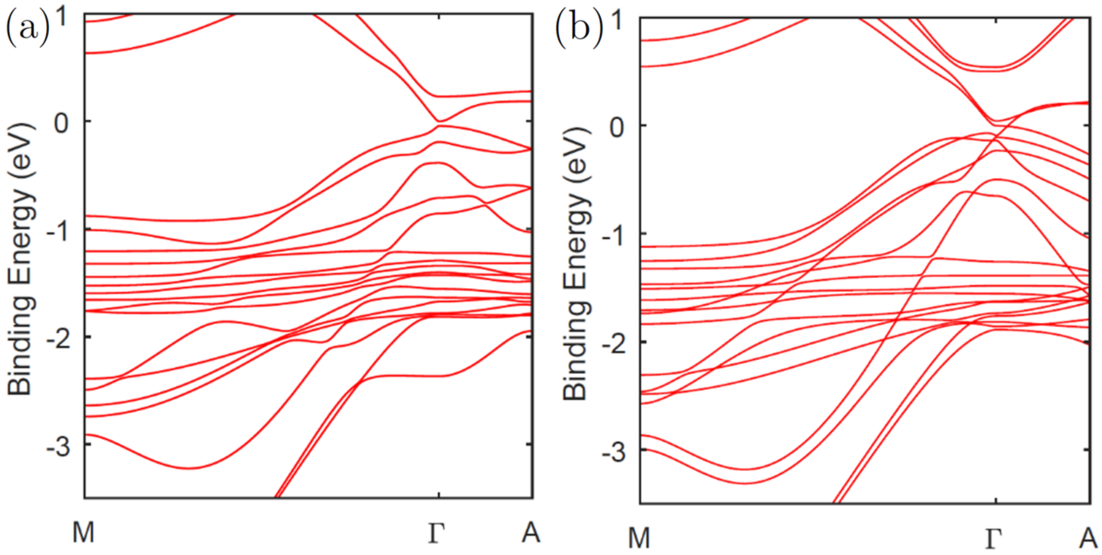

Figure 41: The calculated electronic band structure for $EuCd_2As_2$. (a) The calculated electronic band structure for $EuCd_2As_2$ for the ground state magnetic structure displays a gap at the Γ point. (b) When the moments are fully pointing along the c axis, this gap is closed at a Weyl point along the $\Gamma - A$ high symmetry line.

sequent DFT studies were performed by Maia G. Vergniory,[19] who used the Vienna *Ab initio* Simulation Package (VASP) [163, 164]. The exchange correlation term is described according to the Perdew-Burke-Ernzerhof (PBE) prescription together

---

[19] Donostia International Physics Center, 20018 Donostia-San Sebastian, Spain; IKERBASQUE, Basque Foundation for Science, Maria Diaz de Haro 3, 48013 Bilbao, Spain.

with projected augmented-wave pseudopotentials [145]. For the self-consistent calculations a 10×10×5 k-points mesh was used. The kinetic energy cut-off was set to 550 eV. The spin-polarised band structures are calculated within GGA+U, with the value of U chosen to be 5 eV. As the lattice parameters of $\mathrm{EuCd_2As_2}$ for $T < T_\mathrm{N}$ has not been measured, the cell parameters used in the DFT calculation were estimates based on the powder neutron diffraction work by May *et al.* on $\mathrm{AZn_2Sb_2}$ (A = Ca, Yb) [130], which is isostructural to $\mathrm{EuCd_2As_2}$. In $\mathrm{AZn_2Sb_2}$, the a and c lattice parameters decreased by 0.2% and 0.5% respectively when the sample was cooled from 300 K to 10 K. Hence, I estimated that the measured $\mathrm{EuCd_2As_2}$ lattice parameters at 300 K, which are $a = 0.4442$ nm and $c = 0.7331$ nm, changes to $a = 0.443$ nm and $c = 0.729$ nm at 10 K.

4.2.7 ARPES

ARPES measurements were performed at the high-resolution branch line of the beamline I05 at the Diamond Light Source, UK [165]. I accompanied Niels B. M. Schröter,[20] who was leading the ARPES study, on three of the four beamtimes where the electronic spectrum of $\mathrm{EuCd_2As_2}$ was measured. The sample preparation and the analysis of the results were done by the both of us. To compensate for the effect of selection rules that suppress the photoemission signal from certain bands under certain light polarisations, the intensities from two measurements taken at linear-vertical and linear-horizontal polarisation (with respect to the sample normal) were combined. Measurements were performed with a Scienta R4000 analyser at a photon energy of 130 eV, which approximately corresponds to the $k_z = \Gamma$ measurement plane, at a temperature of $T \sim 5$K.

4.3 Results

In summary, the preliminary data shows that the magnetisation, magnetotransport and crystallographic parameters of the $\mathrm{EuCd_2As_2}$ crystals are fully consistent with earlier reports [131, 152, 155]. The europium ions carry a localised magnetic moment with spin $S = 7/2$ and zero orbital angular momentum. Below $T_\mathrm{N} = 9.5\,\mathrm{K}$ the spins order in an A-type antiferromagnetic structure in which the spins form ferro-

---

[20] Paul Scherrer Institute, WSLA/202, 5232 Villigen PSI, Switzerland.

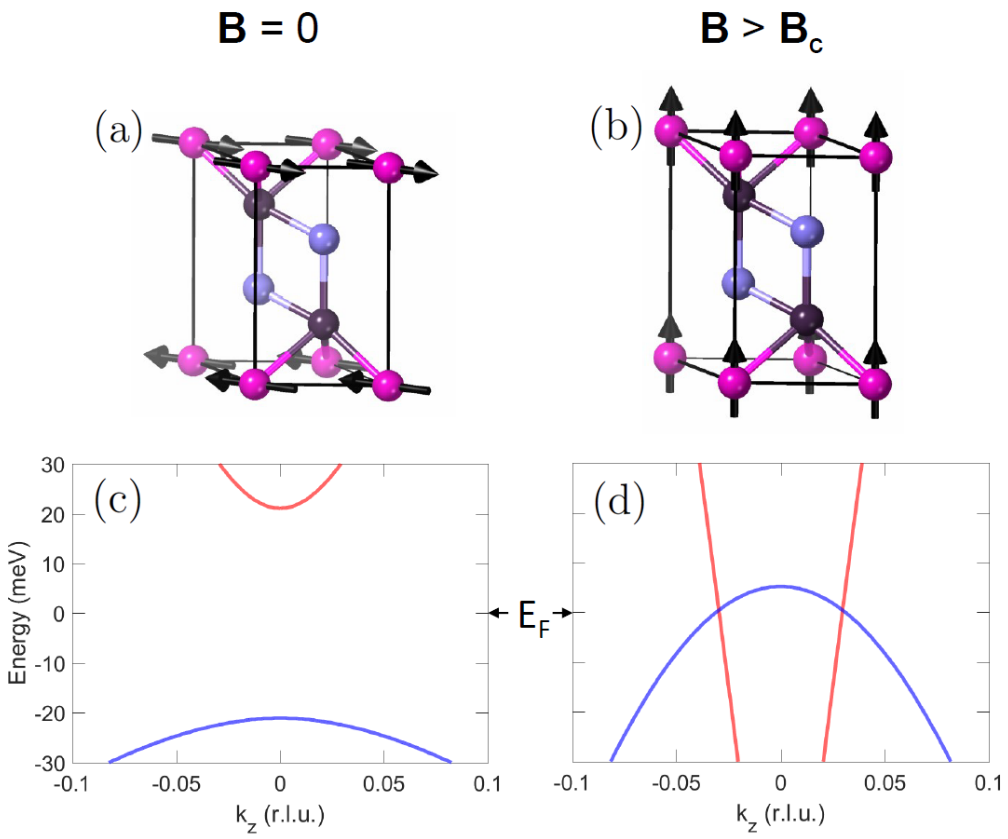

Figure 42: Exchange-induced Weyl nodes in $EuCd_2As_2$. (a), (c) In zero field, the Eu spins order in an A-type antiferromagnetic structure at $T < T_N$, with the spins lying in the *ab* plane. The corresponding band structure is gapped at Γ. (b), (d) The Eu moments can be fully polarised along the c axis in a small coercive field ($B > B_c$), lifting the double degeneracy of the bands and creating a pair of Weyl nodes along Γ–A, at $k_z = 0.03$ r.l.u.

magnetic layers which stack antiferromagnetically along the c axis [Fig. 42(a)][152]. A relatively small magnetic field ($B_c = 1.6\,\mathrm{T}$ at $T = 2\,\mathrm{K}$ for $B \parallel c$) can be used to coerce the Eu spins into a fully aligned state [152]. $EuCd_2As_2$ is metallic at temperatures down to $T \sim 80\,\mathrm{K}$, but for lower temperatures the resistivity increases to a sharp maximum at T_N before falling again at lower temperatures. This behaviour has been interpreted as being due to scattering of conduction electrons by fluctuations of localised Eu magnetic moments which are exchange-coupled to the Cd and As orbitals [152, 155].

In previous *ab initio* electronic structure calculations, where spins in the AFM state were found to be aligned with the c axis, $EuCd_2As_2$ was predicted to host a band inversion of doubly-degenerate As $4p$ and Cd $5s$ states near the Fermi level (E_F), producing a crossing along the $\Gamma - A$ line protected by C_3 symmetry [152, 154]. Experimentally [152] (and in more recent calculations [166]) the spins are in fact found to point perpendicular to the c axis [Fig. 42(a)] breaking C_3 symmetry, so an avoided crossing at finite momentum would be expected.

The new *ab initio* calculations of the electronic structure of $\mathrm{EuCd_2As_2}$ in which the spins are configured in the AFM state [Fig. 42(a)] and in the ferromagnetic state with Eu spins fully aligned along the c axis [Fig. 42(b)] are presented in Figs. 41(a), (b) and 42(c), (d). In the AFM state, Vergniory found for a wide range of parameters a small direct gap at Γ [Figs. 41(a) and 42(c)] which is mostly insensitive to the orientation of the spins. When the Eu spins are fully spin-polarised along the c axis the double degeneracy is lifted, and a single pair of Weyl nodes appears at E_F with no other Fermi surface pockets in the Brillouin zone [Figs. 41(b) and 42(d)]. These Weyl nodes lie along the Γ−A high symmetry line [see Fig. 34(b)] at wavevector $\vec{k} = (0, 0, k_0)$ with $k_0 \simeq \pm 0.03 \times 2\pi/c = \pm 0.26\,\mathrm{nm}^{-1}$. $\mathrm{EuCd_2As_2}$ in a small magnetic field applied along the c axis, therefore, is predicted to be a Weyl semimetal with a single pair of Weyl nodes located at E_F.

The band splitting in the saturated phase is found to be $\sim$100 meV, which is two orders of magnitude larger than the Zeeman splitting in the saturation field B_c. From this I can conclude, first, that the calculations, which include exchange but no Zeeman interaction, are a good representation of the experimental situation in which a small magnetic field is used to align the Eu spins, and second, that the existence of the Weyl nodes is driven by exchange coupling to the Eu spins.

In order to validate the *ab initio* predictions I discuss the ARPES and quantum oscillations measurements. ARPES data on $\mathrm{EuCd_2As_2}$ for $T < T_\mathrm{N}$ and zero applied magnetic field are presented in Fig. 43(a), (c). These k–E plots are for k along the M–Γ–M path [see Fig. 34(b)] and show steeply dispersing bands approaching E_F. Qualitatively, the spectra are in good agreement with the *ab initio* band structure [Figs. 43(b) and (d)] calculated for the observed AFM state with spins lying in the plane. The agreement is best when E_F is shifted slightly downward by about 50 meV, which indicates that the sample is very slightly hole-doped.

The quantum oscillations measurements are summarised in Figs. 43(e)–(g). Fig-

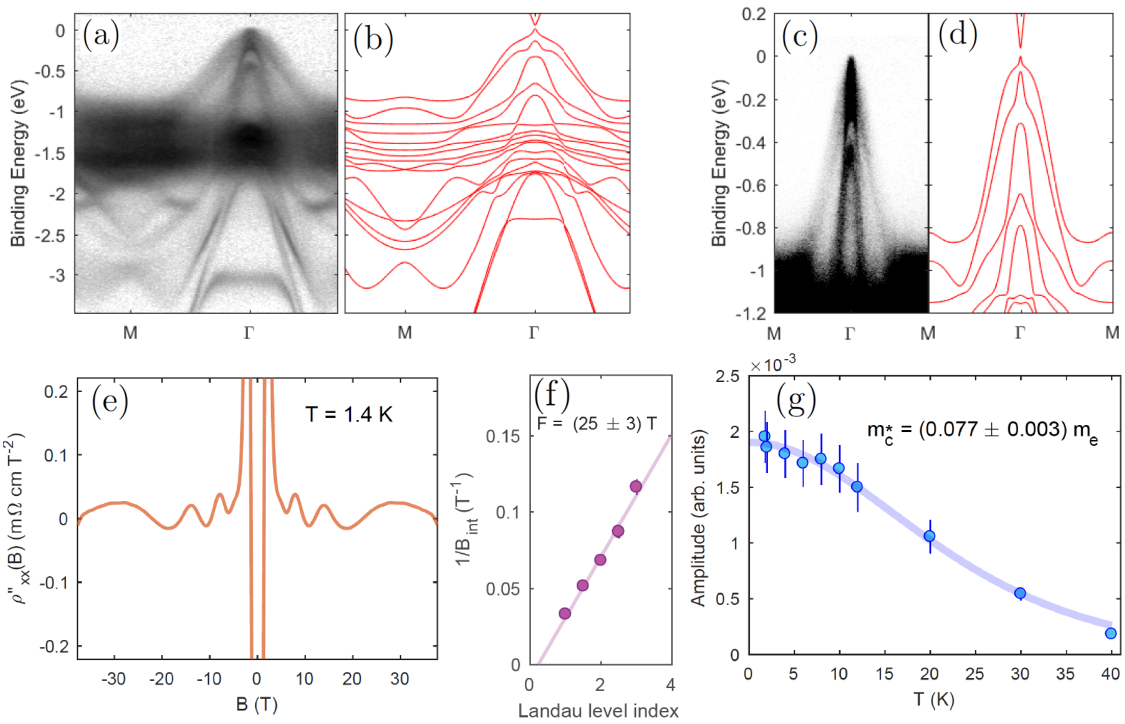

Figure 43: ARPES and high-field magnetotransport of $EuCd_2As_2$. (a), (c) ARPES spectrum as a function of wavevector along the M–Γ–M high symmetry line measured at $T \simeq 5$ K with incident photon energy of 130 eV. The data shown here are a sum of two measurements taken with linear-vertical and linear-horizontal polarisation, respectively, to compensate the effect of selection-rules. Nonlinear scaling was applied to the intensity to enhance the visibility of bands with a small photoemission cross-section. (b), (d) Electronic bands calculated by DFT (in red). (e) The second derivative of the longitudinal resistivity $\rho''_{xx}(B)$ as a function of field applied along the c axis. (f) Plot of $1/B_{\text{int}}$ at the minima and maxima in ρ_{xx} against Landau level index, with integers assigned to the minima, where $B_{\text{int}} = B + \mu_0 M$ is the internal field. The SdH frequency F is obtained from the gradient of the linear fit shown. (g) Temperature dependence of the amplitude in the SdH oscillation, measured at $B = 10$ T. The line is a fit to the Lifshitz–Kosevich formula, from which the cyclotron effective mass m^*_{c} of the charge carriers is estimated. The quoted error in m^*_{c} derives from the least-squares fit, but the uncertainty in the measurement is expected to be larger because of the long period of the oscillations and the relatively narrow field range.

ure 43(e) shows the second derivative of the in-plane longitudinal resistance measured at $T = 1.4\,\mathrm{K}$ in magnetic fields applied parallel to the c axis ($B \parallel c$) up to $37\,\mathrm{T}$, well above the coercive field. For $B < B_\mathrm{c}$ there is a very strong variation in magnetoresistance associated with the progressive canting of the spins towards the c axis, shown also in Fig. 44(a), but at higher fields the curve displays clear Shubnikov–de Haas (SdH) oscillations. Only a single SdH oscillation frequency could be resolved, consistent with a single band. Moreover, I do not find any evidence for a spin-splitting of the Landau levels, in contrast to the SdH data on the structurally-related Dirac semimetal $\mathrm{Cd_3As_2}$ (Ref. [167]). A lack of spin splitting would be consistent with the prediction that for $B > B_c$ the bands are already split by a constant exchange field, implying that the observed SdH oscillations correspond to the small pockets derived from the Weyl points when E_F is shifted downwards slightly, as suggested by the ARPES measurements.

The maxima and minima of the oscillations are plotted on a Landau level index plot in Fig. 43(f), with minima in ρ_{xx} assigned to the integers [168]. The SdH frequency obtained from the gradient is $F = 25 \pm 3\,\mathrm{T}$, which converts via the Onsager relation $F = (\hbar/2\pi e)A_\mathrm{ext}$ to an extremal area of the Fermi surface perpendicular to the c axis of $A_\mathrm{ext} = 0.24\,\mathrm{nm}^{-2}$, or $k_\mathrm{F} = 0.28\,\mathrm{nm}^{-1}$ assuming a circular cross-section.

Measurements at higher fields up to $45\,\mathrm{T}$ did not find any additional oscillation frequencies (see Fig. 40), and confirmed that the maximum centred on $30\,\mathrm{T}$ in Fig. 43(d) corresponds to the quantum limit (first Landau level).

Figure 43(g) shows the temperature dependence of the SdH oscillation amplitude up to $40\,\mathrm{K}$. By fitting the data to the Lifshitz–Kosevich formula (amplitude $\sim X/\sinh X$, where $X = 2\pi^2 k_\mathrm{B} T m_\mathrm{c}^*/e\hbar B$ and $m_\mathrm{c}^* = (\hbar^2/2\pi)\,\mathrm{d}A_\mathrm{ext}/\mathrm{d}E$) I obtain a cyclotron effective mass of about $m_\mathrm{c}^* = 0.08 m_\mathrm{e}$. The observation that $m_\mathrm{c}^*/m_\mathrm{e} \ll 1$ is consistent with quasiparticles near a Dirac or Weyl node.

A small effective mass is also found in the *ab initio* calculations. Assuming $k_\mathrm{F} = 0.28\,\mathrm{nm}^{-1}$, as determined from the SdH data, and a circular Fermi surface cross-section, I obtain $m_\mathrm{c}^* = 0.18 m_\mathrm{e}$ from the calculated band structure. I caution, however, that the measured and calculated m_c^* are not directly comparable because the Lifshitz–Kosevich formula assumes that the Landau levels are equally-spaced and that many levels are filled, neither of which applies here.

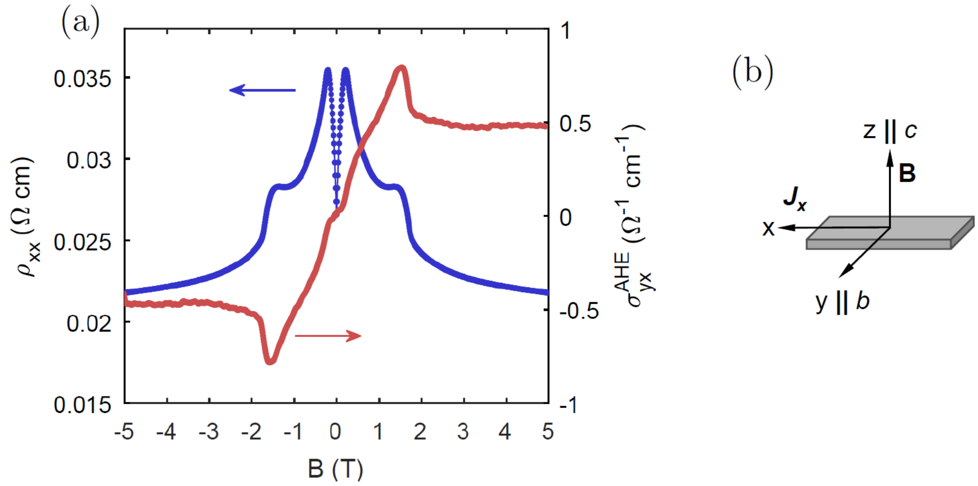

Figure 44: Magnetotransport of $EuCd_2As_2$. (a) ρ_{xx} and σ_{yx} as a function of field. (b) Definition of the xyz axes relative to the crystal orientation and directions of the current and applied field used in the measurement.

The quantum oscillations and ARPES results, as well as previous optical reflectivity measurements which found clear evidence for a very low carrier density [155], all point to a very small Fermi surface, and support the prediction that in the spin-polarised state of $EuCd_2As_2$ there is a single pair of Weyl nodes located close to Γ along Γ−A, in a small window of energy free from other bands. The small effective mass and Fermi surface area from the SdH data, together with p-type Hall transport [152], indicate that the crystals used in this study are slightly hole-doped. From the SdH measurements and *ab initio* in-plane dispersion Fernando de Juan[21] estimated that E_F is located approximately 52 meV below the Weyl node, which is consistent with the shift applied to the DFT bands in order to match the ARPES data.

In recent years, there has been a great deal of interest in measuring anomalous transport effects caused by Berry curvature in topological semimetals, especially the anomalous Hall effect (AHE) [158, 169]. In a Weyl semimetal, the Berry curvature is associated with the separation Δk of the Weyl nodes in **k**-space, as illustrated in

---

[21] Department of Physics, University of Oxford, Clarendon Laboratory, Oxford, OX1 3PU, UK; Donostia International Physics Center, 20018 Donostia-San Sebastian, Spain; IKERBASQUE, Basque Foundation for Science, Maria Diaz de Haro 3, 48013 Bilbao, Spain.

Fig. 34(c), and for a single pair of nodes at E_{F} the anomalous Hall conductivity has the universal form [158],

$$\sigma_{yx}^{\mathrm{AHE}} = \frac{e^2}{2\pi h}\Delta k. \tag{14}$$

In experiments, Δk is typically field-dependent due to the effect of field on the band splitting. This makes it difficult to separate the anomalous and semi-classical contributions to the Hall effect, as the latter is also field-dependent. In $\mathrm{EuCd_2As_2}$, however, Δk is almost constant for fields above the saturation field $B_{\mathrm{c}} = 1.6\,\mathrm{T}$, which makes it straightforward to isolate the anomalous part of the Hall resistivity. In principle, therefore, $\mathrm{EuCd_2As_2}$ is an ideal system for studying the AHE experimentally.

Figure 44(a) presents measurements of the longitudinal magnetoresistance ρ_{xx} and the anomalous part of the transverse (Hall) conductivity $\sigma_{yx}^{\mathrm{AHE}}$ at $T = 2\,\mathrm{K}$ as a function of field applied parallel to the c axis (the experimental geometry is shown in Fig. 44(b), and the procedure to obtain the anomalous part of σ_{yx} is described earlier). There are rapid changes in ρ_{xx} at low field due to the reorientation of the Eu spins in the magnetic field, as noted earlier, but above the saturation field $B_{\mathrm{c}} = 1.6\,\mathrm{T}$ ρ_{xx} decreases monotonically with field. The field range in Fig. 44(a) is below that where quantum oscillations become observable [see Fig. 43(e)]. The $\sigma_{yx}^{\mathrm{AHE}}(B)$ curve is an odd function of field, increasing rapidly for $0 < B < B_{\mathrm{c}}$ and remaining constant for $B > B_{\mathrm{c}}$, consistent with a non-zero anomalous Hall conductivity.

Assuming $\Delta k \simeq 0.52\,\mathrm{nm}^{-1}$ from the *ab initio* results, equation (14) predicts the anomalous Hall conductance for $\mathrm{EuCd_2As_2}$ to be $\sigma_{yx}^{\mathrm{AHE}} \simeq 30\,\Omega^{-1}\mathrm{cm}^{-1}$, which is significantly larger than observed. This prediction, however, applies only when the Weyl nodes lie exactly at E_{F}. In the samples used here the nodes are slightly shifted from E_{F}, and in this situation other factors are expected to affect the Berry phase [169]. One such factor is disorder. I have found the AHE in $\mathrm{EuCd_2As_2}$ to be reduced by the polishing process used to shape the Hall bar samples. Although it has been argued that disorder-induced contributions to the AHE are absent when E_{F} is near the nodes [158], the presence of a tilt in the dispersion makes these contributions possible in the form of skew scattering [170, 171]. The significant tilt predicted in the *ab initio* calculations [Fig. 42(d)] might explain why the AHE is so reduced.

4.4 Conclusion

The simple structure of the Weyl nodes in $\mathrm{EuCd_2As_2}$ makes it an ideal material with which to study the different contributions to the AHE. This could be achieved by tuning the position of E_F relative to the Weyl nodes by doping or application of pressure, or by controlling the level of defects by irradiation. The degrading effects of polishing could be avoided by studying transport phenomena with thin film samples.

More generally, $\mathrm{EuCd_2As_2}$ could provide the means to test predictions of other exotic physics in Weyl semimetals, such as the anomalous Nernst and thermal Hall effects [160, 172], non-reciprocal effects in light propagation [173], the repulsive Casimir effect [174], or to probe the effects of the chiral anomaly in the optical absorption [175] and non-local transport [176].

CHAPTER 5

Magnetic structure and excitations of the topological semimetal $YbMnBi_2$

In this chapter, I present the magnetic structure and dynamics of $YbMnBi_2$. These were investigated with elastic and inelastic neutron scattering to shed light on the topological nature of the charge carriers in the antiferromagnetic phase. I confirm C-type antiferromagnetic ordering of the Mn spins below $T_{\mathrm{N}} = 290\,\mathrm{K}$, and determine that the spins point along the c axis to within about 3°. The observed magnon spectrum can be described very well by the same effective Heisenberg spin Hamiltonian as was used previously to model the magnon spectrum of $CaMnBi_2$. My results show conclusively that the creation of Weyl nodes in $YbMnBi_2$ by the time-reversal-symmetry breaking mechanism can be excluded in the bulk.

---

5 Magnetic structure and excitations of the topological semimetal YbMnBi$_2$

5.1 Introduction

Dirac and Weyl materials are semimetals whose valence and conduction bands have a linear dispersion in the vicinity of the Fermi energy [10, 11]. These gapless band crossings, which are protected by topology or crystalline symmetries, can give rise to massless quasiparticle excitations which can be described by the relativistic Dirac or Weyl equations. Materials that host such fermions possess a range of desirable physical properties: exceptionally high electrical and thermal conductivities, immunity to disorder and ballistic electronic transport [124, 125, 126].

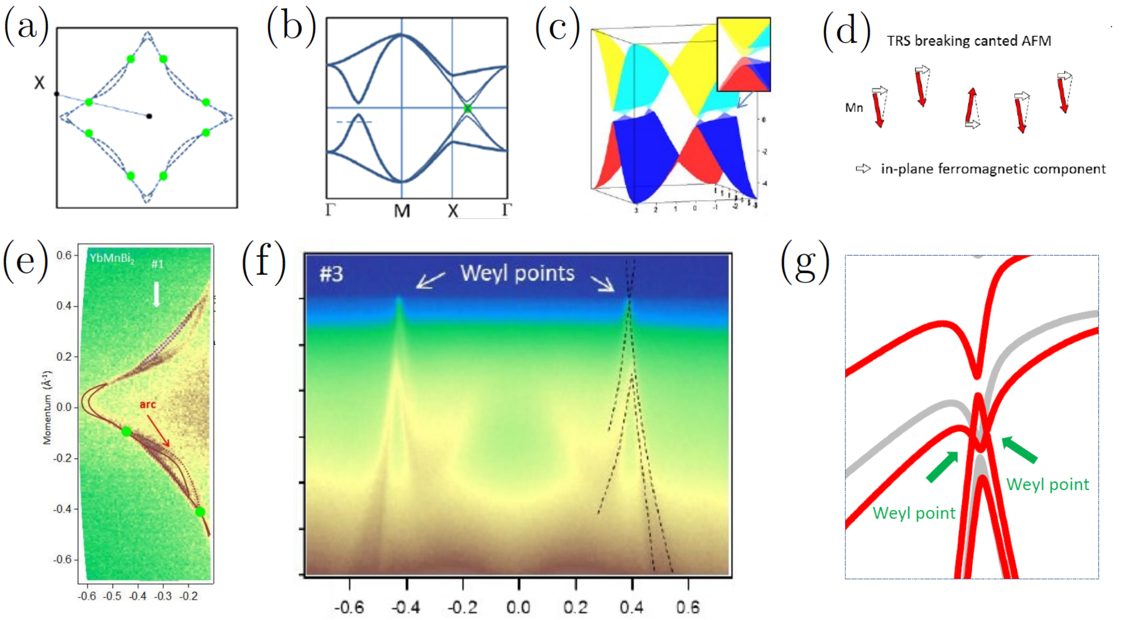

Figure 45: (adapted from Ref [74]) The calculated electronic band structure of YbMnBi$_2$ in, (a) the $k_x - k_y$ plane, (b) along the $\Gamma - M - X - \Gamma$ high symmetry line and (g) along k_x. (c) depicts the energy dispersion within the $k_x - k_y$ plane. (e) and (f) show the experimental electronic spectrum measured with ARPES. In (a), (b) and (e), the Weyl points are depicted by the green points, which are connected by the purported Fermi arcs in (e). The splitting in the bands (g) is driven by the canted magnetic structure (d) that gives rise to an in-plane ferromagnetic component in YbMnBi$_2$.

Weyl semimetals (WSMs) can occur in crystals with broken spatial inversion symmetry (IS), broken time-reversal symmetry (TRS), or both. Examples of the first type (with broken IS only) were found in 2015 [15, 36, 37, 38], but realisations of WSMs with broken TRS are still rare [11]. Very recently, the layered AFM $\mathrm{YbMnBi_2}$ was proposed as a potential candidate [74]. The evidence from ARPES is quite convincing [74], and there is also some support from optics [75, 76]. The tetragonal unit cell of $\mathrm{YbMnBi_2}$, which can be described by the $P4/nmm$ space group (No. 129), includes alternating Bi square layers that host the possible Weyl fermions [74, 75, 76, 77, 78, 79, 80], and $\mathrm{MnBi_4}$ tetrahedral layers which contain magnetic moments on the Mn atoms [see Fig. 46(a)]. In the antiferromagnetically ordered phase, below $T_{\mathrm{N}} = 290\,\mathrm{K}$, neighbouring Mn spins are reported to be antiparallel within the *ab* plane, but crucially, they are ferromagnetically stacked along the *c* axis [78, 79, 177]. This means that magnetic coupling to the Bi conduction states is allowed at the mean-field level, which can lead to band splitting.

In Ref. [74], it was argued that creation of Weyl points by TRS breaking in $\mathrm{YbMnBi_2}$ requires a ∼10° canting of the Mn moments away from the *c* axis [See Fig. 45(d)]. If present, this canting would generate a net ferromagnetic component in the *ab* plane of $\mathrm{YbMnBi_2}$, and would account for the Weyl nodes and arcs observed in the ARPES data. Such a small deviation in the moment direction from the *c* axis would not have been discernible in the (100) magnetic peak studied in the previous neutron diffraction measurements [78, 79, 177], so the possibility that $\mathrm{YbMnBi_2}$ might be a WSM by this mechanism remains to be tested.

Moreover, if the AFM order of manganese creates Weyl fermions, which then dominates the electronic transport [78, 79], then these quasiparticle excitations could be expected to play some role in the exchange coupling between Mn moments which could in turn influence the magnon spectrum. As the magnetic order is key to the behaviour of $\mathrm{YbMnBi_2}$ as a topological material, measurements of the magnon spectrum, and the exchange parameters derived from it, could provide additional information on the presence of Weyl fermions near the Fermi energy.

In light of this, I set out in this study, (i) to search for evidence of a canted magnetic structure by neutron diffraction, and (ii) to investigate the magnon spectrum in the AFM phase of $\mathrm{YbMnBi_2}$ through inelastic neutron scattering. To

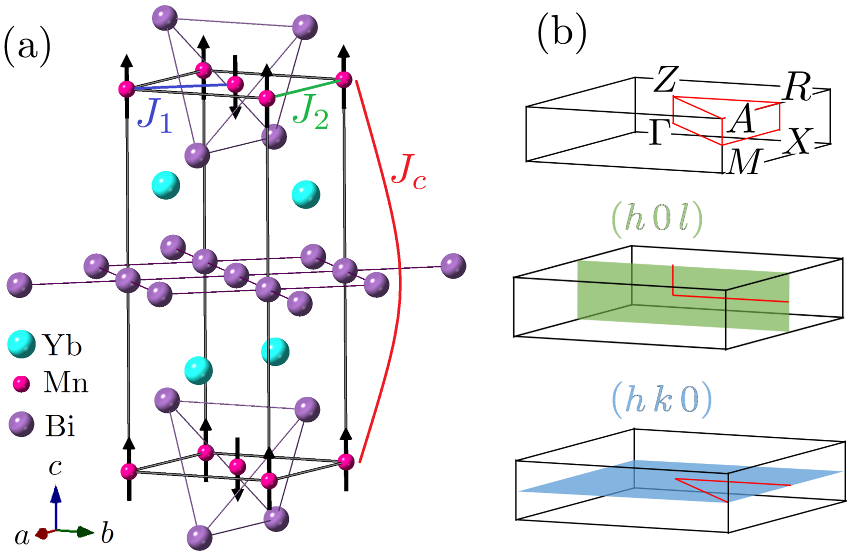

Figure 46: (a) The unit cell of $YbMnBi_2$ for the space group $P4/nmm$ (No. 129). The proposed Weyl fermions are contained in the Bi square net in the center of the unit cell. The magnetic exchange between the ab plane nearest neighbour (J_1), ab plane next-nearest neighbour (J_2), and c axis nearest neighbour (J_c) Mn^{2+} ions were used in the linear spin-wave model to describe the magnon spectrum. (b) The definition of high symmetry lines and planes in the first Brillouin zone of the tetragonal lattice. The spin-wave spectrum in the $(h\,0\,l)$ and $(h\,k\,0)$ reciprocal lattice planes was mapped in this work. Here, the reciprocal lattice vector is defined as, $\mathbf{G} = h\mathbf{b}_1 + k\mathbf{b}_2 + l\mathbf{b}_3$, where $|\mathbf{b}_1| = |\mathbf{b}_2| = 2\pi/a$ and $|\mathbf{b}_3| = 2\pi/c$.

achieve the required sensitivity to the predicted ferromagnetic component of the proposed canted magnetic structure, I performed careful measurements of the weak $(0\,0\,l)$ nuclear reflections [see Fig. 20]. Furthermore, to identify any anomalies in the magnetic exchange between Mn moments associated with the presence of Weyl fermions, I compare the observed magnon spectrum with that of Dirac semimetal $CaMnBi_2$ [122], which is isostructural to $YbMnBi_2$. I demonstrate that the Mn sublattice in $YbMnBi_2$ has C-type AFM ordering below $T_N = 290\,K$, with the moments aligned along the c axis to within 3° (at 95% confidence level). Moreover, I find no evidence from the magnon spectrum for anomalous magnetic coupling between the Mn spins. My results rule out the existence of magnetically-induced Weyl fermions in the bulk of $YbMnBi_2$, but leave open the possibility that the ∼10° canting of the Mn moments needed to form the Weyl nodes might occur at the surface.

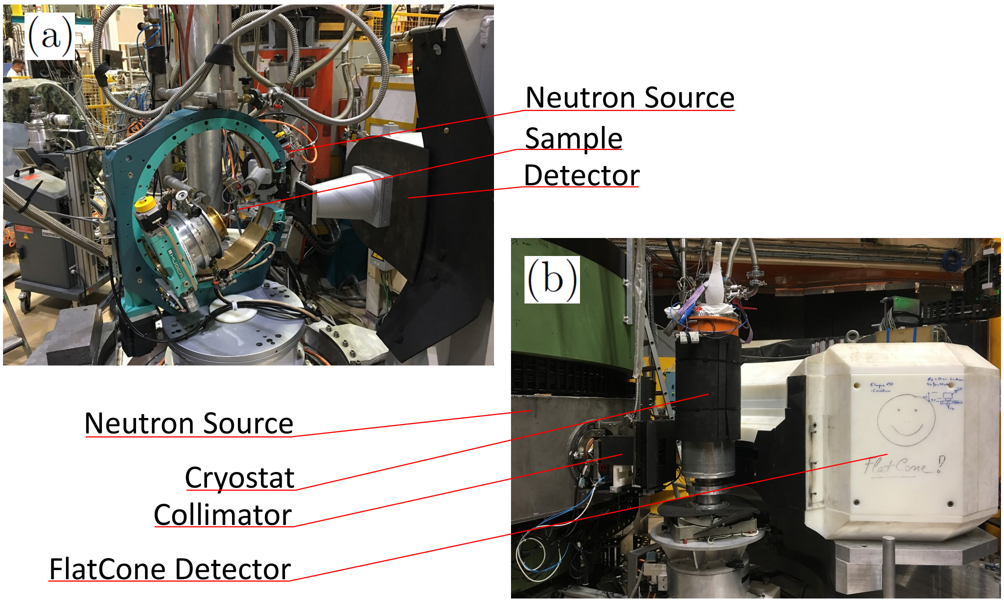

Figure 47: The experimental setup at beamlines (a) D10 and (b) IN8 in ILL respectively.

5.2 Experimental details

Single crystalline $YbMnBi_2$ was grown by Hongyuan Wang, Hao Su, Yanfeng Guo,[22] Zili Feng and Youguo Shi[23] using the self-flux method. The mixture was placed into an alumina crucible, sealed in a quartz tube, then slowly heated to 900°C and kept at this temperature for 10 hours. The assembly was subsequently cooled down at a rate of 3°C/hour. It was finally taken out of the furnace at 400°C and was put into a centrifuge immediately to remove the excess Bi. The structure and quality of the single crystals was checked with laboratory X-rays on a 6-circle diffractometer (Oxford Diffraction) and Laue diffractometer (Photonic Science). A SQUID magnetometer (Quantum Design) was used to study the magnetisation of $YbMnBi_2$ as a function of temperature. These zero-field-cooled (ZFC) magnetometry measurements were performed in the temperature range 10 to 370 K in a field of 1 T applied parallel to the a- and c-axes of $YbMnBi_2$.

Elastic neutron scattering of a $YbMnBi_2$ single crystal with a mass of 76 mg was performed on a 4-circle diffractometer (D10) at the Institut Laue-Langevin (ILL)

---

[22] School of Physical Science and Technology, ShanghaiTech University, Shanghai 201210, China.

[23] Beijing National Laboratory for Condensed Matter Physics, Institute of Physics, Chinese Academy of Sciences, Beijing 100190, China.

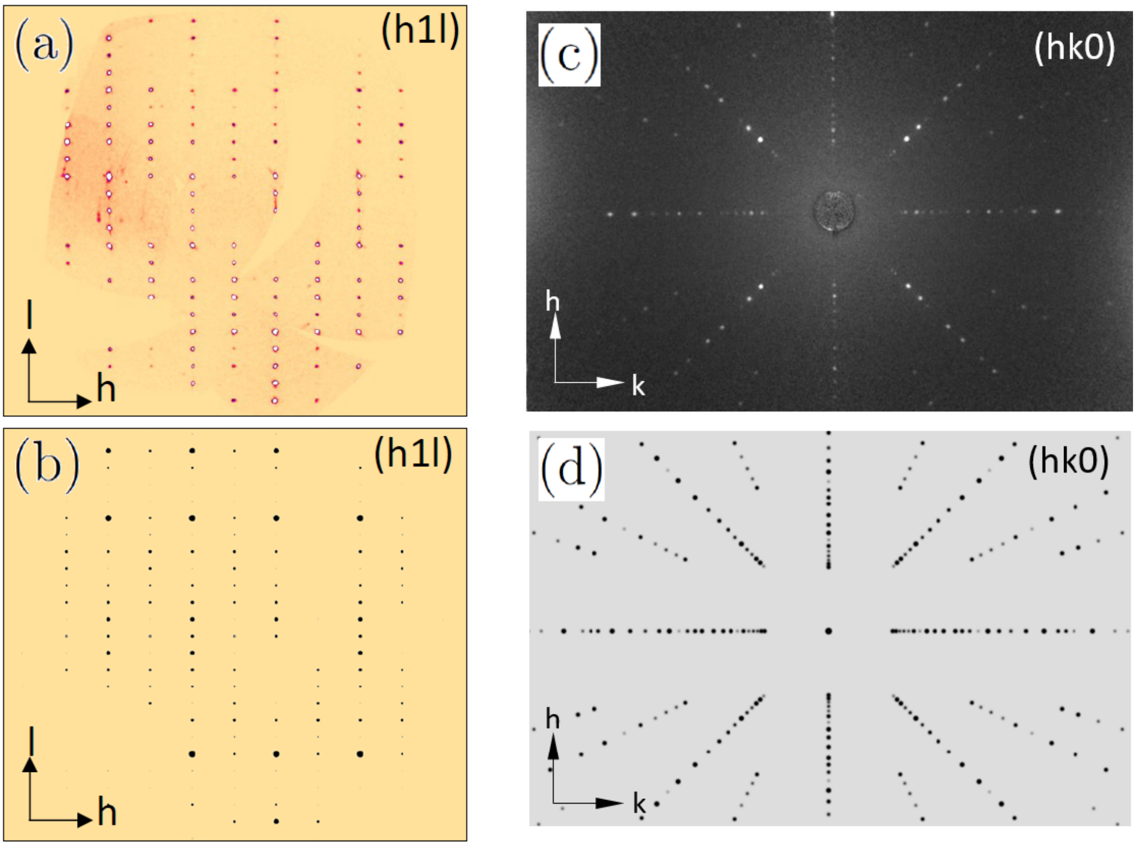

Figure 48: (a), (b) Reciprocal space maps of the $(h\,1\,l)$ plane obtained from a $YbMnBi_2$ single crystal on the 6-circle X-ray (Mo, K_α) diffractometer (Oxford Diffraction). The positions and relative intensities of the experimental peaks (a) are in good agreement with that of the calculated plots (b). Moreover, the peaks display a very narrow mosaic, reflecting the good quality of the crystals. Similarly, the (c) Laue pattern of a $YbMnBi_2$ crystal agrees strongly with the (d) model. Here, the incident X-ray was directed along the $[0\,0\,1]$ direction of the crystal axes. The pattern also shows the 4-fold symmetry about the $YbMnBi_2$ c axis (out of the page).

reactor source with Andrew Boothroyd, Henrik Jacobsen[24] and Bachir Ouladdiaf,[25] the instrument scientist. The intensities of the reflections were studied over the temperature range of 20 to 400 K. A pyrolytic graphite (PG) monochromator was used to select the incident neutron wavelength of $\lambda = 2.36\,\text{Å}$. The rocking curve of each peak was obtained by measuring the number of scattered neutrons at each

---

[24] Department of Physics, University of Oxford, Clarendon Laboratory, Parks Road, Oxford OX1 3PU, UK.

[25] Institut Laue-Langevin, 6 rue Jules Horowitz, 38042 Grenoble Cedex 9, France.

rocking angle (ω) with a 80×80 mm^2 area detector.

Inelastic neutron scattering measurements were performed on the triple-axis neutron spectrometer IN8 [178] with the FlatCone detector [179] at the ILL with Henrik Jacobsen, Tim Tejsner, Alexandre Ivanov and Andrea Piovano.[26] A YbMnBi$_2$ single crystal (mass 1 g) was initially oriented with the a and c crystal axes horizontal to map the spin-wave spectrum in the $(h\,0\,l)$ scattering plane (see Fig. 46). The crystal was subsequently rotated by 90° (such that the crystalline a and b axes were in the scattering plane) to access the $(h\,k\,0)$ plane. Constant-energy maps were measured at various energies, $\Delta E = E_{\mathrm{i}} - E_{\mathrm{f}}$. The outgoing neutron wavevector was fixed at $k_{\mathrm{f}} = 3\,\text{Å}^{-1}$ ($E_{\mathrm{f}} = 18.6$ meV) by elastically-bent Si (111) analyser crystals, and the required energy transfers were set by selecting the incident wavevector, k_{i}, with an incident beam monochromator. For energy transfers $\Delta E \geq 40\,\text{meV}$, a PG (002) double-focusing monochromator was used, and for $\Delta E < 40\,\text{meV}$ an elastically-bent, perfect Si (111) double-focusing monochromator was used.

The array of 31 detectors on the FlatCone device allows for the simultaneous acquisition of scattered intensity along arcs in reciprocal space. By rotating the single crystal about the scattering plane normal, these arcs can sweep out areas in **k**-space to give reciprocal space maps [see Fig. 22]. To visualise the area in reciprocal space that can potentially be mapped by these arcs, I used the software vTAS [180], which simulates the FlatCone detector in the context of the space constraints at the IN8 beamline at ILL. This allows me to optimise the experimental geometry to acquire maps of the magnon spectrum across several Brillouin zones [see Fig. 22].

5.3 Results and analysis

The X-ray diffraction patterns of single crystalline YbMnBi$_2$ obtained from the 6-circle and Laue diffractometers are fully consistent with the $P4/nmm$ space group, with cell parameters $a = 4.4860(13)$ Åand $c = 10.864(4)$ Åat $T = 300\,\text{K}$ (see Fig. 48).

The temperature dependence of the magnetic susceptibility of YbMnBi$_2$, with the applied field parallel to the a and c crystal axes, is shown in Fig. 49(a). The anomaly in the χ_c data at $T = 290\,\text{K}$ is associated with the onset of AFM order

---

[26] Institut Laue-Langevin, 6 rue Jules Horowitz, 38042 Grenoble Cedex 9, France.

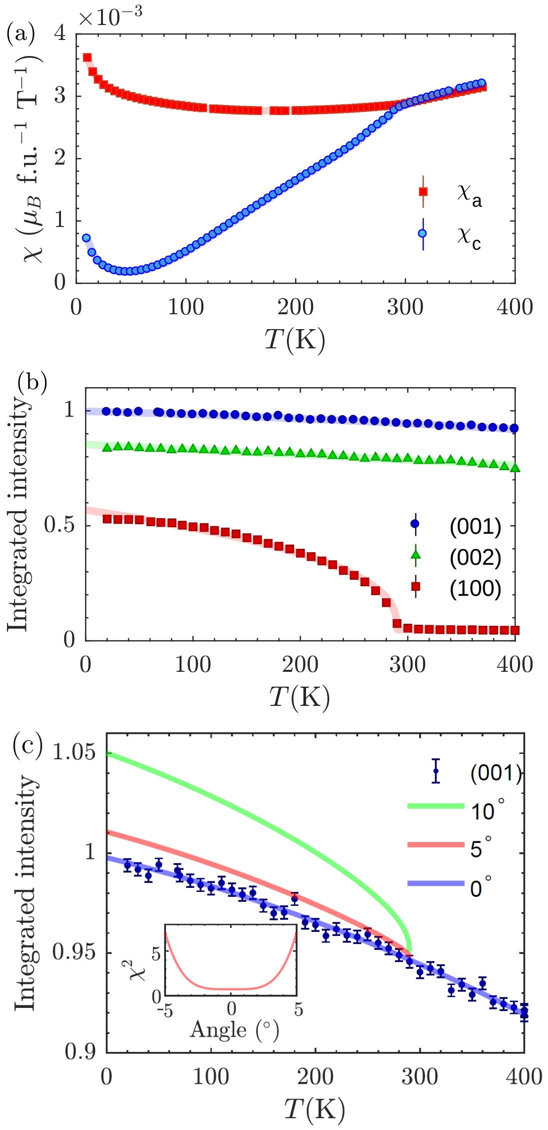

Figure 49: (a) Temperature dependence of the magnetic susceptibility of $\mathrm{YbMnBi_2}$ measured with the field applied along the a and c axes (χ_a and χ_c, respectively). The single crystal was cooled in zero field and measured in an applied field strength of 1 T. (b) Temperature dependence of the integrated intensity of the (001), (002) and (100) peaks. The red line is a power law fit to the temperature dependence of the (100) reflection which gives a transition temperature of T_N=290(1) K. (c) Measured intensity of the (001) peak, together with lines calculated for tilt angles of 0°, 5° and 10°. The inset shows the variation of the χ^2 with tilt angle.

in the $\mathrm{Mn^{2+}}$ sub-lattice. This Néel temperature is consistent with those reported in earlier studies of $\mathrm{YbMnBi_2}$ [74, 78, 79] and the elastic neutron scattering data presented in this work (see later). Below T_N, the magnetic susceptibility becomes strongly anisotropic with respect to applied field, where $\chi_a > \chi_c$. This bifurcation of $\chi(T)$ at T_N suggests that the manganese moments, in the ordered phase, are more susceptible to an in-plane applied field compared to the field along the c axis, in agreement with earlier reports [74, 78]. At low temperatures (below 50 K), the susceptibility grows in both field directions. This upturn is likely due to a small concentration of a Mn-containing paramagnetic impurity phase, and is observed in other members of the $A\mathrm{MnBi}_2$ family (A = Sr, Ca, Ba) [181, 182, 183].

5.3.1 Elastic neutron scattering

Neutron diffraction data in the temperature range 20 to 400 K are presented in Fig. 49(b). As the sample was cooled below T = 290 K, the (100) peak, which is otherwise forbidden in the $P4/nmm$ space group, was observed. This reflection is consistent with a magnetic propagation vector of $\mathbf{k} = \mathbf{0}$. The onset of this purely magnetic peak at T_N reveals the incipient AFM order of the Mn^{2+} sub-lattice. The temperature dependence of the integrated peak intensity fits very well to a power law, $I_{obs} \propto |T_\mathrm{N} - T|^{2\beta}$, with exponent $\beta = 0.38(2)$.

The predicted canting of the Mn^{2+} moments away from the c axis [74, 75, 76] should produce a small ab plane ferromagnetic component. Given that magnetic neutron scattering is sensitive to the component of the ordered moment perpendicular to the scattering vector $\mathbf{q}$ [184], I can isolate this small in-plane component by studying the intensity of reflections with $\mathbf{q} \parallel c$ [see Fig. 20]. If there were an in-plane ferromagnetic component then the intensity of $(00l)$ peaks should increase on cooling below T_N, as was observed in a sister compound SrMnSb_2 [84], where a small in-plane ferromagnetic contribution to the nuclear peak was reported.[27]

To minimise the reduction of the scattered intensity due to the magnetic form factor of Mn^{2+}, I studied the reflections with the smallest $\mathbf{q}$, namely the (001) and (002) peaks, as shown in Fig. 49(b). I observe no discernible change in the integrated intensity of these peaks apart from the gradual increase with decreasing temperature which can be attributed to the Debye-Waller factor.

---

[27] Note that the a and c axis in Ref. [84] are interchanged with respect to those defined in the present work. SrMnBi_2 suffers from an off stoichiometry and is better described by $\mathrm{Sr}_{1-y}\mathrm{Mn}_{1-z}\mathrm{Sb}_2$ $(y, z < 0.1)$.

In Fig. 49(c) I show the intensity of the (001) peak on a magnified scale, together with lines calculated assuming tilt angles of 0°, 5° and 10°. The 0° curve is a quadratic fit to the data, and the other two curves are obtained by adding the calculated magnetic intensity of the (001) peak to the 0° curve based on the measured intensity of the (100) peak. I also calculated the variation of the χ^2 goodness-of-fit statistic as a continuous function of tilt angle, see inset to Fig. 49(c). From the χ^2 distribution, I find that the probability of a tilt angle greater than 3° is only 5%.

These results imply that the ordered moments in $\mathrm{YbMnBi_2}$ are collinear and aligned along the c axis to within 3° at a 95% confidence level. Hence, a 10° canting of $\mathrm{Mn^{2+}}$ moments away from the c axis, as required to create the Weyl nodes, can be excluded.

5.3.2 Inelastic neutron scattering

The inelastic neutron scattering data were processed in several steps. First, the spurions were removed from the raw data by hand using the nplot software provided by Paul Steffans.[28] Following which, the powder rings, which appear as concentric circles around $\mathbf{q} = (0\,0\,0)$, was smoothed out using a mask. Next, the intensity of the constant energy maps was normalised according to the magnetic form factor of $\mathrm{Mn^{2+}}$. Finally, a summed average of all the symmetry related planes was made. Here, each symmetry related plane was obtained by applying the symmetry elements associated with each scattering plane to the measured spectrum. The processed constant energy maps in the $(h\,0\,l)$ and $(h\,k\,0)$ planes at various energy transfers, ΔE, are shown in Figs. 50 and 51 respectively. I discuss the data from the different scattering planes in turn, starting with the measured $(h\,0\,l)$ data, which correspond to the top half of each panel in Fig. 50.

At $\Delta E = 10$ meV, I find the lowest energy spin-wave mode at Γ. To excite this non-propagating magnon, the incoming neutrons have to overcome the anisotropy energy associated with the tendency of the ordered $\mathrm{Mn^{2+}}$ moments to point along the c axis. Hence the magnitude of this energy gap in the spin-wave spectrum gives a measure of the strength of this easy axis.

---

[28] nplot: a toolset for neutron data evaluation in matlab, developed at the Institut Laue Langevin. Jan (2017). Available at https://github.com/nplot

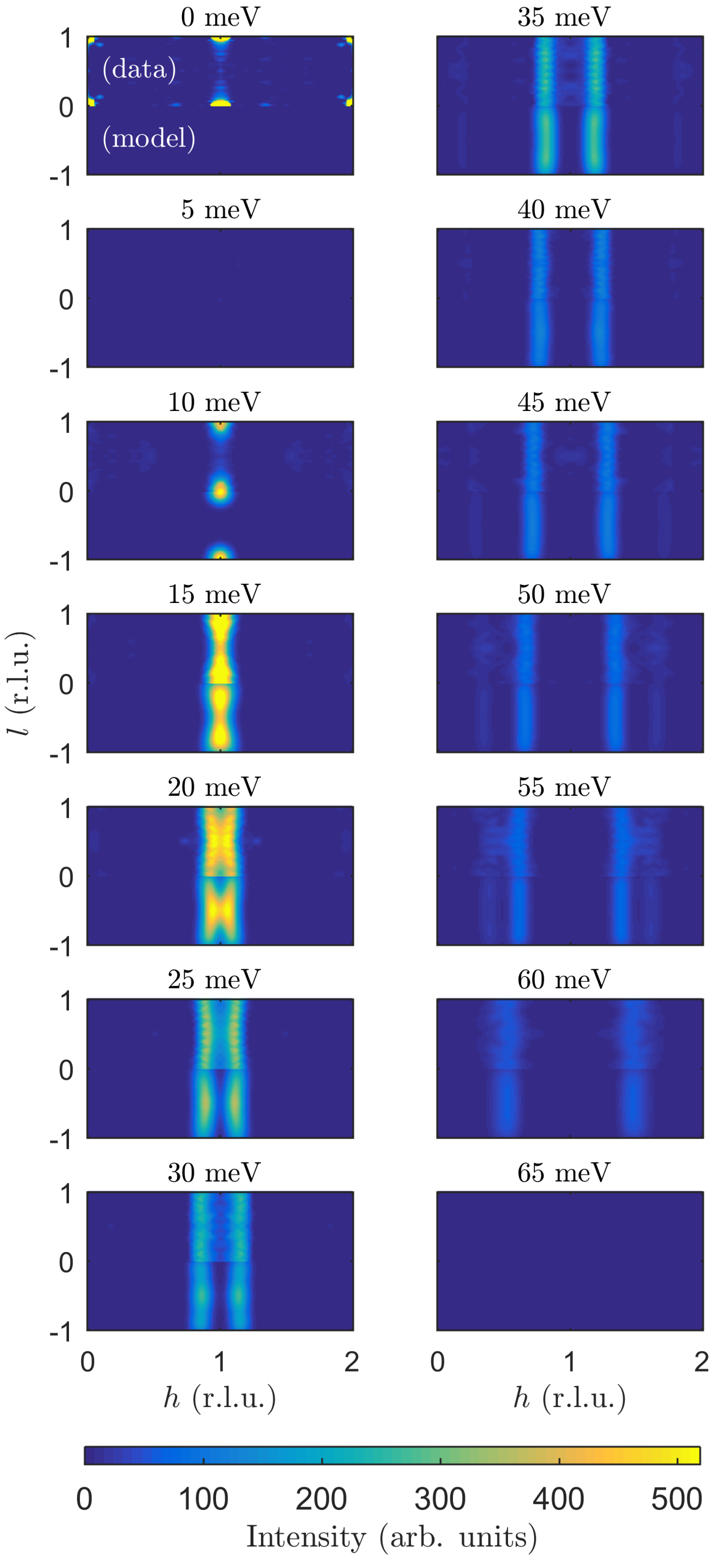

Figure 50: Constant-energy maps in the $(h\,0\,l)$ plane in reciprocal space, illustrated in Fig. 46(b), at various ΔE, plotted in reduced lattice units (r.l.u.). In each panel, the top and bottom half correspond to the data and model, respectively.

At $\Delta E = 20$ meV, I find pinch points[29] in the magnon spectrum at the high symmetry point Z, that is, halfway between Γ points in adjacent Brillouin zones along l. This correspond to propagating spin-wave modes along the c axis where the Mn^{2+} spins are precessing π out of phase.

For energy transfers $\Delta E \geq 30$ meV, the magnon spectrum loses the k_z dependence and becomes progressively linear along l. In other words, at these energies, the eigenfrequency of the spin-wave modes propagating along a (or b) is independent of the phase of the spin-waves in adjacent ab-planes. This indicates that the cross-plane magnetic exchange coupling in the ordered Mn^{2+} moments is relatively weak compared to the coupling within the ab plane. Moreover, given the large separation of the manganese ions along the c axis compared to that within the plane, this also suggests that the spin-wave spectrum of $YbMnBi_2$, at these energy transfers, can be described by ordered Mn^{2+} moments on an isolated 2D square lattice.

The spin-wave spectrum terminates along the $R - X - R$ high symmetry line at $\Delta E = 60$ meV. This propagating magnon mode along the a axis corresponds to the case where the ferromagnetically aligned Mn^{2+} moments are precessing π out of phase. Given that this is the highest energy excitation suggests that the net exchange coupling in $YbMnBi_2$ favours the ferromagnetic alignment of next-nearest neighbour Mn ions.

I now turn to discuss the reciprocal space maps in the $(h\,k\,0)$ scattering plane at various energy transfers, which correspond to the left half of each panel in Fig. 51. No propagating spin-wave modes were observed in the reciprocal space maps for $\Delta E \leq 10\,\text{meV}$. Just as in the $(h\,0\,l)$ plane, I observe the lowest energy excitations at the Γ point in the Brillouin zone at $\Delta E = 10$ meV.

For $10\,\text{meV} \leq \Delta E \leq 26.5\,\text{meV}$, the spectrum develops into rings centred at Γ, which is characteristic of isotropically dispersing 2D plane waves. At these small wave vectors ($|\boldsymbol{k}| = 2\pi/\lambda$) the in-plane exchange coupling between Mn^{2+} moments appear to be isotropic. This arises because the magnon excitations at large wavelengths ($\lambda \gg a$) are insensitive to the periodicity of the square lattice. When the wavelength of the spin-wave becomes the same order of magnitude as the lattice spacing, that is $\lambda \sim a$, the magnon spectrum becomes progressively less isotropic,

---

[29] points where the spin-wave bands meet

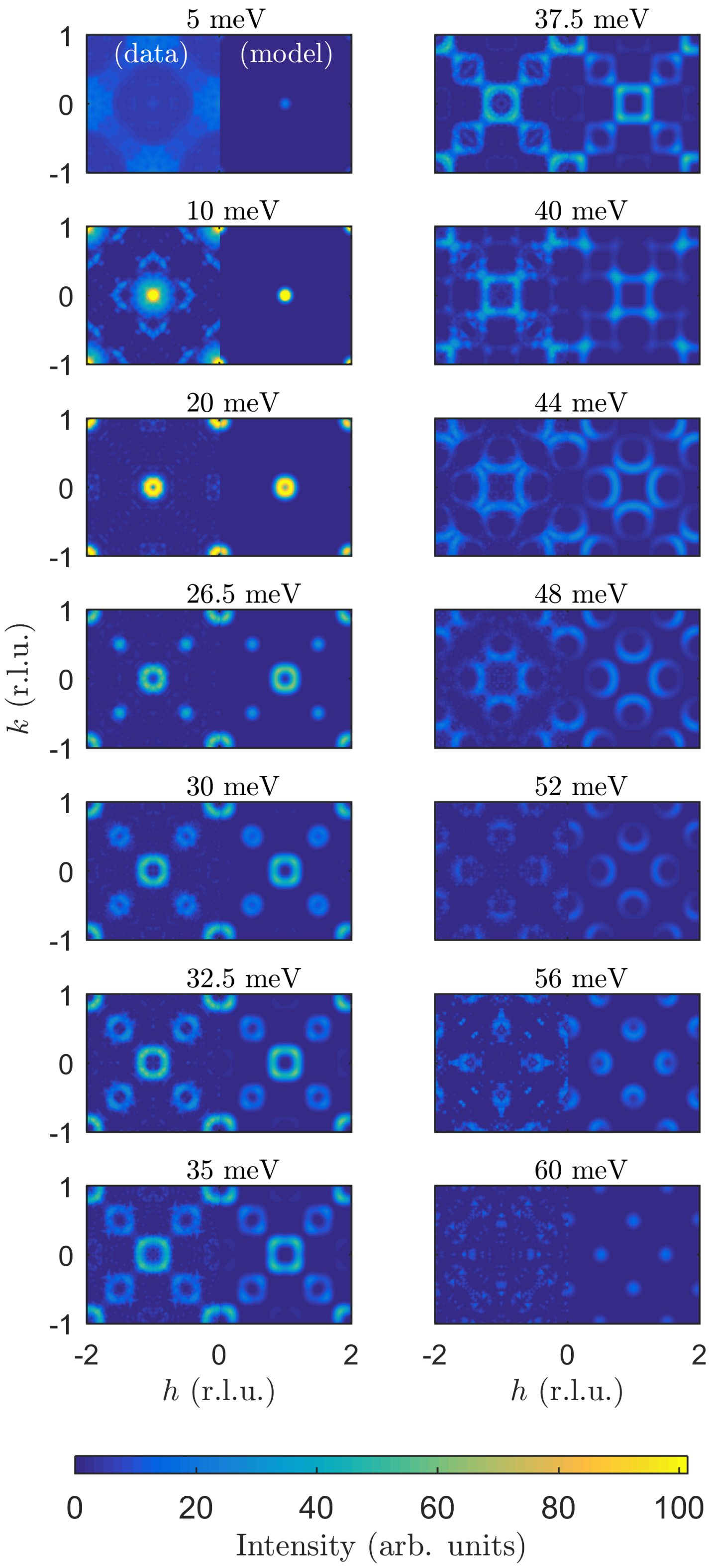

Figure 51: Constant-energy maps in the $(h\,k\,0)$ plane in reciprocal space, illustrated in Fig. 46(b), at various ΔE. In each panel, the left and right half correspond to the data and model, respectively.

as shown in the $\Delta E \geq 30\,\mathrm{meV}$ data. Here the spin-wave excitations become sensitive to the different exchange coupling strength between the *ab* plane nearest and next-nearest neighbour interactions. This breaks the rotational symmetry about Γ and the spin-wave spectrum adopts the lower $\bar{4}m2$ symmetry of the Mn^{2+} ions in the *ab* plane.

At ΔE= 26.5 meV, I observe a saddle in the spin-wave spectrum appearing at the high symmetry point M. This corresponds to propagating spin wave modes in which the antiferromagnetically aligned nearest-neighbour Mn^{2+} moments precess π out of phase. Similarly, this mode also displays rotational symmetry which becomes lowered at higher energy transfers.

Eventually, at ΔE = 40 meV, these magnon modes emanating from M and Γ meet at pinch points in the constant energy maps at $\sim 1/4$ and $\sim 3/4$ along the $\Gamma - M - \Gamma$ high symmetry line. Here the spectrum develops into a square network which is relatively linear in h and k.

At larger energy transfers, 44 meV $\leq \Delta E \leq$ 60 meV, the in-plane spin wave modes propagating along a eventually terminates at the high symmetry point X, in agreement with the $(h\,0\,l)$ data.

To obtain the the energy dispersion curve (ΔE–k) for k along the $\Gamma - X - \Gamma - M - \Gamma - Z - \Gamma$ path, cuts were made along the $Z - \Gamma - X$ and $M - \Gamma - X$ high symmetry lines, as defined in Fig. 46(b), in the measured constant energy maps in the $(h\,0\,l)$ and $(h\,k\,0)$ planes respectively. The scattered intensity along these high symmetry cuts at various ΔE was fitted with peak functions to identify the position of the magnons in ΔE–k space. In Fig. 52, I present the measured spin wave spectrum, which is denoted by the red markers.

In order to model the observed magnon dispersion, I calculated the spin-wave spectrum with SpinW [185], assuming Heisenberg interactions up to the second nearest neighbour in the *ab* plane, nearest neighbour inter-planar coupling and an easy axis along c. I arrive at the following magnetic Hamiltonian,

$$\hat{H} = \sum_{\langle i,j \rangle} J_{ij} \hat{\mathbf{S}}_i \cdot \hat{\mathbf{S}}_j - \sum_i D(\hat{S}_i^z)^2, \tag{15}$$

where the three exchange parameters used to describe the spin-wave are the *ab* plane

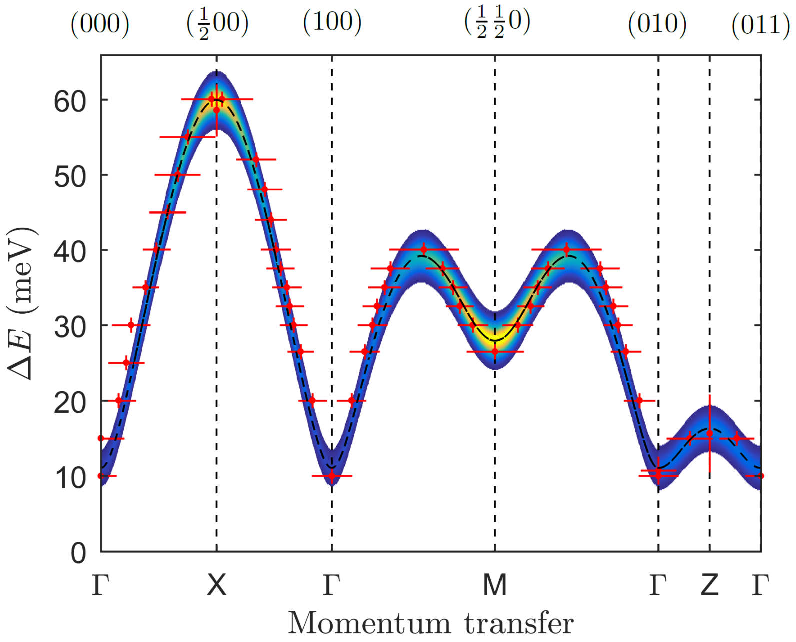

Figure 52: The observed and calculated spin-wave spectrum of the Mn spins in $YbMnBi_2$ along high symmetry directions, as defined in Fig. 46(b). The calculated magnon spectrum is in good agreement with the measured spin-wave dispersion (red markers), which was obtained from constant-energy cuts through the intensity maps in the $(h\,0\,l)$ and $(h\,k\,0)$ planes.

nearest neighbour (J_1), *ab* plane next-nearest neighbour (J_2) and c axis nearest neighbour (J_c), defined in Fig. 46(a), and an anisotropy energy (D) along the c axis.

By fitting the linear spin-wave model to the measured dispersion I find values for the parameters $SJ_1 = 22.6(5)$ meV, $SJ_2 = 7.8(5)$ meV, $SJ_c = -0.13(5)$ meV and $SD = 0.37(4)$ meV, where S is the spin quantum number, which for Mn^{2+} is $S = 5/2$. This is done in three stages:

- **Step 1:** A global fit of all parameters for the data along the high symmetry line $\Gamma - X - \Gamma - M - \Gamma - Z - \Gamma$, as shown by the red markers in Fig. 52, was made using the SpinW program [185]. This accounts for the magnetic exchange between *ab* plane nearest neighbour (J_1), *ab* plane next nearest neighbour (J_2) and the c axis nearest neighbour (J_c). The c axis anisotropy of the Mn moments (D) was also accounted for.

- **Step 2:** Following which, to obtain a better constrain on the estimates of SJ_1 and SJ_2, I calculated the χ^2 values of the least squares fit of the modelled

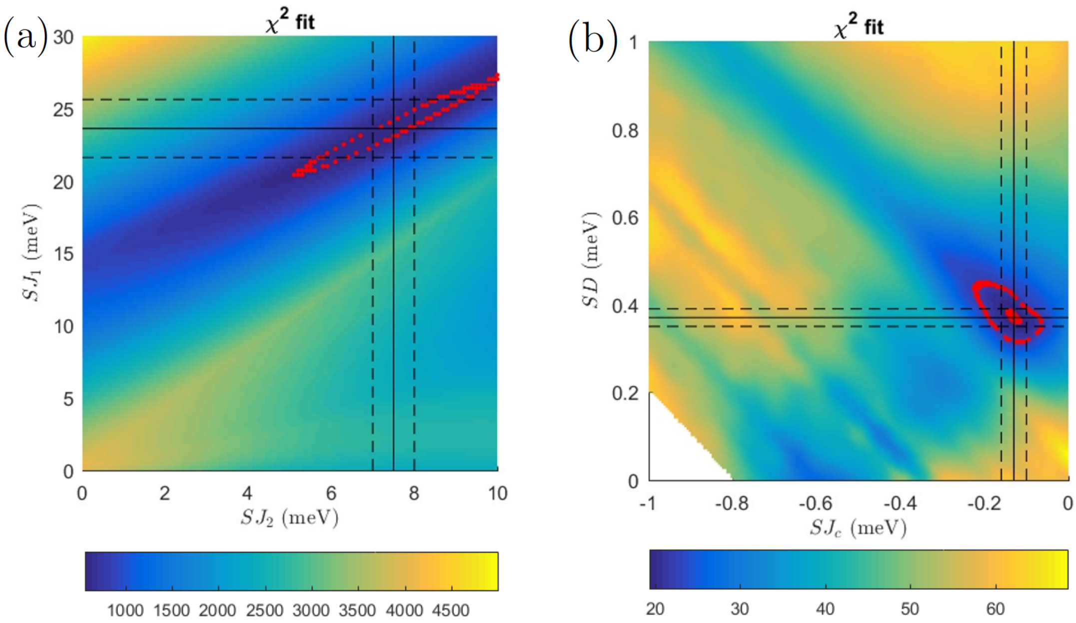

Figure 53: (a) depicts the χ^2 map of the least squares fit of the linear spin-wave model to the measurements for the parameter space 0 meV $< SJ_1 <$ 30 meV and 0 meV $< SJ_2 <$ 10 meV. (b) illustrates the χ^2 map for the least squares fit of the modelled spectrum to the constant-**q** energy cuts over the range of values of $0\,\text{meV} < SD < 1\,\text{meV}$ and $-1\,\text{meV} < SJ_c < 0$. In both panels, the black solid lines represent the best-fit values with the margin of error shown by the dashed black lines. The constant χ^2 contours are depicted by the red points for $\chi^2 \gtrapprox \chi^2_{min}$.

spectrum to the measured data over the parameters space of values $0 < SJ_1 <$ 30 meV and $0 < SJ_2 <$ 10 meV for fixed values of SJ_c and SD obtained from step 1. This χ^2 map, which is presented in Fig. 53(a), provides me estimates of the magnetic exchange $SJ_1 = 22.6(5)$ meV and $SJ_2 = 7.8(5)$ meV which correspond to χ^2_{min}. I depict the constant χ^2 contour for $\chi^2 \gtrapprox \chi^2_{min}$ by the red markers.

- **Step 3:** Finally, using the newly refined values of SJ_1 and SJ_2 obtained from step 2 as constraints, I further refine the estimates of SJ_c and SD. I calculated the χ^2 values of the least squares fit of the linear spin-wave model to the constant-**q** energy cuts from energy transfers $\Delta E = 5$ to $\Delta E = 25\,\text{meV}$ measured at $\mathbf{q} = (1, 0, 2)$ and $\mathbf{q} = (1, 0, 2.5)$. In this case, I also include the resolution properties of the scattered neutrons that is unique to the IN8 triple-axis spectrometer at ILL. This was estimated by the ray-tracing routine RESTRAX [186, 187]. I present, in Fig. 53(b), the χ^2 map for the range of values of 0 meV $< SD <$ 1 meV and -1 meV $< SJc <$ 0 meV. From this map I obtain estimates of SD and SJ_c.

Based on these parameters, I plot the corresponding calculated energy dispersion along k in Fig. 52. Furthermore, to compare the modelled spectrum in Fig. 54 with the measured planes in Fig. 50 and Fig. 51, I used the SpinW program [185] to generate the constant energy slices in the $(h\,0\,l)$ and $(h\,k\,0)$ planes. To account for the fact that the magnetic neutron scattering is proportional to the component of the magnetic moments that is perpendicular to the scattering vector $\mathbf{q}$, the modelled maps in the $(h\,0\,l)$ planes are taken from the same Brillouin zone as that for the data. This is not required for $(h\,k\,0)$ plane, given that the scattering vector is always orthogonal to the Mn^{2+} magnetic moment in this scattering geometry. Moreover, the same symmetry transformations that was done to the measured spectrum was also applied to the modelled spectrum. The modelled spectrum for the $(h\,0\,l)$ and $(h\,k\,0)$ planes are presented in the bottom- and right-half of each panel Figs. 50 and 51 respectively. Overall, I find that the calculated spectrum agrees very well with the data.

5.4 Discussion

As neutron diffraction probes the entire volume of the sample, my results rule out the possibility of magnetically-induced Weyl nodes in the bulk of $YbMnBi_2$. On the other hand, neutron diffraction would not be sensitive to a canting of the magnetic moments at the surface of the sample. Such a canting, if present, would reconcile the results of the present study with the work by Borisenko *et al.* [74].

In $YbMnBi_2$, the spontaneous magnetic order in the Mn sub-lattice coexists with massless quasiparticle excitations arising from the Bi square net. Armed with the best-fit parameters of the linear spin-wave model, we are now in a position to address whether the magnon spectrum in $YbMnBi_2$ differs in any detectable way compared with other related systems. For instance, one might expect to see differences in the inter-layer exchange coupling parameter J_c if the conducting states on the Bi layers were very unusual in $YbMnBi_2$.

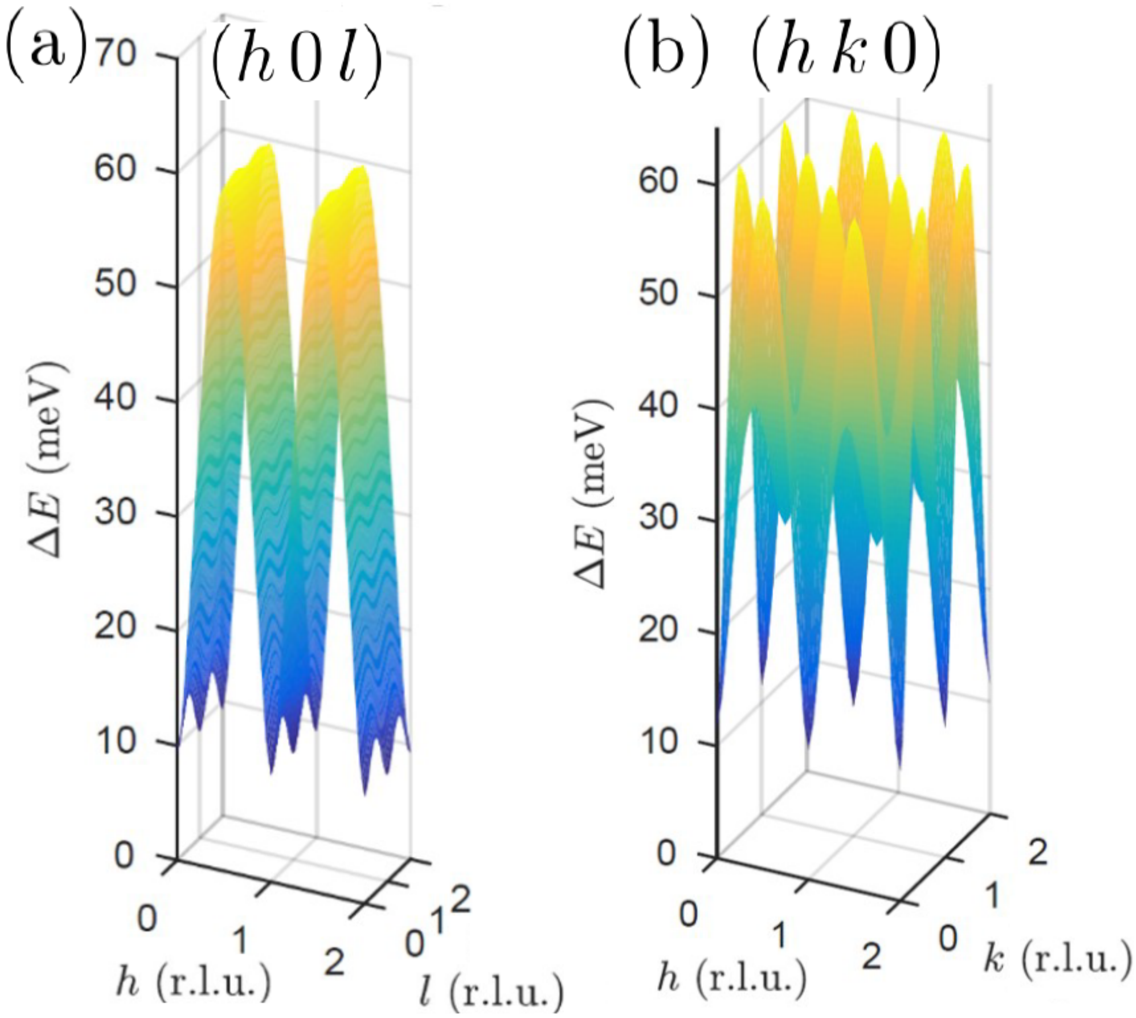

Figure 54: (a), (b) The modelled magnon spectrum of YbMnBi$_2$ in the $(h\,0\,l)$ and $(h\,k\,0)$ planes respectively in reciprocal space based on the best-fit parameters.

To elucidate this, I compare the fitted spin-wave model parameters obtained in this work with those of CaMnBi$_2$, which is isostructural to YbMnBi$_2$. CaMnBi$_2$ possesses a near identical Néel temperature to YbMnBi$_2$ of $T_{\mathrm{N}} = 290\,\mathrm{K}$ [181, 122], and is predicted to be a Dirac semimetal [188, 189, 190]. Using the same Hamiltonian (15), the three magnetic exchange parameters in CaMnBi$_2$ were found to be $SJ_1 = 23.4(6)\,\mathrm{meV}$, $SJ_2 = 7.9(5)\,\mathrm{meV}$ and $SJ_c = -0.10(5)\,\mathrm{meV}$ [122], which are the same as those of YbMnBi$_2$ to within experimental error. The anisotropy parameter for CaMnBi$_2$, $SD = 0.18(3)\,\mathrm{meV}$, is about half that for YbMnBi$_2$, which reflects that the energy gap at Γ is slightly smaller in CaMnBi$_2$ than in YbMnBi$_2$. These results demonstrate that the magnon spectrum of YbMnBi$_2$ does not show any anomalous behaviour relative to that of CaMnBi$_2$.

More broadly, this suggests that replacing the divalent alkali-earth metal Ca^{2+} on the A site of AMnBi$_2$ with the rare-earth Yb^{2+} ion does not significantly enhance the coupling between the magnetism in the tetrahedral MnBi$_4$ layers and the charge carriers in the Bi square net. This is despite the fact that the A atom is situated along the direct exchange path between the Mn and Bi atoms. In a recent review of the wider AMnPn_2 family of compounds, Klemenz *et al.* [77] suggested another route to enhance the coupling between magnetism and the topological charge carriers, namely to have a magnetic ion on the A site (like Eu^{2+}) rather than non-magnetic ions such as Ca^{2+}, Sr^{2+}, Ba^{2+} and Yb^{2+}. This was prompted by the fact that the A site atom is in closer proximity to the square Bi compared to the Mn^{2+} ion and might lead to a greater orbital overlap and thus magnetic exchange interaction. In fact, this was considered in Refs. [74, 76], where the electronic structure and optical properties of EuMnBi$_2$ and YbMnBi$_2$ were compared. The divalent rare-earth ions on the A site of both AMnBi$_2$ compounds have comparable ionic radius and very similar relative positions to the Bi square layer, but with the difference that Eu^{2+} has half-filled $4f$ orbitals compared to the fully-filled case for Yb^{2+}. This leads to a large pure-spin magnetic moment of $7\mu_B$ on the A site of EuMnBi$_2$, and a non-magnetic ion on the A site of YbMnBi$_2$. These studies demonstrate a marked increase in coupling between magnetism and the topological charge carriers in EuMnBi$_2$ compared to that in YbMnBi$_2$, which is consistent with magnetotransport studies [74, 78, 81, 82, 83]. This suggests that in EuMnBi$_2$, compared to YbMnBi$_2$, a greater coupling of magnetism to the pnictide square net can be achieved with magnetic species on the A site which, for the extended AMnPn_2 (or 112-pnictide) family, is closer to the pnictide layer compared to Mn.

Finally, it is instructive to compare the physical properties of YbMnBi$_2$ with that of YbMnSb$_2$, which is isostructural to YbMnBi$_2$ [87, 191] and also exhibits Mn AFM order with a similar magnetic ordering temperature of $T_N = 345\,K$. A comparison of the band structures of the two 112-pnictides reveal a greater extent of inversion in the conduction and valence bands in YbMnBi$_2$, with several band crossings at E_F as shown Refs. [74, 75], compared to that in YbMnSb$_2$ [87]. Moreover, the Shubnikov–de Haas (SdH) oscillation of the magnetotransport in both compounds reveals that the effective mass of the charge carriers in YbMnBi$_2$ ($m_c^* \sim 0.24\, m_e$ [79])

is approximately twice that of $YbMnSb_2$ as reported in Refs. [87, 191].

These features can be understood from the relative sizes of the SOC in the pnictide square conducting layers, which is significantly larger in $YbMnBi_2$ as Bi is ~ 1.7 times heavier than Sb. Given that the linear band crossing along the Γ–M high symmetry line is not protected by symmetry, the doubly-degenerate pnictide (Sb $5p$ or Bi $6p$) bands hybridise and give rise to an avoided Dirac crossing. As such, the stronger SOC in $YbMnBi_2$ produces a larger energy gap in the electronic bands, resulting in a heavier effective mass of the charge carriers compared to that in $YbMnSb_2$. This is consistent with the work in Ref. [192], which explored the effect of the masses of pnictides on the physical properties of $BaMn\mathit{Pn}_2$ (Pn = Sb, Bi). In that work, Liu *et al.* also proposed that a more suitable platform to realise massless Dirac fermions is in replacing Bi with lighter elements in the same group. This demonstrates that the 112-pnictide family of compounds offers strong tunability of the effective mass of the charge carriers from the size of the SOC.

5.5 Conclusion

I have presented the magnetic structure and magnon spectrum of the candidate Weyl semimetal $YbMnBi_2$. The $(0\,0\,l)$ family of nuclear reflections does not display any additional magnetic contribution below T_{N}, and this rules out the mechanism for creation of Weyl nodes via TRS-breaking through canting of the Mn spins. Hence, I rule out that bulk $YbMnBi_2$ is a Dirac semimetal rather than a host for the WSM state. I have not ruled out the possibility of spin canting at the surface, which could reconcile the present results with those of Ref. [74]. The lack of any anomalous features in the magnon spectrum implies a weak coupling between magnetism and the topological charge carriers. $YbMnBi_2$ belongs to the wider $A\mathrm{Mn}\mathit{Pn}_2$ family of compounds which is currently attracting strong interest owing to its strong potential for spintronic applications. I hope that the understanding of $YbMnBi_2$ achieved here will contribute to the development of strategies for enhancing the exchange coupling between charge transport and magnetism, and for reducing the effective mass of the quasiparticles.

Chapter 6

Ground state magnetic structure of Mn_3Ge

I have used spherical neutron polarimetry to investigate the magnetic order of the Mn spins in the hexagonal semimetal Mn_3Ge, which exhibits a large intrinsic anomalous Hall effect. I show that only one of the six non-collinear in-plane spin configurations permitted by symmetry is consistent with the polarimetric data.

---

6 Ground state magnetic structure of the Mn_3Ge

6.1 Introduction

Very recently Mn_3Ge was found to display spontaneous large anomalous Hall effect (AHE) ($\sim$50 Ω^{-1}cm^{-1}) at room temperature [193, 194]. This is very unusual for an antiferromagnet as the zero-field AHE phenomenon is usually associated with ferromagnetic metals [169]. Furthermore, these studies found that the spontaneous AHE in Mn_3Ge is strongly anisotropic and can be switched with a small applied magnetic field (see Fig. 55 and Refs. [193, 194]). From a technological standpoint, the concept of an antiferromagnetic memory device that can be switched is very attractive as there is no demagnetisation field, which limits the size of ferromagnetic materials. This possibility of scaling down the size of magnetic devices has prompted many studies of thin-film Mn_3Ge [195, 196, 197, 198, 199, 200] and the initial results look very promising.

On the other hand, from a theoretical standpoint, understanding the origin of this spontaneous large AHE in an antiferromagnet is also intellectually very stimulating

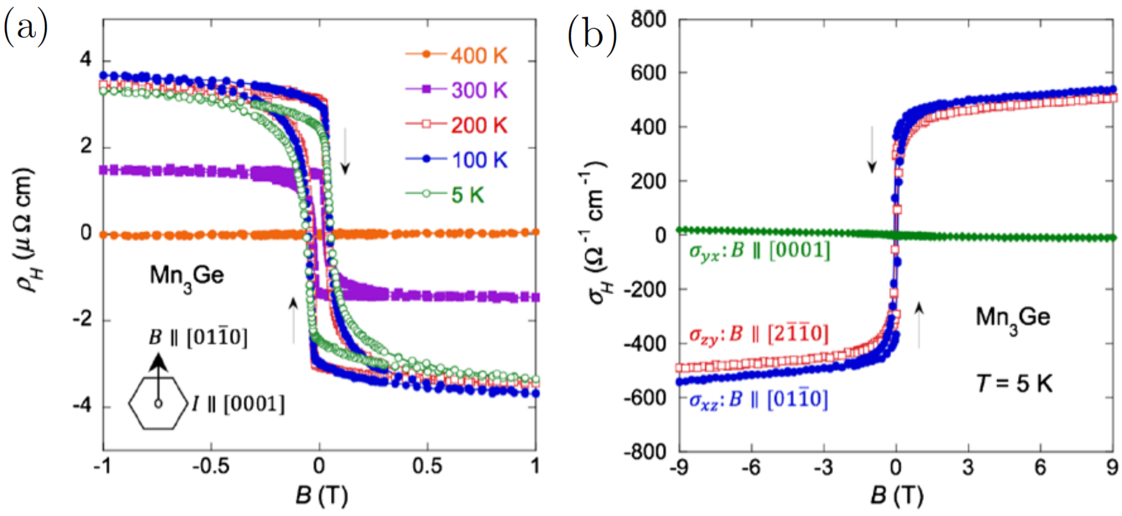

Figure 55: (adapted from Ref. [193]) (a) The temperature dependent measurements show that the spontaneous AHE in Mn_3Ge grows with decreasing temperature. (b) shows that the AHE is strongly anisotropic and can be switched with a small applied magnetic field.

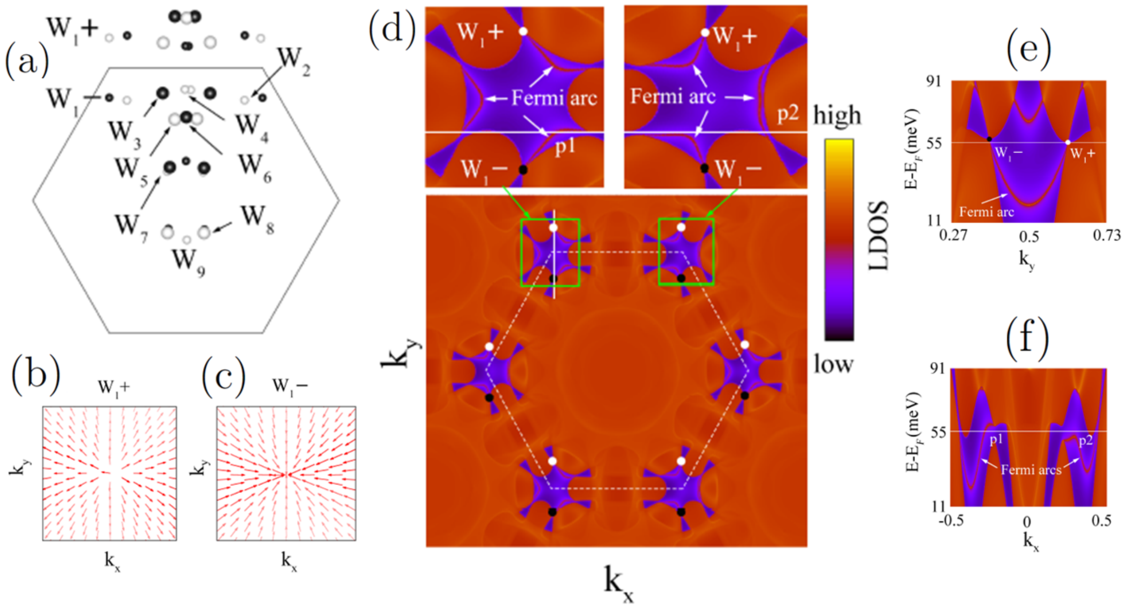

Figure 56: (adapted from [56, 204]) (a) depicts the projection of the position of the Weyl nodes in Mn_3Ge onto the $k_x - k_y$ plane. Depending on the chirality of the nodes, it will either be a (b) source or (c) sink of Berry curvature. (d) shows the calculated constant energy surface, in the $k_x - k_y$ plane, which depicts the Fermi arcs that emanate from these predicted Weyl nodes in the Brillouin zone. (e) and (f) show the Fermi arcs in an energy momentum plot along k_y and k_x respectively. (g) depicts the energy-momentum dispersion surface with (h) highlighting one particular Weyl node in Mn_3Ge.

and has led to many theoretical studies [56, 193, 194, 201, 202, 203, 204, 205]. Some studies have suggested that this could come from the non-vanishing Berry curvature in momentum space [194, 201, 202] due to the chiral Mn spin structure, an idea which is inspired by an earlier work [206]. Other studies point to topological Weyl nodes in Mn_3Ge as the source of the large AHE [56, 193, 203, 204, 205]. Furthermore, it has also led to the prediction of other related phenomena, arising from these sources and sinks of Berry curvature in Mn_3Ge: large anomalous Nernst [201], spin Nernst [201] and the spin Hall effect [194, 203]. Given that all of these theoretical predictions depend on the fine details of the magnetic structure, it is important to work with an unambiguous solution for the zero-field spin structure of Mn_3Ge.

The hexagonal unit cell of Mn_3Ge can be described by the $P6_3/mmc$ space group (No. 194) with Mn and Ge on the $6h$ and $2c$ Wyckoff sites respectively. This gives rise to a magnetic Mn sub-lattice which can be described by Kagome layers stacked along the c axis [see Fig. 57].

Initial powder neutron diffraction studies of $\mathrm{Mn_3Ge}$ revealed that these Mn moments lie in the ab plane with a magnetic propagation vector of $\mathbf{k}=\mathbf{0}$ and a non-collinear spin structure [207, 208]. However, the magnetic order within the plane could not be determined because the measured diffraction pattern could be described by several different candidate in-plane spin configurations [209]. Although the neutron spin is very sensitive to the magnetic moment direction and distinguishing between the different magnetic structures should be routinely possible, if unpolarised neutrons are used, as is the case for these experiments, this rich information is lost as the various neutron polarisations are spherically averaged [209].

In light of this, subsequent studies were performed on $\mathrm{Mn_3Ge}$ single crystals with polarised neutrons [210, 211]. However, the polarisation of the scattered beam, which contains information essential for a complete magnetic structure determination, was not analysed in the flipping ratio method employed in these experiments [212, 213, 214, 215]. Moreover, to maintain the beam polarisation, this technique requires the

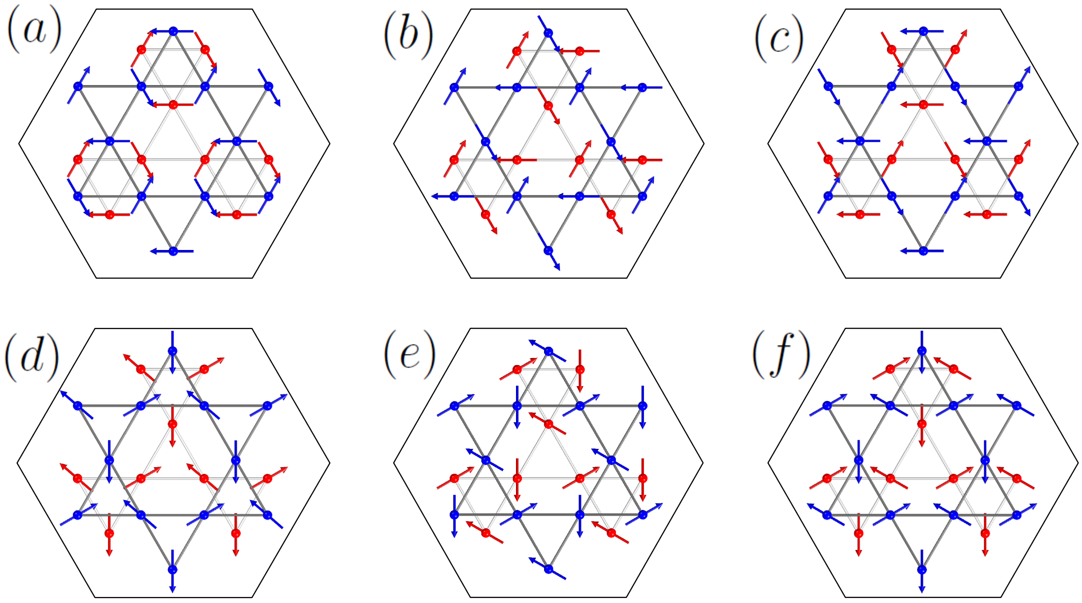

Figure 57: (a)–(f) Various spin configurations of manganese moments adapted from Ref. [209]. The red and blue spheres correspond to Mn ions residing at Wyckoff position $6h$ with $z = 1/4$ and $3/4$ respectively. Here, the Ge atoms are omitted for clarity.

sample to be in an applied field which preferentially orients the Mn moments along the field direction, undermining the elucidation of the true ground state magnetic structure [193, 194, 209, 210, 211, 216]. Ideally, what is needed is a zero-field sample environment where the direction and magnitude of the polarisation of the scattered neutrons are measured.

This technique, known as spherical neutron polarimetry (SNP), was performed on Mn_3Sn, which is isostructural to Mn_3Ge. In that work, Brown *et al.* considered 6 different symmetry allowed magnetic structures shown in Fig. 57. The true ground state structure of Mn_3Sn, however, still remains an open question as the study found essentially no difference between models (c) and (f) in the least squares fit between the calculations and measurements [209]. As this was attributed to the magnetic domains being equally populated, Brown *et al.* suggested magnetising the sample beforehand in future studies, an endeavour that has not yet been undertaken. Since a similar SNP study for Mn_3Ge is still lacking, all of the reports of the magnetic structure of Mn_3Ge thus far are based on *ab initio* density functional theory (DFT) calculations [56, 193, 194, 201, 202, 203, 204, 217]. This is done by systematically studying various spin configurations and selecting the one with the smallest self-consistent energy.

However, there is little agreement in these DFT studies: Refs. [56, 194, 203, 204, 217] predict that the most stable spin configuration is (f) while Ref. [201] found that the most stable magnetic structure correspond to (c). Yet another DFT study suggests that the Mn moments display non-planar order [202] which cannot be described by models (a)–(f). Some of these reports even concede that the equilibrium energies of models (c) and (f) are very similar and the differences are within the margin of computational uncertainty [193, 201, 202, 204]. This might arise because the spin configurations of models (c) and (f) are very similar, related by an in-plane rotation of all the Mn moments by 90° about the crystal c axis. Furthermore, there are discrepancies between the calculated and measured AHE based on these spin structures [193, 194, 202, 204].

In this work, the AFM structure of Mn_3Ge was investigated by SNP to determine which of the theoretically proposed magnetic structures best describes the magnetic order of the Mn sub-lattice. I arrive at an unambiguous magnetic struc-

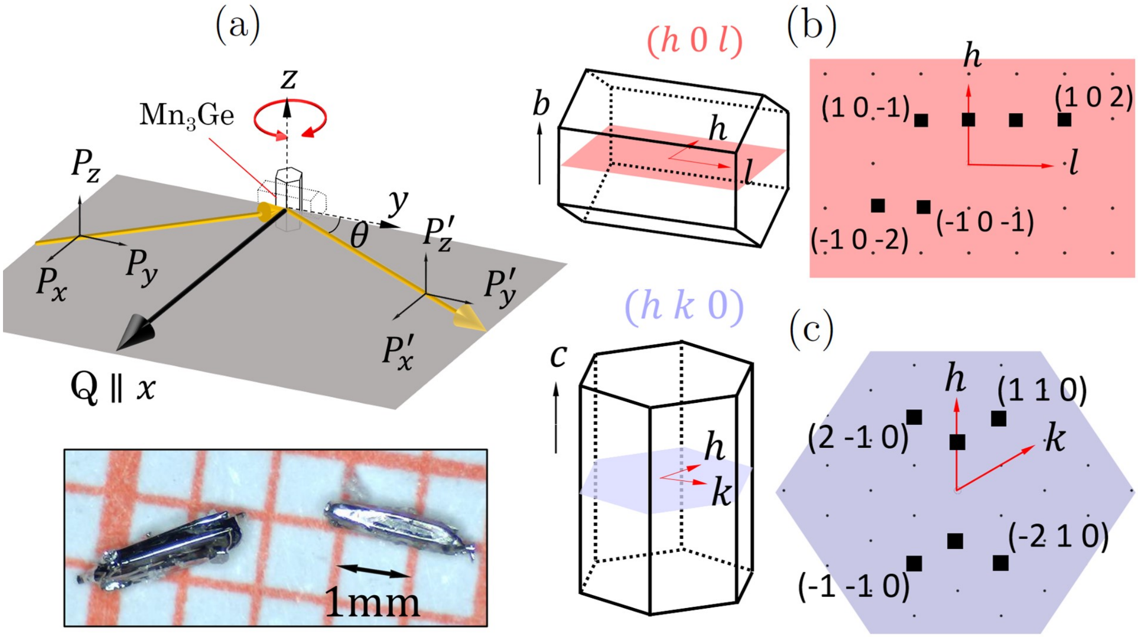

Figure 58: (a) The experimental set-up of the SNP of Mn_3Ge in the horizontal diffraction geometry. The insert shows single crystals obtained by the flux growth. (b), (c) depict the crystal orientations with b and c axis vertical, respectively, to access the $(h\,0\,l)$ and $(h\,k\,0)$ family of peaks. The reflections that were studied in this work are labelled with black squares.

ture for Mn_3Ge by demonstrating that the measured polarisation matrices can only be described by model (f).

6.2 Experimental methods

Mn_3Ge single crystals were grown by the flux method by Hongyuan Wang[30] and Yanfeng Guo.[31] Manganese powder (99.9%), germanium powder (99.99%) and cadmium pieces were mixed in a molar ratio of Mn:Ge:Cd = 7:2:48 and placed an alumina crucible. This was sealed in a quartz tube under vacuum and heated to 950 °C in 5 hours. The temperature was maintained for 20 hours before being slowly reduced to 650 °C at a rate of 2 °C/h. The quartz tube was subsequently removed from the furnace to cool to room temperature before being centrifuged to separate the single crystals from the cadmium flux. I characterised the structure and quality

---

[30] School of Physical Science and Technology, ShanghaiTech University and CAS-Shanghai Science Research Center, Shanghai 201210, China.

[31] University of Chinese Academy of Sciences, Beijing 100049, China.

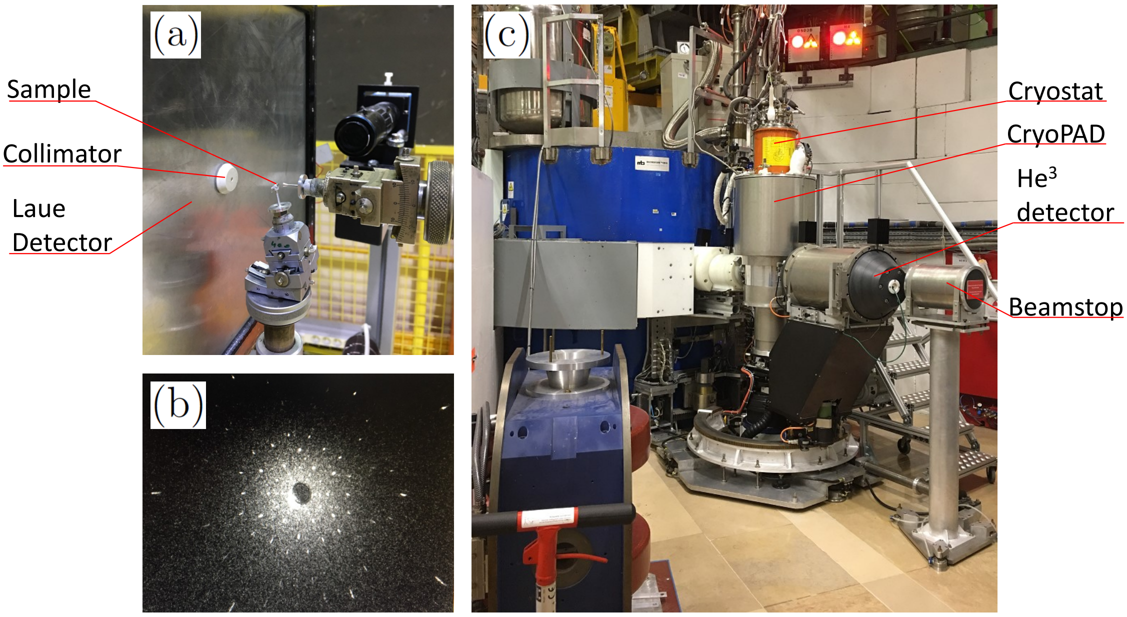

Figure 59: (a) The crystal alignment was checked on the neutron Laue source CYCLOPS (CYlindrical Ccd Laue Octagonal Photo Scintillator) at the ILL. The Laue pattern corresponding to the crystal aligned with the b axis perpendicular to the scattering plane is shown in (b). (c) The experimental set-up at the D3 beamline with the CRYOPAD [218].

of the flux-grown single crystals with X-ray diffraction and SQUID magnetometry.

Elastic neutron scattering of Mn_3Ge was performed on the D3 diffractometer at the ILL (Grenoble, France) in the horizontal scattering geometry with Henrik Jacobsen[32] and Navid Qureshi,[33] who is the beamline scientist. The crystal was initially mounted with the b axis vertical to access the $(h\,0\,l)$ reflections and was subsequently rotated by 90°, with the c axis vertical, to study the $(h\,k\,0)$ family of peaks [see Fig. 58].

As described earlier, given that the $\boldsymbol{k} = \mathbf{0}$ magnetic structure is complex, we have to examine these reflections with SNP. This was performed in the zero-field polarimeter CRYOPAD [218]. It involves determining the magnitude and direction of the polarisation of the scattered neutrons for incident neutron polarisations along the principal directions x, y and z. Here x is along the scattering vector $\mathbf{q}$, z is

---

[32] Department of Physics, University of Oxford, Clarendon Laboratory, Parks Road, Oxford OX1 3PU, UK.

[33] Institut Laue-Langevin, 6 rue Jules Horowitz, 38042 Grenoble Cedex 9, France.

Table 6: The full list of reflections studied in this work and the corresponding incident and scattered polarisation components. Columns 1–3 and 4–6 correspond to measurements performed in the $(h\,0\,l)$ and $(h\,k\,0)$ planes respectively. For each of the listed reflection, I obtain the 9 polarisation matrix elements, P_{ij}. This involves analysing the polarisation of the scattered neutrons along the 3 principal directions $j(=x,\ y,\ z)$ for incident neutron polarisations along $i(=x,\ y,\ z)$. The principal axes x, y and z are defined in Fig. 58(a). (* These reflections were repeated with the incident and scattered polarisation reversed.)

$(h\,0\,l)$	i	j	$(h\,k\,0)$	i	j
(1 0 0)	x, y, z	x, y, z	(1 0 0)	x, y, z	x, y, z
(1 0 1)	x, y, z	x, y, z	(1 0 0)*	$-x, -y, -z$	$-x, -y, -z$
(1 0 2)	x, y, z	x, y, z	(-2 1 0)	x, y, z	x, y, z
(1 0 0)*	$-x, -y, -z$	$-x, -y, -z$	(-2 1 0)*	$-x, -y, -z$	$-x, -y, -z$
(1 0 1)*	$-x, -y, -z$	$-x, -y, -z$	(1 1 0)	x, y, z	x, y, z
(1 0 2)*	$-x, -y, -z$	$-x, -y, -z$	(1 1 0)*	$-x, -y, -z$	$-x, -y, -z$
(-1 0 -1)	x, y, z	x, y, z	(-1 0 0)	x, y, z	x, y, z
(-1 0 -2)	x, y, z	x, y, z	(2 -1 0)	x, y, z	x, y, z
(1 0 -1)	x, y, z	x, y, z	(-1 -1 0)	x, y, z	x, y, z

perpendicular to the scattering plane and y orthogonal to both to complete the right-handed Cartesian set [see Fig 58(a)].

To achieve this, the neutron beam is first polarised and monochromised by the (1 1 1) Bragg reflection of a ferromagnetic Heusler crystal, Cu_2MnAl, with the polarisation vector along $\mathbf{k}_i$, the incident wave vector. These polarised neutrons are subsequently oriented along the principal directions[34] by means of a nutator field and precession field before being introduced into the zero-field sample environment, achieved by cryogenically cooled Meissner shields. This ensures that any change in polarisation of the neutrons comes from the scattering with the sample.

The polarisation analysis involves decomposing the polarisation of the scattered neutrons into the three components along the principal axes. This polarisation

---

[34] Or more generally, along any direction.

analyser comprises a beam nutator, precession coil and a ^{3}He spin filter[35] which transmits the selected component and absorbs the other polarisation components. The intensity of the transmitted polarisation component was estimated by a ^{3}He detector. This gives us the 9 matrix elements P_{ij} for each Bragg peak which is defined as the polarisation ratio of scattered neutrons along the $j(=x,\, y,\, z)$ direction to incident neutrons with polarisation vector parallel to the $i(=x,\, y,\, z)$ direction.

To limit neutron depolarisation due to magnetic domain boundaries in the sample, the crystal was cooled to $T = 2\,\mathrm{K}$ in an applied field of $\mu_0 H = 1\,\mathrm{T}$ along b from room temperature before it was mounted in the CRYOPAD. Furthermore, I also used incident neutrons with a relatively short wavelength of $\lambda = 0.850\,\text{Å}$, which was readily available at D3, a hot neutron source (T = $2000°C$).

6.3 Results and analysis

The flux growth produced shiny metallic rods [see insert of Fig. 58(a)] with hexagonal cross-sections and dimensions of up to 2 × 0.4 × 0.4 mm^3 (length along the crystal c axis). The full polarisation matrices for the various reflections are shown in Fig. 60. The panels (a) and (c) correspond to measurements performed in the $(h\,0\,l)$ and $(h\,k\,0)$ planes respectively. For each reflection, I present the 9 elements of the measured matrix P_{ij} from left to right, P_{xx}, P_{xy}, P_{xz}, P_{yx}, P_{yy}, P_{yz}, P_{zx}, P_{zy} and P_{zz}. I find that the neutrons suffer from negligible depolarisation. This is best exemplified in the matrix elements P_{zz} for the (1 0 0)* reflection in Fig. 60(a) and P_{yy} for peaks (1 0 0), (-2 1 0), (1 1 0)*, (-1 -1 0) in Fig. 60(c) which are all almost unity.

Using the MAG2POL program [214], Qureshi and I set up the 6 different magnetic structure models depicted in Fig. 57. Magnetic domains were also incorporated in each spin configuration model (giving rise to three domains) where all of the in-plane Mn moments in each domain are rotated by ±120° about the c axis relative to those in the other two domains. For each model (a)–(f), I calculated the associated 9 matrix elements for all of the measured reflections and refined the domain population in a least-squares fit to the measured polarisation matrices of all the reflections. The reduced χ^2 values (χ^2_{red}) obtained from 6 of the different refined models are tabulated

---

[35] The raw data were corrected for the decrease in the efficiency of the ^{3}He spin filter cell based on the magnitude of the neutron polarisation measured at weak magnetic reflection $(3, 0, 4)$.

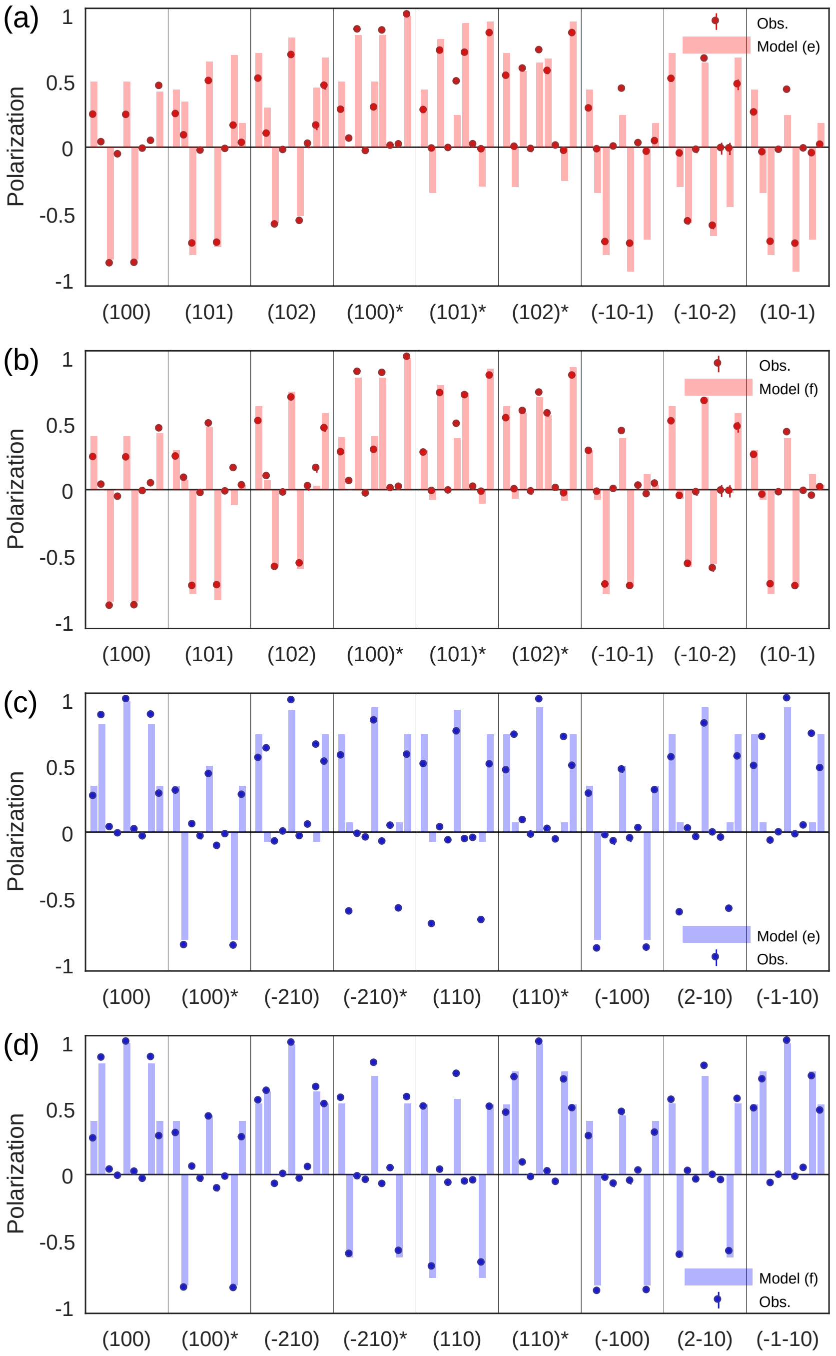

Figure 60: Comparisons between observed and calculated polarisation matrix elements P_{ij} for the Bragg peaks. Panels (a) and (c) correspond to model (e) for the ($h\,0\,l$) and ($h\,k\,0$) planes respectively. The corresponding panels for model (f) are in (b) and (d). For each reflection, the symbol and bar represent P_{xx}, P_{xy}, P_{xz}, P_{yx}, P_{yy}, P_{yx}, P_{zx}, P_{zy} and P_{zz} from left to right. (* These reflections were repeated with the incident and scattered polarisation reversed.)

Table 7: χ^2 obtained from the refinement of the model to the measured polarisation matrices.

	(a)	(b)	(c)	(d)	(e)	(f)
$(h\,0\,l)$	118434	577	1181	21173	298	365
$(h\,k\,0)$	16561	9560	9559	9664	4564	113

in Table 7.

Although the SNP technique is generally not sensitive to the length of the moment [215], in this case, the nuclear and magnetic peaks coincide as the magnetic propagation vector is $\mathbf{k} = \mathbf{0}$. Hence I was also able to refine the length of the Mn moments which is possible due to the interference between the magnetic and nuclear terms [215].

For spin configuration models (a) and (d), I observe large discrepancies between the observed and calculated matrix elements P_{xz} and P_{yz} in the following $(h\,0\,l)$ reflections: (1 0 0), (1 0 1), (1 0 2), (-1 0 -1), (-1 0 -2) and (1 0 -1). Moreover, the χ^2_{red} values obtained from the refinement of these models to the measured matrices are significantly larger than those from the other models. Notably, the χ^2_{red} for models (a) and (d), respectively, are about 400 and 70 times larger than that for model (e) [see Table 7]. Hence I can exclude spin configurations (a) and (d).

Models (b) and (c) also show strong disagreement between the observed and calculated P_{xy} and P_{zy} matrix elements for the (1 0 0), (-2 1 0)*, (1 1 0), (-1 0 0) and (2 -1 0) reflections measured in the $(h\,k\,0)$ plane. The χ^2_{red} for both spin configurations are at least 80 times larger than that for model (f) [see Table 7]. These models, too, can be ruled out.

This leaves me with models (e) and (f) to consider. I present the calculated polarisation matrices for both spin configurations in Fig. 60. For the $(h\,0\,l)$ reflections, there is strong agreement between the measured and calculated P_{ij} [Figs. 60(a) ,(b)]. Moreover, in terms of the χ^2_{red} values obtained from the refinement of the domain population and Mn^{2+} moment length, both models provide a significantly better description of the measured matrices compared to the other spin configurations [Table 7]. However, as the calculated matrix elements from both models are very similar, it is difficult to ascertain, solely based on the measurements in the $(h\,0\,l)$

plane, which model uniquely describes the magnetic structure of $\mathrm{Mn_3Ge}$.

This ambiguity can be resolved by considering the $(h\,k\,0)$ reflections. For instance in model (e), there are disparities between the measured and calculated P_{xy} and P_{zy} matrix elements for the (-2 1 0)*, (1 1 0) and (2 -1 0) reflections [Fig. 60(c)]. Conversely, this discrepancy is not seen in model (f), which fits the measured matrices very well [Fig. 60(d)] with a χ^2 that is at least one order of magnitude smaller than that of all the other models [Table 7]. This strongly suggests that the $\mathrm{Mn^{2+}}$ moments in $\mathrm{Mn_3Ge}$ orders with a magnetic structure shown in Fig. 57(f).

For model (f), the estimated moment length is $2.69(2)\,\mu_\mathrm{B}$, which larger than the $1.93\,\mu_\mathrm{B}$ that was predicted in an earlier study [210]. This discrepancy can arise from the fact that this previous study did not account for domains, which might understate the net moment in $\mathrm{Mn_3Ge}$. The domain populations that give the best fit to the data for neutron scattering in the $(h\,0\,l)$ plane are 65.9%, 12(1)% and 22(6)%, respectively. The significantly larger population of one domain over the other two in-plane orientations of Mn spins is consistent with the sample being cooled from room temperature in a 1 T field along the crystal b axis.

The estimated domain populations for the data obtained in the $(h\,k\,0)$ scattering plane are 42.3%, 14(2)% and 44(5)%. The domain populations are relatively more uniform as the sample was not cooled in a field for this scattering geometry.

6.4 Discussion

Since the discovery of the large AHE in $\mathrm{Mn_3Ge}$ [193, 194], there have been many theoretical studies attempting to explain the source of this phenomena [56, 193, 194, 201, 202, 203, 204, 205]. As the magnetic structure of $\mathrm{Mn_3Ge}$ was not known, it was difficult for these studies to satisfactorily address the discrepancies between the calculated and measured AHE. In fact, the study in Ref. [193] considered two different magnetic structures and found that they gave different estimates of AHE. Some studies even speculated that this AHE arises from the presence of Weyl nodes in the Brillouin zone [56, 193, 203, 204, 205]. Again, band structure calculations for different Mn spin configurations were made in these studies as the actual ground state magnetic structure was not known. For instance, Yang *et al.* found that different Mn order gave rise to Weyl points in different locations of the Brillouin zone [56, 203]. In fact there is even a study for which there are no Weyl nodes predicted [202]. Furthermore, it is difficult to ascertain which band structure calculation best describes the electronic bands in Mn_3Ge with ARPES as the Mn $3d$ states are strongly correlated, giving rise to bands which are smeared out near E_F as seen in the sister compound Mn_3Sn [88].

My hope is that the knowledge of this magnetic structure would lead to more fruitful theoretical studies of the origin of the large AHE in Mn_3Ge. To that end, I sought the help of Fernando de Juan[36] to study the spin Hamiltonian describing the magnetic order in Mn_3Ge, to (i) understand the origin of this in-plane anisotropy and (ii) study how this structure can give rise to the large anomalous Hall effect in Mn_3Ge.

---

[36] Donostia International Physics Center, 20018 Donostia-San Sebastian, Spain; IKERBASQUE, Basque Foundation for Science, Maria Diaz de Haro 3, 48013 Bilbao, Spain.

Conclusion

When I first embarked on my thesis (in 2016), there were many theoretical studies predicting the existence of quasiparticles that behave like Weyl fermions in magnetic semimetals. However, as many of these assertions were based on *ab initio* calculations, they warranted experimental verifications. The overarching aim of my work is to address some of those outstanding questions by identifying the magnetic structure of some of these candidate materials and the implications it poses in terms of the topology of the electronic band structures.

In my thesis, I have investigated four different crystalline materials[37] that display spontaneous magnetic order and electronic bands that are predicted to be topologically non-trivial. In this concluding chapter, I outline the ways in which the body of work presented in my thesis has advanced our current understanding of these materials.

---

[37] These materials have different chemical constituents, magnetic ordering temperatures, crystal space groups ($P6_3/mmc$, $P\bar{3}m1$, $P4/mmm$) and magnetotransport properties.

7 Conclusion

7.1 $EuCd_2Sb_2$

I identified, computationally with DFT *ab initio* calculations, that the crystalline C_3 symmetry (along the c axis) is crucial for the stabilisation of Dirac nodes in the electronic spectrum of $EuCd_2Sb_2$. I then demonstrated experimentally, with resonant magnetic X-ray diffraction, how the C_3 symmetry is spontaneously broken below the Néel temperature due to the in-plane orientation of the Eu moments, giving rise to avoided band crossings near the chemical potential. I augmented these with magnetotransport and magnetisation measurements, to map out the $\mu_0 H - T$ phase diagram of $EuCd_2Sb_2$.

I also demonstrated that the electronic band calculations presented in Ref. [133], particularly the position of the Eu $4f$ bands with respect to energy, is wrong as it failed to account for the strong correlations in the europium bands. Since then, there have been two independent ARPES studies which demonstrate that the measured electronic spectrum in $EuCd_2Sb_2$ agrees strongly with my DFT calculations [60, 219].

More significantly, I have identified that $EuCd_2Sb_2$ has the potential for realising non-trival topological bands and how the ground state magnetic structure is crucial for controlling these exotic quasiparticles. Very recently, Su *et al.* [60] predicted that $EuCd_2Sb_2$ can harbour Weyl fermions if the Eu moments are fully polarised along the c axis. This suggests that there is a possibility of creating Weyl fermions in single crystalline $EuCd_2Sb_2$.

There are now efforts to mechanically exfoliate thin layers of $EuCd_2Sb_2$ crystal onto back-gated field effect transistors (FETs) to tune the Fermi energy to the position of the topological nodes.

7.2 $EuCd_2As_2$

A common theme in the concluding remarks of the key review articles concerning the field of topological materials is the call to search for better Weyl semimetal candidate materials [3, 9, 11, 12]. The ideal Weyl crystal is one in which there is a minimum number of Weyl nodes, namely two, in the Brillouin zone, at the chemical potential in an energy window free from other bands. I have identified that crystalline $EuCd_2As_2$, in an applied field along the crystal c axis with a field of $B > B_c$, fulfills all three criteria – the first example of an ideal WSM. This prediction was supported with evidence from ARPES, high-field magnetotransport data and DFT calculations. The exchange-induced ideal Weyl semimetallic phase in $EuCd_2As_2$ can serve as a test bed for fundamental studies of Weyl physics.

In the final stages of preparing the manuscript detailing my work on $EuCd_2As_2$, I became aware of an *ab initio* study on the same compound, which predicted the same ideal WSM phase (albeit without any experimental verifications) induced by magnetic exchange [59]. It is encouraging that Wang's group (see Ref. [59]), which is independent of mine, arrived at the same conclusions. Moreover, some time after the submission of my manuscript, a paper on the ARPES study of $EuCd_2As_2$ appeared [219]. Ma *et al.* mapped the electronic spectrum of $EuCd_2As_2$ at three temperature regimes: (i) $T < T_N$, the AFM phase, (ii) $T > 100\,\mathrm{K}$, the *true* PM phase, and (iii) $T_N < T < 100\,\mathrm{K}$, a PM phase with FM correlations. The measured spectrum in the AFM phase of the study agrees well with our data. Intriguingly, Ma *et al.* also reported a transient WSM phase in the temperature regime $T_N < T < 100\,\mathrm{K}$, induced by the FM correlation. The average position of the Weyl nodes, created by the fluctuating Eu moments, agree well with my predictions. This too, is an encouraging result, as it complements my findings.

Nonetheless, there is a strong impetus to improve the crystal quality such that the chemical potential is at the position of the induced Weyl nodes. Ideas include, mechanical exfoliation [220], filling Cd vacancies in an excess of cadmium vapour, doping the $EuCd_2As_2$ crystal with Yb, creating heterostructures with normal metallic layers [221], etc. Several of these efforts are currently underway and are part of future studies of $EuCd_2As_2$.

7.3 $YbMnBi_2$

Weyl semimetals can occur in two types of crystal, one having broken spatial inversion symmetry, and the other broken time-reversal symmetry. Examples of the former type were found in 2015, the first being TaAs [15, 36, 37, 38], but for a long while, there was no confirmed realisation of the latter type [11].

This was the case until Borisenko *et al.* [74] claimed to have found evidence (from ARPES measurements) for Weyl nodes in crystalline $YbMnBi_2$, the first magnetically induced WSM. The study proposed that the Weyl nodes are created via spontaneous time-reversal symmetry breaking due to a 10° degree canting of the Mn moments away from the crystal c axis. Since then, there have been many studies citing $YbMnBi_2$ as a WSM (For example, see Refs. [84, 222, 223, 224, 225]). Other studies were more cautious and cited $YbMnBi_2$ as a *candidate* WSM instead (see Refs. [192, 226, 227, 228, 229]). In fact, there is good reason for their expressed caution: the purported Fermi arcs, observed in the measured electronic spectrum with ARPES, are difficult to distinguish from the hole pocket that is immediately adjacent to the arcs [74]. Furthermore, there was no strong experimental evidence for the proposed canting of the Mn moments. Subsequent neutron diffraction [78, 79, 177] and optical [75, 76] studies of $YbMnBi_2$, aimed at verifying the claims of Borisenko *et al.* [74], were, however, inconclusive.

I prove definitively, with single crystalline elastic neutron diffraction measurements, that the creation of Weyl nodes in $YbMnBi_2$ by the time-reversal symmetry breaking mechanism suggested by Borisenko *et al.* can be excluded. My hope is that this will stop fuelling the speculation that $YbMnBi_2$ hosts Weyl fermions in the bulk.

The next natural step in the exploration of the compounds within the 112-pnictide family is to map the spin-wave excitations of $YbMnSb_2$ and $EuMn\mathit{Pn}_2$ (Pn = Sb, Bi). All three compounds display signatures of a strong coupling between magnetism and the charge carriers in the pnictide layer [74, 81, 82, 83, 87, 191]. While the magnon spectrum of $YbMnSb_2$ can be measured with inelastic neutron spectroscopy, resonant inelastic X-ray scattering will be a more suitable probe for $EuMn\mathit{Pn}_2$ as these contain the strongly neutron absorbing ion Eu.

7.4 Mn_3Ge

Some theoretical studies have attributed the large anomalous Hall effect observed in the antiferromagnetic Mn_3Ge [193, 194] to the existence of Weyl nodes in the hexagonal Brillouin zone [56, 193, 203, 204, 205]. Given that the true ground state magnetic structure has not yet been identified, these theoretical studies are based on magnetic structures predicted by DFT. Experimentally, the standard powder neutron diffraction techniques are insufficient to conclusively determine the complex spin configuration of the Mn moments.

I performed spherical neutron polarimetry on single crystalline Mn_3Ge and uniquely identified the ground state magnetic structure of the Mn spins. Prior to this, the prevailing model (since 1990) of the magnetic structure of the Mn_3X (X = Ge, Sn, Si) family of compounds was presented by Brown *et al.* [209]. It was based on the SNP of Mn_3Sn, which is isostructural to Mn_3Ge. However that study was not conclusive as two different models describe the measured data set. In my Mn_3Ge study, I demonstrated that the set of peaks measured within the $(h\,0\,l)$ plane in Ref. [209] (for Mn_3Sn) was insufficient to uniquely determine the ground state structure but additional reflections, which are accessible in the $(h\,k\,0)$ plane, are sufficient to solve it. I also show that the premagnetisation of the sample prior to the measurements, suggested by Brown [209], does not help in the elucidation of the structure.

My hope is that this work will invite more theoretical studies to determine the origin of the large anomalous Hall effect Mn_3Ge and aid in the incorporation of this material into a viable topological antiferromagnetic spintronic device. To further the work on Mn_3Ge, I propose studying the spin structure with Mn_3Ge under pressure, as was done on a powdered sample of Mn_3Ge, where a new magnetic phase – with all the Mn moments pointing along the crystal c axis – was identified [230]. This can potentially lead to a pressure-induced shift of the position of the Weyl nodes.

References

[1] H. Weyl. Elektron und Gravitation. I. *Zeitschrift fur Physik*, 56:330–352, 1929.

[2] P. A. M. Dirac and R. H. Fowler. The quantum theory of the electron. *Proc. Royal Soc. Ldn. Series A*, 117(778):610–624, 1928.

[3] M. Z. Hasan *et al.* . Discovery of Weyl Fermion Semimetals and Topological Fermi Arc States. *Ann. Rev. Condens. Matter Phys.*, 8(1):289–309, 2017.

[4] M. Antonello *et al.* . Measurement of the neutrino velocity with the ICARUS detector at the CNGS beam. *Phys. Lett. B*, 713(1):17–22, 2012.

[5] T. Adam *et al.* . Measurement of the neutrino velocity with the OPERA detector in the CNGS beam. *JHEP*, 10:093, 2012.

[6] M. C. Gonzalez-Garcia and M. Maltoni. Phenomenology with massive neutrinos. *Phys. Rep.*, 460(1):1–129, 2008.

[7] R. A. Battye and A. Moss. Evidence for Massive Neutrinos from Cosmic Microwave Background and Lensing Observations. *Phys. Rev. Lett.*, 112:051303, 2014.

[8] C. Herring. Accidental Degeneracy in the Energy Bands of Crystals. *Phys. Rev.*, 52:365–373, 1937.

[9] A. A. Burkov. Weyl metals. *Ann. Rev. Condens. Matter Phys.*, 9(1):359–378, 2018.

[10] A. A. Burkov. Topological semimetals. *Nat. Mater.*, 15:1145–1148, 2016.

[11] N. P. Armitage, E. J. Mele, and A. Vishwanath. Weyl and Dirac semimetals in three-dimensional solids. *Rev. Mod. Phys.*, 90:015001, 2018.

[12] B. Yan and C. Felser. Topological Materials: Weyl Semimetals. *Ann. Rev. Condens. Matter Phys.*, 8(1):337–354, 2017.

[13] W. Shuo *et al.* . Quantum transport in Dirac and Weyl semimetals: a review. *Adv. Phys.: X*, 2(3):518–544, 2017.

[14] H. B. Nielsen and M. Ninomiya. The Adler-Bell-Jackiw anomaly and Weyl fermions in a crystal. *Phys. Lett. B*, 130(6):389–396, 1983.

[15] S.-M. Huang *et al.* . A Weyl Fermion semimetal with surface Fermi arcs in the transition metal monopnictide TaAs class. *Nat. Comms.*, 6:7373, 2015.

[16] S. Rao. Weyl semi-metals: A short review. *J. Ind. Inst. Sci.*, 96:2, 2016.

[17] R. J. Cava *et al.* . Crystal structure and chemistry of topological insulators. *J. Mater. Chem. C*, 1:3176–3189, 2013.

[18] L. M. Schoop, F. Pielnhofer, and B. V. Lotsch. Chemical Principles of Topological Semimetals. *Chem. Mater.*, 30:3155–3176, 2018.

[19] A. Bansil, H. Lin, and T. Das. Colloquium: Topological band theory. *Rev. Mod. Phys.*, 88:021004, 2016.

[20] M. G. Vergniory *et al.* . A complete catalogue of high-quality topological materials. *Nat.*, 566:480–485, 2019.

[21] M. Z. Hasan and C. L. Kane. Colloquium: Topological insulators. *Rev. Mod. Phys.*, 82:3045–3067, 2010.

[22] O. Vafek and A. Vishwanath. Dirac Fermions in Solids: From High-Tc Cuprates and Graphene to Topological Insulators and Weyl Semimetals. *Ann. Rev. Condens. Matter Phys.*, 5(1):83–112, 2014.

[23] B. Keimer and J. E. Moore. The physics of quantum materials. *Nat. Phys.*, 13:1045, 2017.

[24] F. Tang *et al.* . Topological materials discovery by large-order symmetry indicators. *Sci. Adv.*, 5(3):eaau8725, 2019.

[25] X. Zhou *et al.* . Topological crystalline insulator states in the Ca_2As family. *Phys. Rev. B*, 98:241104, 2018.

[26] B. Bradlyn *et al.* . Topological quantum chemistry. *Nat.*, 547:298, 2017.

[27] K. Hartnett. The Hidden Twist to Making a Möbius Strip. *Quanta Mag.*, 2017.

[28] L. Hui *et al.* . Negative magnetoresistance in Dirac semimetal Cd_3As_2. *Nat. Comms.*, 7:10301, 2016.

[29] Z. K. Liu *et al.* . A stable three-dimensional topological Dirac semimetal Cd_3As_2. *Nat. Mater.*, 13(7):677–681, 2014.

[30] S. Borisenko *et al.* . Experimental Realization of a Three-Dimensional Dirac Semimetal. *Phys. Rev. Lett.*, 113:027603, 2014.

[31] Z. Wang *et al.* . Three-dimensional Dirac semimetal and quantum transport in Cd_3As_2. *Phys. Rev. B*, 88:125427, 2013.

[32] M. Neupane *et al.* . Observation of a three-dimensional topological Dirac semimetal phase in high-mobility Cd_3As_2. *Nat. Comms.*, 5:3786, 2014.

[33] Z. Wang *et al.* . Dirac semimetal and topological phase transitions in A_3Bi (A = Na, K, Rb). *Phys. Rev. B*, 85:195320, 2012.

[34] Z. K. Liu *et al.* . Discovery of a Three-Dimensional Topological Dirac Semimetal, Na_3Bi. *Sci.*, 343(6173):864–867, 2014.

[35] Q. D. Gibson *et al.* . Three-dimensional Dirac semimetals: Design principles and predictions of new materials. *Phys. Rev. B*, 91:205128, 2015.

[36] L. X. Yang *et al.* . Weyl semimetal phase in the non-centrosymmetric compound TaAs. *Nat. Phys.*, 11:728–733, 2015.

[37] S.-Y. Xu *et al.* . Discovery of a Weyl fermion semimetal and topological Fermi arcs. *Sci.*, 349:613–617, 2015.

[38] B. Q. Lv *et al.* . Observation of Weyl nodes in TaAs. *Nat. Phys.*, 11:724–728, 2015.

[39] F. Arnold *et al.* . Chiral Weyl Pockets and Fermi Surface Topology of the Weyl Semimetal TaAs. *Phys. Rev. Lett.*, 117:146401, 2016.

[40] X. Huang *et al.* . Observation of the Chiral-Anomaly-Induced Negative Magnetoresistance in 3D Weyl Semimetal TaAs. *Phys. Rev. X*, 5:031023, 2015.

[41] I. Belopolski *et al.* . Observation of surface states derived from topological Fermi arcs in the Weyl semimetal NbP. *arXiv:1509.07465*.

[42] S.-Y. Xu *et al.* . Discovery of a Weyl fermion state with Fermi arcs in niobium arsenide. *Nat. Phys.*, 11:748–755, 2015.

[43] S.-Y. Xu *et al.* . Experimental discovery of a topological Weyl semimetal state in TaP. *Sci. Adv.*, 1(10):e1501092, 2015.

[44] Z. Wang *et al.* . Time-Reversal-Breaking Weyl Fermions in Magnetic Heusler Alloys. *Phys. Rev. Lett.*, 117:236401, 2016.

[45] H. Zhang *et al.* . Topological insulators in Bi_2Se_3, Bi_2Te_3 and Sb_2Te_3 with a single Dirac cone on the surface. *Nat. Phys.*, 5:438, 2009.

[46] O. Madelung, U. Rössler, and M. Schulz, editors. *Antimony selenide* (Sb_2Se_3) *band structure, energy gap*, pages 1–4. Springer Berlin Heidelberg, Berlin, Heidelberg, 1998.

[47] Y.-L. Chen *et al.* . Experimental Realization of a Three-Dimensional Topological Insulator, Bi_2Te_3. *Sci.*, 325(5937):178–181, 2009.

[48] Z. Zhu, Y. Cheng, and U. Schwingenschlögl. Band inversion mechanism in topological insulators: A guideline for materials design. *Phys. Rev. B*, 85:235401, 2012.

[49] S. Murakami *et al.* . Emergence of topological semimetals in gap closing in semiconductors without inversion symmetry. *Sci. Adv.*, 3(5):e1602680, 2017.

[50] M. Dzero *et al.* . Topological Kondo Insulators. *Phys. Rev. Lett.*, 104:106408, 2010.

[51] L. Fu *et al.* . Topological Crystalline Insulators. *Phys. Rev. Lett.*, 106:106802, 2011.

[52] Z.-H. Pan *et al.* . Electronic Structure of the Topological Insulator Bi_2Se_3 Using Angle-Resolved Photoemission Spectroscopy: Evidence for a Nearly Full Surface Spin Polarization. *Phys. Rev. Lett.*, 106:257004, 2011.

[53] C. Pauly *et al.* . Probing two topological surface bands of Sb_2Te_3 by spin-polarized photoemission spectroscopy. *Phys. Rev. B*, 86:235106, 2012.

[54] Z. K. Liu *et al.* . Evolution of the Fermi surface of Weyl semimetals in the transition metal pnictide family. *Nat. Mater.*, 15:27, 2015.

[55] S. Murakami *et al.* . Tuning phase transition between quantum spin Hall and ordinary insulating phases. *Phys. Rev. B*, 76:205304, 2007.

[56] H. Yang *et al.* . Topological Weyl semimetals in the chiral antiferromagnetic materials Mn_3Ge and Mn_3Sn. *New J. Phys.*, 19(1):015008, 2017.

[57] J. Cano *et al.* . Chiral anomaly factory: Creating Weyl fermions with a magnetic field. *Phys. Rev. B*, 95:161306, 2017.

[58] C. Shekhar *et al.* . Anomalous Hall effect in Weyl semimetal half-Heusler compounds RPtBi (R = Gd and Nd). *Proc. Ntnl. Acad. Sci.*, 115(37):9140–9144, 2018.

[59] L.-L. Wang *et al.* . Single pair of Weyl fermions in the half-metallic semimetal $EuCd_2As_2$. *Phys. Rev. B*, 99:245147, 2019.

[60] S. Hao *et al.* . Magnetic exchange induced Weyl state in a semimetal $EuCd_2Sb_2$. *arXiv:1903.12532.*

[61] X. Wan *et al.* . Topological semimetal and Fermi-arc surface states in the electronic structure of pyrochlore iridates. *Phys. Rev. B*, 83:205101, 2011.

[62] H. Zhang, K. Haule, and D. Vanderbilt. Metal-insulator transition and topological properties of pyrochlore iridates. *Phys. Rev. Lett.*, 118:026404, 2017.

[63] H. Guo *et al.* . Magnetic order in the pyrochlore iridate $Nd_2Ir_2O_7$ probed by muon spin relaxation. *Phys. Rev. B*, 88:060411, 2013.

[64] E. Lefrançois *et al.* . Anisotropy-Tuned Magnetic Order in Pyrochlore Iridates. *Phys. Rev. Lett.*, 114:247202, 2015.

[65] H. Guo, C. Ritter, and A. C. Komarek. Direct determination of the spin structure of $Nd_2Ir_2O_7$ by means of neutron diffraction. *Phys. Rev. B*, 94:161102, 2016.

[66] C. Donnerer *et al.* . All-in–all-Out Magnetic Order and Propagating Spin Waves in $Sm_2Ir_2O_7$. *Phys. Rev. Lett.*, 117:037201, 2016.

[67] Z. Tian *et al.* . Field-induced quantum metal–insulator transition in the pyrochlore iridate $Nd_2Ir_2O_7$. *Nat. Phys.*, 12:134, 2016.

[68] K. Ueda *et al.* . Spontaneous Hall effect in the Weyl semimetal candidate of all-in all-out pyrochlore iridate. *Nat. Comms.*, 9:3032, 2018.

[69] K. Ueda *et al.* . Magnetic Field-Induced Insulator-Semimetal Transition in a Pyrochlore $Nd_2Ir_2O_7$. *Phys. Rev. Lett.*, 115:056402, 2015.

[70] R. Asih *et al.* . Magnetic Moments and Ordered States in Pyrochlore Iridates $Nd_2Ir_2O_7$ and $Sm_2Ir_2O_7$ Studied by Muon-Spin Relaxation. *J. Phys. Soc. Jpn.*, 86(2):024705, 2017.

[71] W. Witczak-Krempa *et al.* . Correlated Quantum Phenomena in the Strong Spin-Orbit Regime. *Ann. Rev. Condens. Matter Phys.*, 5(1):57–82, 2014.

[72] M. Nakayama *et al.* . Slater to Mott Crossover in the Metal to Insulator Transition of $Nd_2Ir_2O_7$. *Phys. Rev. Lett.*, 117:056403, 2016.

[73] G. Lee *et al.* . Anisotropic Dirac electronic structures of AMnBi$_2$ (A = Sr,Ca). *Phys. Rev. B*, 87:245104, 2013.

[74] S. Borisenko *et al.* . Time-Reversal Symmetry Breaking Type-II Weyl State in $YbMnBi_2$. *Nat. Comms*, 10:3424, 2019.

[75] D. Chaudhuri *et al.* . Optical investigation of the strong spin-orbit-coupled magnetic semimetal $YbMnBi_2$. *Phys. Rev. B*, 96:075151, 2017.

[76] M. Chinotti *et al.* . Electrodynamic response of the type-II Weyl semimetal $YbMnBi_2$. *Phys. Rev. B*, 94:245101, 2016.

[77] S. Klemenz, S. Lei, and L. M. Schoop. Topological Semimetals in Square-Net Materials. *Ann. Rev. Mater. Research*, 49(1):185–206, 2019.

[78] A. Wang *et al.* . Magnetotransport study of Dirac fermions in $YbMnBi_2$ antiferromagnet. *Phys. Rev. B*, 94:165161, 2016.

[79] J. Y. Liu *et al.* . Magnetotransport study of Dirac fermions in $\mathrm{YbMnBi_2}$ antiferromagnet. *Nat. Comms.*, 8:646, 2017.

[80] A. Pal *et al.* . Optical properties of $\mathrm{YbMnBi_2}$: A type II Weyl semimetal candidate. *Physica B*, 536:64–67, 2018.

[81] A. F. May, M. A. McGuire, and B. C. Sales. Effect of Eu magnetism on the electronic properties of the candidate Dirac material $\mathrm{EuMnBi_2}$. *Phys. Rev. B*, 90:075109, 2014.

[82] H. Masuda *et al.* . Quantum Hall effect in a bulk antiferromagnet $\mathrm{EuMnBi_2}$ with magnetically confined two-dimensional Dirac fermions. *Sci. Adv.*, 2(1):e1501117, 2016.

[83] H. Masuda *et al.* . Impact of antiferromagnetic order on Landau-level splitting of quasi-two-dimensional Dirac fermions in $\mathrm{EuMnBi_2}$. *Phys. Rev. B*, 98:161108, 2018.

[84] J. Y. Liu *et al.* . A magnetic topological semimetal Sr_{1-y} Mn_{1-z} Sb $_2$ $(y, z < 0.1)$. *Nat. Mat.*, 16:905, 2017.

[85] S. V. Ramankutty *et al.* . Electronic structure of the candidate 2D Dirac semimetal $\mathrm{SrMnSb_2}$: a combined experimental and theoretical study. *SciPost Phys.*, 4:010, 2018.

[86] C. Yi *et al.* . Large negative magnetoresistance of a nearly Dirac material: Layered antimonide $\mathrm{EuMnSb_2}$. *Phys. Rev. B*, 96:205103, 2017.

[87] R. Kealhofer *et al.* . Observation of a two-dimensional Fermi surface and Dirac dispersion in $\mathrm{YbMnSb_2}$. *Phys. Rev. B*, 97:045109, 2018.

[88] K. Kuroda *et al.* . Evidence for magnetic Weyl fermions in a correlated metal. *Nat. Mater.*, 16:1090, 2017.

[89] S. Nakatsuji, N. Kiyohara, and T. Higo. Large anomalous Hall effect in a non-collinear antiferromagnet at room temperature. *Nat.*, 527:212–215, 2015.

[90] Y. P. Du *et al.* . Dirac and Weyl Semimetal in XYBi (X = Ba, Eu; Y = Cu, Ag, Au). *Sci. Rep.*, 5:14423, 2015.

[91] J. Tong *et al.* . Magnetic properties of EuCuAs single crystal. *J. Alloys Comp.*, 602:26–31, 2014.

[92] T. Liang *et al.* . Anomalous Hall effect in $ZrTe_5$. *Nat. Phys.*, 14:451–455, 2018.

[93] J. Xiong *et al.* . Evidence for the chiral anomaly in the Dirac semimetal Na_3Bi . *Sci.*, 350(6259):413–416, 2015.

[94] C.-Z. Li *et al.* . Giant negative magnetoresistance induced by the chiral anomaly in individual Cd_3As_2 nanowires. *Nat. Comms.*, 6:10137, 2016.

[95] T. Liang *et al.* . Ultrahigh mobility and giant magnetoresistance in the Dirac semimetal Cd_3As_2. *Nat. Mater.*, 14:280, 2014.

[96] C. Y. Guo *et al.* . Evidence for Weyl fermions in a canonical heavy-fermion semimetal YbPtBi. *Nat. Comms.*, 9:4622, 2018.

[97] M. Hirschberger *et al.* . The chiral anomaly and thermopower of Weyl fermions in the half-Heusler GdPtBi. *Nat. Mater.*, 15:1161, 2016.

[98] T. Suzuki *et al.* . Large anomalous Hall effect in a half-Heusler antiferromagnet. *Nat. Phys.*, 12:1119–1123, 2016.

[99] K. Manna *et al.* . Heusler, Weyl and Berry. *Nat. Rev. Mater.*, 3:244, 2018.

[100] H. Weng *et al.* . Weyl Semimetal Phase in Noncentrosymmetric Transition-Metal Monophosphides. *Phys. Rev. X*, 5:011029, 2015.

[101] Y. Yamaji and M. Imada. Metallic Interface Emerging at Magnetic Domain Wall of Antiferromagnetic Insulator: Fate of Extinct Weyl Electrons. *Phys. Rev. X*, 4:021035, 2014.

[102] G. Chang *et al.* . Magnetic and noncentrosymmetric Weyl fermion semimetals in the RAlGe family of compounds (R = rare earth). *Phys. Rev. B*, 97:041104, 2018.

[103] S.-Y. Xu *et al.* . Discovery of Lorentz-violating type II Weyl fermions in LaAlGe. *Sci. Adv.*, 3(6):e1603266, 2017.

[104] J. Ruan *et al.* . Ideal Weyl Semimetals in the Chalcopyrites $\mathrm{CuTlSe_2}$, $\mathrm{AgTlTe_2}$, $\mathrm{AuTlTe_2}$, and $\mathrm{ZnPbAs_2}$. *Phys. Rev. Lett.*, 116:226801, 2016.

[105] J. Ruan *et al.* . Symmetry-protected ideal Weyl semimetal in HgTe-class materials. *Nat. Comms.*, 7:11136, 2016.

[106] T.-R. Chang *et al.* . Prediction of an arc-tunable Weyl Fermion metallic state in $\mathrm{Mo}_x\mathrm{W}_{1-x}\mathrm{Te}_2$. *Nat. Comms.*, 7:10639, 2016.

[107] Z. Wang *et al.* . $\mathrm{MoTe_2}$: A Type-II Weyl Topological Metal. *Phys. Rev. Lett.*, 117:056805, 2016.

[108] Y. Sun *et al.* . Prediction of Weyl semimetal in orthorhombic $\mathrm{MoTe_2}$. *Phys. Rev. B*, 92:161107, 2015.

[109] A. A. Soluyanov *et al.* . Type-II Weyl semimetals. *Nat.*, 527:495, 2015.

[110] E. Liu *et al.* . Giant anomalous Hall effect in a ferromagnetic kagome-lattice semimetal. *Nat. Phys.*, 14:1125–1131, 2018.

[111] J.-R. Soh *et al.* . An ideal Weyl semimetal induced by magnetic exchange. *arXiv:1901.10022*.

[112] D. S. Sivia. *Elementary Scattering Theory: For X-ray and Neutron Users*. OUP Oxford, 2011.

[113] G. L. Squires. *Introduction to the Theory of Thermal Neutron Scattering*. Dover books on physics. Dover Publications, 1978.

[114] E. Beaureparie *et al.* , editor. *Magnetism: A synchrotron radiation approach*. Springer Berlin Heidelberg, 2006.

[115] S. W. Lovesey and S. P. Collins. *X-ray Scattering and Absorption by Magnetic Materials*. Oxford science publications. Clarendon Press, 1996.

[116] J. Als-Nielsen and D. McMorrow. *Elements of Modern X-ray Physics*. Wiley, 2011.

[117] S. Grenier and Y. Joly. Basics of Resonant Elastic X-ray Scattering theory. *J. Phys.: Conf. Ser.*, 519(1):012001, 2014.

[118] J. P. Hill and D. F. McMorrow. X-ray resonant exchange scattering: polarization dependence and correlation functions. *Acta Crystallogr.*, A52:236–244, 1996.

[119] M. Blume and D. Gibbs. Polarization dependence of magnetic X-ray scattering. *Phys. Rev. B*, 37(4):1779–1789, 1988.

[120] S. W. Lovesey. *Theory of neutron scattering from condensed matter (Volume 1)*. International series of monographs on physics 72. Oxford University Press, 1984.

[121] S. W. Lovesey. *Theory of neutron scattering from condensed matter (Volume 2)*. Oxford University Press, 1984.

[122] M. C. Rahn *et al.* . Spin dynamics in the antiferromagnetic phases of the Dirac metals $A\text{MnBi}_2$ ($A = \text{Sr}, \text{Ca}$). *Phys. Rev. B*, 95:134405, 2017.

[123] P. Giannozzi *et al.* . QUANTUM ESPRESSO: a modular and open-source software project for quantum simulations of materials. *J. Phys.: Condens. Mater.*, 21(39):395502, 2009.

[124] J. G. Rau, E. K.-H. Lee, and H.-Y. Kee. Spin-orbit physics giving rise to novel phases in correlated systems: Iridates and related materials. *Ann. Rev. Condens. Matter Phys.*, 7(1):195–221, 2016.

[125] M. Z. Hasan and C. L. Kane. Colloquium: Topological insulators. *Rev. Mod. Phys.*, 82:3045–3067, 2010.

[126] D. Pesin and L. Balents. Mott physics and band topology in materials with strong spin–orbit interaction. *Nat. Phys.*, 6:376, 2010.

[127] V. K. Anand and D. C. Johnston. Antiferromagnetism in EuCu_2As_2 and $\text{EuCu}_{1.82}\text{Sb}_2$ single crystals. *Phys. Rev. B*, 91:184403, 2015.

[128] S. Das *et al.* . Structural, magnetic, thermal, and electronic transport properties of single-crystal EuPd_2Sb_2. *Phys. Rev. B*, 81:054425, 2010.

[129] F. Weber *et al.* . Low-temperature properties and magnetic order of EuZn_2Sb_2. *Phys. Rev. B*, 73(1):014427, 2006.

[130] A. F. May *et al.* . Properties of single crystalline $A\text{Zn}_2\text{Sb}_2$ (A = Ca, Eu, Yb). *J. Appl. Phys.*, 111(3):033708, 2012.

[131] I. Schellenberg *et al.* . A 121Sb and 151Eu Mössbauer spectroscopic investigation of EuCd_2X_2 (X = P, As, Sb) and YbCd_2Sb_2. *Z. Anorg. Allg. Chem.*, 637(12):1863–1870, 2011.

[132] L. Paolasini *et al.* . ID20: A beamline for magnetic and resonant X-ray scattering investigations under extreme conditions. *J. Synchr. Rad.*, 14(4):301–312, 2007.

[133] H. Zhang *et al.* . Synthesis and properties of CaCd_2Sb_2 and EuCd_2Sb_2. *Intermetallics*, 18(1):193–198, 2010.

[134] H. Zhang *et al.* . Thermoelectric properties of $\text{Yb}_x\text{Eu}_{1-x}\text{Cd}_2\text{Sb}_2$. *J. Chem. Phys.*, 133:194701, 2010.

[135] H. Zhang *et al.* . Thermoelectric properties of $\text{Eu}(\text{Zn}_{1-x}\text{Cd}_x)_2\text{Sb}_2$. *Dalton Trans.*, 39:1101–1104, 2010.

[136] W. Min *et al.* . Effect of manganese doping on the thermoelectric properties of Zintl phase EuCd_2Sb_2. *J. of Rare Earths*, 33(10):1093–1097, 2015.

[137] Y. Goryunov *et al.* . The ESR Study of Eu Ternary Pnictides EuCd_2Sb_2 , EuZn_2As_2. *J. Phys. Conf. Ser.*, 391:012015, 2012.

[138] A. Artmann *et al.* . AM_2X_2-Verbindungen mit CaAl_2Si_2 -Struktur . XI [I] Struktur und Eigenschaften der Verbindungen ACd_2X_2 (A: Eu, Yb; X: P, As, Sb). *Z. Anorg. Allg. Chem.*, 622:679–682, 1996.

[139] U. Englisch *et al.* . The elliptical undulator UE46 and its monochromator beam-line for structural research on nanomagnets at BESSY-II. *7th Int. Conf. on Synchr. Rad. Instrum.*, 467-468:541–544, 2001.

[140] C. Detlefs. Polarization analysis of K-edge resonant X-ray scattering of germanium. *Physica B: Condens. Matt.*, 345(1-4):45–48, 2004.

[141] C. Mazzoli *et al.* . Disentangling multipole resonances through a full X-ray polarization analysis. *Phys. Rev. B*, 76:195118, 2007.

[142] C. Detlefs, M. Sanchez del Rio, and C. Mazzoli. X-ray polarization: General formalism and polarization analysis. *Euro. Phys. J.: Spec. Topics*, 208(1):359–371, 2012.

[143] H. J. Monkhorst and J. D. Pack. Special points for Brillouin-zone integrations. *Phys. Rev. B*, 13(12):5188–5192, 1976.

[144] L. A. Hemstreet, C. Y. Fong, and J. S. Nelson. First-principles calculations of spin-orbit splittings in solids using nonlocal separable pseudopotentials. *Phys. Rev. B*, 47(8):4238–4243, 1993.

[145] J. P. Perdew, K. Burke, and M. Ernzerhof. Generalized Gradient Approximation Made Simple. *Phys. Rev. Lett.*, 77:3865–3868, 1996.

[146] J. Kübler. *Theory of Itinerant Electron Magnetism.* Int. Ser. Monog. Phys. OUP Oxford, 2017.

[147] V. I. Anisimov, J. Zaanen, and O. K. Andersen. Band theory and Mott insulators: Hubbard U instead of Stoner I. *Phys. Rev. B*, 44(3):943–954, 1991.

[148] V. I. Anisimov *et al.* . Density-functional theory and NiO photoemission spectra. *Phys. Rev. B*, 48(23):16929–16934, 1993.

[149] V. I. Anisimov, F. Aryasetiawan, and A. I. Lichtenstein. First-principles calculations of the electronic structure and spectra of strongly correlated systems : the LDA + U method. *J. Phys.: Condens. Mat.*, 9:767, 1997.

[150] A. I. Liechtenstein, V. I. Anisimov, and J. Zaanen. Density-functional theory and strong interactions: Orbital ordering in Mott-Hubbard insulators. *Phys. Rev. B*, 52(8):R5467–R5470, 1995.

[151] G. Kotliar and D. Vollhardt. Strongly Correlated Materials : Insights From Dynamical Mean-Field Theory. *Phys. Today*, 57(3):53–59, 2004.

[152] M. C. Rahn *et al.* . Coupling of magnetic order and charge transport in the candidate Dirac semimetal $EuCd_2As_2$. *Phys. Rev. B*, 97:214422, 2018.

[153] N. Schroeter. $EuCd_2As_2$ update Diamond Light Source (unpublished). *unpublished*, 2016.

[154] G. Hua *et al.* . Dirac semimetal in type-IV magnetic space groups. *Phys. Rev. B*, 98:201116, 2018.

[155] H. P. Wang *et al.* . Anisotropic transport and optical spectroscopy study on antiferromagnetic triangular lattice $\mathrm{EuCd_2As_2}$: An interplay between magnetism and charge transport properties. *Phys. Rev. B*, 94:045112, 2016.

[156] X. Wang *et al.* . Single parabolic band transport in p-type $\mathrm{EuZn_2Sb_2}$ thermoelectrics. *J. Mater. Chem. A*, 5:24185–24192, 2017.

[157] H. Zhang *et al.* . A new type of thermoelectric material. *J. Chem. Phys.*, 129(164713):5, 2008.

[158] A. A. Burkov. Anomalous Hall Effect in Weyl Metals. *Phys. Rev. Lett.*, 113:187202, 2014.

[159] S.-Y. Xu *et al.* . Experimental discovery of a topological Weyl semimetal state in TaP. *Sci. Adv.*, 1(10):e1501092, 2015.

[160] A. Sakai *et al.* . Giant anomalous Nernst effect and quantum-critical scaling in a ferromagnetic semimetal. *Nat. Phys.*, 14:1119–1124, 2018.

[161] A. A. Coelho. *TOPAS* and *TOPAS-Academic*: an optimization program integrating computer algebra and crystallographic objects written in C++. *J. Appl. Crystallog.*, 51(1):210–218, 2018.

[162] C. M. Wang, H.-Z. Lu, and S.-Q. Shen. Anomalous Phase Shift of Quantum Oscillations in 3D Topological Semimetals. *Phys. Rev. Lett.*, 117:077201, 2016.

[163] G. Kresse and J. Furthmüeller. Efficiency of ab-initio total energy calculations for metals and semiconductors using a plane-wave basis set. *Comp. Mater. Sci.*, 6:15, 1996.

[164] G. Kresse and J. Furthmüller. Efficient iterative schemes for ab initio total-energy calculations using a plane-wave basis set. *Phys. Rev. B*, 54:11169–11186, 1996.

[165] M. Hoesch *et al.* . A facility for the analysis of the electronic structures of solids and their surfaces by synchrotron radiation photoelectron spectroscopy. *Rev. Sci. Instr.*, 88(1):013106, 2017.

[166] J. Krishna, T. Nautiyal, and T. Maitra. First-principles study of electronic structure, transport, and optical properties of $\mathrm{EuCd_2As_2}$. *Phys. Rev. B*, 98:125110, 2018.

[167] A. Narayanan *et al.* . Linear Magnetoresistance Caused by Mobility Fluctuations in n-Doped $\mathrm{Cd_3As_2}$. *Phys. Rev. Lett.*, 114:117201, 2015.

[168] Y. Ando. Topological Insulator Materials. *J. Phys. Soc. Jpn.*, 82(10):102001, 2013.

[169] N. Nagaosa *et al.* . Anomalous Hall effect. *Rev. Mod. Phys.*, 82:1539–1592, 2010.

[170] J. F. Steiner, A. V. Andreev, and D. A. Pesin. Anomalous Hall Effect in Type-I Weyl Metals. *Phys. Rev. Lett.*, 119:036601, 2017.

[171] S. P. Mukherjee and J. P. Carbotte. Anomalous DC Hall response in noncentrosymmetric tilted Weyl semimetals. *J. Phys.: Condens. Matter*, 30(11):115702, 2018.

[172] Y. Ferreiros, A. A. Zyuzin, and J. H. Bardarson. Anomalous Nernst and thermal Hall effects in tilted Weyl semimetals. *Phys. Rev. B*, 96:115202, 2017.

[173] O. V. Kotov and Y. E. Lozovik. Giant tunable nonreciprocity of light in Weyl semimetals. *Phys. Rev. B*, 98:195446, 2018.

[174] J. H. Wilson, A. A. Allocca, and V. Galitski. Repulsive Casimir force between Weyl semimetals. *Phys. Rev. B*, 91:235115, 2015.

[175] P. E. C. Ashby and J. P. Carbotte. Chiral anomaly and optical absorption in Weyl semimetals. *Phys. Rev. B*, 89:245121, 2014.

[176] S. A. Parameswaran *et al.* . Probing the Chiral Anomaly with Nonlocal Transport in Three-Dimensional Topological Semimetals. *Phys. Rev. X*, 4:031035, 2014.

[177] I. A. Zaliznyak *et al.* . Polarized neutron scattering on HYSPEC: the HYbrid SPECtrometer at SNS. *J. Phys.: Conf. Ser.*, 862(1):012030, 2017.

[178] A. Hiess *et al.* . ILL's renewed thermal three-axis spectrometer IN8: A review of its first three years on duty. *Physica B*, 385-386:1077–1079, 2006.

[179] M. Kempa *et al.* . The FlatCone multianalyzer setup for ILL's three-axis spectrometers. *Physica B*, 385-386:1080–1082, 2006.

[180] M. Boehm *et al.* . The vTAS suite: A simulator for classical and multiplexed three-axis neutron spectrometers. *Nuclear Instruments and Methods in Physics Research A*, 697:40–44, 2013.

[181] Y.-F. Guo *et al.* . Coupling of magnetic order to planar Bi electrons in the anisotropic Dirac metals $A\mathrm{MnBi}_2(A = \mathrm{Sr}, \mathrm{Ca})$. *Phys. Rev. B*, 90:075120, 2014.

[182] L. Li *et al.* . Electron-hole asymmetry, Dirac fermions, and quantum magnetoresistance in BaMnBi_2. *Phys. Rev. B*, 93:115141, 2016.

[183] Y.-Y. Wang, Q.-H. Yu, and T.-L. Xia. Large linear magnetoresistance in a new Dirac material BaMnBi_2. *Chin. Phys. B*, 25(10):107503, 2016.

[184] G. L. Squires. *Introduction to the Theory of Thermal Neutron Scattering.* Cambridge University Press, 3 edition, 2012.

[185] S. Toth and B. Lake. Linear spin wave theory for single-q incommensurate magnetic structures. *J. Phys.: Condens. Matter*, 27(16):166002, 2015.

[186] J. Saroun and J. Kulda. RESTRAX - a program for TAS resolution calculation and for scan profile simulation. *Physica B*, 234:1102, 1997.

[187] J. Saroun and J. Kulda. Monte Carlo Ray-Tracing Code for RESTRAX. *Neutron News*, 13:15, 2002.

[188] Y. Feng *et al.* . Strong Anisotropy of Dirac Cones in SrMnBi_2 and CaMnBi_2 Revealed by Angle-Resolved Photoemission Spectroscopy. *Sci. Rep.*, 4:5385, 2014.

[189] K. Wang *et al.* . Two-dimensional Dirac fermions and quantum magnetoresistance in $\mathrm{CaMnBi_2}$. *Phys. Rev. B*, 85:041101, 2012.

[190] A. Zhang *et al.* . Interplay of Dirac electrons and magnetism in $\mathrm{CaMnBi_2}$ and $\mathrm{SrMnBi_2}$. *Nat. Comms.*, 7:13833, 2016.

[191] Y.-Y. Wang *et al.* . Quantum oscillations and coherent interlayer transport in a new topological Dirac semimetal candidate $\mathrm{YbMnSb_2}$. *Phys. Rev. Mater.*, 2:021201, 2018.

[192] J. Y. Liu *et al.* . Nearly massless Dirac fermions hosted by Sb square net in $\mathrm{BaMnSb_2}$. *Sci. Rep.*, 6:30525, 2016.

[193] N. Kiyohara, T. Tomita, and S. Nakatsuji. Giant Anomalous Hall Effect in the Chiral Antiferromagnet $\mathrm{Mn_3Ge}$. *Phys. Rev. Appl.*, 5:064009, 2016.

[194] A. K. Nayak *et al.* . Large anomalous Hall effect driven by a nonvanishing Berry curvature in the noncolinear antiferromagnet $\mathrm{Mn_3Ge}$. *Sci. Adv.*, 2(4):e1501870, 2016.

[195] J. Balluff *et al.* . Enhancing magnetic properties in $\mathrm{Mn_3Ge}$ thin films by doping. *Phys. Rev. B*, 97:014403, 2018.

[196] H. Kurt *et al.* . Magnetic and electronic properties of $D022$-$\mathrm{Mn_3Ge}$ (001) films. *Appl. Phys. Lett.*, 101(13):132410, 2012.

[197] D. D. Dung *et al.* . Magnetism and transport properties of α-Mn structure $\mathrm{Mn_3Ge}$ thin film. *J. Appl. Phys.*, 109(7):07C310, 2011.

[198] A. Sugihara *et al.* . Epitaxial Growth of Hard Ferrimagnetic $\mathrm{Mn_3Ge}$ Film on Rhodium Buffer Layer. *Metals*, 5(2):910–919, 2015.

[199] T. Ogasawara *et al.* . Structural and antiferromagnetic characterization of noncollinear $D019$ $\mathrm{Mn_3Ge}$ polycrystalline film. *J. Magn. Magn. Mater.*, 473:7–11, 2019.

[200] J. Jeong *et al.* . Termination layer compensated tunnelling magnetoresistance in ferrimagnetic Heusler compounds with high perpendicular magnetic anisotropy. *Nat. Comms.*, 7:10276, 2016.

[201] G.-Y. Guo and T.-C. Wang. Large anomalous Nernst and spin Nernst effects in the noncollinear antiferromagnets $\mathrm{Mn_3}X$ $(X = \mathrm{Sn, Ge, Ga})$. *Phys. Rev. B*, 96:224415, 2017.

[202] J. Kübler and C. Felser. Non-collinear antiferromagnets and the anomalous Hall effect. *Europhys. Lett.*, 108(6):67001, 2014.

[203] Y. Zhang *et al.* . Strong anisotropic anomalous Hall effect and spin Hall effect in the chiral antiferromagnetic compounds $\mathrm{Mn_3}X$ (X = Ge, Sn, Ga, Ir, Rh, and Pt). *Phys. Rev. B*, 95:075128, 2017.

[204] J. Kübler and C. Felser. Weyl fermions in antiferromagnetic $\mathrm{Mn_3Sn}$ and $\mathrm{Mn_3Ge}$. *Europhys. Lett.*, 120(4):47002, 2017.

[205] J.-P. Liu and L. Balents. Anomalous Hall Effect and Topological Defects in Antiferromagnetic Weyl Semimetals: $\mathrm{Mn_3Sn/Ge}$. *Phys. Rev. Lett.*, 119:087202, 2017.

[206] H. Chen, Q. Niu, and A. H. MacDonald. Anomalous Hall Effect Arising from Noncollinear Antiferromagnetism. *Phys. Rev. Lett.*, 112:017205, 2014.

[207] J. S. Kouvel and J. S. Kasper. Neutron diffraction study of $\mathrm{Mn_3Ge}$. *Proc. Conf. on Magn.*, page 169, 1965.

[208] G. Kádár and E. Krén. Neutron diffraction study of $\mathrm{Mn_3Ge}$. *Int. J . Magn.*, page 143, 1971.

[209] P. J. Brown *et al.* . Determination of the magnetic structure of $\mathrm{Mn_3Sn}$ using generalized neutron polarization analysis. *J. Phys.:Condens. Matter*, 2(47):9409, 1990.

[210] S. Tomiyoshi, Y. Yamaguchi, and T. Nagamiya. Triangular spin configuration and weak ferromagnetism of $\mathrm{Mn_3Ge}$. *J. Magn. Magn. Mater.*, 31-34:629–630, 1983.

[211] T. Nagamiya, S. Tomiyoshi, and Y. Yamaguchi. Triangular spin configuration and weak ferromagnetism of $\mathrm{Mn_3Sn}$ and $\mathrm{Mn_3Ge}$. *Solid State Commun.*, 42(5):385–388, 1982.

[212] P. J. Brown *et al.* . Antiferromagnetism in CuO studied by neutron polarimetry. *J. Phys.: Condens. Matter*, 3(23):4281, 1991.

[213] P. J. Brown. Polarised neutrons and complex antiferromagnets: an overview. *Physica B: Condens. Matter*, 297(1):198–203, 2001.

[214] N. Qureshi. *Mag2Pol*: a program for the analysis of spherical neutron polarimetry, flipping ratio and integrated intensity data. *J. Appl. Crystallogr.*, 52(1), 2019.

[215] T. Chatterji, editor. *Neutron Scattering from Magnetic Materials*. Elsevier, 2006.

[216] T. Nagamiya. Triangular Spin Ordering in Mn_3Sn and Mn_3Ge. *J. Phys. Soc. Jpn.*, 46(3):787–792, 1979.

[217] D. Zhang *et al.* . First-principles study of the structural stability of cubic, tetragonal and hexagonal phases in Mn_3Z (Z=Ga, Sn and Ge) Heusler compounds. *J. Phys.:Condens. Matter*, 25(20):206006, 2013.

[218] E. Leliévre-Berna *et al.* . Advances in spherical neutron polarimetry with Cryopad. *Physica B: Condens. Matter*, 356(1):131–135, 2005.

[219] J. Z. Ma *et al.* . Spin fluctuation induced Weyl semimetal state in the paramagnetic phase of $EuCd_2As_2$. *Sci. Adv.*, 5(7):eaaw4718, 2019.

[220] C. Niu *et al.* . Quantum anomalous Hall effect and gate-controllable topological phase transition in layered $EuCd_2As_2$. *Phys. Rev. B*, 99:235119, 2019.

[221] S. S.-L. Zhang *et al.* . Spin-to-charge conversion in magnetic Weyl semimetals. *arXiv:1904.07181*.

[222] L. Schoop *et al.* . Dirac cone protected by non-symmorphic symmetry and three-dimensional Dirac line node in ZrSiS. *Nat. Comms.*, 7:11696, 2016.

[223] A. Cortijo *et al.* . Elastic gauge fields in weyl semimetals. *Phys. Rev. Lett.*, 115:177202, 2015.

[224] R. Singha *et al.* . Large nonsaturating magnetoresistance and signature of nondegenerate Dirac nodes in ZrSiS. *Proc. Nat. Acad. Sci.*, 114(10):2468–2473, 2017.

[225] A. G. Grushin *et al.* . Inhomogeneous Weyl and Dirac Semimetals: Transport in Axial Magnetic Fields and Fermi Arc Surface States from Pseudo-Landau Levels. *Phys. Rev. X*, 6:041046, 2016.

[226] J. Hu *et al.* . Evidence of topological nodal-line fermions in zrsise and zrsite. *Phys. Rev. Lett.*, 117:016602, 2016.

[227] L. Šmejkal *et al.* . Topological antiferromagnetic spintronics. *Nat. Phys.*, 14:242, 2018.

[228] J. Hu *et al.* . π Berry phase and Zeeman splitting of Weyl semimetal TaP. *Sci. Rep.*, 6:18674, 2016.

[229] J. Hu *et al.* . Nearly massless Dirac fermions and strong Zeeman splitting in the nodal-line semimetal ZrSiS probed by de Haas–van Alphen quantum oscillations. *Phys. Rev. B*, 96:045127, 2017.

[230] A. S. Sukhanov *et al.* . Gradual pressure-induced change in the magnetic structure of the noncollinear antiferromagnet mn_3Ge. *Phys. Rev. B*, 97:214402, 2018.

8 Appendix

8.1 Derivations for $\frac{d\sigma}{d\Omega}$

The derivations for the expressions that describe the scattering cross-section in the soft X-ray resonant scattering in $EuCd_2Sb_2$ are based on the work by Hill and McMorrow [118]. I start with an expression of the scattering cross-section at the M_5 resonant edge which is given by,

$$\begin{aligned}
\frac{d\sigma}{d\Omega} &= \sum_{\lambda\lambda'} P_\lambda \left|\langle\lambda'\left|M_{E1}^{XRES}\right|\lambda\rangle\right|^2 \\
&= \left|\langle M_{E1}^{XRES}\rangle\right|^2 \\
&= \left|\left\langle a\left|\sum_n e^{i\mathbf{Q}\cdot\mathbf{r}_n} f_{nE1}^{XRES}\right|a\right\rangle\right|^2 \\
&= \left|\left\langle a\left|\sum_n e^{i\mathbf{Q}\cdot\mathbf{r}_n}\left[(\hat{\boldsymbol{\epsilon}}'\cdot\hat{\boldsymbol{\epsilon}})\,F^{(0)} - i\,(\hat{\boldsymbol{\epsilon}}'\times\hat{\boldsymbol{\epsilon}})\cdot\hat{\mathbf{z}}_n F^{(1)} + (\hat{\boldsymbol{\epsilon}}'\cdot\hat{\mathbf{z}}_n)(\hat{\boldsymbol{\epsilon}}\cdot\hat{\mathbf{z}}_n)F^{(2)}\right]\right|a\right\rangle\right|^2.
\end{aligned}$$

The first term refer to the charge Bragg peaks while the last two terms refer to the magnetic dipolar interactions, where $\mathbf{r}_n$ refers to the lattice sites of the magnetic species, $\mathbf{Q}$ is the scattering vector, $\hat{\mathbf{z}}_n$ is the magnetic moment at site n, $|a\rangle$ and $\langle a|$ is the initial and final state of the crystal respectively. Here $\hat{\boldsymbol{\epsilon}}$ and $\hat{\boldsymbol{\epsilon}}'$ refers to the polarisation of the incident and scattered X-ray respectively with λ and λ' being the corresponding wavelengths. It is not necessary, as it will become apparent later on in the derivation, to compute the dimensionless[38] co-efficients $F^{(0)}$, $F^{(1)}$ and $F^{(2)}$. When the incident radiation is tuned to the resonance of the species, we can assume that the dipolar terms will dominate to give,

$$\frac{d\sigma}{d\Omega} \simeq \left|\left\langle a\left|\sum_n e^{i\mathbf{Q}\cdot\mathbf{r}_n}\left[-i\,(\hat{\boldsymbol{\epsilon}}'\times\hat{\boldsymbol{\epsilon}})\cdot\hat{\mathbf{z}}_n F^{(1)} + (\hat{\boldsymbol{\epsilon}}'\cdot\hat{\mathbf{z}}_n)(\hat{\boldsymbol{\epsilon}}\cdot\hat{\mathbf{z}}_n)F^{(2)}\right]\right|a\right\rangle\right|^2.$$

---

[38] These co-efficients are the strongly energy dependent resonant strengths for the dipole transitions [115]

Resolving the magnetic moments along $\mathbf{U}_1$, $\mathbf{U}_2$, $\mathbf{U}_3$, I obtain the expressions for $(\hat{\boldsymbol{\epsilon}}' \times \hat{\boldsymbol{\epsilon}}) \cdot \hat{\mathbf{z}}_n$ and $(\hat{\boldsymbol{\epsilon}}' \cdot \hat{\mathbf{z}}_n)(\hat{\boldsymbol{\epsilon}} \cdot \hat{\mathbf{z}}_n)$ which are given by

$$\begin{aligned}
(\hat{\boldsymbol{\epsilon}}' \times \hat{\boldsymbol{\epsilon}}) \cdot \hat{\mathbf{z}}_n &= \begin{bmatrix} 0 & z_1 \cos\theta + z_3 \sin\theta \\ z_3 \sin\theta - z_1 \cos\theta & -z_2 \sin 2\theta \end{bmatrix}, \\
(\hat{\boldsymbol{\epsilon}}' \cdot \hat{\mathbf{z}}_n)(\hat{\boldsymbol{\epsilon}} \cdot \hat{\mathbf{z}}_n) &= \begin{bmatrix} z_2^2 & -z_2(z_1 \sin\theta + z_3 \sin\theta) \\ z_2(z_1 \sin\theta + z_3 \sin\theta) & -\cos^2\theta(z_1^2 \tan^2\theta + z_3^2) \end{bmatrix}.
\end{aligned}$$

Here the matrix elements refer to the scattering from the various channels,

$$\begin{bmatrix} \sigma \to \sigma' & \sigma \to \pi' \\ \pi \to \sigma' & \pi \to \pi' \end{bmatrix},$$

with $\mathbf{U}_1$, $\mathbf{U}_2$, $\mathbf{U}_3$ defined as,

$$\begin{aligned}
\mathbf{U}_1 &= -\hat{\mathbf{k}} \times \widehat{\mathbf{k}'}/\sin 2\theta, \\
\mathbf{U}_2 &= \hat{\mathbf{k}} + \widehat{\mathbf{k}'}/2\cos\theta, \\
\mathbf{U}_3 &= \hat{\mathbf{k}} - \widehat{\mathbf{k}'}/2\sin\theta. \qquad (16)
\end{aligned}$$

To elucidate if the magnetic moments are in-plane or perpendicular to the plane, I rotate the sample about the c axis. In the case of the Γ_5 irrep where $z_3 = 0$, we have $d\sigma/d\Omega$ as,

$$\left| \left\langle a \left| \sum_n e^{i\mathbf{Q}\cdot\mathbf{r}_n} \left[-iF^{(1)} \begin{bmatrix} 0 & z_1 \cos\theta \\ -z_1 \cos\theta & -z_2 \sin 2\theta \end{bmatrix} + F^{(2)} \begin{bmatrix} z_2^2 & -z_1 z_2 \sin\theta \\ z_1 z_2 \sin\theta & -z_1^2 \sin^2\theta \end{bmatrix} \right] \right| a \right\rangle \right|^2.$$

Here, I describe the magnetic moment as,

$$\hat{\mathbf{z}}_n = \cos(\tau \cdot \mathbf{r}_n)\mathbf{U}_1 + \sin(\tau \cdot \mathbf{r}_n)\mathbf{U}_2.$$

When the incident beam is polarised with the σ scattering configuration, the measured signal intensity is given by the contributions from the $\sigma \to \sigma'$ and the $\sigma \to \pi'$ channels which is given by,

$$\begin{aligned}\left.\frac{d\sigma}{d\Omega}\right|_{\sigma\Gamma_5} &= \left|\left\langle a\left|\sum_n e^{i\mathbf{Q}\cdot\mathbf{r}_n}\sin^2(\tau\cdot\mathbf{r}_n)F^{(2)}\right|a\right\rangle\right|^2 \\ &+\left|\left\langle a\left|\sum_n e^{i\mathbf{Q}\cdot\mathbf{r}_n}\left[i\cos(\tau\cdot\mathbf{r}_n)\cos\theta F^{(1)}+\sin(\tau\cdot\mathbf{r}_n)\cos(\tau\cdot\mathbf{r}_n)\sin\theta F^{(2)}\right]\right|a\right\rangle\right|^2 \\ &= 1/4F^{(2)2}\delta(\mathbf{Q}-\mathbf{G}) \\ &+ 1/4\cos^2\theta F^{(1)2}\delta(\mathbf{Q}-\mathbf{G}\pm\tau) \\ &+ 1/16\left(\sin^2\theta+1\right)F^{(2)2}\delta(\mathbf{Q}-\mathbf{G}\pm 2\tau).\end{aligned}$$

If the incident polarisations is in the π scattering configuration we obtain contributions from the $\pi \rightarrow \sigma'$ and the $\pi \rightarrow \pi'$ channels which is given by,

$$\begin{aligned}\left.\frac{d\sigma}{d\Omega}\right|_{\pi\Gamma_5} &= \left|\left\langle a\left|\sum_n e^{i\mathbf{Q}\cdot\mathbf{r}_n}\left[i\cos(\tau\cdot\mathbf{r}_n)\cos\theta F^{(1)}+\sin(\tau\cdot\mathbf{r}_n)\cos(\tau\cdot\mathbf{r}_n)\sin\theta F^{(2)}\right]\right|a\right\rangle\right|^2 \\ &+\left|\left\langle a\left|\sum_n e^{i\mathbf{Q}\cdot\mathbf{r}_n}\left[i\sin(\tau\cdot\mathbf{r}_n)\sin 2\theta F^{(1)})-\cos^2(\tau\cdot\mathbf{r}_n)\sin^2\theta F^{(2)}\right]\right|a\right\rangle\right|^2 \\ &= 1/4\sin^4\theta F^{(2)2}\delta(\mathbf{Q}-\mathbf{G}) \\ &+ 1/4\left(\cos^2\theta+\sin^2 2\theta\right)F^{(1)2}\delta(\mathbf{Q}-\mathbf{G}\pm\tau) \\ &+ 1/16\left(\sin^2\theta+\sin^4\theta\right)F^{(2)2}\delta(\mathbf{Q}-\mathbf{G}\pm 2\tau).\end{aligned}$$

Likewise, I repeat this treatment with the Γ_3 irrep where $z_1 = z_2 = 0$. Here $d\sigma/d\Omega$ is given by,

$$\left|\left\langle a\left|\sum_n e^{i\mathbf{Q}\cdot\mathbf{r}_n}\left[-iF^{(1)}\begin{bmatrix}0 & z_3\sin\theta\\ z_3\sin\theta & 0\end{bmatrix}+F^{(2)}\begin{bmatrix}0 & 0\\ 0 & -z_3^2\cos^2\theta\end{bmatrix}\right]\right|a\right\rangle\right|^2.$$

If I take the magnetic moment to be,

$$\hat{\mathbf{z}}_n = \sin(\tau\cdot\mathbf{r}_n)\mathbf{U}_3,$$

the corresponding expression for $d\sigma/d\Omega$ in the $\sigma \rightarrow \sigma'$ and the $\sigma \rightarrow \pi'$ channel is given by,

$$\begin{aligned}\left.\frac{d\sigma}{d\Omega}\right|_{\sigma\Gamma_3} &= \left|\left\langle a\left|\sum_n e^{i\mathbf{Q}\cdot\mathbf{r}_n} i\sin(\tau\cdot\mathbf{r}_n)\sin\theta F^{(1)}\right|a\right\rangle\right|^2 \\ &= 1/4\sin^2\theta F^{(1)2}\delta(\mathbf{Q}-\mathbf{G}\pm\tau),\end{aligned}$$

while the expression for $d\sigma/d\Omega$ in the $\pi \rightarrow \sigma'$ and the $\pi \rightarrow \pi'$ channel is given by,

$$\begin{aligned}
\left.\frac{d\sigma}{d\Omega}\right|_{\pi\Gamma_3} &= \left|\left\langle a \left| \sum_n e^{i\mathbf{Q}\cdot\mathbf{r}_n} i \sin(\tau \cdot \mathbf{r}_n) \sin\theta F^{(1)} \right| a \right\rangle\right|^2 \\
&+ \left|\left\langle a \left| \sum_n e^{i\mathbf{Q}\cdot\mathbf{r}_n} \sin^2(\tau \cdot \mathbf{r}_n) \cos^2\theta F^{(2)} \right| a \right\rangle\right|^2 \\
&= 1/4 \sin^2\theta F^{(1)2} \delta(\mathbf{Q} - \mathbf{G} \pm \tau) \\
&+ 1/16 \cos^4\theta F^{(2)2} \delta(\mathbf{Q} - \mathbf{G} \pm 2\tau).
\end{aligned}$$